

**Moving beyond the tensor:  
Advanced characterisation of white matter microstructure  
in Huntington's Disease using translational neuroimaging**

Chiara Casella



Thesis submitted for the degree of  
Doctor of Philosophy 2021

School of Psychology  
Cardiff University



# Thesis Summary

Huntington's disease (HD) is a genetic neurodegenerative disorder leading to devastating cognitive, psychiatric and motor symptoms. Currently, this disease cannot be cured, and a research priority is to increase the understanding of its pathogenesis and to provide biomarkers for evaluating the efficacy of targeted therapies.

Subtle and progressive white matter (WM) alterations have been observed early in HD progression, before clinical onset of the disease. However the aetiology of WM degeneration and its role in disease pathogenesis remain unclear. The assessment of early WM microstructural changes in the HD brain is therefore of fundamental importance, as this might prove useful for the identification of disease-related biomarkers and for measuring responsiveness to pharmaceutical and other therapeutic approaches.

The primary aim of this work was to exploit both ultra-strong gradients (300 mT/m) and ultra-high field (7 Tesla, 9.4 Tesla) to assess WM microstructure in HD, using a variety of MRI techniques in premanifest and manifest patients, as well as in a mouse model of the disease. Specifically, this Thesis moved beyond the diffusion tensor framework, with the application of advanced WM microstructural imaging.

Using these advanced MR techniques I was able to provide a comprehensive and detailed characterisation of WM microstructural alterations in the HD brain, and to better tease apart changes in apparent myelin from alterations in axon microstructure. Assessing both human patients and a mouse model of HD allowed for direct cross-species comparisons and bi-directional translation of results.

Additionally, I was able to exploit the improved compartmental specificity obtained by complementing standard DTI metrics with advanced MRI measurements, to study the effects of two months of a novel drumming training on WM plasticity in patients with manifest HD.

This in turn allowed to assess whether tailored cognitive-motor stimulation may lead to neural benefits in early HD, that could be exploited for delaying disease progression.

## Acknowledgements

I would like to express my sincere gratitude to my primary supervisors, Prof Derek Jones and Dr Claudia Metzler-Baddeley, for their guidance and continuous support throughout the course of this PhD. Their encouragement, motivation and optimism were fundamental not only for my academic progress but also for making my passion for science grow instead of wither. I consider myself very lucky to have had the opportunity to be their student.

I also wish to thank Dr Greg Parker, Dr Elena Kleban and Dr Ilona Lipp for answering my countless questions with patience, and for teaching me a lot of what I have learnt in these four years. And I would like to extend my appreciation to my secondary supervisor, Prof Anne Rosser, and to the Brain Repair Group, in particular Dr Mariah Lelos and Rachel Hills, who with their patience and willingness to train me were of invaluable help with my laboratory and animal work. Thanks also to the Wellcome Trust for their financial support and excellent training programme, without which this Thesis would not have been possible.

Thanks to my Welsh family, who have welcomed me and taken care of me in these four years. I have never felt so much part of a family outside my own, and this is thanks to you! And of course thank you to all of my Cardiff friends, for standing by my side and encouraging me to move forward even in the darkest moments, and for sharing with me the hardships a PhD can carry, as well as some of the best years of my life. You have made me feel loved and supported all along, and knowing that I was not alone really helped me to push through. I will treasure our Welsh adventures together forever!

Thanks to my London family, Zia Luci, Pankesh, Monya, Checco, and to my London friends, Naya, Seb, Lorie and Ellie, for giving me shelter from the storms of these four years, for offering me a place where to recharge, for fuelling my ambition, for the many stimulating conversations, the good wine(s) and food, and all the fun. It was extremely comforting to know I had a little piece of Home to come back to, especially at the beginning of this journey.

Most of all, I would like to thank my partner, Sam, who has shared with me every moment of this whole experience, and has supported me and this work in so many different ways; for always patiently listening to me, for all the useful input, for the countless hours spent teaching me to code, for the perpetual encouragement and for always helping me to believe in myself by believing in me.

Mamma, Papà, Checco, grazie per il vostro amore incondizionato e per non aver mai lasciato il mio fianco in questi (quasi) 32 anni, neanche nei miei momenti più bui. Grazie per avermi insegnato passione, ambizione, perserveranza, umiltà, e per avermi supportato nella lotta per i miei sogni. Siete il mio esempio più grande e questa Tesi è dedicata a voi.

## **Publications arising from this Thesis**

- **Chapter 1 has been published as a review article in Movement Disorders**

**Casella, C., Lipp, I., Rosser, A., Jones, D. K., & Metzler-Baddeley, C. (2020).** A critical review of white matter changes in Huntington's disease. *Movement Disorders*, 35(8), 1302-1311.

- **Chapter 6 has been published as a research report in the Journal of Huntington's Disease**

**Casella, C., Bourbon-Teles, J., Bells, S., Coulthard, E., Parker, G. D., Rosser, A., Jones, D. K., & Metzler-Baddeley, C. (2020).** Drumming Motor Sequence Training Induces Apparent Myelin Remodelling in Huntington's Disease: A Longitudinal Diffusion MRI and Quantitative Magnetization Transfer Study. *Journal of Huntington's disease*, 9(3), 303–320.

- **The work described in Chapter 4 has been submitted to Neuroimage: Clinical**

**Casella, C., Kleban, E., Rosser, A., Rickards, H., Coulthard, E., Metzler-Baddeley, C. & Jones, D. K. (2020).** Frequency difference mapping quantifies myelin breakdown in premanifest Huntington's disease.

# Abbreviations

## A

---

AD	Axial diffusivity
ANCOVA	Analysis of covariance
ANOVA	Analysis of variance

## C

---

CAG	Cytosine, adenine, and guanine
CC	Corpus callosum
CHARMED	Composite Hindered and Restricted Model of Diffusion
CI	Confidence intervals
CST	Cortico-spinal tract
CV	Coefficient of variation

## D

---

DBS	Disease burden score
DCL	Diagnostic confidence level
dMRI	Diffusion MRI
DT MRI	Diffusion tensor magnetic resonance imaging
DTI	Diffusion tensor imaging

## E

---

EPI	Echo planar imaging
EV	Explanation variable

## F

---

FA	Fractional anisotropy
FAS	Functional assessment score
FDM	Frequency difference mapping
FDR	False discovery rate

fODF	Fiber orientation density function
FoV	Field of view
FR	Restricted fraction
FSPGR	Fast spoiled gradient echo
FWE	Family-wise error
FWF	Free-water fraction

## **G**

---

GM	Grey matter
----	-------------

## **H**

---

HD	Huntington's disease
<i>HTT</i>	Huntingtin

## **I**

---

ICV	Intra-cranial volume
-----	----------------------

## **K**

---

KMO	Kaiser-Meyer-Olkin
-----	--------------------

## **M**

---

MD	Mean diffusivity
mGRE	Multi-echo gradient-recalled echo
MoCA	Montreal Cognitive Assessment
MPF	Macromolecular proton fraction
MPRAGE	Magnetization prepared - rapid gradient echo
MRI	Magnetic resonance imaging
MT	Magnetization transfer
MT-w	MT-weighted
MTI	Magnetization transfer imaging

MTR	Magnetization transfer ratio
MWF	Myelin water fraction
MWI	Myelin water imaging

## **P**

---

PBS	Phosphate buffered saline
PCA	Principal component analysis
PEBL	Psychology Experiment Building Language
PFA	Paraformaldehyde

## **Q**

---

qMT	Quantitative magnetization transfer
-----	-------------------------------------

## **R**

---

RD	Radial diffusivity
RF	Radio-frequency
ROI	Region of interest

## **S**

---

SD	Standard deviation
SE	Spin-echo
SMA	Supplementary motor area
SPGR	Spoiled gradient recalled-echo

## **T**

---

T <sub>1</sub> -w	T <sub>1</sub> -weighted
TBSS	Tract-based spatial statistics
TE	Echo time
TEM	Transmission electron microscopy
TFC	Total functional score
TMS	Total motor score

TOPF-UK      Test of Premorbid Functioning - UK Version

TOPF-UK FSIQ      TOPF-UK full scale IQ

TR              Repetition time

## **U**

---

UHDRS          Unified Huntington's Disease Rating Scale

## **V**

---

VBM            Voxel-based morphometry

## **W**

---

WAIS-R        Wechsler Adult Intelligence Scale-Revised

WM            White matter

# Table of Contents

<b>CHAPTER 1 GENERAL INTRODUCTION .....</b>	<b>1</b>
1.1. HUNTINGTON'S DISEASE (HD).....	1
1.2. SYMPTOMS OF HD.....	2
1.2.1. <i>Motor profile</i> .....	3
1.2.2. <i>Cognitive profile</i> .....	4
1.2.3. <i>Psychiatric profile</i> .....	6
1.3. NEUROPATHOLOGY OF HD .....	8
1.3.1. <i>Grey matter (GM) pathology</i> .....	9
1.3.2. <i>Macroscopic changes in GM as detected with neuroimaging</i> .....	12
1.3.3. <i>White matter (WM) changes in HD</i> .....	14
1.4. WM IMPAIRMENT IN HD: SECONDARY TO, OR INDEPENDENT OF, NEURONAL DEGENERATION? .....	18
1.4.1. <i>Evidence from neurochemical studies</i> .....	18
1.4.2. <i>Evidence from imaging studies</i> .....	20
1.4.3. <i>Moving beyond volumetric and DT-MRI to assess WM microstructure changes in HD</i> .....	27
1.5. WHY STUDY WM MICROSTRUCTURE IN HD? .....	31
1.6. ANIMAL MODELS OF HD .....	34
1.7. A TRANSLATIONAL NEUROIMAGING APPROACH TO STUDY HD: ADVANTAGES AND CHALLENGES .....	37
1.8. AIMS OF THE PRESENT WORK.....	41
<b>CHAPTER 2 GENERAL METHODS .....</b>	<b>43</b>
2.1. OVERVIEW .....	43
2.2. ADVANTAGES AND CHALLENGES OF ULTRA-HIGH FIELD AND ULTRA-STRONG GRADIENTS MRI .....	44
2.2.1. <i>Imaging the brain at ultra-high field</i> .....	45
2.2.2. <i>Microstructural imaging of the brain with ultra-strong gradients</i> .....	48
2.3. MRI TECHNIQUES TO CHARACTERIZE WM MICROSTRUCTURE .....	53
2.3.1. <i>Diffusion-weighted imaging (DWI)</i> .....	54
2.3.2. <i>Analysis of DWI data: the diffusion tensor and beyond</i> .....	56
2.3.3. <i>Magnetization transfer (MT) imaging</i> .....	58
2.3.4. <i>Susceptibility-weighted imaging (SWI) and frequency difference mapping</i> .....	62
2.4. ANALYSIS TECHNIQUES FOR THE ASSESSMENT OF WM MICROSTRUCTURE .....	64
2.4.1. <i>Moving beyond voxel-based (VB) analyses</i> .....	65
2.4.2. <i>Using tractometry for a multi-modal assessment of WM microstructure</i> .....	70
2.5. OVERVIEW OF MRI ACQUISITION AND ANALYSIS APPROACHES UTILISED IN THE PRESENT WORK.....	72
2.6. RECAP OF INTRODUCTORY CHAPTERS .....	78
<b>CHAPTER 3 INVESTIGATION OF WHITE MATTER MICROSTRUCTURE IN PREMANIFEST HD WITH ULTRA-STRONG GRADIENTS .....</b>	<b>79</b>
3.1. CHAPTER SUMMARY .....	79
3.2. DECLARATION OF COLLABORATIONS.....	79
3.3. INTRODUCTION.....	80
3.4. MATERIALS AND METHODS .....	84
3.4.1. <i>Participants</i> .....	84
3.4.2. <i>Data acquisition</i> .....	90
3.4.3. <i>Image processing</i> .....	97
3.4.4. <i>Statistical analysis</i> .....	100
3.5. RESULTS.....	106
3.5.1. <i>Premanifest HD patients present impairments in the encoding, temporary storage and updating of information</i> .....	106
3.5.2. <i>Computation of a composite cognitive score in the HD sample</i> .....	109
3.5.3. <i>Premanifest HD patients present reduced striatal volume</i> .....	110
3.5.4. <i>Premanifest HD patients present alterations in callosal apparent myelin</i> .....	112

3.5.5.	<i>Striatal atrophy in premanifest HD relates to cognitive performance and disease burden; apparent callosal myelin is associated with CAG repeat length, cognitive performance and striatal atrophy, but not with disease burden</i>	118
3.5.6.	<i>Whole-brain analysis with TBCA reveals WM microstructure alterations in the posterior CC, the left CST and the right fronto-striatal projections</i>	123
3.6.	DISCUSSION	127
3.6.1.	<i>Premanifest HD patients present impairments in the encoding, temporary storage and updating of information</i>	127
3.6.2.	<i>Premanifest HD patients present atrophy in the striatum but not in the thalamus</i>	128
3.6.3.	<i>Premanifest HD patients present alterations in callosal apparent myelin, which are associated with CAG repeat length, cognitive performance and striatal atrophy</i>	130
3.6.4.	<i>Whole-brain analysis with TBCA reveals WM microstructure alterations in the posterior CC, the left CST and the right fronto-striatal projections</i>	135
3.6.5.	<i>Methodological considerations</i>	137
<b>CHAPTER 4 FREQUENCY DIFFERENCE MAPPING QUANTIFIES MYELIN BREAKDOWN IN PREMANIFEST HD .140</b>		
4.1.	CHAPTER SUMMARY	140
4.2.	DECLARATION OF COLLABORATIONS	140
4.3.	INTRODUCTION	140
4.4.	MATERIALS AND METHODS	143
4.4.1.	<i>Participants</i>	143
4.4.2.	<i>MRI data acquisition and processing</i>	146
4.4.3.	<i>Cognitive tests</i>	148
4.4.4.	<i>Statistical analysis</i>	150
4.5.	RESULTS	151
4.5.1.	<i>The precision of FDM in the corpus callosum is anatomically variable</i>	151
4.5.2.	<i>FDM reveals HD-related myelin changes in the posterior segment of the CC</i>	156
4.5.3.	<i>Premanifest HD is associated with greater age-related decline in executive functions</i>	158
4.5.4.	<i>Interindividual differences in myelin content in the posterior callosum relate to executive function but not to proximity to disease onset in premanifest HD patients</i>	159
4.6.	DISCUSSION	160
4.6.1.	<i>Reproducibility of the FDM signal across the CC</i>	160
4.6.2.	<i>Application of FDM to assess myelin content in premanifest HD</i>	161
4.6.3.	<i>Conclusions, future directions and methodological considerations</i>	164
<b>CHAPTER 5 MRI ASSESSMENT OF WM MICROSTRUCTURE IN THE R6/1 MOUSE MODEL OF HD: A HIGH-RESOLUTION, EX VIVO STUDY .....165</b>		
5.1.	CHAPTER SUMMARY	165
5.2.	DECLARATION OF COLLABORATIONS	166
5.3.	INTRODUCTION	166
5.4.	MATERIALS AND METHODS	168
5.4.1.	<i>Mice</i>	168
5.4.2.	<i>Perfusion</i>	169
5.4.3.	<i>MRI tissue preparation</i>	169
5.4.4.	<i>MRI data acquisition</i>	170
5.4.5.	<i>Image processing</i>	171
5.4.6.	<i>Tractography of the CC</i>	173
5.4.7.	<i>Ultra-structural analysis of axons in the CC using TEM</i>	175
5.4.8.	<i>Statistical analysis</i>	175
5.5.	RESULTS	180
5.5.1.	<i>R6/1 mice present alterations in apparent myelin and axon density across the CC</i>	180
5.5.2.	<i>R6/1 mice present areas of increased WM volume</i>	183
5.5.3.	<i>TBSS reveals widespread increases in apparent axon density in R6/1 mice</i>	184
5.5.4.	<i>The frequency distribution of myelinated axon diameters is skewed towards thinner axons in R6/1 mice</i>	186
5.6.	DISCUSSION	188
5.6.1.	<i>Methodological considerations</i>	191

<b>CHAPTER 6 DRUMMING MOTOR SEQUENCE TRAINING INDUCES APPARENT MYELIN REMODELLING IN HD PATIENTS .....</b>	<b>193</b>
6.1. CHAPTER SUMMARY .....	193
6.2. DECLARATION OF COLLABORATIONS.....	193
6.3. INTRODUCTION.....	194
6.4. MATERIALS AND METHODS .....	197
6.4.1. <i>Participants</i> .....	197
6.4.2. <i>Training intervention: Drumming-based rhythm exercises</i> .....	200
6.4.3. <i>Drumming assessment</i> .....	201
6.4.4. <i>Cognitive assessments</i> .....	201
6.4.5. <i>MRI data acquisition</i> .....	203
6.4.6. <i>MRI data processing</i> .....	204
6.4.7. <i>Deterministic Tractography</i> .....	205
6.4.8. <i>Statistical analyses</i> .....	207
6.5. RESULTS.....	210
6.5.1. <i>Training effects on drumming performance</i> .....	210
6.5.2. <i>Group differences in the effect of training on cognitive performance</i> .....	211
6.5.3. <i>Training effects on WM microstructure</i> .....	212
6.5.4. <i>Changes in microstructure do not correlate with improvement in drumming performance</i> .....	214
6.5.5. <i>HD patients present reductions in apparent myelin before training</i> .....	214
6.6. DISCUSSION .....	219
<b>CHAPTER 7 GENERAL DISCUSSION .....</b>	<b>224</b>
7.1. THESIS OVERVIEW .....	224
7.2. SUMMARY OF FINDINGS .....	226
7.3. BRINGING IT ALL TOGETHER.....	229
7.3.1. <i>Myelin pathology in HD: excessive myelin or myelin breakdown?</i> .....	229
7.3.2. <i>Axon pathology in HD: pathologically driven morphological alterations?</i> .....	231
7.3.3. <i>FR from CHARMED and <math>f_m</math> from FDM: novel HD imaging biomarkers?</i> .....	233
7.3.4. <i>Drumming rhythm training: possible therapeutic approach to symptomatic HD?</i> .....	234
7.3.5. <i>The importance of a translational neuroimaging approach</i> .....	235
7.3.6. <i>Conclusions and future directions</i> .....	236
<b>APPENDIX 1 SOLUTIONS.....</b>	<b>239</b>
A1.1. CHEMICAL-GRADE PHOSPHATE BUFFER SALINE (PBS) .....	239
A.1.2. PARAFORMALDEHYDE SOLUTION (PFA).....	239
A.1.3. SUCROSE SOLUTION .....	239
<b>REFERENCES.....</b>	<b>240</b>

## List of Figures

Figure 1. An overview of HD pathology. ....	8
Figure 2. Scheme of the neuron-glia cytoarchitectural relationship. ....	16
Figure 3. Two hypotheses of HD pathogenesis. ....	17
Figure 4. Translational MRI-based framework combining multi-modal imaging techniques in animal models and humans. ....	39
Figure 5. Schematic representation of the CHARMED model of diffusion. ....	58
Figure 6. Representation of the magnetization transfer effect. ....	61
Figure 7. Effect of magnetization transfer on the MRI signal. ....	62
Figure 8. Schematic representation of the 3-pool model for describing mGRE signal evolution in WM fibres of perpendicular to $B_0$ . ....	65
Figure 9. Schematic representation of hypervoxels. ....	68
Figure 10. The TBCA analysis pipeline. ....	69
Figure 11. Different approaches to the analysis of MRI data employed in the present work. ....	73
Figure 12. Segmentation of the CC. ....	100
Figure 13. Group differences in cognition. ....	108
Figure 14. Relationship of 2-back task performance with age and DBS. ....	109
Figure 15. Principal component analysis (PCA) of the cognitive data with varimax rotation. ....	110
Figure 16. Assessment of subcortical grey matter atrophy. ....	111
Figure 17. Principal component analysis (PCA) of the microstructure metrics with varimax rotation. ....	112
Figure 18. Callosal microstructure: patient-control differences across callosal segments, and relationship between age and inter-individual variability in callosal microstructure. ....	116
Figure 19. Conditional effects of group on apparent myelin for each callosal segment. ....	117
Figure 20. Relationship between apparent myelin in each callosal segment and cytosine, adenine, and guanine (CAG) repeat length in patients. ....	122
Figure 21. Results of the cluster-analysis obtained with tract-based cluster analysis (TBCA) between patients and controls. ....	124
Figure 22. Spearman correlations between significant tract based cluster analysis (TBCA) clusters in patients. ....	125
Figure 23. Schematic representation of the processing pipeline. ....	147
Figure 24. Schematic representation of the callosal segmentation protocol. ....	147
Figure 25. Example reproducibility data from on representative subject. ....	153
Figure 26. Assessment of the similarity of frequency difference curves. ....	154
Figure 27. Fitting parameters estimated from the three-pool model, grouped for all subjects. ....	155
Figure 28. Relationship between age and the myelin water signal fraction ( $f_m$ ), and between age and the frequency offsets between myelin and axonal water pools ( $\Delta\omega$ ) in the posterior callosal segment, split by group. ....	157
Figure 29. Principal component analysis (PCA) of the cognitive data with varimax rotation. ....	159
Figure 30. Relationship of executive function with age and myelin water signal fraction ( $f_m$ ). ....	160
Figure 31. Tractography of the corpus callosum (CC). ....	175
Figure 32. Schematic illustration of the axon and myelin sheath, measurement of the axon diameter and g-ratio calculation. ....	180
Figure 33. Tractometry analysis of the corpus callosum (CC). ....	183

Figure 34. Group-differences in white matter volume.....	184
Figure 35. Tract-based spatial statistics (TBSS) analysis of white matter microstructure in R6/1 mice.....	185
Figure 36. Ultra-structural analysis of axons in the corpus callosum (CC) using transmission electron microscopy.....	187
Figure 37. White matter pathway regions of interest.....	201
Figure 38. Sagittal views of the tractography protocols. ....	207
Figure 39. Mean ratings for drumming performance.....	213
Figure 40. Training-associated macromolecular proton fraction (MPF) changes. ....	218
Figure 41. Tract-based spatial statistics (TBSS) analysis of baseline macromolecular proton fraction (MPF) values. ....	218

## List of Tables

Table 1. Summary of MRI studies of HD animal models. ....	25
Table 2. MRI changes observed in the reviewed in vivo studies in HD patients. ....	33
Table 3. Overview of some of the potential advantages and disadvantages associated with increasing magnetic field strength. ....	47
Table 4. Overview of some of the potential advantages and disadvantages associated with increasing gradient strength. ....	52
Table 5. Overview of the mouse and patient MRI acquisition and analysis methods in reference to the different experimental chapters. ....	74
Table 6. Comparison of mouse and patient MRI parameters. ....	75
Table 7. Summary of participants' demographic and clinical background information. ....	87
Table 8. Background clinical information of the patients' cohort. ....	88
Table 9. Information about patients' medication. ....	89
Table 10. Cognitive outcome variables employed to assess patient-control differences in cognition and/or create a composite cognitive score to assess disease-related brain-function relationships. ....	94
Table 11. Scan parameters. ....	97
Table 12. Data structure input for PCA of callosal tractometry data. ....	103
Table 13. Correlations between apparent myelin scores, cognitive component scores, cytosine, adenine, and guanine (CAG) repeat-length, disease burden score (DBS) and striatal component scores. ....	120
Table 14. Correlations of significant clusters of microstructure metrics as detected with TBCA with cognitive component scores, striatal component scores, disease burden score (DBS) and CAG repeat length. ....	126
Table 15. Summary of participants' demographic and clinical background information. ....	144
Table 16. Background clinical information of the patients' cohort. ....	145
Table 17. Information about patients' medication. ....	145
Table 18. Cognitive outcome variables employed to assess patient-control differences in cognition. ....	149
Table 19. Coefficients of variation of the fitting parameters. ....	156
Table 20. Scan parameters. ....	170
Table 21. Demographics and background clinical information of the patients' cohort. ....	198
Table 22. Demographics and general cognitive profile of patients and controls. ....	199
Table 23. Cognitive outcome variables assessed in this study. ....	202
Table 24. Scan-parameters. ....	204
Table 25. Rotated component loadings on change in the cognitive benchmark tests. ....	214
Table 26. Summary statistics for the permutation analysis of training effects on FA, RD, FR and MPF, across the investigated tracts. Abbreviations: FA: fractional anisotropy; RD: radial diffusivity; FR: restricted volume fraction; MPF: macromolecular proton fraction. ....	216

# Chapter 1

## General Introduction

### 1.1. Huntington's disease (HD)

A distinct clinical profile, onset in midlife and an autosomal dominant inheritance pattern: these were the characteristics reported in the first ever description of HD (Huntington, 1967), or “hereditary chorea”, as it was originally termed. From the Latin “choreus”, meaning “dance”, chorea identifies hyperkinetic movements, characterized by involuntary brief, random, and irregular contractions, which make up the motor phenotype of HD (Lanska, 2000). HD has an estimated prevalence of 3.6 to 5.7 cases per 100,000 in the Caucasian population (Pringsheim et al., 2012).

The modern history of HD began on March 26<sup>th</sup>, 1993, with the identification of the single-gene mutation responsible for the disease (MacDonald et al. 1993): a cytosine, adenine and guanine (CAG) trinucleotide expansion within the Huntingtin (*HTT*) gene, located on the short arm of chromosome 4 (4p16.3), leading to an alteration in the form of the coded protein (Nance et al., 1999). Specifically, while repeat lengths of less than 27 and in the range of 27–35 are not associated with HD pathology, lengths between 36 and 39 cause HD at incomplete penetrance, leading to variable symptoms; the threshold for complete penetrance, and HD phenotype, is around 37-39 CAG repeats (Nopoulos, 2016; Roos, 2010). Additionally, the expanded CAG repeat is somatically unstable, and therefore “intermediate” CAG repeats ranging from 27-35 are at increased risk of expanding into the pathological range when transmitted to subsequent generations, especially in male intergenerational transmissions (Wheeler et al., 2007).

The discovery of the genetic mutation accountable for HD made this disease amenable to predictive genetic testing with estimation of years to the onset of symptoms (Pflanz et al., 2019). The number of CAG repeats is inversely related to the age of symptom onset, so that longer expansions cause earlier onset and more rapid progression (Rosenblatt et al., 2006, 2012; Tabrizi et al., 2013). Nevertheless, although CAG mutation length accounts for approximately 50% of variability in age of onset (Paulson & Albin, 2011), it is uncertain whether the rate of disease progression is linked to CAG size (Kiebertz et al., 1994; Marder et al., 2002). Specifically, knowledge of the CAG mutation size does not necessarily associate with the kind of HD-related symptoms the carrier is going to develop, their severity or how rapidly they're going to progress (Paulsen, 2011). The pathogenesis that results in the phenotype still remains to be fully understood, with disease progression clearly being influenced by factors, both genetic and environmental, other than mutation length (Paulson & Albin, 2011). In turn, the prognosis once symptoms begin is, unfortunately, predictable (Wild & Tabrizi, 2019), and though there is a strong potential for “gene silencing” (Kay et al., 2014) and mutant huntingtin concentration reduction (Tabrizi et al., 2019) as a possible therapeutic strategy, HD is currently incurable.

## **1.2. Symptoms of HD**

Clinical diagnosis of “symptomatic” HD onset requires the beginning of motor abnormalities such as chorea, motor impersistence (i.e. the inability to sustain simple voluntary movements), along with the presence of a family history of the disease (Paulsen et al. 2008). The mean age for HD onset ranges between 30 and 50 years of age, but the range of age of onset varies between 2 and 85 years of age (Roos, 2010).

Importantly, HD symptomatology is more widespread than purely motor. This indeed includes behavioural and psychiatric problems and a progressive decline in cognitive function

(Wild & Tabrizi, 2019). Additionally, although less well-known, unintended weight loss, sleep and circadian rhythm alterations, and autonomic nervous system dysfunction are also prevalent and debilitating features of HD (Roos, 2010). Crucially, cognitive and behavioural abnormalities are frequently present in HD carriers at least 15 years prior to motor diagnosis (Paulsen et al., 2006, 2008), and have been shown to both represent the greatest burden on families, and to be highly associated with functional decline (Hamilton et al., 2003; Nehl et al., 2004; Williams et al., 2010).

The characterisation of HD is constantly evolving, and cognitive and behavioural factors are increasingly being taken into account (Bates et al., 2015). These features imply the existence of critical pathogenic events prior to overt clinical evidence of motor impairments in HD, and are considered below, in addition to the HD motor phenotype.

### **1.2.1. Motor profile**

Motor symptoms of HD can be described as having two main elements: rapid involuntary movements of the face, trunk, and limbs (or chorea), and impairment of voluntary movements, leading to coordination disturbances and bradykinesia (Bates et al., 2015). Chorea is often prominent early in disease course, however this plateaus or even diminishes later on, when parkinsonism, dystonia and rigidity supervene. Further, this is not present in juvenile patients, that is, in those patients that are diagnosed with the disease before the age of 21 (Bates et al., 2015). Finally, although choreiform movements are striking to observers, affected individuals report these to be less of a problem than their caregivers do (Simpson et al., 2016), and consistently show reduced awareness of their presence (Sitek et al., 2011). Impairments in fine motor movements (e.g. incoordination, bradykinesia and rigidity), on the other hand, are characteristic of the patients with early disease onset, especially in juvenile HD, and also appear in patients with adult onset in late stages of the disease course (Bates et al., 2015; van Dijk et

al., 1986). Interestingly, this latter component progresses more steadily than chorea (Rosenblatt et al., 2006) and better predicts functional disability (Rosenblatt et al., 2012).

The motor features of HD can be assessed using the unified Huntington's disease rating scale (UHDRS) motor examination ("Unified Huntington's Disease Rating Scale," 1996). This has ratings for several items, including eye movements, speech, chorea, dystonia, rapid alternating movements, bradykinesia, and gait. Though motor findings upon neurological exams are quite sensitive, there has been increasing awareness of the fundamental role of cognitive and emotional features of HD in leading to functional disability, and therefore the importance of including them in diagnosis has been stressed (Bates et al., 2015).

### **1.2.2. Cognitive profile**

Cognitive decline in HD progresses gradually and is consistent with that observed in disorders associated with striatal-subcortical pathology, such as Parkinson's disease (Bates et al., 2015). More specifically, cognitive impairments in HD relate to psychomotor and executive functions (Roos, 2010; Snowden, 2017), along with prominent changes in working memory, emotion processing and social cognition (Snowden, 2017). Additionally, learning and information retrieval are decreased (Bates et al., 2015). Finally, although language in HD is relatively spared, most patients develop dysarthria, and therefore speech is disrupted (Chan et al., 2019).

One of the earliest detectable cognitive impairments in HD relates to emotion processing, with a particular difficulty concerning negative emotions, such as disgust, anger and fear (Henley et al., 2012; Snowden et al., 2008; Sprengelmeyer et al., 1996). Impairments can be detected in HD carriers who are more than 15 years from their predicted motor symptom onset (Paulsen, 2011; Stout et al., 2011). Difficulties are cross-modal, affecting both recognition of vocal and facial emotions (Calder et al., 2010; Snowden et al., 2008), and

concern emotional expression and well as recognition (Trinkler et al., 2013). Emotion processing impairment contributes to the social breakdown and decline in social cognition, sympathy and empathy that are common features of HD, leading to difficulties with interpersonal relationships, reduced flexibility and therefore impaired regulation of behaviour in accordance with social conventions (Snowden, 2017). Accordantly, families' anecdotal reports describe early difficulties in social relations in HD mutation carriers (Paulsen, 2011).

Additionally, aspects of social cognition other than emotion processing have also been shown to be compromised in HD, even in the premanifest stages (Adjeroud et al., 2016; Eddy & Rickards, 2015). Specifically, poor performance in tests of "Theory of mind", which require the ability to attribute intentions, beliefs and mental states, has been demonstrated (Allain et al., 2011; Brüne et al., 2011; Eddy et al., 2012; Snowden et al., 2003).

Psychomotor slowing is another change already present in the premanifest stage of HD (Maroof et al., 2011; Stout et al., 2012; Tabrizi et al., 2012), as demonstrated by performance on timed tasks such as Stroop, Digit symbol substitution and Trail making (Snowden et al., 2002; Stout et al., 2012; Tabrizi et al., 2012), and has been reported to be a significant predictor of functional capacity in everyday life (Beglinger et al., 2012; Eddy & Rickards, 2015). This highlights the tight relationship between motor and cognitive features of HD, both of which rely on cortical-basal ganglia circuits (Bates et al., 2015).

Moving closer to disease onset, cognitive symptoms appear to manifest as a dysexecutive syndrome (Papp et al., 2011). Specifically, impairments in functions known to rely on frontal-striatal networks, including multi-tasking (e.g. driving and talking), learning, working memory, planning, processing speed and mental flexibility can be identified (Duff et al., 2010; Lawrence et al., 1996, 1998a, 1998b; Robins Wahlin et al., 2015; Snowden et al., 2002; Stout et al., 2011; Williams et al., 2015). For example, patients with HD lose the ability to perform goal-directed actions and planned behaviours, or the capability to distinguish what

is relevant and what, on the other hand, can be ignored; flexibility of mind and the ability to make mental adjustments become impaired (Roos, 2010)

Memory problems as well are commonly reported in HD patients, and nearly 40% of premanifest participants were found to meet criteria for mild cognitive impairment, the transitional stage between normal cognition and dementia (Duff et al., 2010). A strong executive contribution to memory failures has been suggested (Snowden, 2017). Specifically, memory difficulties have been shown more in free recall than in recognition memory and cued recall; this suggests that, contrarily to what is observed in patients with Alzheimer's disease, memory impairment in HD patients involves an inefficient search of memory, rather than deficient memory per se (Rohrer et al., 1999). Nevertheless, a meta-analysis of studies examining episodic memory performance in HD (Montoya et al., 2006) indicated at least some degree of encoding impairment is present in HD patients.

### **1.2.3. Psychiatric profile**

Although not as consistent as motor and cognitive symptoms, the psychiatric features of HD can cause significant disability and be prominent early in the course of the illness (Bates et al., 2015). Psychiatric symptoms include a dysexecutive syndrome, leading to problems with behaviour initiation and inhibition, irritability, aggression, agitation, perseveration and lack of awareness of deficits (Loi et al., 2018; Papoutsis et al., 2014). Less common, although clinically important, are other symptoms such as delusional depression or a schizophrenia-like psychosis (Bates et al., 2015; Loi et al., 2018). Importantly, psychiatric deficits have been shown to be associated with reduced functional capacity (Sellers et al., 2020), and represent the most distressing aspect for HD and their families (Hamilton et al., 2003; Loi et al., 2018).

Depressive symptoms are the most common psychiatric symptom of HD and are reported by up to 50% of patients at some point during disease course (Thompson et al., 2012).

Importantly, they may predate the onset of motor symptoms by many years and can manifest throughout the disease course (Epping et al. 2016; Julien et al. 2007; van Duijn et al. 2008). Furthermore, depression may lead to an exacerbation in apathy and social withdrawal, worsened cognitive performance (Smith, Mills, Epping, Westervelt, & Paulsen, 2012), contribute to functional decline (Beglinger et al. 2010; Marder et al. 2000; Mayeux et al. 1986) and further impair quality of life (Read et al. 2013). Similarly, apathy has been shown to have a significant effect on functional disability and quality of life (Banaszkiewicz et al. 2012; Hamilton et al. 2003; Read et al. 2013). Irritability and poor temper are also the most common and problematic neuropsychiatric symptoms in HD (Craufurd & Snowden, 2014), and increased frequency of irritability has been observed up to 10 years before the onset of motor symptoms (Berrios et al. 2002; Julien et al. 2007).

Interestingly, depression, apathy and irritability have been shown to differentially relate to disease progression (Thompson et al. 2012). In general, loss of motivation and drive are present early in the disease course, and worsen as HD progresses. On the other hand, irritability is worse initially but seems to subside in later disease stages, probably because of apathy onset. Finally, depression may emerge at any time during the disease course. Importantly, while apathy is associated with motor, cognitive and functional markers of disease progression (Baudic et al. 2006; Naarding et al. 2009; Thompson, Snowden, Craufurd, & Neary, 2002), depression and irritability do not correlate with disease stage (Snowden, 2017). This highlights the multifactorial origin of psychiatric symptoms in HD, possibly involving psychological and genetic susceptibility factors, as well as the disease itself (Loi et al., 2018).

### 1.3. Neuropathology of HD

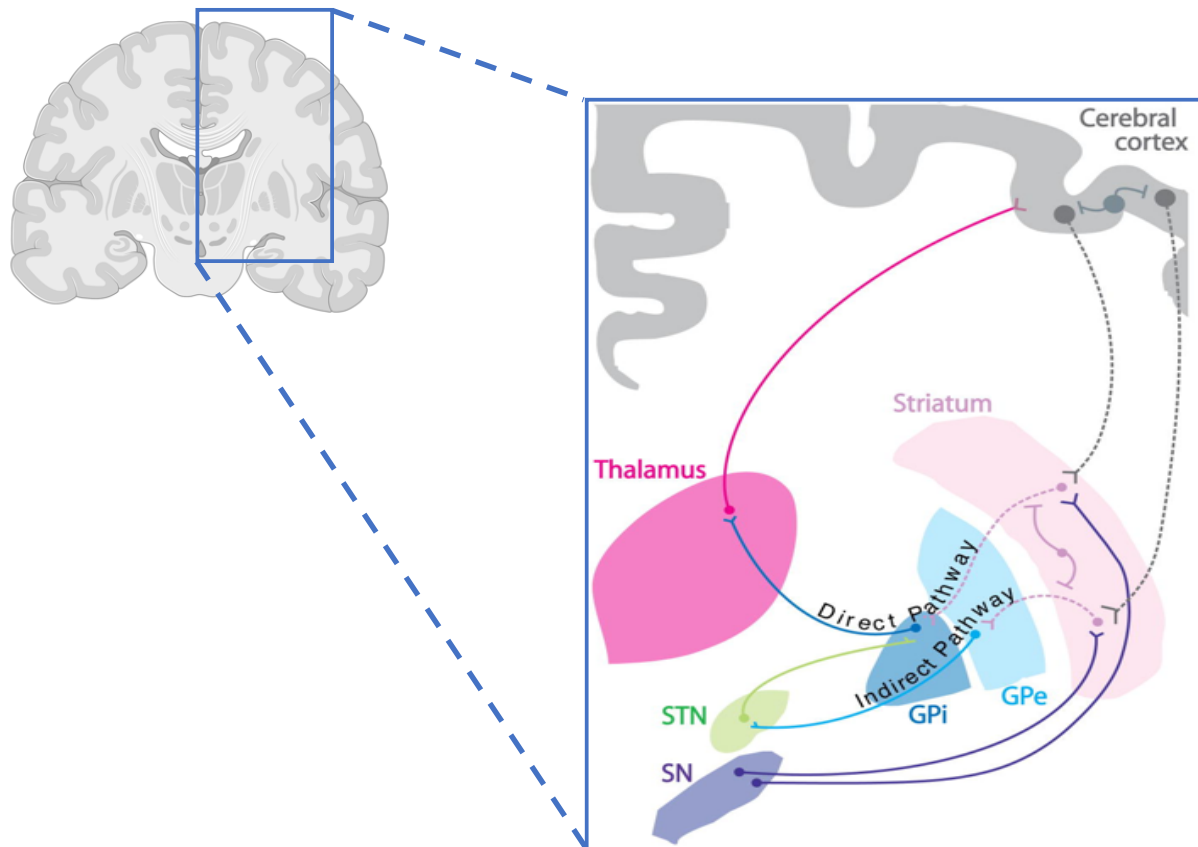


**Figure 1. An overview of HD pathology.**

The dashed lines represent the subset of projection neurons that are particularly vulnerable in HD. These are the medium spiny neurons of the striatum (MSNs, pink dashed lines), and the large pyramidal projection neurons in layers V, VI, and III of the cortex (grey dashed lines). Early stages of the disease affect MSNs in the “indirect pathway” of the basal ganglia, which project to the external segment of the globus pallidus (GPe). As HD progresses, pathology can be detected in MSNs projecting to the internal segment of the GPi via the “direct pathway” and in cortical pyramidal cells projecting to the striatum. On the other hand, interneurons in both the striatum (pink solid lines) and the cerebral cortex (grey solid lines) are mostly spared. Abbreviations: STN: subthalamic nucleus; GPe: external globus pallidus; GPi: internal globus pallidus; SN: substantia nigra (Figure adapted from Han et al. 2010).

### 1.3.1. Grey matter (GM) pathology

Normal *HTT* protein is ubiquitously expressed throughout the body, but its level of expression is higher in the brain, where it is found in all neurons, as well as glial cells (Bhide et al., 1996; Hebb et al., 1999; Landwehrmeyer et al., 1995; Li et al., 1993; Strong et al., 1993). *HTT* is one of the biggest proteins encoded by the genome, is highly conserved across species and is involved in diverse functions, including early development of the nervous system and other tissues, the recycling of vesicles and their fast transport along axons, direct and indirect control of gene transcription, metabolism, and regulation of cell division (Saudou & Humbert, 2016).

Mutant *HTT* (*mHTT*) is toxic to cells by affecting transcription, mitochondrial function, synaptic transmission and axonal transport (Orr & Zoghbi, 2007). Though *mHTT* is ubiquitously expressed like the normal protein, toxicity of *mHTT* is region-specific, and it especially affects certain neuronal subpopulations in the striatum and cerebral cortex (Figure 1) (DiFiglia et al., 1997; Gutekunst et al., 1999; Schulte & Littleton, 2011). More precisely, HD pathology is principally characterised by the death of the medium-sized spiny neurons of the striatum that utilise  $\gamma$ -aminobutyric acid (GABA), and cortical pyramidal neurons projecting to the striatum (Albin et al., 1992).

The striatum has a “direct” and an “indirect” output projection pathways. The former projects axons mono-synaptically to the internal segment of the of the globus pallidus (GPi) or the substantia nigra; the latter projects axons polysynaptically to the external segment of the globus pallidus (GPe). Early stages of HD are characterised by death of medium-sized spiny neurons of the striatum (MSN) projecting along the indirect pathway to the external globus pallidus; this in turn causes a disinhibition of the external globus pallidus, which in turn leads to disinhibition in the subthalamic nucleus (STN). As a consequence, the excitation in the GPi and the firing rate of the thalamus are altered. This increase in thalamic firing to neurons in the

motor areas of the cortex produces the motor phenotype, which identifies the clinical onset of HD. On the other hand, MSNs which project along the direct pathway to the GPi are affected later in the course of the disease (Figure 1) (Albin et al., 1990, 1991, 1992).

At the histological level, neuronal loss, astrocytosis and microgliosis can be observed in the HD brain within the basal ganglia, which consists of a set of subcortical brain structures (including the striatum), involved in various aspects of motor control and cognition (Graybiel, 1990; Mitchell et al., 1999). As HD progresses, neuropathology progressively extends along the caudal-rostral, and dorsal-ventral direction towards the putamen (Vonsattel & DiFiglia, 1998). Dramatic degeneration within the adjacent caudate nucleus leads to a prominent expansion of the lateral ventricles which is typical of advanced HD patients.

Significant neuronal loss is also observed in the cerebral cortex, including frontal, parietal, and temporal regions (Heinsen et al., 1994; Mann et al., 1993), and volumetric loss of up to 29% has been found post-mortem (de la Monte et al., 1988). Specifically, pyramidal neurons in layers III and V have been shown to be particularly vulnerable (Vonsattel et al., 1985), while overall neuronal loss appears most prominent in layers V and VI, and is associated with decreased thickness of the dorsolateral prefrontal cortex and a decrease in glial cell density in layer VI (Selemon et al., 2004). Importantly, as layer VI neurons do not project to the striatum, neuronal loss within this layer suggests that cortical pathology is not a secondary effect of Wallerian degeneration of axons projecting from the striatum, but it is instead an independent process (Ramaswamy & Kordower, 2012).

Another prominent pathological feature of HD is accumulation of *mHTT* aggregates in the nucleus, cytoplasm, and neuronal processes (DiFiglia et al., 1997; Gutekunst et al., 1999), in greater concentrations in the cortex than in the striatum (Gutekunst et al., 1999). Whether aggregates are pathogenic, incidental or a beneficial coping response in HD is yet to be clarified (Arrasate et al., 2004; Arrasate & Finkbeiner, 2012; Wanker, 2000).

Evidence has shown that protein aggregates in intra- and perinuclear inclusions have, in whole or in part, a fibrillar morphology (DiFiglia et al., 1997), leading to the suggestion that HD could be the result of a toxic amyloid fibrillogenesis (Wanker, 2000), as Alzheimer's disease, Parkinson's disease and prion diseases are (Lansbury, 1997). Consistent with this proposal, several studies have shown that protein aggregation plays a role in disease pathogenesis. For example, inclusions containing aggregates of huntingtin are detected in the HD brain but not in healthy individuals. Furthermore, inclusions are primarily found in neurons and regions most susceptible to degeneration and there is a clear association between aggregations and symptom severity (Wanker, 2000). Accordingly, it has been suggested that a possible therapeutic approach to treat HD may be to inhibit *mHTT* aggregation, to alleviate its downstream harmful effects (Kim & Kim, 2014; Wanker, 2000). There is indeed evidence that inhibition of aggregates alleviates the symptoms of disease in mouse models of HD and exerts protective effects on survival, striatal atrophy, weight loss and motor function (Sánchez et al., 2003; Tanaka et al., 2004).

However, the idea that protein aggregation plays a primary role in HD pathogenesis and induces neuronal degeneration has been challenged (Kim & Kim, 2014). Studies have shown that the formation of aggregates does not always correlate with the pattern of neurodegeneration, and that inclusion body formation predicts improved neuronal survival and leads to decreased levels of *mHTT* elsewhere in a neuron. Therefore, formation of aggregates may be beneficial to neuronal cells by protecting against huntingtin-induced cell death (Arrasate et al., 2004; Filimonenko et al., 2010; Klement et al., 1998; Saudou et al., 1998). It has to be noted that protein aggregation is a slow, progressive process, and therefore aggregate formation at any given time might not be an accurate indicator of disease progression. Furthermore, it might be that it is the formation of intermediate structures, such as transient

microaggregates, not easily detected by histochemical analyses, that initiate the neurodegenerative changes (Wanker, 2000).

### **1.3.2. Macroscopic changes in GM as detected with neuroimaging**

Imaging biomarkers play a fundamental role in aiding diagnosis, monitoring disease progression and assessing the effectiveness of disease-modifying therapies, providing support to clinical outcomes that may either show limited sensitivity, or need longer evaluation times (Fazio et al., 2018). Structural magnetic resonance imaging (MRI) has been the most widely studied imaging modality in HD to date (McColgan & Tabrizi, 2018). As with cognitive and motor abnormalities, differences in brain structure can already be detected in HD mutation carriers up to a decade prior to clinical diagnosis (Aylward et al. 2013; Harrington et al. 2014; Paulsen et al. 2014).

Consistent with the progressive neuronal death and gliosis, especially of MSN, observed at the histological level, striatal atrophy has been the most sensitive and robust finding in MRI studies, and has been proposed as a biomarker for future clinical trials (Georgiou-Karistianis et al., 2013b). Imaging evidence from PREDICT-HD, TRACK-HD and other studies, has shown that striatal atrophy is present in HD carriers as early as 15 years before disease onset, and that this progresses into the manifest disease phase (Aylward et al., 2012; Paulsen et al., 2014a, 2014b; Tabrizi et al., 2012, 2013). Furthermore, striatal volume correlates with CAG repeat size (Rosas et al., 2001) and adds predictive power for motor onset beyond age and CAG size (Aylward et al., 2012, 2013; Paulsen et al., 2014a, 2014b).

Nevertheless, brain neurodegeneration in HD is far more widespread than previously thought, even at the earliest disease stage, and includes extensive GM concentration reductions and significant annual changes in putamen, caudate and nucleus accumbens (Ciarochi et al., 2016; Harrington et al., 2016; Paulsen et al., 2008). Further, evidence shows that premanifest

subjects exhibit cortical thinning in frontal, parietal and temporal areas, suggesting that cortical atrophy occurs prior to clinical diagnosis, and possibly before basal ganglia pathology (Brundin et al., 2010; Rosas et al., 2005). This latter suggestion is consistent with histological evidence of degeneration of neurons in cortical layer VI, which do not project to the striatum, therefore indicating that neurodegeneration in this area may constitute an independent pathological process (Ramaswamy & Kordower, 2012). Additionally, premanifest individuals show decreased cortical folding in the left superior parietal and the right superior temporal regions, and increased cortical thinning at the bilateral pre-central and the superior frontal gyri, the left caudal middle frontal gyrus and the superior parietal region (Shishegar et al., 2019). Cortical thinning increases with disease progression, from premanifest to symptomatic stages (Tabrizi et al., 2009).

In general, in accord with histological evidence, recent studies have described a central-to-peripheral and posterior-to-anterior pattern of atrophy (Faria et al., 2016); furthermore, they have shown that estimates of atrophy of different areas correlate with functional, motor, and cognitive decline (Tabrizi et al., 2009). Later stages of the disease present severe cerebral and neo-striatal atrophy, enlarged frontal ventricles and multisystem degeneration (Ross et al., 2014; Rüb et al., 2015), affecting the cerebral cortex, pallidum, thalamus, brainstem and cerebellum (Rüb et al., 2016). Further research is needed to understand the additional involvement of other subcortical regions anatomically linked with these established targets of the disease, such as the amygdala, hypothalamus, subthalamic nucleus and claustrum (Rüb et al., 2015, 2016; Vonsattel & DiFiglia, 1998).

### 1.3.3. White matter (WM) changes in HD

Over the past years HD research has identified WM changes as relevant pathophysiological feature of HD (Bardile et al. 2018; Bartzokis et al. 2007; Beglinger et al. 2007; Ciarmiello et al. 2006; Gregory et al. 2018; Paulsen et al. 2008; Reading et al. 2005; Rosas et al. 2018; Wang & Yang, 2019). WM abnormalities have been shown both in animal models and in human HD carriers by histopathological *post-mortem* studies (de la Monte et al. 1988; Halliday et al. 1998; Huang et al. 2015; Jin et al. 2015), and MRI studies (Bartzokis et al. 2007; Jin et al. 2015; Meng et al. 2017; Rosas et al. 2018; Rosas et al. 2006; Tabrizi et al. 2009, 2011). Specifically, these have shown widespread WM volume loss (Aylward et al. 2011; Beglinger et al. 2007; Ciarmiello et al. 2006; Paulsen et al. 2008; Rosas et al. 2006; Tabrizi et al. 2009, 2011, 2012) and WM alterations at the microstructural and molecular level (Bartzokis et al. 2007; Dumas et al. 2012; Huang et al. 2015, 2015; Jin et al. 2015; Mascalchi et al. 2004; Matsui et al. 2014; Reading et al. 2005; Rosas et al. 2006; Stoffers et al. 2010; Wang & Yang, 2019).

The earliest WM alterations are seen in HD human carriers years before the onset of signs and symptoms of manifest HD. Prominent areas of damage include the striatum, corpus callosum (CC) and posterior WM tracts (Di Paola et al. 2014; Dumas et al. 2012; Faria et al. 2016; McColgan et al. 2018; Tabrizi et al. 2011). Furthermore, the severity of WM changes has been shown to correlate with predicted time to symptom onset in pre-manifest patients (Ciarmiello et al. 2006; Paulsen et al. 2008; Stoffers et al. 2010), with measures of motor dysfunction (Rosas et al. 2006), and with cognitive deficits (Bohanna et al. 2008; Rosas et al. 2006).

However, despite a subcortical WM volume loss of 29-34% already having been reported in *post-mortem* HD brains over 20 years ago (de la Monte et al. 1988), the aetiology of WM degeneration, and its role in disease pathogenesis and progression remain unclear.

While some work suggests that WM damage in HD is secondary to the loss of GM volume in the form of Wallerian degeneration (Di Paola et al. 2014; Gauthier et al. 2004; Rosas et al. 2018; Weaver et al. 2009), there is evidence suggesting that WM aberrations are a feature of HD that occurs independent of neuronal cell loss (Beglinger et al. 2007; Mascalchi et al. 2004; Myers et al. 1991; Paulsen et al. 2008; Reading et al. 2005; Rosas et al. 2008; Tabrizi et al. 2009). Accordingly, WM changes are present very early in the disease course, even in children at risk for HD (Lee, 2016), and in premanifest individuals who are several years away from symptom onset (Aylward et al. 2011; Bartzokis et al. 2007; Tabrizi et al. 2009). Notably, WM is composed of axons as well as myelin-producing oligodendrocytes (Figure 2), and it is unclear whether axons, myelin, or both are predominantly responsible for the WM loss (Gregory et al. 2018).

An increasing body of research suggests that WM in HD is subject to alterations in myelin-associated biological processes at the cellular and molecular level (Gómez-Tortosa et al. 2001; Huang et al. 2015; Jin et al. 2015; Myers et al. 1991; Teo et al. 2016). Myelin is an axon wrapping multi-layered sheath and is produced by oligodendrocytes (Figure 2). Axon myelination is vital during brain development and critical for healthy brain function, as it plays a fundamental role in the regulation of efficiency and speed of action potential propagation during synaptic transmission (Grydeland et al. 2013; Martenson, 1992). Dysfunction of oligodendrocytes and of myelin can slow down or stop otherwise fast axonal transport, which in turn can result in synaptic loss and eventually axonal degeneration (Han et al. 2010). Furthermore, as myelination patterns across the brain enable the temporal synchronisation of information processing, local demyelination can disrupt the performance of functional networks (Nickel & Gu, 2018).

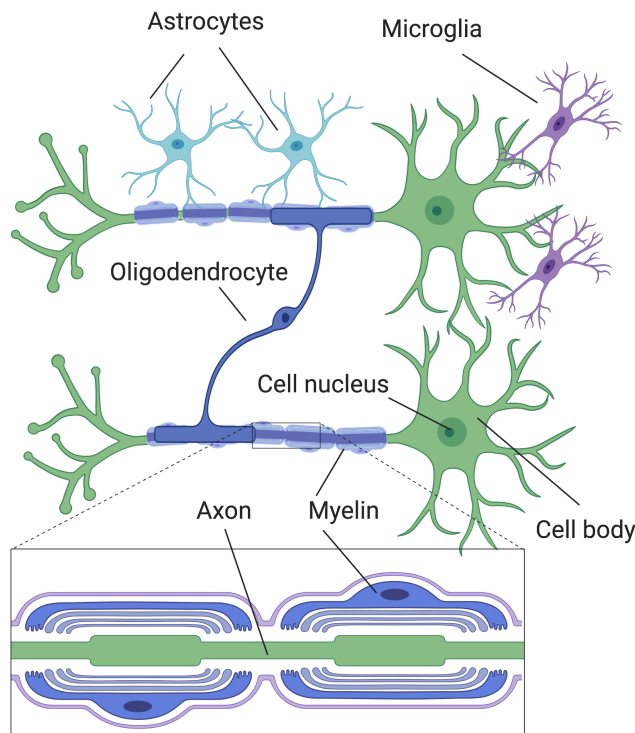


**Figure 2. Scheme of the neuron-glia cytoarchitectural relationship.**

*Glial cells (i.e. astrocytes, neuroglia and oligodendrocytes) interact with neurons in many different ways to maintain neural tissue's health, for which a peculiar cytoarchitecture is required, as shown here. Myelin is an insulating layer, or sheath, that wraps around axons, and is produced by oligodendrocytes; it allows electrical impulses to transmit quickly and efficiently along nerve cells, is vital during brain development and critical for healthy brain function.*

In clear opposition to the long-held conceptualisation of HD as a disorder of striatal GM (Figure 3), the “Demyelination Hypothesis” of HD (Bartzokis et al. 2007) suggests that *mHTT* leads to premature myelin breakdown in HD. More precisely, the gene mutation may interfere with the nourishment-delivery system by which brain-derived neurotrophic factor (BDNF) travels down axons and nourishes myelin sheaths. This interference results in a breakdown of myelin, leading to a disruption in cell signalling and neuronal death. A dysfunction of oligodendrocytes, in turn, might impair repair of de-myelinated axons, leading to chronic demyelination. Alternatively, as oligodendrocytes are the major iron-containing

cells of the CNS, it might be that homeostatic increases in these cells, related to their role in re-myelinating axons, cause significant increases in ferritin iron content (an iron storage protein). High ferritin iron is proposed to have toxic effects and could further contribute to impairments in WM and myelination (Bartzokis et al., 1999, 2007; Bartzokis & Tishler, 2000).

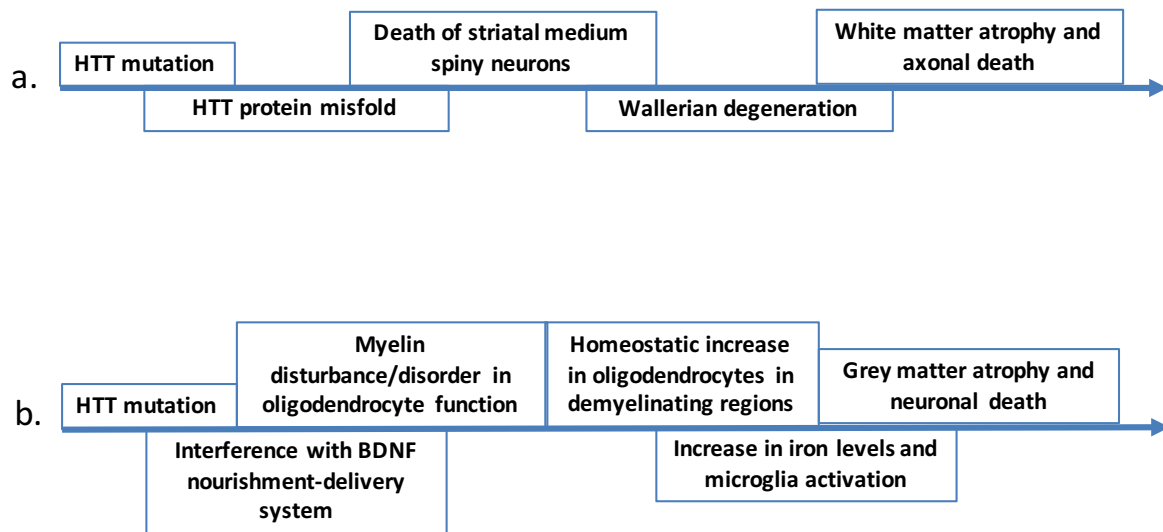


**Figure 3. Two hypotheses of HD pathogenesis.**

(a) Mutant huntingtin (mHTT) protein misfolding leads to protein aggregates, which in turn cause dysfunction of striatal medium spiny neurons, eventually leading to neuronal death. White matter abnormalities are a secondary effect of Wallerian degeneration of axon terminals from the striatum. (b) The Demyelination Hypothesis: HD pathogenesis originates from a toxic effect of mHTT on brain-derived neurotrophic factor (BDNF) which results in a breakdown of myelin, in turn leading to a disruption of cell signalling and neuronal death.

## **1.4. WM impairment in HD: secondary to, or independent of, neuronal degeneration?**

### **1.4.1. Evidence from neurochemical studies**

This section reviews evidence for molecular and neurochemical changes in oligodendrocyte lineage cells and myelin sheaths in HD. These changes have been reported in some human subjects and also in studies of animal models of HD.

#### ***Abnormalities of oligodendrocyte lineage cells in HD***

An increase in oligodendroglia differentiation in neural progenitor cells was observed during postnatal development in transgenic HD rats (Siebzehnrübl et al. 2018). Similarly, enhanced proliferation of oligodendrocyte precursor cells (OPCs) was found in adult HdhQ250 mice (Jin et al. 2015). Additionally, Simmons and colleagues (Simmons et al., 2007) reported increased immunostaining for ferritin, which is mostly found in oligodendrocytes, in the striatum, cortex and hippocampus of the R6/2 transgenic mouse model of HD, detectable before any behavioural abnormalities could be observed. Human *post-mortem* histopathological studies have also demonstrated an increase in the density of oligodendrocytes in the striatum of HD patients compared to healthy controls, years before striatal atrophy or loss of neurons occurs (Gómez-Tortosa et al. 2001; Myers et al. 1991). The increased number of oligodendrocytes observed suggests the presence of a homeostatic myelin repair mechanism, aiming to compensate deficits in myelination that seem to occur in HD.

In contrast, evidence suggests that oligodendrocyte lineage cells are the most depleted cell types amongst all non-neuronal cells in the symptomatic HD brain (Ernst et al. 2014). Furthermore, a dramatically lower number of mature oligodendrocytes during the postnatal myelination period has been shown in the HdhQ250 knock-in mouse model of HD (Jin et al. 2015). This evidence suggests that HD might be associated with a lack of oligodendrocytes,

which cannot repair demyelinated axons. Accordingly, silencing oligodendroglia-specific *mHTT* expression in BACHD mice rescues deficits in thickness and compactness of myelin sheaths that otherwise occur in these mice (Bardile et al. 2018), and expressing *mHTT* selectively in oligodendrocytes of transgenic mice induces impairments in myelination (Huang et al. 2015). Overall, the present findings suggest that there is a relationship between the HD mutation and oligodendrocyte dysfunction.

To summarize, while increased numbers of oligodendrocytes have been observed in the HD brain, their dysfunctionality may lead to unsuccessful myelination. It is also possible that the observed increased levels of oligodendrocytes are helpful at first but eventually lead to toxicity because of increased iron levels. Both explanations fit within the Demyelination Hypothesis (Bartzokis et al. 2007), as they implicate an increasingly unsuccessful compensation for the disease-related myelin loss.

### ***Myelin changes in HD***

Reports from human post-mortem studies have demonstrated a striking breakdown of myelin in the HD brain (Bruyn & von Wolferen, 1973). Additionally, some studies on animal models have indirectly demonstrated impairments in developmental myelination in HD. These have shown that the expression of a mutant huntingtin transgene in cells and in R6/2 transgenic mice leads to reduced activity in the cholesterol biosynthesis pathway; this in turn results in lower levels of newly synthesized cholesterol and its intermediates (Valenza et al. 2005, 2007), which are essential for the synthesis of myelin (Dietschy & Turley, 2004).

Electron microscopy investigations have reported thinner myelin sheaths, as reflected by higher g-ratios (the ratio of the inner axonal diameter to the outer diameter), in transgenic BACHD rats and in the HdhQ250 knock-in mouse model (Jin et al., 2015; Teo et al., 2016). HD myelin changes might either represent a breakdown of myelin into fragments because of toxicity, or thinner myelin sheaths because of a developmental dysfunction in myelination

mechanisms. Consistent with the latter, alterations in myelin sheaths are paralleled by reduced expression of myelin-related genes such as myelin basic protein (MBP) and myelin oligodendrocyte glycoprotein (MOG) in transgenic R6/2 and HdhQ250 knock-in mice (Blockx et al. 2012; Jin et al. 2015; Xiang et al. 2011). Reduced levels of MBP and MOG in brain regions known to be affected by HD throughout the critical postnatal myelination stage, and significantly fewer myelinated axons, have been reported in knock-in HdhQ250 mice (Jin et al. 2015). The reduction in myelin proteins may be due to a decreased expression of myelin regulatory factor (MRF), a transcription factor which controls expression of myelin-related proteins (Jin et al. 2015). Moreover, abnormalities in myelin sheaths and myelin-related gene transcripts in YAC128 transgenic mice are evident well before any striatal neuronal loss can be detected (Teo et al. 2016). These findings imply that a dysregulation of the temporal profile of myelination might underlie WM abnormalities and that disordered myelination during the post-natal period might constitute an important early pathogenic event in HD (Jin et al. 2015).

#### **1.4.2. Evidence from imaging studies**

Structural neuroimaging studies in animal models of HD (Table 1) and in HD carriers have shown that WM atrophy can be found across several WM areas, including the CC, the anterior commissure (AC), internal and external capsules (IC, EC), and the cingulum (CG). Furthermore they suggest that these WM changes happen very early in the disease course (Aylward et al. 2011; Ciarmiello et al. 2006; Di Paola et al. 2014; Ruocco et al. 2008; Tabrizi et al. 2009). Importantly, deficits in brain growth and WM changes are already found in children at risk for HD (Lee et al., 2012; Lee, 2016), further pointing to a neurodevelopmental effect of *mHTT*.

Some studies have suggested that WM is more affected than GM in the HD brain. For example, Tabrizi and colleagues (Tabrizi et al. 2012) showed that the rate of change of WM

volume over 24 months was greater than that of GM in premanifest and early HD patients (Tabrizi et al. 2012). Specifically, individuals carrying the *mHTT* gene who were far away from clinical diagnosis showed WM loss only around the striatum and within the CC and posterior WM tracts, while those close to clinical diagnosis and symptomatic HD patients showed extensive WM loss across the whole brain. Loss of WM volume over this time period ranged between 2% in HD carriers over 10 years away from disease onset and 4% in early HD patients. Effect sizes for atrophy rates between early HD participants and healthy controls were larger in WM (1.70, 1.40 to 2.08) than in GM. Additionally, a 2-year longitudinal study found that, when controlling for normal age-related variations, brain atrophy of premanifest patients was more pronounced in WM than in striatal GM (Aylward et al. 2011). Similarly, in another patient cohort WM volume was drastically reduced in premanifest participants as compared to controls ( $35.3 \pm 2.5$  mL vs  $37.7 \pm 2.2$  mL), whereas no significant differences were observed for GM volumes (Ciarmiello et al. 2006). These findings suggest that there might be a dissociation between neurodegenerative processes that happen in GM and WM aberrations in HD. Further, the temporal pattern of reported WM changes suggests that WM impairment in HD unlikely reflects solely a secondary result of neuronal cell death in GM, and may instead represent an independent factor of HD pathology.

Evidence for a link between GM and WM changes comes from studies that show significant atrophy of the cortical mantle of HD patients both cross-sectionally (Douaud et al., 2006; Kassubek et al., 2004; Rosas et al., 2002, 2005) and longitudinally (Ruocco et al. 2008), suggesting that WM volume loss may be a consequence of the withdrawal of axons projecting from cortical neurons. These studies have relied on measures of WM volumes. However, WM volume loss as quantified using structural MRI is a rather un-specific marker of disease stage and progression, as it is not sensitive to changes in microstructure. This makes it hard to capture differential effects across the various stages of the disease (Pflanz et al., 2019). As such,

reductions in WM volume observed in structural neuroimaging studies can be the consequence of several factors, including a decrease in the number of axons because of Wallerian degeneration (Douaud et al., 2006; Kassubek et al., 2004; Rosas et al., 2002, 2005; Ruocco et al., 2008), a decrease in axon myelination (Ciarmiello et al. 2006; Squitieri et al. 2009), or a combination of both.

New MRI methods allow us to move beyond traditional macrostructural volumetric methods, and provide more in-depth information about tissue integrity and organization at the microstructural and biochemical levels. To date, most neuroimaging studies of WM microstructure have used diffusion tensor MRI (DT-MRI) (Pierpaoli & Basser, 1996) to quantify tissue properties. This technique allows to characterize the three-dimensional diffusion of water as a function of spatial location and it is based on differential diffusion of water molecules depending on tissue type and architecture (Beaulieu, 2002). For example, the molecular diffusion rate [mean diffusivity (MD)], the extent to which diffusion is restricted [fractional anisotropy (FA)], the diffusion rate along the main axis of diffusion [axial diffusivity (AD)], and the rate of diffusion in the transverse direction [radial diffusivity (RD)] can be inferred.

Some evidence from DT-MRI studies suggests that WM aberrations in HD are a consequence of Wallerian axonal degeneration. For example, it has been shown that WM changes correlate with reductions in cerebral GM density (Di Paola et al. 2014; Rosas et al. 2018). Similarly, a DT-MRI study suggested that WM changes in HD are a consequence of axonal injury rather than demyelinating mechanisms, based on the observation of greater changes in AD, as compared to RD changes, in the brain of HD patients (Weaver et al. 2009).

On the other hand, there are several DT-MRI studies which have suggested a role for myelin in HD pathology (Bartzokis et al. 2007; Bourbon-Teles et al. 2017; Di Paola et al. 2012, 2014; Mascalchi et al. 2004; Rosas et al. 2018). These studies parallel findings from *post-*

*mortem*, histopathological studies in HD patients (Bruyn & von Wolferen, 1973). Firstly, insufficient myelination was suggested to be present in children at risk of HD, as they showed increased RD in the external capsule. Specifically, the authors hypothesized that this increase may reflect an impairment in myelin integrity due to a dysfunction in the trophic support mechanisms usually carried out by normal *HTT*. This, in turn, is suggested to affect myelin integrity by hindering the production and maintenance of large lipid membranes (Lee, 2016). Additionally, Di Paola and colleagues (Di Paola et al. 2012) suggested that demyelination is present in the premanifest HD brain, while both myelin breakdown and axonal damage are present in manifest HD. This proposal was based on the observation of decreased FA and increased RD in the isthmus of the CC of premanifest patients compared to age- and sex-matched controls, in the absence of any changes in AD (Di Paola et al. 2012). On the other hand, they reported both increased RD and decreased AD in the CC of manifest HD patients, compared to matched controls. Similarly, Rosas and colleagues showed increased RD in the WM of premanifest HD patients, which correlated with impaired performance on neuropsychological tests, and was proposed to reflect early deficits in myelin. Moreover, they suggested that axonal pathology, as shown by changes in AD, is present only later in the disease course (Rosas et al. 2018).

All of the above interpretations are built on the assumption of a direct correspondence between a specific microstructural property of WM and variations in DT-MRI metrics. However, although DT-MRI metrics are often regarded as probes of WM microstructure, these indices do not tap specifically onto biological subcomponents of WM microstructure (Alexander et al. 2007) in that the tensor measured in the DT-MRI model is an average of all the cellular compartments within a specific voxel (Assaf & Basser, 2005). It is therefore very hard to interpret changes in DT-MRI metrics in terms of changes in specific microstructural properties (Jones et al. 2013). Very different configurations of, for example, axonal packing,

axonal size and myelination may generate very similar outcome measures. Furthermore, the radial and axial diffusivities become hard to interpret when multiple fibre orientations are present within a voxel, such as at fibre bundle crossings (Wheeler-Kingshott & Cercignani, 2009), and this situation affects between one and two thirds of the voxels in the human brain (Behrens et al. 2007; Descoteaux, 2008).

Specifically, these interpretations are built on the assumption that AD and RD are uniquely sensitive to axonal degeneration and demyelination, respectively (Budde et al. 2007; Mac Donald et al. 2007; Song et al. 2002, 2005; Sun et al. 2006, 2007; Wu et al. 2007). Such inferences are based on one study on Shiverer mice, where changes in myelin content were linked to increased RD, but unchanged AD (Song et al. 2002). However, an increase in RD might not necessarily correspond to myelin loss; rather, it can have multiple meanings, including axonal loss (Jones et al. 2013). Furthermore, in regions of crossing fibres, increased RD within a specific tract could be due to a less coherent alignment of fibres, more crossing fibres from other bundles, lower density or less myelination of the fibres, or a combination of any or all these factors (Jones et al. 2013; Wheeler-Kingshott & Cercignani, 2009).

**Table 1. Summary of MRI studies of HD animal models.**

*WM disturbance appears to be an early pathogenic event. An altered developmental trajectory of WM is suggested by asymmetric age-related changes of MRI metrics between HD models and wild-types.*

Species/Model	MRI Technique ( <i>In vivo/ex vivo</i> )	Findings	Neurochemical validation	References
<b>R6/2 mice</b>	DT-MRI ( <i>Ex vivo</i> )	FA reductions in genu and splenium of the corpus callosum.	Yes	(Xiang et al., 2011)
<b>YAC128 mice</b>	Structural MRI ( <i>Ex vivo</i> )	Progressive loss of WM volume. Corpus callosum, anterior commissure and fimbria are amongst the most discriminatory areas in genotype separation.	No	(Carroll et al., 2011)
<b>YAC128 mice</b>	DT-MRI ( <i>In vivo</i> )	FA reductions in the anterior commissure, corpus callosum, internal capsule, external capsule, from 1.5 months of age; in the cingulum and cerebral peduncle from 3 months of age.	Yes	(Teo et al., 2016)

<b>BACHD rats</b>	DT-MRI <i>(In vivo)</i>	FA reductions in the anterior corpus callosum, the cingulum and the external capsule at 12 months of age.	Yes	(Teo et al., 2016)
<b>TgHD rats</b>	DT-MRI and PET <i>(In vivo)</i>	Increased MD in HD rats at 12 months of age, compared to earlier time points; this parameter remained constant in WT animals.  Age-related RD decreases at 6 months of age in HD animals but only at 12 months in WT animals.	Yes	(Blockx et al., 2011)
<b>TgHD rats</b>	Diffusion Kurtosis Imaging <i>(In vivo)</i>	Neuronal development in HD rat pups occurs differently compared to controls: higher MD values at P15 but lower MD and AD values at P30 in external capsule.	Yes	(Blockx et al., 2012)
<b>rHD1 rhesus monkeys</b>	DT-MRI <i>(In vivo)</i>	Widespread WM changes in FA, MD, and RD.  HD monkeys reached the maximal FA value earlier ( $22.7 \pm 4.8$ months) compared to controls ( $47.8 \pm 11.7$ ), revealing an arrest of WM maturation in the HD group; across ages, HD monkeys had significantly lower maximal FA values in all areas investigated.  Significantly higher minimum RD values of HD monkeys in the striatal bundle.	No	(Meng et al., 2017)

### **1.4.3. Moving beyond volumetric and DT-MRI to assess WM microstructure changes in HD**

Biophysical models of diffusion MRI, such as neurite orientation and dispersion density imaging (NODDI) (Zhang et al., 2012) and the composite hindered and restricted model of diffusion (CHARMED) (Assaf & Basser, 2005), model compartment-specific water diffusion to dissociate hindered extra-cellular and restricted intra-cellular diffusion properties of WM, and should therefore provide a more biologically specific characterization of WM microstructural organization within the neural system (Alexander et al. 2010).

Zhang and colleagues (Zhang et al., 2018) used NODDI to examine WM pathology in premanifest HD patients. They reported widespread reductions in the neurite density index (NDI) - a proxy of axonal density - in tracts including the CC and in WM surrounding the basal ganglia of pre-symptomatic HD patients. Importantly, axonal density reductions in callosal regions predicted clinical markers of disease progression. Finally, increased coherence of axonal organization, as suggested by a smaller orientation dispersion index (OD), was shown in HD patients in tracts surrounding the basal ganglia and in the IC and EC, suggesting the presence of possible compensatory pruning of axons in WM regions. Nevertheless, estimation of specific tissue quantities from these models requires simplifying assumptions whose accuracy and generality, in the HD brain especially, are unknown. These techniques indeed still represent a relatively simple approach to modelling neural tissue and therefore cannot fully characterize pathological changes in WM microstructure (Lampinen et al. 2019).

Quantitative magnetization transfer (qMT) imaging has enabled greater sensitivity to myelin content in WM (Ou et al. 2009). This method models the exchange rate between macromolecular protons and protons in surrounding tissue water, when macromolecular protons are subjected to a radiofrequency pulse with a frequency that is off-resonance for protons in free water (Henkelman et al. 1993). One of the outcome measures of qMT, the

macromolecular proton fraction (MPF), has been shown to reflect demyelination in Shiverer mice and puppies (Ou et al. 2009; Samsonov et al. 2012), to be sensitive to dysmyelination processes in multiple sclerosis patients (Levesque et al. 2010) and to reflect myelin content of WM in *post-mortem* studies of multiple sclerosis brains (Schmierer et al. 2007). A study by Bourbon-Teles and colleagues (Bourbon-Teles et al. 2017) used DTI and qMT to investigate HD-related effects on WM pathways of the basal ganglia and motor systems. Specifically, the study compared HD patients (twenty-four manifest and one premanifest), to age- and sex-matched healthy controls. While HD patients relative to controls exhibited significant reductions in an MPF component with high loadings of MPF in all WM regions, no differences were observed for components with loadings of axial and radial diffusivity or fractional anisotropy respectively. The authors concluded that this pattern of results was consistent with a myelin impairment in HD. Interestingly, the MPF component score of the one premanifest individual in the study differed more than three times the standard deviation from the control mean. This observation suggests that MPF might already be reduced prior to disease onset and that MPF may be assessed as an early disease biomarker in a group of premanifest gene carriers (Bourbon-Teles et al. 2017).

Though MPF is sensitive to WM myelin, this metric can also be affected by changes in cells and water content due to inflammation (Henkelman et al., 2001). Odrobina and colleagues (Odrobina et al., 2005) for example, measured MPF *ex vivo* in a demyelinated rat sciatic nerve and confirmed its correlation with myelin content, but also noted the difficulty of separating demyelination from inflammation by qMT alone. Nevertheless, while in manifest HD it is likely that inflammation goes hand in hand with myelin breakdown (Rocha et al. 2016), a recent cerebrospinal fluid biomarker study found no evidence of neuro-inflammation in early-manifest HD (Vinther-Jensen et al., 2015). It is therefore plausible that changes in the MPF observed in this study were a reflection of aberrant myelination in these patients.

Human MRI studies have also shown that HD is associated with changes in iron levels across several brain areas (Bartzokis et al., 1999, 2007; Bartzokis & Tishler, 2000; Phillips et al., 2014; Simmons et al., 2007). Tissue iron can be measured by MRI *in vivo* through its effect on transverse relaxation times ( $T_2$ ). Ferritin has been shown to strongly affect the MRI signal and markedly shorten  $T_2$  both *in vitro* and *in vivo* (Bartzokis, 1997; Malisch et al. 1991).

Increased ferritin levels are already present in the premanifest stage of HD (Jurgens et al. 2010; Phillips et al. 2014). As oligodendrocytes are the major iron-containing cells in the adult CNS (Connor & Menzies, 1995), the increased density of oligodendrocytes in HD that was demonstrated in mice models (Jin et al. 2015; Simmons et al. 2007) should result in significant increases in iron and ferritin content in the HD brain. Evidence for increases in MRI-based iron measures in HD further supports the suggestion for a homeostatic increase in oligodendrocytes as an active repair mechanism in premanifest HD subjects.

Early and heavily myelinated fibres are the most susceptible to myelin breakdown in HD (Bartzokis et al., 2007), with WM degeneration starting in the caudate and putamen striatum structures and then spreading in a predictable, bilateral and symmetric pattern to involve other earlier-myelinating regions. In turn, later-myelinating regions like the medial temporal lobe, are left much less affected (Bartzokis et al., 1999; DiFiglia et al., 1997). This is consistent with neuroimaging evidence that the earliest WM changes in HD are seen before disease onset, in early myelinating regions, such as around the striatum, within the CC, and in posterior WM tracts (Di Paola et al., 2014; Dumas et al., 2012; Faria et al., 2016; Tabrizi et al., 2011). The spatial pattern of pathology is in contrast with the “last-in-first-out hypothesis” that was proposed for degenerative processes of normal brain aging (Raz, 2000), which postulates that later-myelinating fibres are more vulnerable to insult in later life, as compared to earlier-myelinating ones.

Consistent with the suggestion of a dissociation between early and late myelinating regions in WM impairment in HD, Bartzokis ( Bartzokis et al. 2007) showed decreased ferritin iron levels in HD in the genu of the CC and frontal WM (late-myelinating regions), and increased ferritin iron levels in the basal ganglia (an early-myelinating region). Decreased iron levels in late myelinating regions are proposed to be due to suboptimal iron availability, due to a redistribution of iron towards earlier-myelinating regions. Furthermore, although remyelination processes may successfully compensate for myelin loss during the premanifest HD stage, these may start failing in later years, likely explaining evidence of decreases in iron content found between the premanifest and symptomatic HD subjects (Di Paola et al. 2014; Phillips et al. 2014).

To summarise, an accumulating body of evidence suggests that alterations in WM microstructure are present early in HD progression (Aylward et al. 2011; Ciarmiello et al. 2006; Paulsen et al. 2008; Ruocco et al. 2008; Tabrizi et al. 2009), even in children at risk for HD (Lee et al., 2012; Lee, 2016), and possibly even before any changes can be detected within the striatum (Aylward et al. 2011). This implies that WM disturbances might independently contribute to HD pathogenesis (Aylward et al. 2011; Bartzokis et al. 2007; Tabrizi et al. 2009) and that, rather than being secondary to axonal insult in the form of Wallerian degeneration (Weaver et al., 2009; Zhang et al., 2018), they might be a direct result of myelin and oligodendrocytes disturbance (Bartzokis et al. 2007; Gómez-Tortosa et al. 2001; Mascalchi et al. 2004; Myers et al. 1991; Radulescu et al. 2018). Demyelination has been associated with severe disabilities in many developmental, psychiatric and neurodegenerative diseases (Martenson, 1992). Therefore, it is possible that also in HD, myelin loss, which leads to altered axonal conduction and axonal damage, may be directly responsible for some of the clinical symptoms. Furthermore, oligodendrocyte dysfunction early in the disease course may impair processes of remyelination and myelin repair (Bartzokis et al. 2007).

## 1.5. Why study WM microstructure in HD?

Abnormalities in WM caused by myelin and oligodendrocytes changes can slow or even stop fast axon transport. This, in turn, might result in synaptic loss and axonal degeneration in a retrograde, “dying back”, fashion (Han et al., 2010). Therefore, from the perspective of the remarkably myelinated human brain, the development and maintenance/repair of myelin function may be the single most significant and susceptible element, or the “weakest link”, in brain development and age-related degeneration. Further, this is fundamental for both acquiring and maintaining optimal cognitive and behavioral function (Bartzokis, 2012).

The assessment of changes in glia and myelin in the HD brain is therefore of fundamental importance, as it will allow insight into disease pathogenesis and progression. Importantly, as no disease-modifying treatment currently exists for HD, understanding WM changes might prove useful for the identification of disease-related biomarkers and in measuring responsiveness to pharmaceutical and other therapeutic approaches, such as environmental stimulation and behavioural interventions. In many neurodegenerative diseases such as Alzheimer’s and Parkinson’s disease, myelin disturbance starts before other pathological changes are evident (Bartzokis et al., 2007, 2010). Similarly, in HD, critical pathogenic events might be present prior to neuronal death, and there might therefore be a decades-long period in which therapeutic intervention could change the course of the disease, before clinical evidence such as behavioral, cognitive and motor decrements, appears.

Nonetheless, *in vivo* investigation of demyelination in premanifest and symptomatic HD patients with neuroimaging remains relatively unexplored when compared to other neurodegenerative diseases such as multiple sclerosis, and very little research has been carried out on the HD brain using these approaches. Notably, though much of our understanding of HD pathology will increasingly rely on advanced neuroimaging techniques, this reliance

stresses the importance to remember and address the shortcomings of these approaches. Table 2 provides a summary of MRI changes observed in HD patients. Interpretations proposed by the respective authors and alternative explanations found in the literature for such changes are reported.

**Table 2. MRI changes observed in the reviewed in vivo studies in HD patients.**

*Interpretations proposed by the respective authors and alternative explanations found in the literature for such changes.*

Reported change	Proposed interpretation	Possible alternative interpretation
Reduced WM volume	Decreased number of axons due to Wallerian degeneration (Douaud et al., 2006; Kassubek et al., 2004; Rosas et al., 2002, 2005; Ruocco et al., 2008).	Decrease in axon myelination (Ciarmiello et al., 2006; Squitieri et al., 2009).
Reduced axial diffusivity	Axonal degeneration (Weaver et al., 2009).	Inflammation, non-uniform axonal oedema, beads, varicosities parallel to the axon segments, microglia/macrophage activation (Xie et al., 2010).
Increased radial diffusivity	Demyelination (Di Paola et al., 2012; Rosas et al., 2018; Song et al., 2002, 2005; Weaver et al., 2009).	Less coherent alignment of fibres, more crossing fibres from other bundles, lower density or less myelination of the fibres, or a combination of any or all these factors (Neema et al., 2009).
Reductions in the neurite density index	Decrease in axonal density (Zhang et al., 2018).	Reduced MRI signal because of demyelination (Grussu et al., 2017).
Reductions in MPF	De-myelination (Bourbon-Teles et al., 2017).	Changes in cells and water content due to inflammation (Henkelman et al., 1993; Odrobina et al., 2005).
Shortened T <sub>2</sub>	Increased ferritin levels (Jurgens et al., 2010; Phillips et al., 2014).	Re-myelination (Stanisz et al., 2004).

## 1.6. Animal models of HD

Findings from animal models of HD need to be considered while keeping in mind the inherent differences between these animals and human patients. Firstly, the equivalent and divergent features of the brain for different species need to be understood. For example, when looking at rodent brains, the most obvious difference is that these are tiny (~0.4g in mice, ~2.0g in rats), lissencephalic (do not have sulci or gyri), and have little WM. On the other hand, the human brain is much larger (approximately 1300g), has a readily evident lobular organization, prominent sulci and gyri, and extensive WM (about 40% of the brain) (Snyder et al., 2018). Most importantly, the phenotype exhibited by each animal model of HD needs to be considered in the context of the different approaches used to generate the respective model (Pouladi et al., 2013). In the broadest terms, animal models of HD can be classified as non-genetic or genetic models.

*Prior* to the discovery of the HD gene in 1993 and the establishment of more specific genetic manipulation, HD models were mostly generated following chemical administration both directly into the striatum and systemically (Kosior & Leavitt, 2018). Specifically, in these models cell death is induced by the delivery of either excitotoxins or metabolic toxins, in the attempt to model HD neuropathology. Neuropathological validity is higher for models in which cell death is induced with metabolic toxins, as these selectively affect MSN in a progressive manner (Borlongan et al., 1997; Brouillet et al., 1993); however, these models are also associated with higher inter-animal variability and higher incidence of gross non-specific striatal damage (Dunnett & Rosser, 2004). Amongst the most commonly used excitotoxic agents, quinolinic acid is currently the most widely used, as this leads to preferential degeneration of GABA-ergic neurons, which are affected in HD (Schwarcz et al., 1983). However, a general drawback of excitotoxic models is the absence of association with the

genetic cause of HD. Lesions indeed do not lead to mutant *HTT* production and formation of neuronal inclusions; also, cell death is sudden rather than progressive (Steventon, 2014).

Knock-out models were the first genetic models to be developed (Duyao et al., 1995; Nasir et al., 1995; Zeitlin et al., 1995). In these models, the *HTT* gene was removed from the genome completely. These models, therefore, were fundamental in determining the function of the *HTT* gene; for example, they showed that knock-out animals do not survive embryonic development, therefore demonstrating the crucial role that *HTT* plays in embryogenesis (Duyao et al., 1995; Nasir et al., 1995; Zeitlin et al., 1995). More recently, conditional knock-out models have been developed, where the *HTT* gene is eliminated from a specific organ being studied. Importantly, inducible knock-out models allow the gene to be knocked out at a specific time, such as after development.

Contrarily to non-genetic models and knockout models, other genetic models of HD aim to reproduce the genetic defect seen in patients; this, in turn, enables the study of early pathological, cellular and molecular alterations caused by the HD mutation (Steventon, 2014). Different genetic models recapitulate specific aspects of the cognitive and motor dysfunction, and the striatal neurodegeneration seen in HD patients (Kosior & Leavitt, 2018). Most genetic models of HD are in mice; however, rat (von Hörsten et al., 2003), primate (Yang et al., 2008), *C. elegans* (Faber et al., 2002), *drosophila melanogaster* (Warrick et al., 1998), zebrafish (Schiffer et al., 2007), sheep (Jacobsen et al., 2010) and minipig (Baxa et al., 2013) models have also been created.

Amongst genetic models, key distinguishing factors are the genetic approach and transgene construct used to create them. For example, the use of full-length or only a fragment of mutant huntingtin (*HTT*); the length of the CAG repeat incorporated into the genome; the expression of the HD mutation from a transgene *versus* knock-in of the mutation into the endogenous *HTT* locus. The several genetic manipulations underlying these models all aim to

recapitulate the human disease, with various degrees of success (Kosior & Leavitt, 2018). Overall, current HD models differ from the human condition in the duration of pathology, symptom severity, striatal specificity of neuropathology. This ultimately poses questions in terms of the effectiveness of animal models in mimicking human disease (Kosior & Leavitt, 2018).

N-terminal fragment models, which express N-terminal human *HTT* fragments along with an expanded CAG repeat within *exon 1*, show the most robust and rapid disease progression, but fail to demonstrate the striatal specific atrophy and cell loss typical of HD patients (Carter et al., 1999; Davies et al., 1997). Furthermore, early phenotype onset and rapid death make these models unsuitable for the study of early disease pathogenesis and preventative therapies (Kosior & Leavitt, 2018). Full-length models, which contain the entire expanded human *HTT* gene, represent an improvement upon the limitations of fragment models, and exhibit a slower disease progression and relatively normal lifespans (Kosior & Leavitt, 2018). Furthermore, they present robust and striatum-specific neuropathological abnormalities (Slow et al., 2003), mimicking changes seen in human patients, therefore providing possibly more valid outcome measures for preclinical trials. Importantly, the full-length protein and slower onset/progression of symptoms allows for the study of pathological changes early in the disease course and of drug targets (Kosior & Leavitt, 2018). Finally, in knock-in models, the CAG repeat mutation is inserted into the endogenous animal *HTT* gene (Lin et al., 2001), or the animal *exon 1* is replaced with the pathologically expanded human *exon 1* (Ishiguro et al., 2001). These models are considered as more accurate genetic models of the human condition, as compared to transgenic models (Menalled, 2005), because they carry the mutation in its appropriate genomic and protein context. However, knock-in models also display the weakest and most variable phenotypes, therefore they are generally considered to be more useful for the investigation of early disease stages (Kosior & Leavitt, 2018).

This Thesis includes work on a the R6/1 fragment model of HD (Chapter 5), which expresses *exon 1* of the human HD gene, with around 115 CAG repeats (Mangiarini et al., 1996). This line was amongst the first to be developed (Mangiarini et al., 1996) and presents a severe phenotype and neuropathology, which occur early in life, with a relatively quick progression of symptoms and reduced lifespan. Specifically, these mice exhibit age-related progressive changes in both motor and cognitive performance from as early as 2 months of age (Brooks et al., 2012) and age-related neuronal loss, brain atrophy and *mHTT* accumulation (Bayram-Weston et al., 2012). Although the R6/1 line is one of the most used models of HD, no studies published so far report on how WM microstructure may be affected in this model.

## **1.7. A translational neuroimaging approach to study HD: advantages and challenges**

In this Thesis, the investigation of human patients as well as a mouse model of HD allowed for bi-directional translation of results, with enhanced insights in human neuropathology affording the foundation for translational research in the R6/1 mouse model, and the increased biological specificity of the work in the HD model informing knowledge and research in the human condition. In the coming section, I will provide an overview of the advantages and challenges associated with the use of a translational neuroimaging approach to the study of HD.

### ***Advantages***

Though neuroimaging studies on human HD patients have greatly contributed to gaining information about the impact of the HD mutation on brain structure and function, these techniques do not provide enough resolution and specificity to elucidate the cellular and molecular consequences of the mutation. Currently, understanding of cellular and molecular

abnormalities underlying pathology may only be achieved with histological analysis; however, histological studies in humans rely on the availability of *post-mortem* tissue, making it difficult to control several confounding variables such as age, gender and other health conditions prior to death (Monoranu et al., 2009).

The study of animal models allows to move closer to the molecular and cellular mechanisms underlying disease pathogenesis and progression (Duty & Jenner, 2011). Importantly, advances in animal imaging techniques have enabled greater translational validity of animal models through comparison of human and animal imaging studies, hence enhancing our confidence on the cellular findings in animals, as well as the translation of therapies to humans (Hoyer et al., 2014) (Figure 4). MRI studies on animal models indeed provide the opportunity to study disease progression and evaluate therapeutic efforts; importantly, MRI enables to obtain whole brain 3-dimensional data instead of highly localised histological measurements from sections of tissue in a single plane.

Additionally, neuroimaging research enables the implementation of the '3R' principles of 'reduction', 'refinement' and 'replacement' for the humane treatment of research animals. These have become recognised worldwide as the fundamental ethical approach to governing animal research (Kirk, 2018). For example, neuroimaging techniques afford the use of smaller group sizes, because of higher experimental control on confounding variables and therefore reduced variance due to intra- and interindividual measurements. Moreover, the number of experimental groups can also be reduced, because of the possibility of performing repeated intraindividual measurements. Furthermore, high-resolution morphological and functional analyses can be obtained with very little distress. Finally, as non-invasive procedures, neuroimaging methods allow performance of multimodal investigations on one and the same animal, allowing for a simultaneous or step-wise analysis of structure and function (Hoyer et al., 2014).

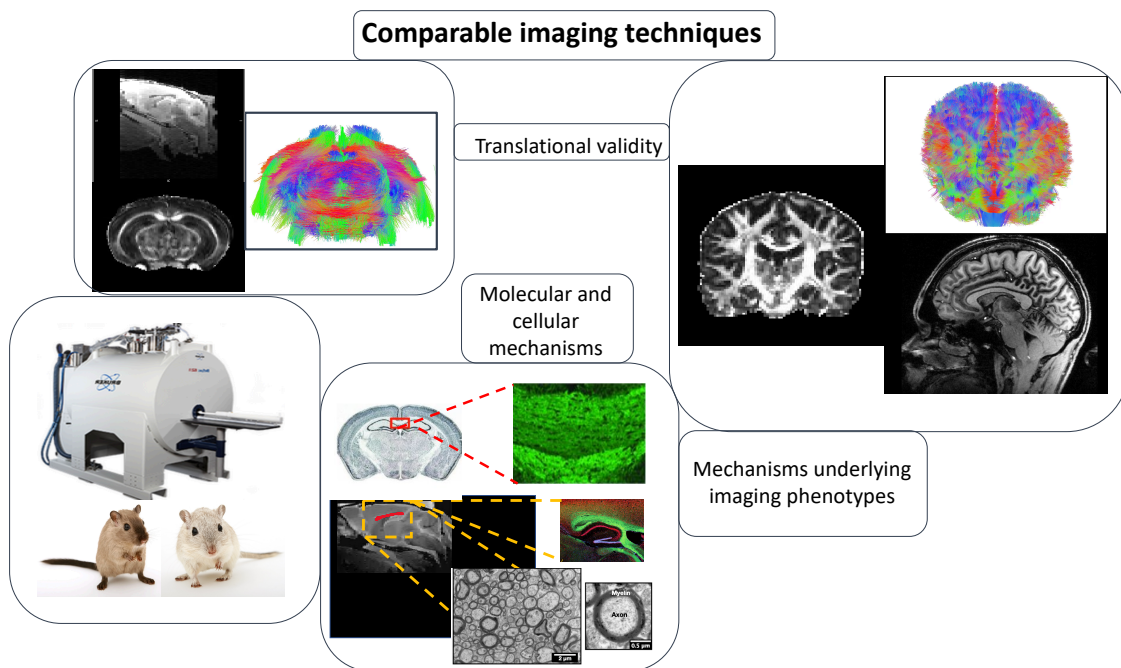


**Figure 4. Translational MRI-based framework combining multi-modal imaging techniques in animal models and humans.**

*Preclinical-to-clinical and genotype-to-endophenotype mapping. Comparable imaging phenotypes increase our confidence on molecular and cellular findings in rodent models, and may elucidate the mechanisms underlying imaging phenotypes in the human brain.*

## **Challenges**

Animal MRI presents unique technical challenges. One of the biggest issues concerns brain size; for example, a mouse brain is approximately 1000 times smaller than a human brain in terms of total volume (Snyder et al., 2018). Accordantly, while most human imaging experiments utilise a resolution of 1 mm, obtaining a comparable anatomical resolution in the mouse brain requires a voxel size that is 1000 times smaller (Hoyer et al., 2014). Though such increased resolution can be achieved by moving to a higher field strength, this has major implications in terms of the signal-to-noise ratio (SNR) that can be achieved, as SNR is directly proportional to the voxel size. Broadly speaking, the SNR of a typical imaging acquisition in a

3 Tesla human MRI scanner exceeds that of a comparable animal measurement in a 9.4 Tesla scanner by a factor of 5. Therefore, multiple averages/repetitions are needed to get appropriate SNR in a rodent imaging experiment; these, in turn, implicate longer duration of measurements (Hoyer et al., 2014).

Another challenge of animal imaging is physiological noise. This is not only due to the fact that at higher field strength, the fraction of physiological noise due to breathing and cardiac pulse increases (Krüger et al., 2001); as well, the degree of movement a small animal produces because of breathing is higher in relation to the size of voxels than in humans. Therefore, due to the high field power and resolution of animal scanners, physiological noise may cause significant artefacts. These can be, at least partially, controlled by triggering acquisition based on the breathing pattern, and thorough the administration of anaesthesia. The latter, however, limits the viable *in vivo* scan time (Steventon, 2014). Worth mentioning is also the fact that geometric distortions due to local magnetic field inhomogeneities increase linearly with field strength; furthermore, higher magnetic fields shorten tissue  $T_2$  and  $T_2^*$  and lengthen tissue  $T_1$ . Despite these challenges, there have been a number of MRI studies in mouse models of Huntington's disease (Table 1).

## 1.8. Aims of the present work

The aim of this Thesis was to use a multi-modal, translational neuroimaging approach to investigate WM microstructural changes in HD. As reviewed above, research has shown evidence of WM damage in both animal models of HD and in subjects carrying the HD mutation. Nevertheless, there is no clear consensus on whether WM damage is due to alterations in axon microstructure or myelin changes, or both. Further, it is unknown whether WM impairment is secondary to, or independent of, atrophy observed in the GM. The present project aimed to test the relevance of the Demyelination Hypothesis (Bartzokis et al. 2007) in explaining HD neuropathology.

To this end, I employed advanced microstructural imaging, including high b-value measurements of restricted diffusion, high-field assessments of susceptibility (frequency difference mapping), along with magnetization transfer assessments of apparent myelin, in the attempt to disentangle the contribution of axon microstructure *versus* myelin to HD pathology, by assessing both HD patients and a mouse model of HD. Results were examined alongside macrostructural and ultrastructural changes, and behavioural measures, in the context of discovering imaging biomarkers in HD.

Chapter 2 will give a critical overview of the acquisition and analysis approaches I utilised, while the experimental work of this PhD project is reported in Chapters 3, 4, 5 and 6. Specifically, Chapter 3 describes the assessment of WM microstructure premanifest HD patients exploiting the ultra-strong gradients offered by the Connectom scanner. Chapter 4 presents an evaluation of WM alterations in premanifest HD patients at 7 Tesla, and specifically describes the investigation of changes in callosal microstructure using frequency difference mapping, a novel approach to the high-field assessment of susceptibility. Chapter 5 presents the evaluation of WM microstructural changes in the R6/1 mouse model of HD using an *ex vivo*, high-resolution MRI approach at 9.4 Tesla. Finally, in Chapter 6 the possible

benefits of a drumming-rhythm training for stimulating myelin remodelling in HD are explored. These chapters are followed by a general discussion in Chapter 7, where wider implications of the experimental data, and suggestions and plans for future experiments are discussed.

# Chapter 2

## General Methods

### 2.1. Overview

MRI provides unprecedented power for the investigation of internal biological tissues, without the need for potentially dangerous ionizing radiation or invasive procedures. MRI is based on nuclear magnetic resonance (NMR). Key to the concept of NMR is the ‘spin’, which is conceptualised as rotation of subatomic particles around their axes. If a nucleus has an odd number of protons or neutrons, there will be a net spin, and this results in a magnetic moment. By far the most commonly-studied nucleus in MRI is the hydrogen nucleus, or proton (but other nuclei are studied, for example  $^{31}\text{P}$  and  $^{19}\text{F}$ ).

In the Earth’s magnetic field, these spins are randomly oriented. However, when placed in a strong magnetic field, the spins align either with or against the field, resulting in a net magnetization vector (NMV). The NMV precesses in a gyroscopic motion around the direction of the main field, with a characteristic angular frequency, known as the Larmor frequency. This is directly proportional to the strength of the magnetic field. The precessional frequency of nuclei placed in a static magnetic field  $B_0$  is calculated from the Larmor Equation (Larmor, 1897):

$$\omega = \gamma B$$

where  $\omega$  is the Larmor frequency in MHz,  $\gamma$  is the gyromagnetic ratio in MHz/Tesla and  $B$  is the strength of the static magnetic field in Tesla.

To perturb the system away from equilibrium, energy needs to be put in (“resonance”), and this requires a radio-frequency pulse at the Larmor frequency. This has the effect of tipping the NMV away from the equilibrium position, and the component of precession in the transverse

plane is detected by the radio-frequency receiver coil. In many applications, the RF pulse is applied to produce a  $90^\circ$  pulse, to give maximum signal in the transverse plane. Once the RF pulse is stopped, two phenomena take place. First, the spins naturally return to their equilibrium longitudinal alignment, and the time taken for the magnetization to return to  $1/e$  of the initial amplitude is known as the longitudinal relaxation time, or  $T_1$ . Moreover, the individual spins forming the NMV can experience slightly different magnetic fields (e.g. due to interactions with other spins), resulting in different precessional frequencies. In turn, this leads to a dephasing of the signal. The time taken for the transverse magnetization to decay to  $1/e$  of its initial value via this mechanism is called the transverse relaxation time, or  $T_2$ . Importantly,  $T_1$  and  $T_2$  reflect the tissue chemical environment, hence providing the image contrast (Duval et al., 2017; Kagawa et al., 2017).

In the next sections, I will describe the MRI hardware and different acquisition techniques applied to the study of the HD brain in this body of work. The analysis approaches utilised are also discussed, together with their advantages and disadvantages.

## **2.2. Advantages and challenges of ultra-high field and ultra-strong gradients MRI**

Over the past few decades there have been exciting developments in MRI hardware, with MR imaging providing increasingly detailed images of brain anatomy and function. Major improvements in MR image quality have been afforded by increasing field strength beyond 3-Tesla (Duyn, 2012), and by incorporating ultra-strong gradient systems into MRI scanners for imaging the human brain (Setsompop et al., 2013). The present research project exploited both ultra-strong gradients (300 mT/m) and ultra-high field (7 Tesla, 9.4 Tesla) to assess WM

microstructure in the HD brain. Potential advantages and disadvantages of these approaches are discussed next.

### **2.2.1. Imaging the brain at ultra-high field**

Although until recently 3 Tesla was the highest clinical field strength available, scanners utilizing “ultra-high” field strengths of 7 Tesla and above, have been explored since the late 1990s (Norris, 2003; Vaughan et al., 2001). Scanning at higher magnetic field strengths has led to several benefits, of which the most obvious is increased spatial resolution. The human brain is a highly complex and heterogeneous structure, and the capability for an imaging method to fully resolve these complexities is in part dependent on its spatial resolution. For most anatomical scans acquired on scanners operating at 3 Tesla, the typical resolution is  $1 \times 1 \times 1 \text{ mm}^3$ , which is equivalent to 1  $\mu\text{l}$  volume for each voxel (Duyn, 2012). While moving to higher resolutions would generally reduce signal-to-noise ratio (SNR) and contrast-to-noise ratio (CNR), SNR and CNR increase with field strength; therefore, scanning at ultra-high magnetic field strengths benefits from higher SNR, in turn enabling increased resolution. More specifically, scanners operating at fields from 7 Tesla to 9.4 Tesla, allow a two- to three-fold increase in image SNR over 3 Tesla systems (Duyn, 2010). Undoubtedly, this leads to several advantages in terms of detection of brain features previously difficult to define using conventional MRI, thus broadening MRI’s possible applications (Duyn, 2012).

Additionally, scanning at higher field strengths is associated with changes in contrast, some of which are particularly valuable for the study of the brain microstructure (Duyn, 2018). For example, increasing field strength is coupled with improved sensitivity to susceptibility effects, in turn providing advantages in the field of susceptibility-weighted imaging (SWI), and for the quantification of substances causing susceptibility differences, such as iron and myelin (Moser et al., 2012). Variations in magnetic field associated with tissue microstructure increase linearly

with field strength; this enables the assessment of properties such as fibre orientation and myelin fraction at ultra-high field, with methods such as frequency difference mapping (FDM) (Wharton & Bowtell, 2013), and by modelling the signal decay curve with multi-exponential fitting (Tendler & Bowtell, 2019). Therefore, combined with the increased spatial resolution, this opens up exciting avenues for mapping variations in cytoarchitecture across different areas, disease processes, and populations (Duyn, 2010).

Though stronger magnetic fields provide numerous advantages, they are also associated with new challenges and artefacts that are less pronounced at lower field strengths. These include, for example, geometric distortion due to increases in magnetic field inhomogeneity; greater impact of physiological noise (such as respiration and brain pulsations) (Krüger et al., 2001); higher radiofrequency energy deposition in the tissue (Ladd et al., 2018). In Table 3, some of the aspects to be considered when performing ultra-high field MR imaging are reported.

**Table 3. Overview of some of the potential advantages and disadvantages associated with increasing magnetic field strength.**

Table adapted from Moser et al. (2012) and Ladd et al. (2018). Abbreviations: SNR–signal-to-noise ratio; SAR – specific absorption rate; RF – radio-frequency; SWI – susceptibility-weighted imaging; TR – repetition time; TOF – time of flight angiography; ASL – arterial spin labelling; DWI – diffusion-weighted imaging.

Characteristic	Trend with increasing field strength	Pros	Cons
SNR	↑	Higher resolution, shorter scan time	None
SAR	↑	None	Fewer slices, smaller flip angle, longer TR
Physiological side-effects	↑	None	Dizziness, nausea, metallic taste
Relaxation times	T <sub>1</sub> ↑	Advantageous for TOF, ASL, cardiac tagging	Longer scan time
	T <sub>2</sub> ↓	Advantageous for SWI	Negative impact on DWI
	T <sub>2</sub> * ↓		
Susceptibility effects	↑	Advantageous for SWI, T <sub>2</sub> *	Geometric distortions, intravoxel dephasing
Chemical shift	↑	Advantageous for fat saturation, MR spectroscopy	Fat/water and metabolite misregistration

### 2.2.2. Microstructural imaging of the brain with ultra-strong gradients

The gradient amplitude usually available on clinical MRI scanners ranges between 40-80 mT/m; in this experimental work, I leveraged the power of ultra-strong gradients (300 mT/m) of the Connectom scanner. The use of ultra-strong gradients to image the brain leads to two main advantages, specifically related to the field of diffusion imaging: 1) the echo time (TE) of spin echo sequences can be significantly reduced for a given b-value, and this has an exponential effect on image sensitivity and SNR per unit b-value, by reducing the amount of signal loss from  $T_2$  processes (Jones et al., 2018; Setsompop et al., 2013); 2) the diffusion time can be significantly decreased, enabling a wider range of b-values to be maintained across all diffusion times, hence allowing a more precise characterisation of the water probability distribution function (Jones et al., 2018; Setsompop et al., 2013). Both of these properties in turn lead to several advantages, some of which I will discuss next, together with mentioning some of the challenges associated with scanning with ultra-strong gradients. Table 4 provides a summary of these factors.

Firstly, hardware currently available on clinical MRI systems does not allow achievement of specificity to relevant microstructural characteristics of tissue. For example, diffusing species within myelin sheaths will not be captured at the TEs of a standard diffusion-weighted experiment, since the macromolecules have ultra-short  $T_2$  (about 80  $\mu$ s) (Fischer et al., 1989, 1990) and water trapped within myelin sheaths has a  $T_2$  lower than  $\sim$ 40 ms (MacKay et al., 1994). This implies that not much signal coming from myelin will be detected in diffusion-weighted experiments performed on standard gradients systems (Beaulieu, 2002; Nair et al., 2005). Additionally, recent studies have demonstrated a b-value dependence on estimates of apparent fibre density, with changes in this parameter estimated at high diffusion-weightings ( $b = 4000$  or  $6000$  s/mm<sup>2</sup>) more directly reflecting a change in the underlying axon density,

because of increased suppression of the extra-axonal signal (Genc et al., 2020). However, on clinical MRI systems it is not possible to produce the level of filtering needed to differentially attenuate the signal coming from intra-axonal and extra-axonal compartments, while maintaining reasonable echo times and thus sufficient SNR (Kleban et al., 2020).

Nevertheless, disentangling the contributions from different properties of WM microstructure, such as myelin and axons, is essential for achieving a better understanding of the pathophysiology of neurological disorders and treatment development (Bodini & Ciccarelli, 2014; Lim & Helpert, 2002). So far, a common solution when modelling the MRI signal has involved fixing certain microstructural model parameters to *a priori* values. However, parameters are sometimes fixed to given values with little or no biological plausibility, and this in turn can generate a shift or bias in the other estimated metrics, therefore challenging their biological specificity (Jelescu et al., 2016). In contrast, high b-value measurements in conjunction with better SNR, and a wider TE range can be sampled with ultra-strong gradients. These allow a much larger portion of the multidimensional experimental parameter space to be studied by enabling the estimation of all parameters, without having to fix them *a priori* (Jones et al., 2018; Novikov et al., 2019). This has not previously been possible *in vivo* on standard clinical MR systems.

Additionally, until recently, diffusion-weighted imaging techniques have been significantly hindered by their low spatial resolution; however, achieving higher-resolution diffusion experiments could benefit the quantification of several microstructural properties because of reduced partial volume artefacts. This could also enhance the accuracy of tractography approaches, for example, by allowing reconstructions of minor WM connections that are often inaccurately reconstructed with standard tractography methods. This, in turn, could yield new insights into the pathophysiology of neurological disorders. Importantly, compared to ultra-high field systems with weaker gradients (e.g., 70 mT/m at 7 Tesla), stronger gradients at lower

field provide an advantage because of the longer  $T_2$ , and lower susceptibility distortions (Jones et al., 2018).

Last but not least, performing measurements on a system equipped with ultra-strong gradients allows the development of a truly translational pipeline, by making it possible to perform measurements in the human brain that previously could only be gained *in vivo*, in animals on preclinical scanners. Comparable translational approaches, in turn, play a fundamental role in aiding the interpretation of clinical and research results from conventional clinical scanners with a much lower resolution (Jones et al., 2018). For example, modern machine learning techniques may be used to build a mapping from images acquired on standard systems to the “higher quality” images obtained on a system with ultra-strong gradients (Alexander et al., 2014, 2017; Ning et al., 2019); this in turn could allow the estimation of the image that could have been obtained from a longer acquisition protocol, or a hard-to-access imaging device (Jones et al., 2018).

The main challenges associated with ultra-strong gradients scanning concern mostly physiological limits and safety constraints. An issue, for example, is peripheral nerve stimulation (PNS) and cardiac stimulation caused by the time-varying magnetic fields produced by fast-switching gradients. Importantly, the threshold for stimulation is dependent upon the spatio-temporal characteristics of the electric fields induced in the body, and their relationship to the peripheral nerves’ anatomy and physiology. This makes it difficult to predict the site and threshold for stimulation at the individual subject level (Davids et al., 2017).

A more technical issue concerns gradient non-linearity (Rudrapatna et al., 2021). Specifically, while the magnetic field produced by imaging gradients should ideally vary linearly with distance from the magnet’s isocentre, residual gradient non-linearity is usually present within the imaging volume. This effect is more significant when dealing with ultra-strong gradients, a trade-off for achieving ultra-high gradient amplitudes. In turn, if not taken

into account during image reconstruction, gradient nonlinearity is associated with geometric spatial distortion in MR images, therefore degrading both geometric and image intensity accuracy. Additionally, gradient non-linearities can affect diffusion-weighted images beyond simple image distortion. Specifically, gradient non-linearities are not rotationally symmetric, implying that head motion will make the temporal evolution of the B-matrix (where the parameters of the gradients for a given sequence are incorporated) at different voxel locations significantly more complex. This therefore means that non-linearities will lead to a spatio-temporal variation of the B-matrices. Altogether, these factors will influence the final microstructure parameters obtained.

**Table 4. Overview of some of the potential advantages and disadvantages associated with increasing gradient strength.**

These are considered mainly in relation to DWI acquisitions. Abbreviations: SNR – signal-to-noise ratio; TR – repetition time; TE – echo time; PNS – peripheral nerve stimulation. For a review, see Jones et al. (2018).

Characteristic	Trend with increasing gradient strength	Pros	Cons
SNR per unit b-value	↑	Higher resolution, shorter scan time, enhanced accuracy of tractography approaches, improved estimation of microstructural parameters	None
Minimum achievable TE for a given b-value	↓	Increased sensitivity to myelin and other microstructure properties with very short T <sub>2</sub>	None
Diffusion weightings per unit time	↑	Drastic shortening of the time needed for diffusion encoding, increased SNR, advantageous for measurements at shorter diffusion times	None
Resolution limit (i.e. window of restriction lengths the diffusion-weighted MR signal is sensitive to)	↓	Advantageous for cell size imaging	None
Physiological side-effects	↑	None	PNS and cardiac stimulation
Gradient non-linearity	↑	None	Geometric distortions, spatiotemporally varying B-matrices

## 2.3. MRI techniques to characterize WM microstructure

Conventional MRI techniques, such as  $T_1$ - and  $T_2$ -weighted sequences, allow to distinguish different structures and identify pathologies, such as inflammation, scar tissue and tumours. However, they lack specificity to different properties of tissue microstructure, and have been shown to have a weak association with clinical manifestations of pathology, likely because they do not suffice to explain the entire spectrum of the disease process (Rovira et al., 2013). This mismatch has been termed “clinico-radiological paradox” (Barkhof, 1999).

Nevertheless, MRI also enables to move beyond detection of simple contrast between tissues, and obtain quantitative metrics which better describe tissue microstructure, composition, and pathological processes. Specifically, by varying, in a controlled fashion, the excitation and dephasing of spins responsible for the MR signal, numerous chemical and physical properties of tissue can be examined, such as the diffusion profile of water molecules in diffusion-weighted imaging, or the proportion of different macromolecules or metabolites (e.g. myelin lipids or iron) in relaxometry and magnetization transfer. Measuring a number of different properties allows for a more comprehensive description of neural tissue, obtaining complementary information, which in turn can help with the characterization of diseases pathogenesis and progression (Alexander et al., 2011).

In the experimental work described in the following chapters, I used a multi-parametric, approach to characterize WM microstructure in both an animal model of HD, and premanifest and manifest HD patients. Specifically, I exploited a range of different contrasts, including high b-value measurements of restricted diffusion, high-field assessment of susceptibility, along with magnetization transfer assessments of apparent myelin. This section briefly describes the MRI modalities I employed, with a focus on the fundamental physics that allow each approach to retrieve meaningful information about tissue microstructure.

### 2.3.1. Diffusion-weighted imaging (DWI)

A popular technique for the assessment of WM microstructure is DWI. This approach exploits the differential diffusion of water molecules depending on tissue type and architecture, to probe microstructure (Beaulieu, 2002). In an environment of complete orientational dispersion, such as in cerebrospinal fluid, water molecules will display isotropic diffusion, and hence move freely in all directions. On the other hand, in highly organized structures such as WM fibre bundles, diffusion will be hampered perpendicularly to the bundle by the presence of axon walls and myelin sheaths, while it will be relatively unobstructed along its length. The anisotropy of water diffusion in the neural tissue results in a directional dependency of the DWI signal. Specifically, when a gradient is applied in a certain direction, any component of displacement in water molecules along that direction will cause an attenuation in the MRI signal. Hence, the anisotropy of water molecules can be probed by observing how the MRI signal varies as the direction of applied gradients is changed. In turn, the direction along which diffusivity is greatest will tend to be aligned with the principal axis of anisotropic structures, and hence will allow to infer the orientational make-up of WM fibres in the brain.

The degree of attenuation produced in the MRI signal will depend not only on the extent of diffusion along the gradient orientation, but also on the strength (**G**), duration (**d**) and separation time (**D**) between the applied gradient pulses; these values combined give the b-value ( $s/mm^2$ ), which can be described by the following equation (Stejskal & Tanner, 1965):

$$b = (gdG)^2(D-d/3)$$

where **g** represents the gyromagnetic ratio, i.e. a constant specific to the type of nucleus of interest - in this case, hydrogen protons. Notably, the degree of signal loss in DWI can be boosted by increasing the strength and duration of the diffusion-encoding gradients, as characterised by the b-value. Specifically, the higher the b-value the greater the signal loss in

most tissues, except for areas where diffusion is highly restricted. Although SNR will be decreased due to greater signal loss, higher b-values can provide information about water mobility in highly restricted compartments, such as the intra-axonal compartment (Assaf & Basser, 2005). Importantly, any image acquired with linear tensor encoding will be sensitised only to the component of displacement along the direction of the applied gradients. As such, multiple different gradient directions need to be sampled in order to obtain information about the directionality of fibres, and this will often imply a trade-off between better image quality and acquisition time (Jones, 2004). It has been suggested that the use of more unique sampling orientations, rather than repeats of the same set of sampling orientations, may increase the detectability of patient-control differences (Papadakis et al., 2000; Skare et al., 2000). Additionally, it has been shown that 30 unique and evenly distributed sampling orientations are required for robust determination of MD, FA and tensor orientation in DTI. This is necessary in order to achieve statistical rotational invariance, so that the variance in measurements does not depend on the orientation of the sample (Jones, 2004). The directional information obtained with DWI can then be utilised to build a set of representative streamlines in such a way that, when viewed as an ensemble, they create a visual representation of the underlying fibre of interest (Basser et al., 2000); this in turn allows localisation of any changes to specific fibre bundles.

### 2.3.2. Analysis of DWI data: the diffusion tensor and beyond

The main approach to analysing DWI data has consisted for a long time in the use of the diffusion tensor (Basser et al., 2000; Catani et al., 2002; Conturo et al., 1999). This is a mathematical construct characterised by a set of eigenvalues (representing the magnitude of diffusion), and corresponding eigenvectors (representing the direction of diffusion). Specifically, the diffusion tensor framework assumes a Gaussian displacement distribution and its shape reflects how anisotropic the diffusion of water molecules in a certain voxel is. Broadly, this will assume an ellipsoidal shape when diffusion is anisotropic and will be spherical when diffusion is isotropic (Basser, 1995; Basser et al., 1994; Basser & Jones, 2002). This 3D ellipsoid (or tensor) can be described by a  $3 \times 3$  symmetric matrix of numbers characterising diffusion displacements in 3D:

$$D = \begin{pmatrix} D_{xx} & D_{xy} & D_{xz} \\ D_{yx} & D_{yy} & D_{yz} \\ D_{zx} & D_{zy} & D_{zz} \end{pmatrix}$$

The diffusion tensor has been used to derive microstructural properties of WM based on the eigenvectors defining the ellipsoid (or tensor) at each voxel. Commonly derived metrics are MD, FA and RD. A description of these metrics, together with a discussion of the limitations of the DTI framework, can be found in Chapter 1. Briefly, although the DTI approach relies on the assumption of Gaussian diffusion, and defines a single tensor for each voxel, a typical MRI voxel contains thousands of axon fibres and multiple fibre orientations (Jeurissen et al., 2011). Crossing, kissing or fanning fibre populations in turn create a “partial

volume effect” (Alexander et al., 2001), generating a non-Gaussian diffusion probability density function, so that the DW-MRI signal profile cannot be accurately described using just one tensor. Hence, although previous histopathological studies have argued that DTI measures are uniquely sensitive to e.g. demyelination or axonal degeneration (Budde et al., 2007; MacDonald et al., 2007; Song et al., 2002, 2005; Sun et al., 2006, 2007; Wu et al., 2007), the tensor framework represents an oversimplification of highly complex WM structures, and may provide invalid/difficult to interpret findings, especially in pathology (Douaud et al., 2011).

Over the past 15 years, novel methods have been proposed to extract more biologically meaningful microstructural information from DWI data. For example, the CHARMED model of diffusion (Assaf & Basser, 2005) (Figure 5) was proposed to provide a more complete physical description of the diffusion process in WM. This model assumes that one contribution to the net signal decay arises from hindered diffusion in the extra-axonal volume (including extra- and intracellular spaces), while another contribution arises from restricted diffusion in the intra-axonal volume. Specifically, this approach is built on the assumption that, at higher b-values (up to 8571 s/mm<sup>2</sup> in Assaf & Basser, 2005), the DW signal attenuation is dominated by slower diffusing species (assumed to be intra-axonal), while at lower b-values, signal attenuation is dominated by the faster-diffusing species, assumed to be hindered molecules in the extra-axonal space. In this model, the diffusion signal coming from an extra-axonal hindered compartment is described by a standard tensor, while the signal coming from one or more intra-axonal restricted compartments is described by restricted diffusion within impermeable cylinders.

CHARMED provides several microstructural metrics, such as fibre orientation, extra- and intra-axonal signal fractions and axonal diffusivities. The intra-axonal volume fraction, or FR, estimated from CHARMED, has been interpreted as an index of axonal density (De Santis et al., 2014) and has been suggested as a potential biomarker for axonal microstructural changes

associated with short term neuro-plasticity (Tavor et al., 2011). Nevertheless, a limitation of the CHARMED model lies in the fact that measuring multiple shells requires longer acquisition times. Additionally, the appropriate number of restricted compartments needs to be chosen *a priori*. Finally, fitting the model is computationally expensive (Parker, 2014).

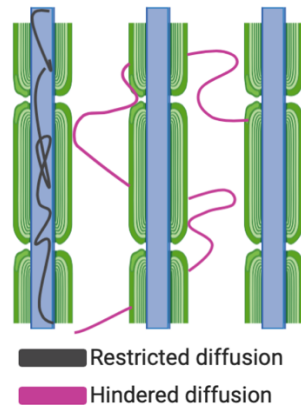


**Figure 5. Schematic representation of the CHARMED model of diffusion.**

*The two modes of diffusion in white matter: hindered outside axons and restricted within axons (Assaf et al. 2004).*

### **2.3.3. Magnetization transfer (MT) imaging**

The typical shortest echo time used in MRI is around 2 ms, implying that MRI cannot directly detect protons with a  $T_2$  of less than 1 ms. Such protons can be found in macromolecules such as large proteins, cell membranes, and myelin. However, protons in free water are in constant motion and come into regular contact with macromolecular protons, so that it is possible for a proton in free-water to exchange with a macromolecule-bound proton, when the water momentarily binds to the surface of the macromolecule. Under these conditions, the magnetization-state of the free-water protons can exchange with that of the macromolecular protons, and vice-versa (Figure 6). This exchange of magnetization can either happen by direct chemical exchange of the hydrogen atom, or by spin-spin interactions, and

forms the foundation of magnetization transfer (MT) imaging (Wolff & Balaban, 1994). The greater the amount of the macromolecules present in a voxel, the more free water spins will be excited *via* this phenomenon. This, in turn, impacts on the MRI signal, so that an attenuation in the free-water signal can be observed (Figure 7).

Under the assumption that, in WM most macromolecular content is associated with myelin, the MT effect can be exploited here as an indirect measure of myelin content (Heath et al., 2018). Specifically, a magnetization transfer ratio (MTR) map can be obtained by taking an image with a single MT pulse applied, and normalizing this with an image with no MT-weighting, while holding all other parameters constant (Heath et al., 2018; Horsfield, 2005). A number of animal studies have indicated a correlation between MTR and myelin content (Dousset et al., 1992, 1995), showing that MTR is decreased when demyelination is experimentally induced in animal models. Correlations with histopathology have also been shown between MTR and demyelination, or remyelination in histological analyses of rat brains respectively (Deloire-Grassin et al., 2000).

However, though MTR maps are quite easily obtained, the amount of MT effect depends on the choice of off-resonance RF power and frequency offset, as well as  $B_0$ ,  $B_1$  and  $T_1$ , therefore making quantitative comparisons between different scanners and studies difficult to implement. Furthermore, other tissue changes such as inflammation (Brochet & Dousset, 1999; Gareau et al., 2000), oedema (Cook et al., 2004), and activation of immune responses (Blezer et al., 2007) have been found to propagate into MTR maps.

Quantitative magnetization transfer (qMT) moves beyond MTR by modelling the MT-induced signal change as a function of multiple RF amplitudes and off-resonance frequencies (Henkelman et al., 1993). Images are therefore sensitized to different portions of the macromolecular spectrum, similar to how different gradient amplitudes and directions sensitize the MR signal to different amplitudes and directions of water diffusion in DWI. The advantage

of modelling MT parameters quantitatively, is that such measures should be independent across multiple experiments, scanners, and vendor platforms. The downside, however, is that many measurements are required to robustly fit all the parameters, and therefore long acquisition times are required (Heath et al., 2018).

One of the outcome measures of qMT, the macromolecular proton fraction (MPF), identifies the ratio of the number of bound macromolecular protons to the total water protons (Ramani et al., 2002), and has been shown to be highly sensitive to myelin content in WM. As mentioned in Chapter 1, this has been shown to reflect demyelination in rodents (Ou et al., 2009), to be sensitive to demyelination processes in multiple sclerosis patients (Levesque et al., 2010), and to reflect myelin content of WM in *post-mortem* studies of multiple sclerosis brains (Schmierer et al., 2007). As discussed in Chapter 1, though MPF is sensitive to WM myelin, this metric can also be affected by changes in cells and water content due to inflammation (Henkelman et al., 2001; Odrobina et al., 2005). It has thus been contended that MT parameters, such as the MPF, are biomarkers for WM pathologies such as inflammation, demyelination and axonal loss (Levesque et al., 2010; Schmierer et al., 2007; Sled, 2018; Stanisz et al., 2004).

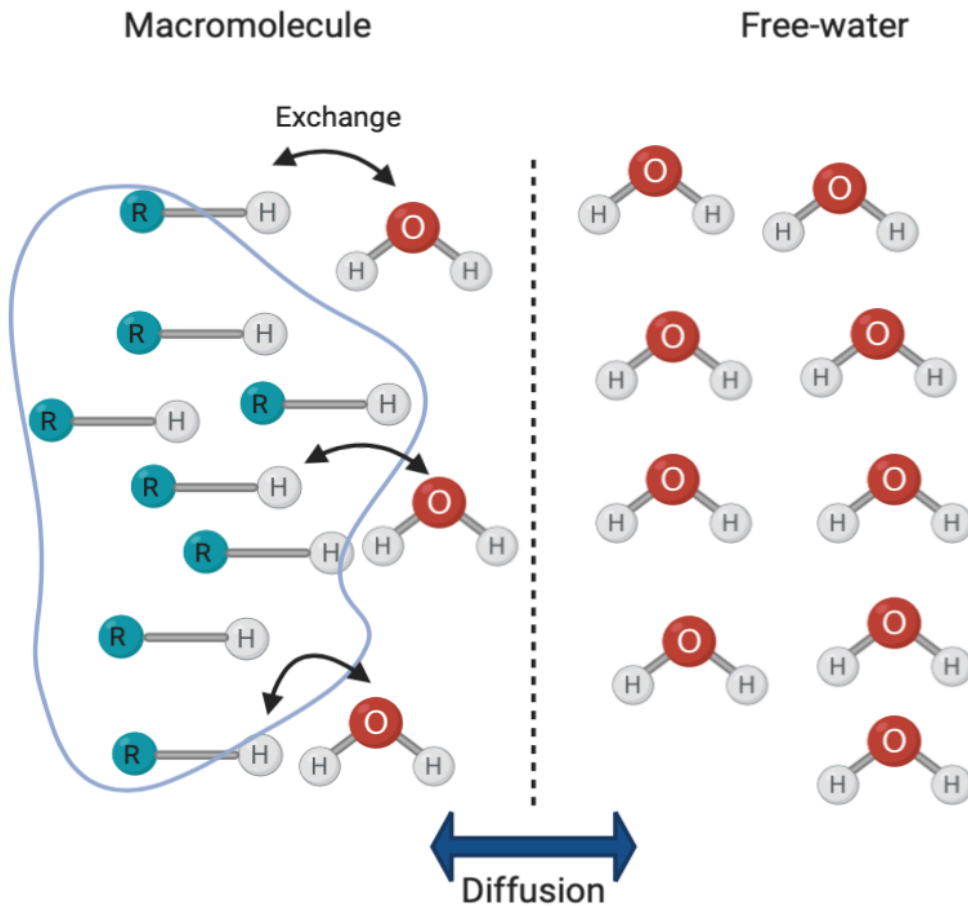


**Figure 6. Representation of the magnetization transfer effect.**

On the left is a macromolecule that has functional groups (R) with bonded hydrogen atoms (H), which are available to exchange with those in the free-water or liquid pool. As macromolecules are relatively immobile, the nuclei of any hydrogen atom on them present a short  $T_2$  ( $T_2 < 100 \mu\text{s}$ ), so that their signal is not normally seen in a MR image. On the other hand, protons in the free-water pool move easily and have a long  $T_2$  ( $T_2 > 100 \mu\text{s}$ ). The spins are in constant exchange between the macromolecular and the free-water pool, either by chemical exchange or spin-spin interactions; in this way, the state of the magnetization in the macromolecular pool can influence that in the free-water pool.

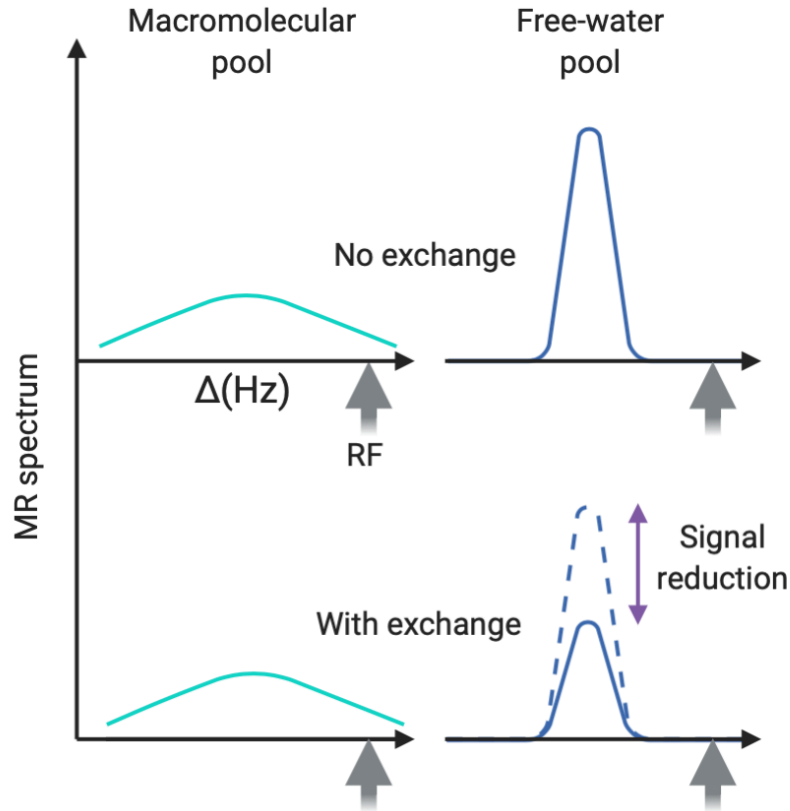


**Figure 7. Effect of magnetization transfer on the MRI signal.**

*If a radio frequency (RF) pulse is applied off-resonance, this has no effect on the observable free-water spectrum if the protons do not exchange magnetization with protons in the macromolecular pool (top). On the other hand, if exchange takes place (bottom), then the macromolecular magnetization is transferred to the liquid pool, resulting in a reduction in the observable signal. This manifests as reduced signal amplitude. Figure adapted from Horsfield (2005).*

### **2.3.4. Susceptibility-weighted imaging (SWI) and frequency difference mapping**

SWI identifies a range of techniques that sensitize the MRI signal to the magnetic properties of tissue. As discussed above, scanning at high field strength improves frequency and phase contrast in susceptibility contrast measurements and provides better  $R_2^*$  contrast due to stronger susceptibility-based field variations. Combined with the SNR increases associated with increased field strength, this has led to a rapid development of techniques with contrast based on the magnetic susceptibility of tissues (Duyn, 2018).

Contrast in SWI can be generated with “gradient echo” (GRE) type pulse sequences which consist of a single radio-frequency signal excitation pulse followed by gradient encoding and signal acquisition over a range of TEs, i.e. a range of delays after RF excitation. While most components of tissue have a magnetic susceptibility that is very close to that of water, and therefore do not influence contrast in SWI, storage iron (in ferritin and hemosiderin), iron in deoxyhaemoglobin (primarily found in the venous vasculature), and myelin, are major contributors to magnetic susceptibility changes in the brain (Duyn & Schenck, 2017; Schenck, 1996). This offers the potential to study myelin and iron levels in the neural tissue (Langkammer et al., 2012) and for structural details to be studied not only between, but also within GM and WM (Duyn et al., 2007; Li et al., 2006).

Interestingly, SWI studies have shown that in major WM tracts, sub-voxel structure also affects MRI susceptibility contrast. Specifically, due to differences in transverse relaxation rates and frequency offsets between different WM compartments, the evolution of the GRE signal from WM tissue is non-mono-exponential. Precisely, myelin water signal decays much faster than intra- and extra-axonal water signals due to its short  $T_2^*$  (<10 ms at 7 Tesla). In turn, this gives rise to local frequency/phase offsets which are sensitive to the local WM microstructure (Sati et al., 2013; Wharton & Bowtell, 2012, 2013). Moreover, this signal has been shown to be sensitive to the orientation of WM fibres with respect to the magnetic field  $B_0$ , so that maximum contrast between compartments is observed when fibres are oriented perpendicularly to the magnetic field (Lee et al., 2010; Schäfer et al., 2009; Wharton & Bowtell, 2012).

Although the phase of the complex MR signal carries valuable information about the local microstructure because of its electromagnetic properties, this information is also affected by large-length scale field variations and RF-related phase offsets. Therefore, when quantifying the local complex signal evolution, a robust method is necessary in order to remove the effects

from non-local field perturbation sources without corrupting the local phase evolution. Accordingly, Frequency Difference Mapping (FDM) has been proposed as complex signal processing method (Tendler & Bowtell, 2019; Wharton & Bowtell, 2013). This relies on the assumption that the large length scale magnetic field perturbations produce a constant rate of phase evolution throughout the GRE train, and removes them by calculating the difference in the rate of phase accumulation at short and long TEs.

One interesting consequence of the unique magnetic architecture of WM is the possibility to estimate the relative size of the myelin, interstitial, and axonal water compartments (Li et al., 2015; Nam et al., 2015a). Specifically, to assess the effects of microstructure on GRE images, signal evolution can be described using a three-pool model in which the external, myelin, and axonal compartments each have different signal amplitudes, decay rates, and frequency offsets (Figure 8) (Tendler & Bowtell, 2019). An estimate of myelin water fraction obtained in this way may be used as proxy for tissue myelin content, which is particularly relevant to the study of demyelination in disease (Laule et al., 2008; Li et al., 2015).

## **2.4. Analysis techniques for the assessment of WM microstructure**

The WM microstructure metrics discussed above can be extracted for each voxel to generate parametric maps. This body of work employed two main approaches to the analysis of these maps to assess WM microstructure changes in the HD brain (Figure 9): i. region of interest (ROI) analyses, ii. voxel-wise whole-brain approaches by registering each map to a common space. Specifically, I first carried out *a priori* analyses of specific ROIs; I then followed-up these assessments with exploratory whole-brain analyses approaches to investigate how localised the detected effects were to specific areas. The following sections discuss these two approaches.

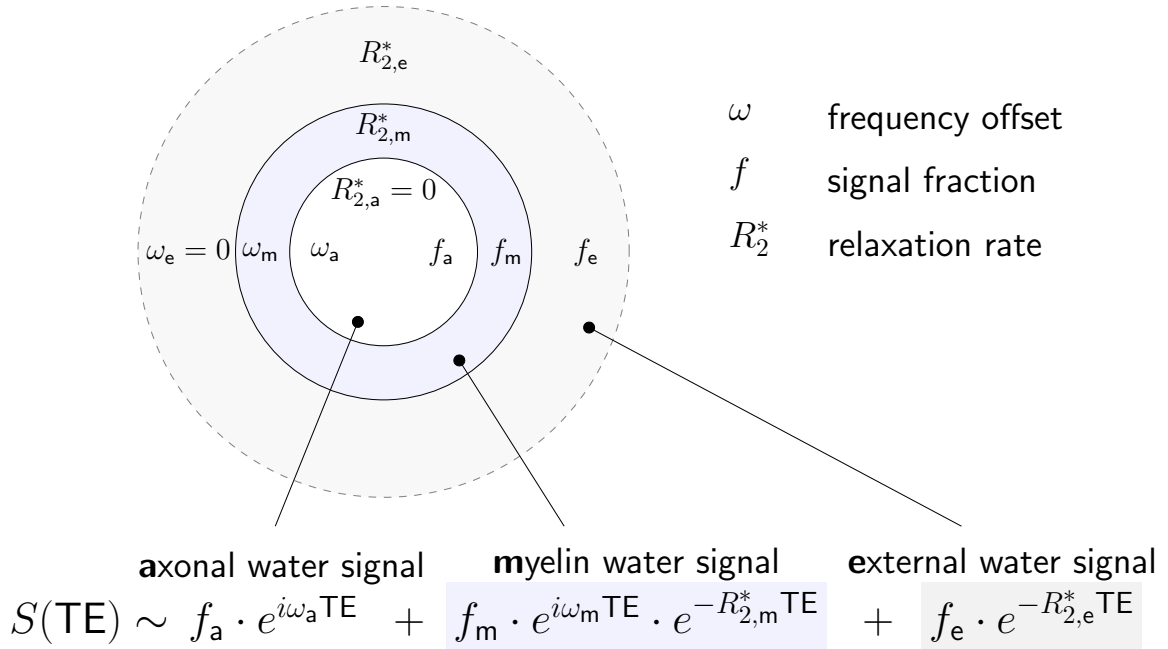


**Figure 8. Schematic representation of the 3-pool model for describing mGRE signal evolution in WM fibres of perpendicular to  $B_0$ .**

Subscripts a/m/e denote intra-axonal/myelin/extra-axonal water pools,  $f$  stands for signal fractions,  $\omega$  are angular frequency offsets relative to the extra-axonal frequency, and  $R_2^*$  stands for the effective transverse relaxation rates.

### 2.4.1. Moving beyond voxel-based (VB) analyses

VB analyses have become more and more popular as a method for analysing quantitative MRI images. While these were originally derived for the analysis of anatomical MRI data (Ashburner & Friston, 2000), they are being increasingly used for the analysis of DT-MRI data. In particular, Tract-Based Spatial Statistics (TBSS) (Smith et al., 2006) has been for a long time the most popular approach to whole-brain, voxel-wise analyses of WM changes. In whole-brain voxel-wise analyses, exact alignment of anatomical structures can be problematic. Additionally, it is common practice to spatially smooth data before computing statistics, which in turn can have a big effect of the final result (Abe et al., 2010; Jones et al., 2005a). TBSS was developed to deal with these issues and correct for residual misalignment so that values on the

skeleton corresponded to the centre of the tract. The TBSS framework typically adopts the Threshold-Free Cluster-Enhancement (TFCE) method (Smith & Nichols, 2009) to improve the statistical estimation of the voxel-wise analysis over the skeleton. This consists in enhancing cluster-like features in a statistical image, and was argued to provide increased sensitivity compared to other commonly used statistical methods (Smith & Nichols, 2009).

However, several problems associated with TBSS have been discussed, together with potential solutions (Edden & Jones, 2011; Keihaninejad et al., 2012; Van Hecke et al., 2010; Zalesky, 2011). For example, one important point of debate is the limited anatomical specificity of TBSS. This method was argued to be “tract-based”, and to allow comparisons of voxels of the same section (assumed to be the centre) of the equivalent WM tract from all subjects (Smith et al., 2006). However, as TBSS utilises the FA map while discarding orientational information captured by the diffusion data, anatomical specificity will be hampered when pathways of different structures merge - for example when looking at projections of the CC and the corona radiata. With no (long-distance) directional tract information, it is indeed virtually impossible to assign the FA values to the same anatomical structure consistently across subjects, because the skeletonization step leads to these different bundles collapsing on top of each other (Bach et al., 2014). Additionally, the shape of the skeleton, together with the statistical outputs of the analysis, have been shown to be rotationally variant (Edden & Jones, 2011). Specifically, the thickness of the skeleton was shown to be a function of fibre orientation, and this in turn modulates the statistical sensitivity of the group comparisons performed. As a consequence, significant differences are more likely to be detected in centrally located WM structures that are obliquely oriented with respect to the imaging matrix (Edden & Jones, 2011).

Importantly, TBSS and standard voxel-based approaches use regular grids of voxels to represent the anatomical space occupied by the brain. However, the topology of the voxel grid given by the adjacency between voxels does not reflect properties of the brain's anatomy such

as its spatial heterogeneity or its heterogeneous connectivity. For example, spatial adjacency between voxels does not take into consideration the underlying anatomy, and adjacent voxels belonging to two different anatomical regions might be clustered together during analysis, thus impairing anatomical specificity. Therefore, the use of voxels to visualise and analyse brain images may constitute a limitation when the topology of the voxel space does not adequately represent the underlying anatomy (Luque Laguna, 2019).

On the other hand, using *a priori* anatomical information can improve statistical analysis of neuroimaging data. In this work, I will exploit a recently developed analysis method called Tract-Based Cluster Analysis (TBCA) (Luque Laguna, 2019), which uses the rich anatomical information from whole-brain tractography reconstructions, to inform the cluster-level inference analysis of voxel-based images. Specifically, the method is based on the novel concept of ‘hyper-voxel’, which combines the anatomical and connectivity information provided by tractography streamlines with the spatial encoding capabilities of multi-dimensional voxels.

Tract-based hypervoxels extend standard 3D voxels with extra dimensions to represent the position ( $\mathbf{p}$ ), the local orientation ( $\mathbf{o}$ ) and the global trajectory ( $\mathbf{t}^{\rightarrow}$ ) of streamlines intersecting a voxel (Figure 9). In TBCA, the clustering of the data is based on the along-tract connectivity and radial adjacency of hypervoxels within an hypervoxel template (Figure 10). The use of tract-based hypervoxels increases the sensitivity of cluster inference analysis and provides the anatomical specificity required to disentangle distinct clusters belonging to different anatomical tracts. When applied to real clinical data, TBCA demonstrated increased sensitivity compared to previous cluster-level inference approaches (Luque Laguna, 2019). In Chapter 3 the TBCA pipeline (Figure 10) is applied to the assessment of whole-brain WM microstructure changes in premanifest HD patients.

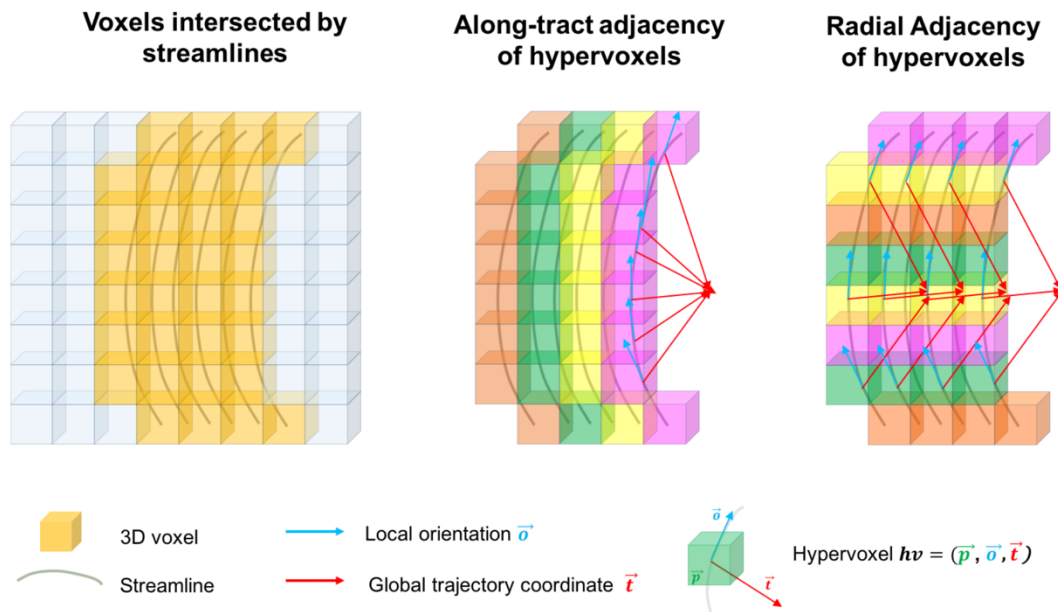


**Figure 9. Schematic representation of hypervoxels.**

On the left standard voxels and intersecting streamlines are represented. In the middle, hypervoxels that are along-tract connected, i.e. they are intersected by the same streamline. On the right are radially adjacent hypervoxels, i.e. those voxels that are spatially adjacent in 3D space, and additionally have the same local orientation ( $\vec{o}$ ) and global trajectory ( $\vec{t}$ ). Figure from Luque Laguna, (2019).

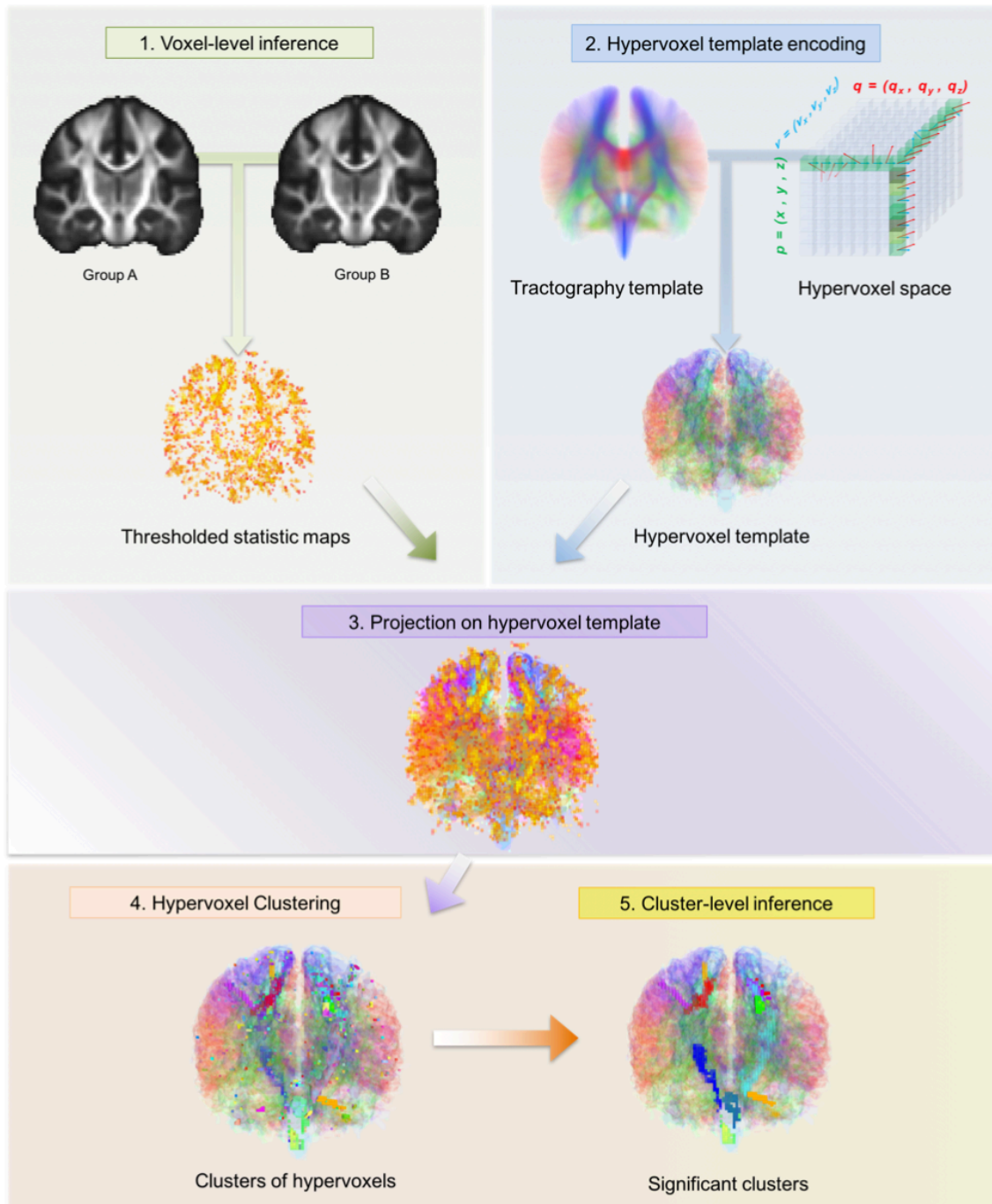


**Figure 10. The TBCA analysis pipeline.**

After all images have been normalized to a common anatomical space, statistics maps are produced based on the voxel-level analysis of the data; this is done by using a non-parametric approach based on a permutation test strategy (Winkler et al., 2014). The statistic maps are thresholded by a value of  $p = 0.01$ . Next, the significant voxel level statistic results are projected on a hypervoxel template. Finally, identification of significant clusters of hypervoxels takes place. Two hypervoxels will belong to the same cluster if they are adjacent (i.e. they have the same local orientation ( $\mathbf{o}$ ) and global trajectory ( $\mathbf{t}$ )), and they share a common streamline. Figure from Luque Laguna, (2019).

### **2.4.2. Using tractometry for a multi-modal assessment of WM microstructure**

In contrast to voxel-wise, whole brain techniques, region-of-interest (ROI) approaches enable the investigation of anatomically pre-defined brain regions. ROI investigations can be carried out following several different approaches. For example, a specific ROI may be manually segmented on each individual brain (see for example the experimental work carried out in Chapter 4). This task is usually done in a slice-by-slice manner, with an expert delineating the ROI, and it is therefore very time consuming and prone to intra- and interobserver variability; this in turn can result in large difference in the extracted values.

Studies using fibre-tracking algorithms to define a particular tract, and then extract the mean of a certain parameter of interest from within that tract have become increasingly common. By employing information afforded by the diffusion data, fibre tractography pieces together the orientation of diffusion in each voxel to infer fibre trajectories. In Chapters 3, 5 and 6, tractography reconstructions are employed to perform a multi-modal, comprehensive assessment of tract-specific microstructural measurements. This method, called ‘tractometry’ (Bells et al. 2011; Jones et al. 2005, 2006), consists in combining multiple tract-specific microstructural metrics to gain complementary information on the microstructural make-up of a specific tract.

Diffusion MRI tractography has offered means to reconstruct specific WM pathways non-invasively in the animal and human brain and provides more anatomically valid segmentations compared to atlas-based approaches, which in turn rely on alignment of all images to a standard template. Until recently, such WM anatomy could only be studied *post-mortem* with dissection, or *via* invasive tracing in non-human animals (Johansen-Berg & Behrens, 2006). However, the anatomical accuracy of diffusion-weighted tractography continues to be controversial, and reconstructions of connectomes that are both highly sensitive and specific remain challenging

(Bastiani et al., 2012; Calabrese et al., 2015; Donahue et al., 2016; Maier-Hein et al., 2017; Reveley et al., 2015; Sporns et al., 2005).

WM tractography is generally performed following two main approaches: those using deterministic (Basser et al., 2000; Conturo et al., 1999; Mori et al., 1999; Poupon et al., 2000) and those using probabilistic (e.g. Behrens et al., 2003, 2007; Jones & Pierpaoli, 2005; Lazar & Alexander, 2005) algorithms. In deterministic tractography, best estimates of the underlying fibre orientation are used to generate a tractogram, after the identification of a suitable initial anatomically defined location (or ‘seed point’), then propagating through the 3D space until a pre-defined termination criterion is met, such as the curvature angle. The reliability of the WM pathways reconstructions is therefore dependent on the choice of the seedpoints and waypoints to constrain the tracking, and therefore on the user’s knowledge of neuroanatomy (Catani et al., 2002). Additionally, deterministic algorithms only provide a single estimate of trajectory for each supplied seed point, and therefore branching tracts are not considered. Finally, they do not indicate how confident one can be in the accuracy of the reconstructed trajectory.

Probabilistic tractography approaches have been proposed to overcome this limitation (Behrens et al., 2007) as they express the “precision” with which a pathway can be reconstructed based on a specific dataset (Jones & Cercignani, 2010). Specifically, by employing diffusion information to infer both fibre orientation and an estimate of orientation uncertainty in each voxel, a probabilistic map of WM connections is constructed (Parker, 2014). As in deterministic approaches, streamlines are propagated from a seed point. However, in probabilistic techniques, at each propagation step an orientation is randomly selected from the underlying distribution, so to build a spatial distribution of streamlines.

Spherical deconvolution methods allow to determine a fibre orientation distribution function (fODF) with multiple peaks from the total signal in a voxel, by employing voxel-based approaches. This function is then used as input to deterministic or probabilistic tracking

methods. In the present work, two fibre orientation distribution (FOD) deconvolution algorithms were employed: a modified damped Richardson-Lucy algorithm (dRL) (Dell'acqua et al., 2010) and the multi-shell, multi-tissue CSD (MSMT-CSD) method (Jeurissen et al., 2014) (see Table 5 for an overview of the approaches utilised with reference to specific experimental chapters; see experimental chapters for specific tractography details). The former assumes a diffusion tensor representation when obtaining the diffusion profile, and uses adaptive regularization, which includes an isotropic term to model partial volume. The latter employs multi-shell DWI data to incorporate the distinct signal from multiple tissue types. Specifically it exploits the unique b-value dependences of different macroscopic tissue types (WM, GM, or cerebrospinal fluid), to estimate the ODF in different tissue compartments, thus leading to a substantial increase in the precision of the fODFs and the resulting tractograms (Jeurissen et al., 2014).

## **2.5. Overview of MRI acquisition and analysis approaches utilised in the present work**

An overview of the mouse and patient MRI acquisition and analysis approaches can be found in Figure 11 and Table 5. For the MRI methodologies in both the animal and patient studies, there was an effort to ensure the pulse sequences were as similar as possible in order for comparisons to be drawn. However, because of: i) differences in the relative size of the brain compared to the scanner bore, ii) differences in magnetic field strength between animal and human MR systems, dissimilarities were present in the scan parameters used between human and animal experiments. Additionally, some of the sequences could not be translated because of hardware-imposed limits or time constraints on the project. A comparison of scan parameters is shown in Table 6. Further details of experimental protocols (i.e. acquisition and analysis approaches) can be found in each individual experimental chapter.

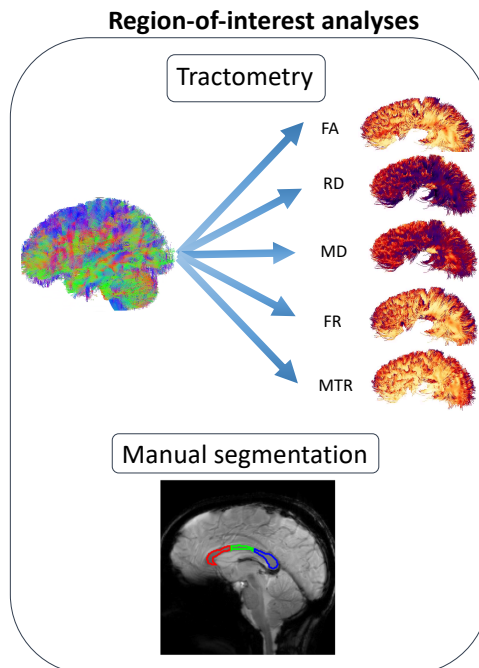
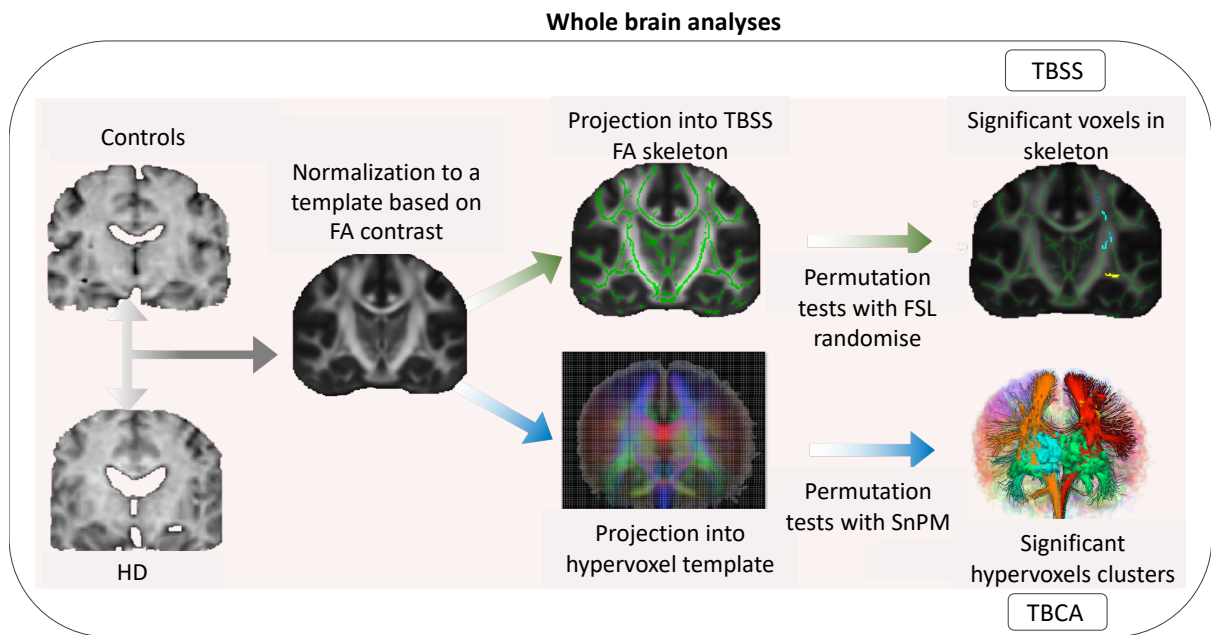


**Figure 11. Different approaches to the analysis of MRI data employed in the present work.**

The top panel shows a comparison between TBSS and TBCA analyses. See Table 5 for an overview of all analysis methods in reference to the different experimental chapters.

**Table 5. Overview of the mouse and patient MRI acquisition and analysis methods in reference to the different experimental chapters.**

*More information about acquisition and analysis pipelines is provided in each experimental chapter.*

	<b>R6/1 mouse model</b>	<b>Premanifest HD patients</b>		<b>Manifest HD patients</b>
Chapter	5	3	4	6
Hardware (field/gradient-strength)	Bruker Biospin (9.4 Tesla/300 mT/m)	Siemens Connectom (3 Tesla/300 mT/m)	Siemens 7 Tesla (7 Tesla/70 mT/m)	3 Tesla GE system (3 Tesla/40 mT/m)
MRI	T <sub>1</sub> -w, DTI, CHARMED, qMT	DTI, CHARMED, MT	mGRE	T <sub>1</sub> -w, DTI, CHARMED, qMT
Processing & Analysis approach	Tractography (MSMTCSD), tractometry, TBSS, voxel-based morphometry	Tractography (MSMTCSD), tractometry, TBSS, Freesurfer segmentation	ROI manual segmentation	Tractography (dRL), tractometry, TBSS

**Table 6. Comparison of mouse and patient MRI parameters.**

*RARE: Rapid Acquisition with Refocused Echoes. MPRAGE: Magnetization prepared - rapid gradient echo. FSPGR: Fast spoiled gradient echo. SE: Spin echo. EPI: echo-planar imaging. SPGR: spoiled gradient echo. FLASH: Fast low angle shot. mGRE: multi-echo gradient recalled echo. FoV: field of view. TR: repetition time. TE: echo time.*

	<b>R6/1 mouse model (Chapter 5)</b>	<b>Premanifest HD patients (Chapters 3, 4)</b>	<b>Manifest HD patients (Chapter 6)</b>
<i>In vivo/ex vivo:</i>	<i>Ex vivo</i>	<i>In vivo</i>	<i>In vivo</i>
<b>Anatomical scan</b>			
Hardware (field/gradient-strength)	Bruker Biospin (9.4 Tesla/300 mT/m)	Siemens Connectome (3 Tesla/300 mT/m)	3 Tesla GE system (3 Tesla/40 mT/m)
Pulse sequence	FLASH (3D)	MPRAGE	FSPGR
Matrix size	192×192×72	256×256	256×256
FoV	19.2×19.2×18	256	230
Slice thickness (mm)	-	1	1
TE, TR (ms)	4, 30	2, 2300	7.8, 2.9
Flip angle (°)	36	9	20
<b>DTI</b>			
Hardware (field/gradient-strength)	Bruker Biospin (9.4 Tesla/300 mT/m)	Siemens Connectome (3 Tesla/300 mT/m)	3 Tesla GE system (3 Tesla/40 mT/m)
Pulse sequence	RARE	SE/EPI	SE/EPI
Matrix size	192×192	495×495	96×96
FoV	19.2×19.2	990	240
b-values (s/mm <sup>2</sup> ) – gradient directions	0, 1200 - 50	0, 500 - 30, 1200 - 30	0, 1200 - 60
Slice thickness (mm)	0.4	2	2.4
TE, TR (ms)	31, 3000	59, 3000	87, 16000
Flip angle (°)	90	9	90

**CHARMED**

Hardware (field/gradient-strength)	Bruker Biospin (9.4 Tesla/300 mT/m)	Siemens Connectome (3 Tesla/300 mT/m)	3 Tesla GE system (3 Tesla/40 mT/m)
Pulse sequence	RARE	SE/EPI	SE/EPI
Matrix size	192×192	495×495	96×96
Fov	19.2×19.2	990	240
b-values (s/mm <sup>2</sup> ) – gradient directions	0, 1200 – 50, 2400 – 50, 4000 - 50	0, 500 - 30, 1200 - 30, 2400 - 60, 4000 - 60, 6000 - 60	0, 1093 - 6, 2188 - 3, 3281 - 4, 4375 - 5, 5469 - 6, 7656 - 7, 8750 - 8
Slice thickness (mm)	0.4	2	2.4
TE, TR (ms)	31, 3000	59, 3000	126, 17000
Flip angles (°)	90	9	90
<b>T<sub>1</sub> map</b>			
Hardware (field/gradient-strength)	Bruker Biospin (9.4 Tesla/300 mT/m)	Siemens Connectome (3 Tesla/300 mT/m)	3 Tesla GE system (3 Tesla/40 mT/m)
Pulse sequence	FLASH (3D)	-	SPGR (3D)
Matrix size	192×192×72	-	96×96×60
Fov	19.2×19.2×18	-	240
Slice thickness (mm)	-	-	-
TE, TR (ms)	4, 30	-	6.85, 1.2
Flip angles (°)	13, 17, 24, 36, 48	-	15, 7, 3
<b>MT/ qMT</b>			
Pulse sequence	FLASH 3D	Turbo FLASH	FSPGR 3D
Matrix size	192×192×72	128 × 128 × 104	96×96×60
FoV	19.2×19.2×18	220 × 220 × 179	240
Slice thickness (mm)	-	1.72	-
TE, TR (ms)	5, 47	2.1, 60	2.18, 25.82
Off-resonance pulses (Hz/°)	0/350, 1000/350, 1500/350, 3000/350, 6000/350, 12000/350, 24000/350, 1000/950, 1500/950, 3000/950, 6000/950, 12000/950, 24000/950	1200/333	1000/332, 1000/333, 12062/628, 47185/628, 56363/332, 2751/628, 1000/628, 1000/628, 2768/628, 2791/628, 2887/628
Flip angles (°)	5	5	5
<b>FDM</b>			
Hardware (field/gradient-strength)	-	Siemens 7 Tesla (7 Tesla/70 mT/m)	-
Pulse sequence	-	mGRE	-
Matrix size	-	256 × 256 × 51.2	-

FoV	-	$256 \times 256 \times 5$	-
Slice thickness (mm)	-	5	-
TE1, $\Delta$ TE, TR (ms)	-	1.62, 1.23, 100	-
Flip angles ( $^{\circ}$ )	-	15	-

## **2.6. Recap of introductory chapters**

This section concludes the introductory part of this Thesis. In these first two chapters, I have provided the relevant clinical and methodological background to serve as a foundation for the following experimental work. In Chapter 1, I reviewed the symptomatology of HD and the current understanding of WM degeneration in this disease, highlighting both macroscopic and microstructural WM changes that have been described in the literature thus far. Additionally, I discussed the advantages and challenges of a translational approach to the study of HD pathology. Finally, I described the major aims of this Thesis, along with an outline of each of the coming chapters.

In the present Chapter, I have been discussing some of the methodological approaches that have been utilised so far in neuroimaging studies to investigate changes in WM microstructure. Specifically, I first provided an overview of the MRI hardware I exploited in the present work, with a focus on the advantages and challenges of scanning at ultra-high field and with ultra-strong gradients. Subsequently, I moved on to talk about the MRI modalities I employed in this work, giving an overview of the fundamental physics that allow each MRI approach to retrieve meaningful information about tissue microstructure. Finally, I critically evaluated the analysis methods utilised in the research described in the chapters to come. The following section (Chapters 3 to 6) constitutes the novel experimental work of this Thesis.

## **Chapter 3**

# **Investigation of white matter microstructure in premanifest HD with ultra-strong gradients**

### **3.1. Chapter summary**

The aim of this Chapter was to exploit ultra-strong gradients to perform a comprehensive assessment of WM microstructure in premanifest HD. Differences in MTR (Wolff & Balaban, 1994) as a proxy measure of myelin content, and FR from CHARMED (Assaf & Basser, 2005) as a proxy marker of axon density (De Santis et al. 2014) were investigated between premanifest patients and age- and sex-matched controls. Additionally, group differences in FA, AD and RD from DT-MRI (Pierpaoli and Basser 1996) were also assessed. A tractometry approach (Bells et al. 2011; Jones et al. 2005, 2006) was employed to investigate region-specific changes across the corpus callosum (CC). Additionally, tract-based cluster analysis (TBCA) (Luque Laguna, 2019) was applied for the first time in HD to explore brain-wise WM microstructure abnormalities associated with the premanifest stage of the disease. Results were examined alongside macrostructural GM changes and behavioural measures to explore the contribution of WM impairments to GM neurodegeneration and clinical symptoms.

### **3.2. Declaration of collaborations**

The processing of the data through the TBCA pipeline was conducted in collaboration with Dr Pedro Luque Laguna (Cardiff University).

### 3.3. Introduction

The investigation of WM microstructure in premanifest HD patients can improve our understanding of WM organization and pathology in this disease and provide an insight as to whether HD pathogenesis is associated with a breakdown of myelin and/or axonal degeneration (Bartzokis et al., 2007; Phillips et al., 2013). Despite a growing body of evidence showing that WM plays a role in HD pathology, the impact of the HD mutation on WM, and the contribution of WM abnormalities to clinical characteristics of the disease are not well understood. Additionally, given the mixed nature of psychiatric, cognitive and motor symptoms associated with HD, it is plausible that multiple WM pathways are involved in the disease, either as a direct effect of pathology, or as part of a compensatory network recruited in response to damage associated with the mutation. Nevertheless, only a minority of studies so far have focused on reconstructing individual WM pathways (Phillips et al., 2013; Saba et al., 2017; Steventon, 2014). Furthermore, the relationship between WM and GM degeneration and their relative contribution to subtle cognitive problems at the premanifest stage remains unknown. Therefore, here I used deterministic tractography, an approach to analysing diffusion MRI data which allows 3D reconstruction of WM fibre pathways *in vivo* (Jones, 2008) (see Chapter 2), to enable detailed assessment of HD-related microstructural alterations in WM pathways and their relation to GM morphology and clinical symptoms.

In terms of the quantitative indices used to evaluate WM pathways, most previous studies on HD-associated WM alterations (Di Paola et al. 2012, 2012; Rosas et al. 2010; Phillips et al. 2013) have employed DT-MRI (Pierpaoli & Basser, 1996) to quantify changes. Though diffusion tensor indices have the advantage of being highly sensitive to local changes in microstructure, they are inherently non-specific to subcomponents of WM microstructure (Alexander et al., 2007; De Santis et al., 2014), and therefore they do not allow the biophysical basis of any detected change to be inferred. On the other hand, in recent years, a number of

different approaches have been developed to increase sensitivity to specific sub-compartments of WM microstructure. Accordingly, parameters obtained from these approaches may provide more biologically sensitive and specific measures compared to tensor-based metrics.

In this Chapter, WM microstructure differences in premanifest HD carriers were explored by combining FA, AD and RD from DT-MRI (Pierpaoli & Basser, 1996), with MTR from magnetization transfer imaging as a proxy measure of myelin, and FR from CHARMED (Assaf & Basser, 2005) as a proxy measure of axon density (De Santis et al., 2014). The aim was to afford a more biologically meaningful interpretation of microstructural alterations in the HD brain and disentangle the contribution of changes in axon microstructure *versus* changes in myelin to HD pathology. Importantly, by exploiting the very latest-in ultra-strong magnetic field gradient technology of the Connectom scanner (Setsompop et al., 2013; Jones et al., 2018), it was possible to produce the level of filtering needed to better tease apart the contribution of these sub-compartments of WM microstructure to HD pathology.

Alterations in microstructural metrics were assessed using two analytical pipelines: i. a tractometry approach (Bells et al. 2011; Jones et al. 2005, 2006) was employed to assess tract-specific changes in microstructure across the CC, and ii. a whole-brain approach was used to further explore WM microstructure abnormalities associated with premanifest HD.

The CC is the largest WM fibre tract in the brain and contains millions of fibres that carry information between the hemispheres; additionally, this tract plays an integral role in relaying sensory, motor and cognitive information between homologous cortical regions (Aboitiz et al., 1992; Phillips et al., 2013). Crucially, callosal fibres vary in size and age of myelination, with larger fibres that myelinate early in life seen in the more posterior portions, and smaller, later myelinating fibres found in anterior regions (Aboitiz et al., 1992). Investigating microstructure along the CC might provide insight into regional differences in the impact of HD on WM myelination and/or axon changes, and elucidate HD-related

pathological processes in the context of the Demyelination Hypothesis of HD (Bartzokis et al., 2007).

This view suggests that *mHTT* leads to premature myelin breakdown in HD, causing a disruption in cell signalling and neuronal death. Furthermore, neuronal degeneration in the HD brain is hypothesised to begin from early myelinating caudate and putamen striatum structures and then spread in a bilateral and symmetric pattern to involve other earlier-myelinating regions. In turn, later-myelinating regions are left much less affected (Bartzokis, Cummings, Perlman, Hance, & Mintz, 1999).

Based on Bartzokis's hypothesis, we would expect microstructural changes to occur in posterior callosal subregions (i.e. within the splenium and isthmus) early in disease progression. Consistent with this hypothesis, previous evidence suggests that early changes in the CC are detectable in posterior callosal areas. Specifically, decreased cross-sectional area and increased diffusivity limited to the callosal isthmus, which become more pronounced in those closer to disease onset, have been shown (Di Paola et al., 2012). In contrast, manifest HD gene carriers display decreased cross-sectional area, alongside widespread alterations in FA, RD and AD, across the whole structure of the CC (Di Paola et al., 2012; Liu et al., 2016; Saba et al., 2017). Accordingly, the aim of the present work was to provide novel evidence on regional callosal changes in HD, and move beyond the existing literature by employing ultra-strong gradient microstructural measurements to disentangle apparent myelin and axon density properties of callosal WM.

Additionally, because of evidence that WM volume loss in HD is not limited to the CC (Aylward et al., 2011; Beglinger et al., 2007; Ciarmiello et al., 2006; Paulsen et al., 2008; Rosas et al., 2006; Tabrizi et al., 2009, 2011, 2012), and the concept of compensatory networks in response to neurodegeneration (Klöppel et al., 2009), the tractometry analysis was followed up with an exploratory, whole-brain analysis. Specifically, TBCA (Luque Laguna, 2019) was

applied to assess brain-wise group differences in FA, AD, RD, FR and MTR. TBCA combines the anatomical and connectivity information provided by tractography streamlines with the spatial encoding capabilities of hyper-voxels. As explained in Chapter 2, the use of tract-based hypervoxels increases the sensitivity of cluster inference analysis and provides the anatomical specificity required to disentangle distinct clusters belonging to different anatomical tracts.

The evidence of cognitive and behavioral impairments in HD carriers early in the disease course, and the strong association of even the most subtle cognitive changes with functional decline such as the inability to hold down employment or looking after one's financial affairs, institutionalization and burden on families (Hamilton et al., 2003; Nehl et al., 2004; Williams et al., 2010), stress the importance of understanding these symptoms and how they may relate to pathological processes, such as changes in WM microstructure. While a recent study showed that no detectable motor, cognitive, or psychiatric differences could be detected in premanifest HD carriers approximately 24 years from predicted clinical onset (Scahill et al., 2020), multisite observational studies in premanifest HD such as TRACK-HD (Tabrizi et al., 2012), PREDICT-HD (Paulsen et al., 2008), and ENROLL-HD (Landwehrmeyer et al., 2017) have consistently reported subtle cognitive impairments at least 10–15 years before the onset of motor symptoms, across attention, working memory, processing speed, psychomotor functions, episodic memory, emotion processing, sensory-perceptual functions, and executive functions (Paulsen et al., 2008, 2014a, 2014b, 2017; Pirogovsky et al., 2009; Stout et al., 2011, 2012). Therefore, another aim of this Chapter was to perform a characterization of premanifest HD at the cognitive level. Performance was compared between patients and healthy controls in a number of tests, selected in order to capture a range of cognitive domains, with a particular focus on executive functions, social cognition, and motor speed, as these have been suggested to represent the earliest cognitive indicators of HD (Paulsen, 2011).

Finally, another objective of this Chapter was to develop a composite cognitive score using principal component analysis (PCA) that could adequately describe the variability in cognitive performance across the HD group, and that could be used for the analysis of relationships with brain structure in premanifest HD patients.

## **3.4. Materials and Methods**

### **3.4.1. Participants**

This study reports on a sample of 25 individuals with premanifest HD and 25 age- and sex-matched healthy controls. Procedures in this study were performed with ethics approval by the local National Health Service (NHS) Research Ethics Committee (Wales REC 5 18/WA/0172) and by the Cardiff University School of Psychology Ethics Committee, and were in accordance with the 1964 Helsinki declaration.

HD patients were recruited from the Cardiff HD Research and Management clinic, Bristol Brain Centre at Southmead Hospital, and the HD clinic at the Birmingham and Solihull NHS Trust. Of the healthy controls assessed, 20 were recruited from Cardiff University and the School of Psychology community panel, while 5 were patients' spouses or family members.

Participants were eligible to take part in the study if they had no history of head injury, stroke or cerebral hemorrhages. Participants also had to be eligible for MRI scanning i.e. to not present contraindications such as pacemakers, metal clips, stents or significant chorea which would have prevented them from lying still in the scanner. Control participants were excluded if they had a history of neurological or psychiatric conditions, and patients if they had a history of any other neurological condition. All patients had to have genetically-confirmed HD but no motor diagnosis.

All participants provided written informed consent prior to taking part in the study. Specifically, consent was taken upon arrival at the imaging center, where the information sheets were discussed and an opportunity to ask any further questions was provided, before participants were asked to read and sign the consent forms. They were informed of their right to withdraw from the study at any point without giving a reason, and were informed that they could request that their data be destroyed and not included in the study.

Three healthy controls and one patient were excluded from the cognitive data analysis because of missing data, therefore datasets from a total of 22 controls and 24 patients were used for the assessment of patient-group differences in cognition. 22 out of the 25 HD patients recruited for the imaging study had pen-and-paper cognitive task data available from their most recent assessment from their participation in the ENROLL-HD study (NCT01574053, <https://enroll-hd.org>). The progression of symptoms in ENROLL-HD participants is monitored longitudinally, and one of the optional components within the ENROLL-HD study is the giving of permission by participants to be contacted about other additional and affiliated HD research studies, and for their coded data to be accessed by researchers conducting HD-related research. As such, a full clinical data set including full medical and medication history is available for each research participant and this data was used in this study.

One control subject had to be excluded from the tractometry analysis because of poor callosal segmentation. Therefore, data from 25 patients and 24 healthy controls were used for tractometry analysis of the CC. On the other hand, this did not impact TBCA, and therefore a sample of 25 patients and 25 controls was used for this analysis. Table 7 summarizes information about demographic variables and performance in the Montreal Cognitive Assessment (MoCA) (Nasreddine et al., 2005) and in the Test of Premorbid Functioning - UK Version (TOPF-UK) for patients and controls. The two groups did not differ significantly in age or MoCA scores. However, controls scored significantly higher on the TOPF-UK FSIQ

than patients, consistent with existing evidence of an association between irregular word reading and disease progression in other neurodegenerative conditions (O'Rourke et al., 2011).

The Unified Huntington Disease Rating Scale (UHDRS) total motor score (TMS), total functional capacity (TFC), diagnostic confidence level (DCL) and patients' CAG repeat size were also obtained from the ENROLL-HD database and used as variables to characterize the patient sample. Table 8 provides background clinical information of the patient cohort. Based on total motor scores (TMS), all patients were at the premanifest disease stage. Based on diagnostic confidence level scores (DCL), four patients presented some motor abnormalities, but none of them presented unequivocal motor signs of HD. Table 9 summarizes information about patients' medication.

**Table 7. Summary of participants' demographic and clinical background information.**

Age is displayed in years. TOPFUK FSIQ = verbal IQ estimate based on the Test of Premorbid Functioning, UK version. There was a significant difference between patients and controls in TOPFUK FSIQ, with patients presenting significantly lower premorbid IQ. MoCA = Montreal Cognitive Assessment out of 30 (the higher the score the better the performance). MoCA scores for patients and controls ranged between 23 and 30. A score of 26 or over is generally considered to be normal, while an average score of 22.1 has been reported in people with mild cognitive impairment (Nasreddine et al., 2005). There was no significant difference in this test between the two groups.

	<b>HD patients (n = 25)</b>	<b>Controls (n = 25)</b>	<b>p-value</b>
<b>Gender male/female (%)</b>	15(60)/ 10(40)	14(56)/ 11(44)	p > 0.05
<b>Mean age (SD, range)</b>	42.04 (12.7, 21-70)	43.19 (12.6, 27-71)	p > 0.05
<b>Mean CAG (SD, range)</b>	41.4 (2.1, 37-45)	-	-
<b>Mean DBS (SD, range)</b>	235.94 (84.5, 61.5-450)	-	-
<b>Mean TOPFUK FSIQ (SD, range)</b>	116.16 (10.2, 98-137.4)	124.96 (6.9, 109-135.4)	p = 0.003
<b>Mean MoCA score (SD, range)</b>	27.92 (2.1, 24-30)	28.2 (1.8, 26-30)	p > 0.05

**Table 8. Background clinical information of the patients' cohort.**

Based on TMS scores, all patients were at the premanifest disease stage. Based on DCL scores, some of the patients ( $n = 4$ ) presented some motor abnormalities. Abbreviations: CAG = cytosine-adenine-guanine; two individuals with CAG repeats of 38 were included in the current study. Although these individuals can be considered “affected”, they may have a lower risk of becoming symptomatic within their life span; DBS = Disease Burden Score, calculated as follows:  $DBS = age \times (CAG - 35.5)$ ; TMS = Total Motor Score out of 124 from “UHDRS Motor Diagnostic Confidence (Motor) – the higher the score, the more impaired the performance. DCL = Diagnostic Confidence Level (normal/no abnormalities = 0, non-specific motor abnormalities = 1, motor abnormalities that may be signs of HD = 2, motor abnormalities that are likely signs of HD = 3, motor abnormalities that are unequivocal signs of HD = 4). Only participants with diagnostic confidence level ratings  $< 4$  were included in the current report.

<b>Mean CAG (SD, range)</b>	<b>Mean DBS (SD, range)</b>	<b>Mean TFC (SD, range)</b>	<b>Mean TMS (SD, range)</b>	<b>Mean DCL (SD, range)</b>
<b>41.5 (1.9, 38-45)</b>	235.4 (79.9, 80-450)	12.863 (0.4, 12-13)	3.3 (4.8, 0-18)	0.91 (1.3, 0-3)

**Table 9. Information about patients' medication.**

*Out of the 25 patients assessed, 11 had been on stable medication for four weeks prior to taking part in the study.*

<b>Patient</b>	<b>Medication</b>
1	Sumatriptan 10 mg, Albuterol 400 mg, Mirtazapine 15 mg
2	Zolmitriptan, Loratadine
3	Ethinyl Estradiol 30 mcg, Trimethoprim 400 mg
4	Ibuprofen 10g, Paracetamol 10g
5	Methylprednisolone with Lidocaine 40 mg/ml
6	Paracetamol 10 g, Mebeverine 405 mg, Prochlorperazine 15 mg
7	Formoterol 10 g, Albuterol 10 g, Prochlorperazine 10 g
8	Tamoxifen 20 mg, Venlafaxine 150 mg, Paracetamol and Codeine 10 g, Paracetamol 1000 mg, Bisoprolol 5 mg
9	Oxybutynin 1 mg, Desogestrel 10 g, Amitriptyline 10 mg
10	Budesonide and Formoterol 10 g, Medroxyprogesterone 10 mg
11	Citalopram 30 mg, Aspirin 75 mg, Mometasone spray, Topiramate 50 mg, Zopiclone 7.5 mg

### 3.4.2. Data acquisition

#### *Assessment of patient-control differences in cognitive ability*

The cognitive testing session was carried out prior to MRI scanning and lasted approximately 60 minutes, after which the participant was offered a break. Tasks were administered either as standard paper and pencil tests or by using the computerized version provided by the Psychology Experiment Building Language (PEBL) test battery (Mueller & Piper, 2014). The tests were presented in a fixed order. Testing was conducted in a cognitive testing room at Cardiff University Brain Research Imaging Centre (CUBRIC). Computerized tests were conducted on a laptop (MacBook Pro Retina, 13-inch), with responses recorded on the keyboard. The researcher was sat beside the participant for the duration of the test battery and was thus available to answer questions regarding the task instructions. A total of 6 cognitive outcome measures was assessed across all tests (see Table 10 for a summary of the outcome measures and cognitive domains assessed).

Firstly, participants were administered the Montreal Cognitive Assessment (MoCA) (Nasreddine et al., 2005) and the Test of Premorbid Functioning – UK Version (TOPF-UK) (Wechsler, 2011) to estimate premorbid intellectual functioning. The former is a brief 30-question test evaluating different types of cognitive abilities including orientation, short-term memory/delayed recall, executive function/visuospatial ability, language abilities, abstraction, animal naming and attention. The TOPF-UK is a revised version of the Wechsler Test of Adult Reading (WTAR) and uses a combined demographics and reading prediction equation involving both performance on an irregularly spelt words-reading task and several demographic variables to derive an estimated premorbid IQ. Subsequently, performance was assessed in the following tests:

- **N-back task:** This is a continuous recognition task during which participants are presented with a series of letters, three seconds apart, and are asked to judge whether

the current letter matched the previous letter (1-back condition) or the letter presented 2 letters back (2-back condition). In this study, the 1-back and 2-back conditions were presented separately in 20 randomly ordered trials. Participants made responses manually by pressing on the letter “A” on the keyboard with their left index finger. No responses were required for non-targets.

- **Forward digit span test adapted from the Wechsler Adult Intelligence Scale-Revised (WAIS-R) (Wechsler, 1997):** Participants were presented with a series of numbers that appeared on the screen one after another. They were required to recall the sequence of numbers by entering them on the keyboard. If the participant could successfully reproduce the series of numbers, they were then presented with a longer series of numbers. Participants continued to receive longer series of numbers until they could no longer repeat them back correctly. The starting list length was 3, and the longest list length possible was 10.
- **Visual patterns test (Della Sala et al., 1997):** Participants were shown a checkerboard-like grid, with the squares in the grid each randomly coloured. This pattern was displayed for 3 seconds and was then removed. Subjects were then shown a blank grid and were asked to reproduce each grid. The number of items was sequentially increased. Participants were given unlimited time to reproduce the shapes being viewed.
- **Eyes test (Baron-Cohen et al., 2001):** Participants were shown 36 still pictures of the eye regions within faces expressing different emotional states. Participants were instructed to look carefully at each photograph and select the word they felt best matched what the person in the picture was feeling. A glossary of these words was provided. There was no time limit.

- **Speeded finger tapping task (Reitan, 1979):** Participants were instructed to form a fist shape with their dominant hand, with their fingernails touching down in front of the keyboard space bar. They were then instructed to extend their index finger in order to contact the “space” bar on the keyboard, and to move only their index finger to tap the space bar as quickly as possible.

***Computation of a composite cognitive score for the assessment of disease-related brain-function relationships***

Patients’ data from the tasks utilised for the assessment of patient-control differences in cognition were merged with cognitive data from the ENROLL-HD database. The latter included information on performance in the following tests (Kiebertz et al., 2001; Siesling et al., 1998; “Unified Huntington’s Disease Rating Scale,” 1996):

- **Phonetic Verbal Fluency Test:** Participants have to spontaneously produce words orally within a fixed time span (60 seconds), beginning with a certain letter.
- **Categorical Verbal Fluency Test:** Same as above but words must be produced according to semantic constraints (e.g. animals, fruits, vegetables).
- **Symbol Digit Modality Test:** Using a reference key, the participant has 90 seconds to pair specific numbers with given geometric figures.
- **Stroop Colour Reading and Word Reading Test:** Participants have to name colours (e.g., red, green, blue) and read the words for colours in black ink.
- **Stroop Interference Test:** Participants have to read words of colours (e.g. red, green, blue) where the word colour is written in a different colour ink.
- **Trail Making:** In part A, participants are asked to connect 25 randomly arrayed dots in numerical order, whereas in part B they are asked to connect dots alternating between numbers and letters in alphabetical order.

The full study protocol can be found at <http://www.enroll-hd.org>. Because each of the tasks yielded several variables, the following strategy was employed to select the variables to be included in this report: (1) for standardized clinical tests, variables known to have the best sensitivity and measurement characteristic were selected, e.g. correctly generated responses instead of error scores (Metzler-Baddeley et al., 2014); (2) for tests with multiple conceptually distinct measures, variables that represented each component were included, e.g., for the n-back task, the number of correct responses from the 1-back and the 2-back condition; and (3) where necessary, variables were excluded from the assessment, e.g. when these presented lots of missing cases and/or they lacked sufficient correlation with the other measures, making them unfit to be included in the PCA. This approach led to a total of 13 cognitive outcome measures, which are summarised in Table 10.

**Table 10. Cognitive outcome variables employed to assess patient-control differences in cognition and/or create a composite cognitive score to assess disease-related brain-function relationships.**

*Outcome variables and cognitive domains assessed are summarized.*

Task	Assessment of patient-control differences/computation of composite cognitive score	Computerized/paper & pencil	Outcome variable	Cognitive domain assessed
N-back (Kirchner, 1958)	- Assessment of patient-control differences; - Computation of composite cognitive score.	Computerized.	Percentage of correct responses in the 1-back and 2-back condition.	Encoding, temporary storage and updating of stored information with new upcoming information, inhibition of irrelevant items.
Digit Span Test from the WAIS-R (Wechsler, 1997)	- Assessment of patient-control differences; - Computation of composite cognitive score.	Computerized.	Maximum span of digits recalled.	Verbal working memory capacity.
Visual Patterns Test (Della Sala et al., 1997)	- Assessment of patient-control differences; - Computation of composite cognitive score.	Paper and pencil.	Maximum grid size recalled correctly.	Spatial working memory capacity.
Eyes Test (Baron-Cohen et al., 2001)	- Assessment of patient-control differences;	Paper and pencil.	Number of emotional states correctly matched.	Social cognition and mentalising.
Speeded Finger Tapping Task (Reitan, 1979)	- Assessment of patient-control differences; - Computation of composite cognitive score.	Computerized.	Mean number of taps over 3 trials.	Motor speed.

Stroop Interference, Word Reading and Colour Naming (Kieburztz et al., 2001; Siesling et al., 1998; “Unified Huntington’s Disease Rating Scale,” 1996)	- Computation of composite cognitive score.	Paper and pencil.	Number of correct responses	Ability to inhibit cognitive interference, selective attention capacity and skills, processing speed, motor control.
Phonetic and Category Verbal Fluency (Kieburztz et al., 2001; Siesling et al., 1998; “Unified Huntington’s Disease Rating Scale,” 1996)	- Computation of composite cognitive score.	Paper and pencil.	Number of correctly generated words within 60 seconds	Working memory, cognitive inhibition, switching ability and language ability including lexical knowledge and lexical retrieval ability.
Trail Making (part A & part B) (Kieburztz et al., 2001; Siesling et al., 1998; “Unified Huntington’s Disease Rating Scale,” 1996)	- Computation of composite cognitive score.	Paper and pencil.	Time needed to complete the task	Visual attention, task switching, speed of processing, mental flexibility.
Symbol Digit Modality (Kieburztz et al., 2001; Siesling et al., 1998; “Unified Huntington’s Disease Rating Scale,” 1996)	- Computation of composite cognitive score.	Paper and pencil.	Number of correct responses achieved in 90 seconds	Attention, perceptual speed, motor speed, and visual scanning.

### ***MRI data acquisition***

MRI data were acquired on a 3 Tesla Siemens Connectom system with ultra-strong (300 mT/m) gradients (MAGNETOM Skyra CONNECTOM). Table 11 summarizes all acquisition parameters. Each MRI session lasted approximately 1 hour, and the protocol comprised the following sequences: MPRAGE T<sub>1</sub>-weighted; a multi-shell dMRI acquisition [ $\delta/\Delta$ : 7/24 ms; b-values: 0 (14 volumes, interleaved), 500 (30 directions), 1200 (30 directions), 2400 (60 directions), 4000 (60 directions), and 6000 (60 directions) s/mm<sup>2</sup>. The larger number of volumes across the higher diffusion weightings were acquired to compensate for lower SNR and to capture the higher angular resolution present at higher b-values (Tournier, et al., 2013). Diffusion MRI data were obtained using electrostatic repulsion generalised across multiple shells (Caruyer, et al., 2013). Data were acquired in an anterior-posterior phase-encoding direction, with one additional posterior-to-anterior volume]. Magnetization transfer (Henkelman et al., 2001) [turbo factor: 4; radial reordering; non-selective excitation; MT contrast was achieved by the application of a 15.36 ms radio-frequency saturation pulse during the TR period, with an equivalent flip angle of 333° applied at a frequency of 1.2 kHz below the water resonance]. Two identical sets of images with different contrasts (one acquired with and one acquired without MT saturation pulses) were obtained.

**Table 11. Scan parameters.**

All sequences were acquired at 3 Tesla with ultra-strong gradients. For each of the sequences, the main acquisition parameters are provided. *T<sub>1</sub>-w*: *T<sub>1</sub>-weighted*; *MT*: *magnetization transfer*; *MPRAGE*: *Magnetization prepared - rapid gradient echo*; *SE*: *spin-echo*; *EPI*: *echo-planar imaging*; *FoV*: *field of view*; *TE*: *echo time*; *TR*: *repetition time*.

	T <sub>1</sub> -w	DTI	CHARMED	MT
Pulse sequence	MPRAGE	SE/EPI	SE/EPI	Turbo FLASH
Matrix size	256×256	495×495	495×495	128 × 128 ×104
FoV (mm)	256	990	990	220 × 220 × 179
Slice thickness (mm)	1	2	2	1.72
TE,TR (ms)	2, 2300	59, 3000	59, 3000	2.1, 60
Off-resonance pulses (Hz/°)	-	-	-	1200/333
Flip angles (°)	9	9	9	5

### 3.4.3. Image processing

All images were skull-stripped in native space using FSL BET (Smith, 2002).

#### ***Extraction of subcortical basal ganglia and thalamic volume from T<sub>1</sub>-weighted anatomical images***

GM subcortical volumes for left and right caudate, putamen, pallidum and thalamus were extracted from the individual T<sub>1</sub>-weighted images using FreeSurfer’s “recon-all” automated procedure for volumetric measures (v5.3) (Fischl et al., 2002). Steps in this pipeline are explained in detail here: <https://surfer.nmr.mgh.harvard.edu/fswiki/recon-all>. In short, a probabilistic atlas from a manually labeled training-set is utilized to normalize each brain and assign each voxel to one of 40 labels. The classification technique in FreeSurfer employs a

registration method that is robust to anatomical variability, including the ventricular enlargement typically associated with neurological diseases and aging (Fischl et al., 2002).

### ***Diffusion data: FA, RD, AD, MD and FR maps***

Pre-processing of diffusion data was carried out in line with recommended steps for standard 3 Tesla systems, interfacing several tools, including FSL (Smith et al., 2004), MRtrix3 (Tournier et al., 2019), and ANTS (Avants et al., 2011). These steps included: denoising (Veraart et al., 2016), slice-wise outlier detection (SOLID) (Sairanen et al., 2018), and correction for drift (Vos et al., 2017); motion, eddy currents, and susceptibility-induced distortions (Andersson et al., 2003; Andersson & Sotiropoulos, 2016); Gibbs ringing artefact (Kellner et al., 2016); bias field (Tustison et al., 2010); and gradient non-linearities (Glasser et al., 2013; Rudrapatna et al., 2021).

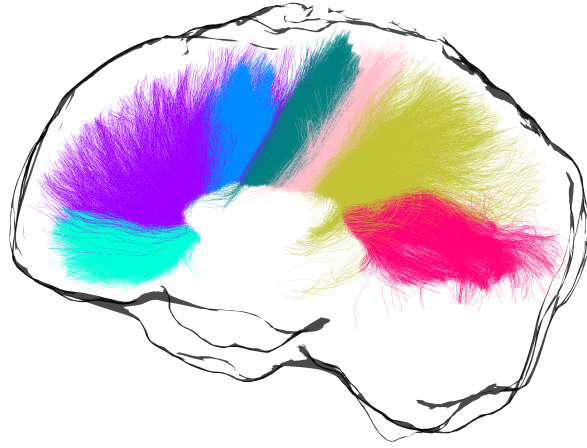
Diffusion tensors were generated using linearly weighted least squares estimation (for  $b < 1200$  s/mm<sup>2</sup> data) providing the following quantitative scalar measures: FA, AD and RD. Since HD is associated with brain tissue atrophy, DT-MRI metrics were corrected for cerebrospinal fluid-based partial volume artifacts. This was done by fitting the diffusion tensor between  $b = 500$  s/mm<sup>2</sup> and  $b = 1200$  s/mm<sup>2</sup>, instead of between  $b = 0$  s/mm<sup>2</sup> and  $b = 1200$  s/mm<sup>2</sup>. Because the signal from free-water decays very rapidly as  $b$  increases due to its higher diffusivity, this approach allowed to reduce cerebrospinal fluid based partial volume artefacts in the DTI metrics. Motion and distortion artefacts of CHARMED data were corrected according to the extrapolation method of Ben-Amitay, Jones, and Assaf (2012). FR maps (Assaf & Basser, 2005) were computed by fitting the CHARMED model to the DWI data, with an in-house software coded in MATLAB (The MathWorks, Natick, MA).

### ***Magnetization transfer: MTR maps***

Both MT-weighted and non-MT-weighted images were corrected for Gibbs ringing artefacts (Kellner et al., 2016). ANTS (Avants et al., 2011) was first used to register the MPRAGE images to the  $b = 0$  s/mm<sup>2</sup> images with nonlinear registration. Then MT-weighted and non-MT weighted images were linearly warped to the registered MPRAGE images using an affine (12 degrees of freedom) technique based on mutual information, with the FMRIB's Linear Image Registration Tool (FLIRT) (Jenkinson & Smith, 2001). All registrations were visually inspected for accuracy. Finally, MTR maps were calculated with the following equation:  $MTR = [(S^0 - S^{MT})/S^0] \times 100$ , whereby  $S^0$  represents the signal without the off-resonance pulse and  $S^{MT}$  represents the signal with the off-resonance pulse.

### ***Tractography of the CC***

Whole-brain streamline tractography was performed with FiberNavigator (Chamberland et al., 2014) using 8 seeds/voxel evenly distributed across the whole brain (approximating 1.8 M seeds), a minimum fODF amplitude of 0.1, a 1 mm step size (i.e.  $0.5 \times$  voxel size), and a 45° maximum curvature angle. Streamlines whose lengths were outside a range of 20 mm–300 mm were discarded. The automated TractSeg technique (Wasserthal et al., 2018) was then applied to segment the CC. This technique provides a balance between manual dissection and atlas-based tracking approaches. Specifically, seven portions of the CC were delineated [1=rostrum, 2=genu, 3=rostral body, 4=anterior midbody, 5=posterior midbody; 6=isthmus, 7=splenium] (Figure 12).



	Segment	Anatomical label	Cortical region
	1	Rostrum	Caudal/orbital prefrontal, inferior premotor
	2	Genu	Prefrontal
	3	Rostral body	Premotor, supplementary motor
	4	Anterior midbody	Motor
	5	Posterior midbody	Somaesthetic, posterior parietal
	6	Isthmus	Superior temporal, posterior parietal
	7	Splenium	Occipital, inferior temporal

**Figure 12. Segmentation of the CC.**

*For each segment, the corresponding anatomical label is reported, together with the cortical area it connects to.*

### 3.4.4. Statistical analysis

Statistical analyses were carried out using RStudio v1.1.456 (Team, 2015), MATLAB (The MathWorks, Natick, MA), SPSS version 20119 (Armonk, 2011), the PROCESS computational tool for mediation analysis (Hayes, 2017), FSL (Smith et al., 2004), and the Statistical Non-Parametric Mapping (SnPM) software (Nichols & Holmes, 2014).

### ***Assessment of patient-control differences in cognitive ability***

One-way analyses of covariance (ANCOVA) could not be carried out to examine differences in cognitive functioning between HD and control participants, because of violation of the assumptions of homoscedasticity and of homogeneity of error variance, as assessed by visual inspection of the studentized residuals plotted against the predicted values for each group, and the Levene's test, respectively.

Therefore, Mann-Whitney-Wilcoxon tests were instead first carried out to examine group differences in each of the tests. Multiple comparison correction was carried out using the Bonferroni method with a family-wise alpha level of 5% (two-tailed).

Whenever a significant group difference was detected, the relationship between group and the dependent variable was further investigated with multiple regression analysis to explore interaction effects between group and age. Correlations between TOPF-UK FSIQ and the dependent variable were explored, and if significant this variable was included as covariate in the analysis. Regression diagnostics were carried out, and QQ plots and outlier profiles were examined to detect any values above or below the upper/lower boundary of 95% confidence intervals of the slope of the regression line.

Finally, Spearman's rho correlation coefficients were calculated for the patients' sample between performance on the cognitive tests showing significant group differences and proximity to disease onset, as measured by disease burden score (DBS).

### ***Computation of a composite cognitive score for the analysis of brain-function relationships in premanifest HD***

PCA of several cognitive outcome variables was performed by only including slopes from premanifest HD subjects, to best capture heterogeneity within this population. Only the first principal component (PC) was extracted, to increase experimental power and reduce the number of multiple comparisons (Steventon, 2014).

First, the Bartlett's test of sphericity and the Kaiser-Meyer-Olkin (KMO) test were used to confirm that the data were suited for PCA. Patients' scores on the Eyes test (Baron-Cohen et al., 2001) lacked sufficient correlation with the other measures, as shown by the diagonal of the anti-image correlation matrix (KMO = 0.2). Therefore, this test was excluded from the PCA. The KMO test of sampling adequacy was 0.54 and the Bartlett's test of sphericity was significant,  $\chi^2(78) = 156.5$ ,  $p < 0.001$ . The PCA was run using centred, standardized (standard deviation = 1) versions of the patients' cognitive outcome scores. A PCA procedure with orthogonal Varimax rotation was used to maximize the factor loadings. Regression values from each component were used as composite cognitive scores for each participant. Outliers that were  $\pm 3$  standard deviations from the mean were removed. The relationship of individual scores and DBS was investigated with Spearman's correlations.

### ***Tractometry of the CC***

Microstructure differences were assessed in each of the seven callosal segments. First, by taking each quantitative metric map (each registered to the  $b = 0$  s/mm<sup>2</sup> during pre-processing), samples of each metric were obtained at each vertex of the reconstructed segments - and segment-specific medians were derived for FA, AD, RD, FR and MTR in MRtrix3 (Tournier, et al., 2019). Next, the overall mean was calculated, so that each dataset comprised  $m = 5$  MRI-derived measures, mapped along  $s = 7$  callosal segments.

### ***Reduction of MRI data dimensionality with PCA***

PCA was employed to reduce the complexity of both the subcortical volumetric data and the callosal microstructure data. For both volumetric and microstructure data, centred, standardized (standard deviation = 1) versions of MRI measures on both groups combined were used for PCA (Phillips et al., 2013). For the volumetric data, the PCA was calculated for left and right caudate, pallidum, putamen, thalamus. The KMO test of sampling adequacy was 0.75

and the Bartlett's test of sphericity was significant,  $\chi^2(28) = 409.953$ ,  $p < 0.001$ . For the WM microstructure data, the PCA was calculated for FA, FR, RD, AD and MTR. The KMO measure was 0.65, and the Bartlett's test of sphericity was significant,  $\chi^2(6) = 1077.231$ ,  $p < 0.001$ . PCA was applied to the concatenated set of segments across subjects (Table 12), in agreement with the *tidy* data standard (Wickham, 2014).

For both PCAs, the minimal number of principal components that accounted for the most variability was extracted based on: 1) their interpretability (Metzler-Baddeley et al., 2017); and 2) the Kaiser criterion of including all components with an eigenvalue greater than 1. Regression values from each component for each participant were used in the following analyses.

**Table 12. Data structure input for PCA of callosal tractometry data.**

*Individual subjects ( $n = 49$ ) and segments ( $s = 7$ ) are concatenated to form observations, while variables represent the measures ( $m = 5$ ) derived from diffusion and MT imaging.*

<b>Subject</b>	<b>Segment</b>	<b>FA</b>	<b>FR</b>	<b>RD</b>	<b>AD</b>	<b>MTR</b>
<b>S<sub>1</sub></b>	Segment <sub>1</sub>	FA <sub>11</sub>	FR <sub>11</sub>	RD <sub>11</sub>	AD <sub>11</sub>	MTR <sub>11</sub>
<b>S<sub>2</sub></b>	Segment <sub>2</sub>	FA <sub>21</sub>	FR <sub>21</sub>	RD <sub>21</sub>	AD <sub>21</sub>	MTR <sub>21</sub>
...	...	...	...	...	...	...
<b>S<sub>1</sub></b>	Segment <sub>2</sub>	FA <sub>12</sub>	FR <sub>12</sub>	RD <sub>12</sub>	AD <sub>12</sub>	MTR <sub>12</sub>
...	...	...	...	...	...	...
<b>S<sub>n</sub></b>	Segment <sub>s</sub>	FA <sub>ns</sub>	FR <sub>ns</sub>	RD <sub>ns</sub>	AD <sub>ns</sub>	MTR <sub>ns</sub>

### ***Investigation of patient-control differences in subcortical GM volume and callosal microstructure***

To assess group differences in subcortical GM volume, as well as callosal microstructure, ANCOVAs were run on the extracted regression values from each component for each participant. Across all analyses, outliers were first identified by examining box-and-whisker plots for each dependent variable, for controls and HD patients separately. Outliers that were  $\pm 3$  standard deviations from the mean were removed. For the investigation of subcortical GM volumes, two ANCOVAs were run on the regression values from each component for each participant, with group as the independent variable. On the other hand, group and segment were used as independent variables in the assessment of microstructure differences, because of a particular interest in understanding the interaction between group effects and different callosal segments.

The correlation of subcortical volume and microstructure outcome measures across patients and controls, with age, ICV and TOPF-UK FSIQ was tested to decide if these variables should be included as covariates in the analysis. Pearson's correlation coefficients greater than 0.3 were treated as indicative of a moderate relationship.

For every ANCOVA, the assumptions of the analysis were first tested. Any covariates were included only when linearly related to the outcome variable, for each group. To test whether the data were normally distributed, the Shapiro-Wilk test was used at  $\alpha = 0.001$ . Homogeneity of regression slopes was tested for all covariates. If violation of homogeneity of regression slopes was detected for a covariate, an interaction term was included in the model. Levene's test was used to assess homogeneity of error variance. Homoscedasticity within each combination of groups was assessed by visual inspection of the studentized residuals plotted against the predicted values for each group.

### ***Assessment of disease-related brain-function relationships***

Spearman correlations were run in the patients' group for:

- i. GM components showing a significant group effect and cognitive composite scores;
- ii. GM components showing a significant group effect and DBS;
- iii. GM components showing a significant group effect and CAG repeat length;
- iv. WM components showing a significant group effect and composite cognitive scores;
- v. WM components showing a significant group effect and CAG repeat length;
- vi. WM components showing a significant group effect and DBS
- vii. WM and GM components showing a significant group effect.

Within each group of correlations, multiple comparison correction was carried out with the Bonferroni correction with a family-wise alpha level of 5% (two-tailed). Whenever a significant association was detected, this was further explored with partial correlations, partialling out ICV and DBS. The latter was done to assess associations independently of disease progression.

### ***Assessment of brain-wise group differences in WM microstructure using the hypervoxel framework***

The hypervoxel framework (Luque Laguna, 2019) was applied to assess group differences in FA, RD, AD, FR and MTR. First, all images were normalised to a common anatomical space by applying the non-linear registration approach of the `tbss_2_reg` script (Smith et al. 2006), part of FSL (Smith et al. 2004), and by employing the `FMRIB58_FA` template ( $1 \times 1 \times 1$  mm isotropic) as reference target. Then, statistics maps were produced based on the voxel-level analysis of the data; this was done by using a non-parametric approach based on a permutation test strategy (Winkler et al., 2014). The statistic maps were thresholded by a value of  $p = 0.01$ .

The significant voxel level statistic results were projected on the hypervoxel template, which was based on whole-brain tractography data from a different group of 20 healthy subjects. Finally, significant clusters of hypervoxels were identified, with two hypervoxels belonging to the same cluster if they were adjacent and if they shared a common streamline. Explanatory variables (EVs) in the randomization tests included age and gender and the effect of group was explored whilst regressing the other EVs. A family-wise error (FWE) corrected (Nichols & Holmes, 2014)  $p < 0.05$  with a cluster-extent-based threshold of 20 or more voxels was considered statistically significant.

Whenever significant clusters were detected for a specific metric, these were extracted, summed and binarized to form an ROI mask. The mask was then projected onto each patient's map in MNI space. The mean value for that metric was calculated for each patient in the ROI with FSL (Smith et al., 2004), and used in the assessment of brain-function relationships. Specifically, Spearman correlations were first run between the WM metrics showing significant clusters. Subsequently, the relationship of each cluster with composite cognitive scores, GM components showing a significant group effect, DBS and CAG was investigated. Within each group of correlations, multiple comparison correction was carried out with the Bonferroni correction with a family-wise alpha level of 5% (two-tailed).

## **3.5. Results**

### **3.5.1. Premanifest HD patients present impairments in the encoding, temporary storage and updating of information**

Patients performed significantly worse (mean = 84.85, standard deviation = 8.75) compared to controls (mean = 93.07, standard deviation = 7.55) in the 2-back task ( $U = 392$ ,  $p = 0.001$ , Bonferroni-corrected  $p = 0.007$ ). No significant difference in performance was

detected between patients and controls in the other tests [1-back:  $U = 180.5$ ,  $p = 0.776$ , Bonferroni-corrected  $p = 1$ ; finger tapping:  $U = 288$ ,  $p = 0.605$ , Bonferroni-corrected  $p = 1$ ; digit span:  $U = 246$ ,  $p = 0.692$ , Bonferroni-corrected  $p = 1$ ; visual patterns test:  $U = 303$ ,  $p = 0.244$ , Bonferroni-corrected  $p = 1$ ; eyes test:  $U = 224.5$ ,  $p = 0.392$ , Bonferroni-corrected  $p = 1$ ) (Figure 13).

Multiple regression was employed to explore interaction effects between age and group on performance in the 2-back task. TOPF-UK FSIQ was related to performance ( $r = 0.292$ ,  $p = 0.051$ ), therefore this variable was included as covariate in the analysis. No significant main effect of group ( $\beta = 11.917$ ,  $p = 0.185$ ), TOPF-UK FSIQ ( $\beta = 0.1178$ ,  $p = 0.397$ ) or age ( $\beta = 0.4867$ ,  $p = 0.131$ ) were detected. However, a significant interaction effect was present between group and age [ $\beta = -0.4578$ ,  $p = 0.021$ ,  $R^2 = 0.39$ ,  $F(4, 40) = 6.57$ ,  $p < 0.001$ ], indicating that, while younger HD patients' performance tends to overlap with that of age-matched healthy controls, the gap in performance between the two groups is significantly greater in older subjects, with HD patients performing worse. Importantly, older HD patients tended to be closer to disease onset, as shown by greater DBS. Thus the difference at older ages likely reflects disease-related influences on this measure (Figure 14, left). Accordingly, there was a trend for a negative relationship between patients' performance on the 2-back task and DBS ( $r = -0.40$ ,  $p = 0.055$ ) (Figure 14, right).

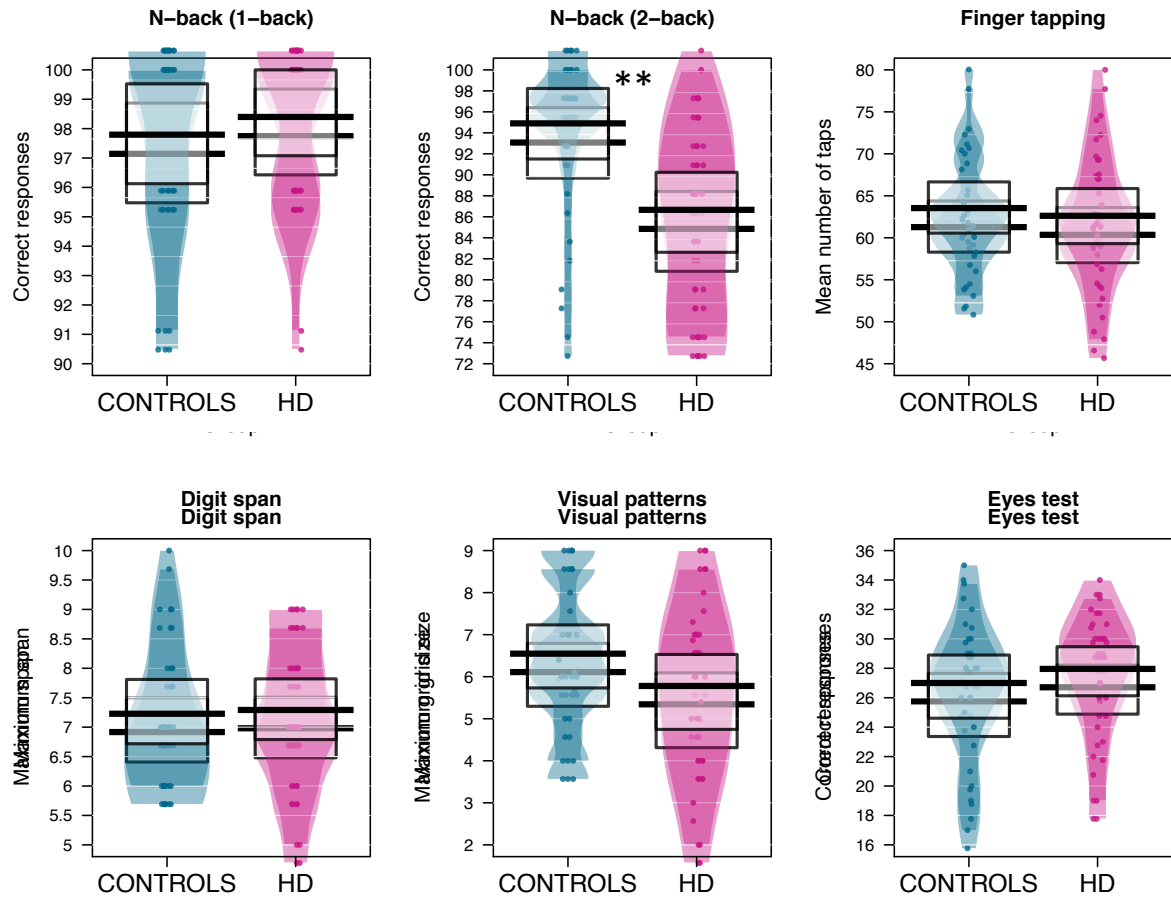


**Figure 13. Group differences in cognition.**

*Patients showed significantly reduced scores in the 2-back task,  $p = 0.007$ , Bonferroni-corrected. No significant differences were detected in performance in the other tests. The final sample, after outlier removal, was  $n = 24$  HD patients and  $n = 23$  controls.*

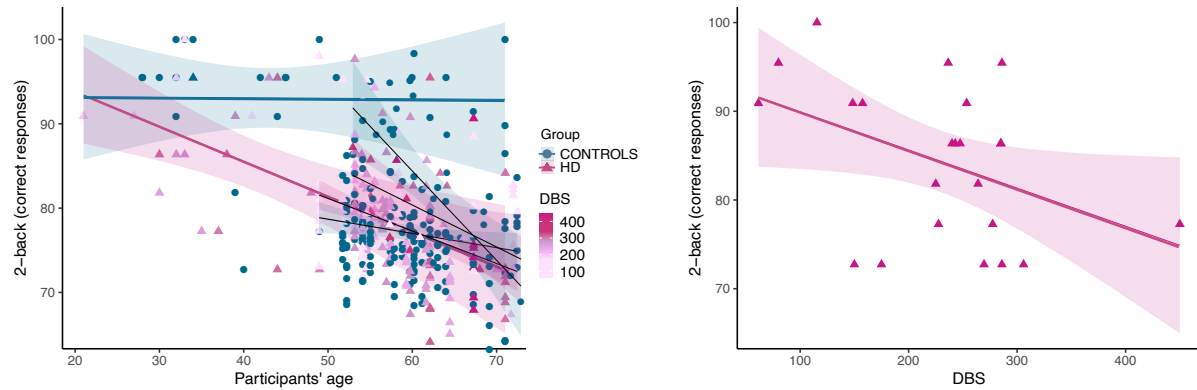


**Figure 14. Relationship of 2-back task performance with age and DBS.**

*Left: Relationship between performance on the 2-back task and age, in patients & controls. Right: Relationship between performance on the 2-back task and disease burden score (DBS) in patients. A significant interaction effect between group and age was detected, suggesting that the group difference is larger in older participants. HD data points are colored by DBS. Older HD patients tend to be closer to disease onset, likely confounding the effect of age on this measure. Right: Relationship between performance on the 2-back task and DBS. A trend for a negative association was detected ( $p = 0.055$ ), suggesting that increased proximity to disease onset is associated with worse performance on this task.*

### 3.5.2. Computation of a composite cognitive score in the HD sample

As shown in Figure 15, the first PC was extracted; this accounted for 38.7% of the total variance. Component loadings of  $\geq 0.5$  were considered as significant. Thus this component reflected general executive functioning with loadings on distractor suppression (Stroop task), attention switching (trail making), updating (n-back), category fluency and motor speed. No significant correlations were detected between patients' scores on this component, and DBS ( $r = -0.137, p = 0.599$ ).

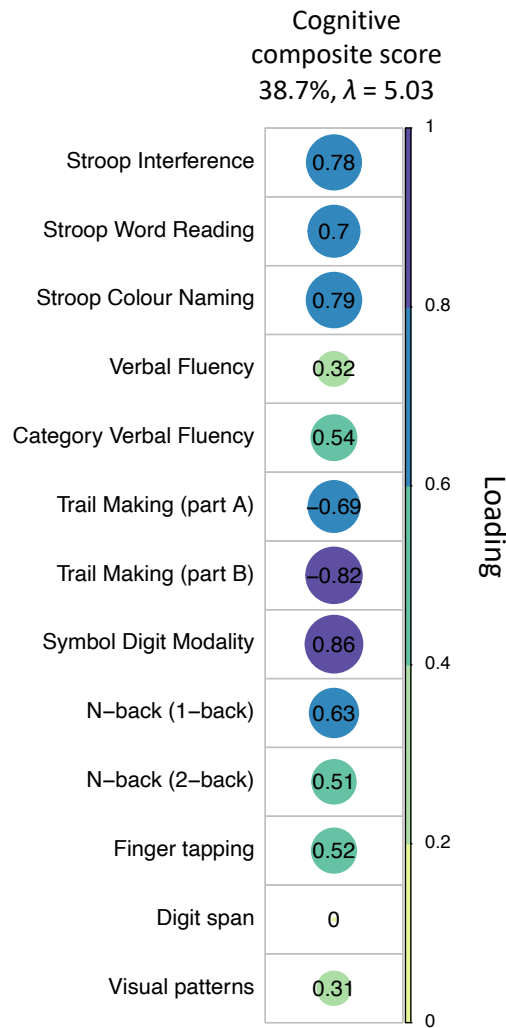


**Figure 15. Principal component analysis (PCA) of the cognitive data with varimax rotation.**

*Plot summarizing how each variable is accounted for in the extracted principal component (PC). The absolute correlation coefficient is plotted. Color intensity and the size of the circles are proportional to the loading. This PC accounted for 38.7% of the total variance and included measures from all test domains, except for the digit span. Four patients were excluded from the PCA because of missing data. The final sample size for the PCA was  $n=21$  patients.*

### 3.5.3. Premanifest HD patients present reduced striatal volume

With PCA, two principal components were extracted, together explaining over 79% of the variability in the subcortical GM volumetric data (PC1, 52.313%,  $\lambda = 4.185$ ; PC2, 27.423%,  $\lambda = 2.194$ ). As shown in Figure 16, the first PC loaded positively on left and right caudate, pallidum and putamen, and was therefore summarized as “striatal” component. On the other

hand, the second component loaded mostly on left and right thalamus, and was therefore summarized as “thalamic” component.

Age, ICV, and TOPF-UK FSIQ, were related to scores on the striatal component (age:  $r = -0.342$ ,  $p = 0.015$ , ICV:  $r = 0.316$ ,  $p = 0.025$ , TOPF-UK FSIQ:  $r = 0.337$ ,  $p = 0.022$ ), therefore these variables were included as covariates in the analysis. On the other hand, age and ICV, but not TOPF-UK FSIQ, were related to scores on the thalamic component (age:  $r = -0.432$ ,  $p = 0.002$ ; ICV:  $r = 0.516$ ,  $p < 0.001$ ; TOPF-UK FSIQ:  $r = 0.096$ ,  $p = 0.528$ ), therefore only age and ICV were controlled for in the analysis of group differences in the thalamic component.

Significant main effects of group [ $F(1, 41) = 6.639$ ,  $p = 0.014$ ] and age [ $F(1, 41) = 4.009$ ,  $p = 0.027$ ] were detected for the striatal component (Figure 16). There was no significant main effect of group on the thalamic component [ $F(1, 46) = 0.254$ ,  $p = 0.617$ ]; however significant main effects of age [ $F(1, 46) = 5.006$ ,  $p = 0.030$ ] and ICV [ $F(1, 46) = 10.661$ ,  $p = 0.002$ ] were detected.

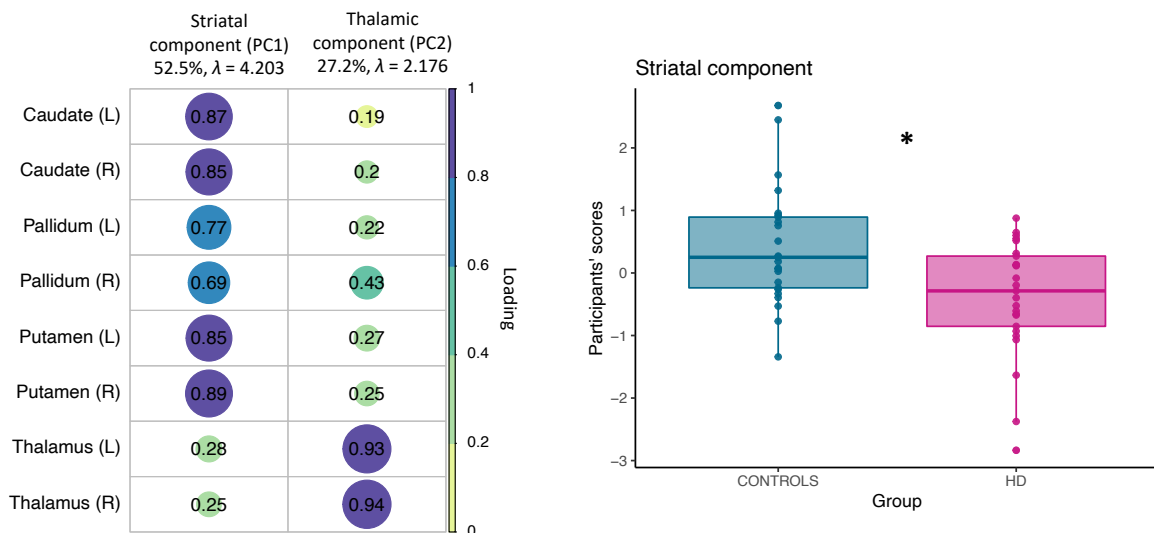


**Figure 16. Assessment of subcortical grey matter atrophy.**

Left: Principal component analysis (PCA) of subcortical gray matter volumes with varimax rotation. Plot summarizing how each variable is accounted for in the principal components (PCs). The absolute correlation coefficient is plotted. Color intensity and the size of the circles are proportional to the loading. Two principal components were extracted, together explaining over 79% of the variability in the data. Right: Group difference in scores on the striatal component. HD patients presented significantly lower scores compared to controls ( $p = 0.014$ ).

### 3.5.4. Premanifest HD patients present alterations in callosal apparent myelin

Results from the PCA of the microstructure data showed that over 80% of the variability in the data was accounted for by the first two principal components (PC1, 58.1%,  $\lambda = 2.90$ ; PC2, 22.6%,  $\lambda = 1.13$ ). As shown in Figure 17, the first PC loaded positively on FA, FR, and AD, and negatively on RD, measuring restriction or hindrance perpendicular to the main axis of the bundle. This PC was therefore summarized as “axon density” component. On the other hand, the second component loaded mostly on MTR, and was therefore summarized as “apparent myelin” component.

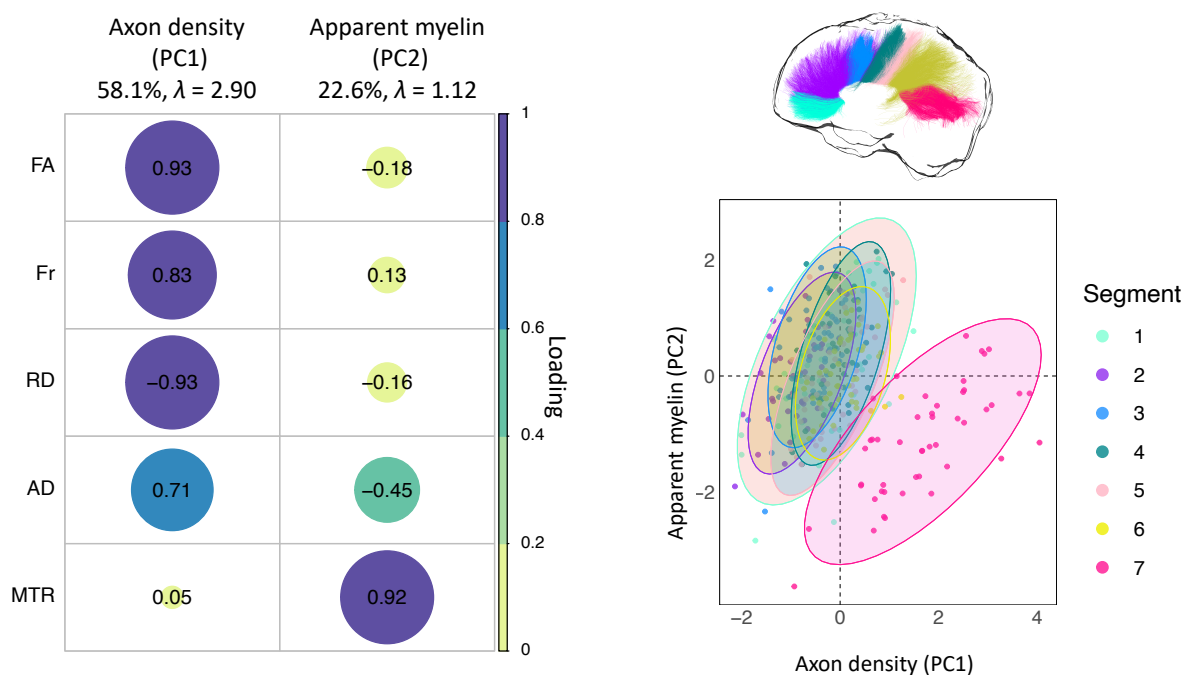


**Figure 17. Principal component analysis (PCA) of the microstructure metrics with varimax rotation.**

Left: Plot summarizing how each variable is accounted for in every principal component. The absolute correlation coefficient is plotted. Color intensity and the size of the circles are proportional to the loading. The final sample size for the PCA was  $n=25$  for the HD group and  $n=24$  for the control group. Right: Segment clustering based on PC1 and PC2. The horizontal axis shows increasing restriction or hindrance perpendicular to the main axis of the bundles. The vertical axis represents an increase in apparent myelin. Each point represents one subject. Concentration ellipsoids cover 95% confidence around the mean. Segment 7 appears to encompass most of the data variability.

### ***Assessment of group differences in the axon density component***

TOPF-UK FSIQ and ICV were not related to axon density scores (TOPF-UK FSIQ:  $r = 0.01$ ,  $p = 0.860$ , ICV:  $r = 0.077$ ,  $p = 0.164$ ), therefore these variables were not included as covariates in the analysis. On the other hand, age was negatively associated with axon density scores (age:  $r = -0.301$ ,  $p < 0.001$ ), and was therefore included as covariate. The final model assessed the effect of group and segment on axon density scores, including age as covariate.

The effect of group was not significant [ $F(1, 312) = 1.677$ ,  $p = 0.196$ ], however a main effect of segment was detected [ $F(6, 312) = 84.671$ ,  $p < 0.001$ ] (Figure 18), together with a main effect of age [ $F(1, 312) = 34.116$ ,  $p < 0.001$ ] (Figure 18). The interaction between group and segment was not significant [ $F(6, 312) = 0.531$ ,  $p = 0.784$ ]. Overall, age was negatively associated with lower scores on this component; additionally, microstructure in the more posterior segments of the CC was associated with higher axon density scores, compared to anterior ones [adjusted means: CC1 = -0.270; CC2 = -0.822; CC3 = -0.546; CC4 = -0.001; CC5 = -0.144; CC6 = 0.083; CC7 = 1.753].

### ***Assessment of group differences in the apparent myelin component***

Age and ICV, but not TOPF-UK FSIQ, were correlated with scores on the apparent myelin component (age:  $r = -0.301$ ,  $p < 0.001$ ; ICV:  $r = -0.332$ ,  $p < 0.001$ ; TOPF-UK FSIQ:  $r = 0.096$ ,  $p = 0.098$ ). The final model assessed the main effects of group and segment, with age as covariate, and age-by-group and a group-by-segment interaction.

There was not a significant main effect of group [ $F(1, 312) = 2.353$ ,  $p = 0.126$ ] and ICV [ $F(1, 312) = 1.875$ ,  $p = 0.172$ ]. However, significant main effects of age [ $F(1,312) = 45.07$ ,  $p < 0.001$ ] and segment [ $F(1, 312) = 19.899$ ,  $p < 0.001$ ] were detected. Overall, scores on this component were lower in segment 7 of the CC and in older participants (Figure 18).

Crucially, a significant interaction was detected between segment and group [ $F(6, 312) = 2.238, p = 0.040$ ], indicating that the effect of group was different for different callosal segments. Therefore, slopes of the effect of group on apparent myelin scores for each segment, while controlling for the effect of age, were investigated with a simple moderation analysis using the PROCESS toolbox for SPSS (Hayes, 2017), to better understand this interaction. This analysis revealed that HD patients presented significantly higher scores on apparent myelin compared to controls in segment 1 ( $p = 0.016$ ), and significantly lower scores in segment 7 ( $p = 0.0343$ ). Overall, scores on the apparent myelin component for the HD group were higher than controls in the more anterior portions of the CC but lower than controls in the posterior portions (segment 1:  $\beta = 0.56, t = 2.41, p = 0.016$ ; segment 2:  $\beta = 0.25, t = 1.08, p = 0.27$ ; segment 3:  $\beta = 0.014, t = 0.06, p = 0.95$ ; segment 4:  $\beta = 0.2098, t = 0.90, p = 0.36$ ; segment 5:  $\beta = 0.44, t = 1.89, p = 0.058$ ; segment 6:  $\beta = -0.028, t = -0.12, p = 0.899$ ; segment 7:  $\beta = -0.5, t = -2.12, p = 0.034$ ) (Figure 19).

As a post-hoc, exploratory analysis, the impact of partial volume artifacts on apparent myelin differences between patients and controls was assessed. HD is associated with tissue atrophy, even very early in disease progression (Aylward et al. 2011; Paulsen et al. 2008). The apparent myelin component loaded mostly on MTR, which measures the magnitude of exchange of magnetization between free water and bound water, after selectively saturating the bound water pool. It is therefore plausible that controlling for partial volume artifacts due to tissue atrophy might provide a more specific insight into myelin-related changes. Therefore, the fractional volume of free water in each voxel was estimated from the DWI data by following the procedure described in section 3.3.3 to produce a free-water signal fraction (FWF) map. The overall mean FWF was then calculated, as described above for the other metrics assessed. Finally, an ANCOVA was run to assess group differences in apparent myelin across the different segments, controlling for FWF. Specifically, the main effects of group and

segment and their interaction effect were assessed, with age, ICV and FWF as covariates. Age-by-group and group-by-FWF interactions were included in the model because of violation of the homogeneity of regression slopes assumption.

Consistent with the main analysis, a significant main effect of age [ $F(1, 300) = 56.08$ ,  $p < 0.001$ ] and segment [ $F(1, 300) = 22.89$ ,  $p < 0.001$ ] and a significant interaction effect between segment and group [ $F(1,300) = 3.2$ ,  $p = 0.005$ ] were detected. The interaction effect between group and age [ $F(1, 300) = 8.736$ ,  $p = 0.003$ ] was now significant, indicating that while scores on this component are lower than age-matched controls in older HD patients, the opposite is true for younger HD patients. Finally, a significant main effect of group [ $F(1, 300) = 13.042$ ,  $p < 0.001$ ], and FWF [ $F(1, 300) = 13.32$ ,  $p < 0.001$ ], and a significant interaction effect between group and FWF [ $F(1, 300) = 19.262$ ,  $p < 0.001$ ], were detected.

A final post-hoc, exploratory analysis consisted in assessing group-differences in the volume of segments 1 and 7 of the CC, for which significant microstructure differences between groups were detected. To do this, volume measurements were obtained by calculating the total number of voxels containing streamlines from the given segment (Barrett et al., 2020). These were then normalised by ICV. Group-differences in normalised volume for each segment were assessed with ANCOVAs, with age as covariate. There was not a significant effect of group [ $F(1, 44) = 0.517$ ,  $p = 0.517$ ] or age [ $F(1, 44) = 2.461$ ,  $p = 0.124$ ] on the volume of segment 1 of the CC. Likewise, no significant effect of group [ $F(1, 44) = 0.449$ ,  $p = 0.506$ ] nor age [ $F(1, 44) = 0.297$ ,  $p = 0.589$ ] on segment 7 volume was detected.

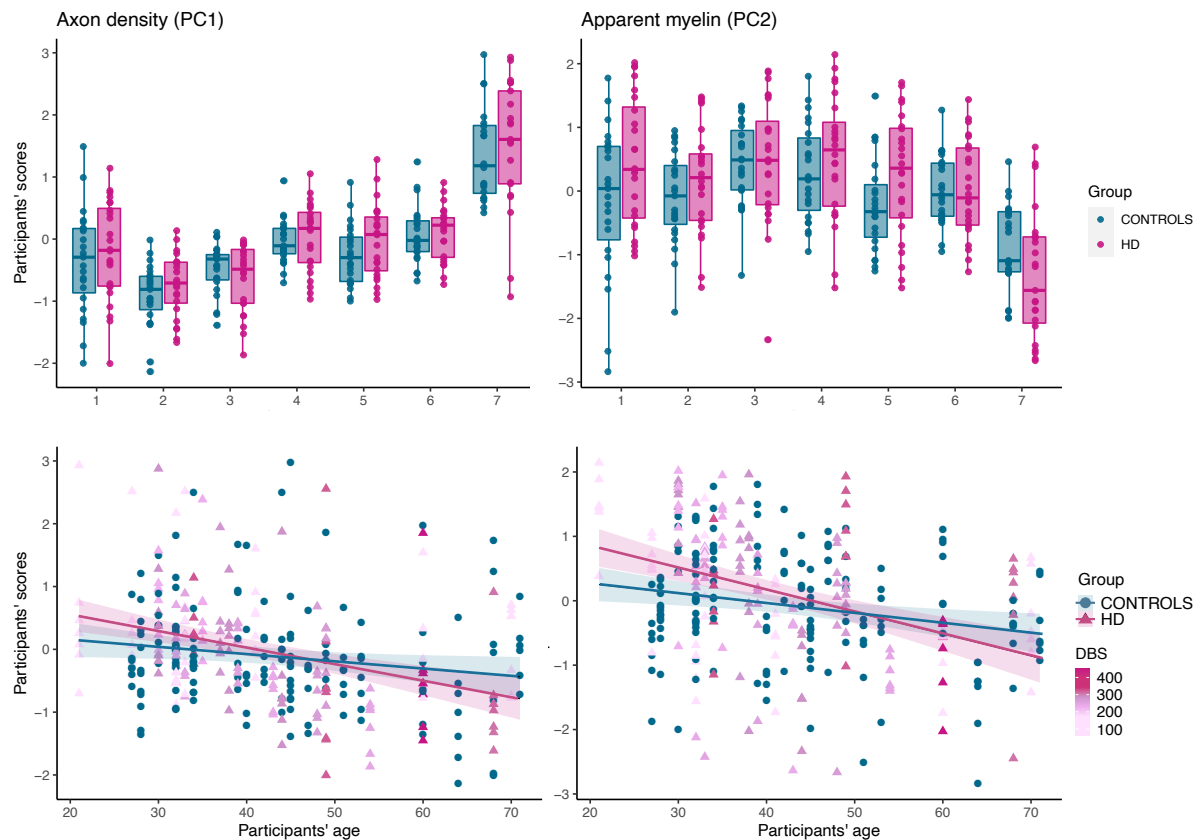


**Figure 18. Callosal microstructure: patient-control differences across callosal segments, and relationship between age and inter-individual variability in callosal microstructure.**

Top: Participants' scores on the axon-density (left) and apparent myelin (right) component, split by group and segment. The most posterior segment of the corpus callosum (CC) was associated with higher scores on the axon density component, and lower scores on the apparent myelin component, compared to anterior ones. Group did not have a significant effect on scores on axon density, however a group-by-segment interaction effect ( $p = 0.04$ ) was observed for the apparent myelin component. Bottom: Age-related variation in scores on the axon density (left) and apparent myelin (right) components, split by group. Overall, greater age was associated with lower scores on both components. When the free water fraction (FWF) was included in the model as a covariate, the interaction effect between group and age was significant, indicating that while scores on this component were significantly lower than age-matched controls in older HD patients, the opposite was true for younger HD patients.

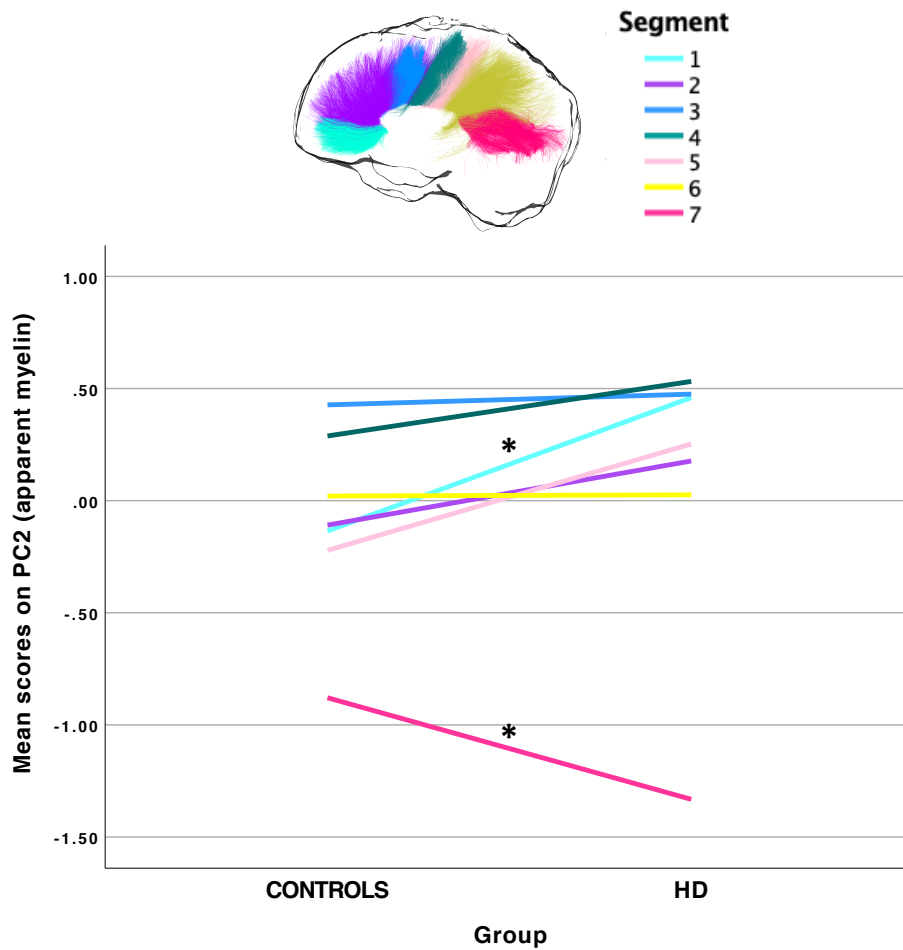


**Figure 19. Conditional effects of group on apparent myelin for each callosal segment.**

*Investigation of simple slopes of the effect of group on apparent myelin scores for each callosal segment, controlling for age, revealed that HD patients presented significantly higher scores compared to controls in segment 1 ( $p = 0.016$ ), and significantly lower scores on apparent myelin in segment 7 ( $p = 0.0343$ ). Overall, scores on the apparent myelin component for the HD group were higher than controls in the more anterior portions of the callosum but lower than controls in the posterior portions.*

### **3.5.5. Striatal atrophy in premanifest HD relates to cognitive performance and disease burden; apparent callosal myelin is associated with CAG repeat length, cognitive performance and striatal atrophy, but not with disease burden**

#### ***Relationship of striatal atrophy with composite cognitive scores, CAG repeat length and disease burden***

There was a significant, positive relationship, between scores on the striatal component and scores on the composite cognitive component ( $r = 0.535$ ,  $p = 0.035$ ), indicating that worse cognitive performance is associated with greater striatal atrophy. However, the relationship was no longer significant after partialling out ICV and DBS ( $r = 0.454$ ,  $p = 0.089$ ), suggesting that disease burden is an important driver in this relationship.

Striatal atrophy was not significantly associated with CAG repeat length ( $r = 0.234$ ,  $p = 0.320$ ). On the other hand, there was a significant negative relationship between scores on the striatal component and DBS, indicating that increased proximity to disease onset is associated with greater striatal atrophy ( $r = -0.41$ ,  $p = 0.046$ ). This suggests that the observed loss in striatal volume might be driven by patients closer to disease onset. The relationship remained significant after partialling out ICV ( $r = -0.442$ ,  $p = 0.035$ ).

#### ***Relationship of apparent callosal myelin with composite cognitive scores, CAG repeat length, disease burden and striatal atrophy***

Spearman rho correlation coefficients and associated p-values for the correlations between apparent callosal myelin with composite cognitive scores, CAG repeat length, disease burden score and striatal atrophy are reported in Table 13. Trends for positive associations were detected between composite cognitive scores and apparent myelin in all segments, except for segment 7; however these associations were no longer significant after multiple comparison correction. Apparent myelin was positively correlated with CAG repeat length in segments 1, 2, 3, 4, 5 and 6. After Bonferroni correction the relationship remained significant in segments 1, 2 and 4. Partial correlations were carried out to further explore the relationships between

apparent myelin and CAG repeat length independently of ICV and disease burden. Even stronger positive associations were now detected; interestingly, the association was now significant also in segment 7, before correction (Figure 20). No significant associations were detected between apparent myelin scores in each of the 7 callosal segments and DBS. Trends for positive associations were detected between apparent myelin in segments 1, 4 and 5, and scores on the striatal component. This suggests that lower scores on apparent myelin may be associated with greater striatal atrophy.

**Table 13. Correlations between apparent myelin scores, cognitive component scores, cytosine, adenine, and guanine (CAG) repeat-length, disease burden score (DBS) and striatal component scores.**

Correlation coefficients that were significant after Bonferroni correction are highlighted in bold. Trends, defined as correlations significant at the uncorrected level, are highlighted in italics.

Apparent myelin scores	Composite cognitive scores
Segment 1	$r = 0.527$ ( $p = 0.032$ , corrected $p = 0.211$ )
Segment 2	$r = 0.559$ ( $p = 0.023$ , corrected $p = 0.141$ )
Segment 3	$r = 0.491$ ( $p = 0.042$ , corrected $p = 0.282$ )
Segment 4	$r = 0.494$ ( $p = 0.054$ , corrected $p = 0.351$ )
Segment 5	$r = 0.451$ ( $p = 0.073$ , <b>corrected <math>p = 0.049</math></b> )
Segment 6	$r = 0.323$ ( $p = 0.03$ , corrected $p = 0.213$ )
Segment 7	$r = -0.098$ ( $p = 0.71$ , corrected $p = 1$ )
	CAG repeat length
Segment 1	$r = 0.641$ ( $p = 0.002$ , <b>corrected <math>p = 0.014</math></b> ), partial correlation: $r = 0.763$ ( $p = 0.001$ , <b>corrected <math>p = 0.007</math></b> )
Segment 2	$r = 0.717$ ( $p = 0.001$ , <b>corrected <math>p = 0.007</math></b> ), partial correlation: $r = 0.879$ ( $p < 0.001$ , <b>corrected <math>p &lt; 0.001</math></b> )
Segment 3	$r = 0.549$ ( $p = 0.012$ , corrected $p = 0.084$ ), partial correlation: $r = 0.841$ ( $p < 0.001$ , <b>corrected <math>p &lt; 0.001</math></b> )
Segment 4	$r = 0.71$ ( $p = 0.001$ , <b>corrected <math>p = 0.007</math></b> ), partial correlation: $r = 0.831$ ( $p < 0.001$ , <b>corrected <math>p &lt; 0.001</math></b> )
Segment 5	$r = 0.525$ ( $p = 0.018$ , corrected $p = 0.126$ ), partial correlation: $r = 0.745$ ( $p = 0.001$ , <b>corrected <math>p = 0.007</math></b> )

Segment 6	$r = 0.513$ ( $p = 0.021$ , corrected $p = 0.147$ ), partial correlation: $r = 0.864$ ( $p < 0.001$ , <b>corrected <math>p &lt; 0.001</math></b> )
Segment 7	$r = 0.107$ ( $p = 0.663$ , corrected $p = 1$ ), partial correlation: $r = 0.5$ ( $p = 0.048$ , corrected $p = 0.336$ )
<b>DBS</b>	
Segment 1	$r = -0.04$ ( $p = 0.853$ , corrected $p = 1$ )
Segment 2	$r = 0.08$ ( $p = 0.697$ , corrected $p = 1$ )
Segment 3	$r = 0.003$ ( $p = 0.986$ , corrected $p = 1$ )
Segment 4	$r = 0.071$ ( $p = 0.739$ , corrected $p = 1$ )
Segment 5	$r = 0.048$ ( $p = 0.824$ , corrected $p = 1$ )
Segment 6	$r = -0.12$ ( $p = 0.642$ , corrected $p = 1$ )
Segment 7	$r = -0.09$ ( $p = 0.662$ , corrected $p = 1$ )
<b>Striatal component scores</b>	
Segment 1	$r = 0.46$ ( $p = 0.024$ , corrected $p = 0.168$ )
Segment 2	$r = 0.375$ ( $p = 0.072$ , corrected $p = 0.504$ )
Segment 3	$r = 0.383$ ( $p = 0.065$ , corrected $p = 0.451$ )
Segment 4	$r = 0.441$ ( $p = 0.032$ , corrected $p = 0.231$ )
Segment 5	$r = 0.367$ ( $p = 0.072$ , corrected $p = 0.552$ )
Segment 6	$r = 0.35$ ( $p = 0.092$ , corrected $p = 0.652$ )
Segment 7	$r = 0.256$ ( $p = 0.241$ , corrected $p = 1$ )

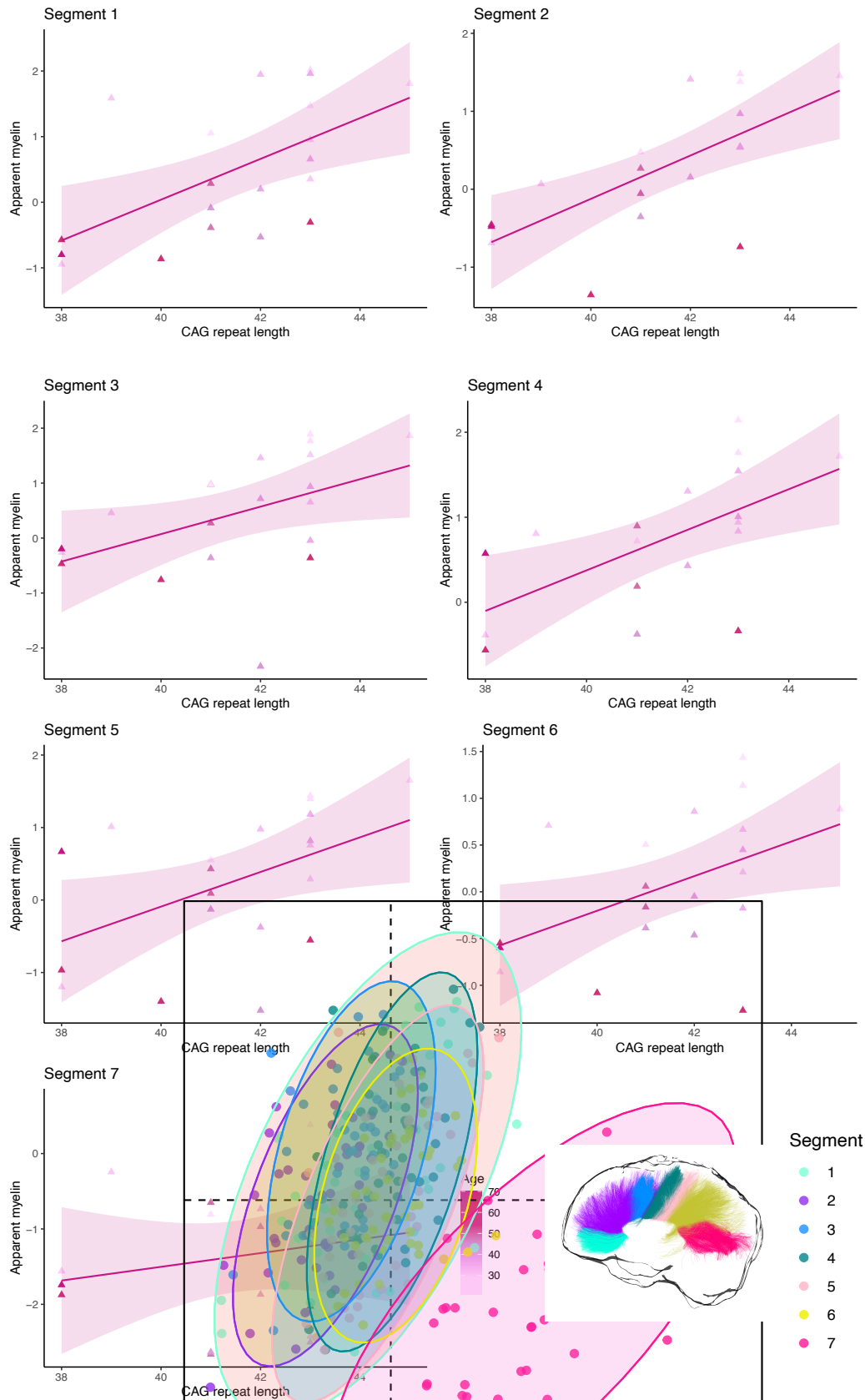


**Figure 20. Relationship between apparent myelin in each callosal segment and cytosine, adenine, and guanine (CAG) repeat length in patients.**

*Trends for positive associations between these two variables were detected in all segments.*

### **3.5.6. Whole-brain analysis with TBCA reveals WM microstructure alterations in the posterior CC, the left CST and the right fronto-striatal projections**

Figure 21 shows the results of the TBCA. Consistent with the PCA results, a significant reduction in MTR in the HD group was detected, compared to controls, in the most posterior portion of the CC [cluster mass ( $\sum$  t-score) = 1530,  $p < 0.001$  (uncorrected),  $p = 0.030$  (FWE-corrected)]. Furthermore, a significant increase in FR along most of the left CST was found [cluster mass ( $\sum$  t-score) = 1004,  $p < 0.001$  (uncorrected),  $p = 0.030$  (FWE-corrected)]. Finally, right-lateralized clusters of significantly higher FA in the HD group were identified in the fronto-striatal projections [cluster mass ( $\sum$  t-score) = 956,  $p < 0.001$  (uncorrected),  $p = 0.03$  (FWE-corrected)].

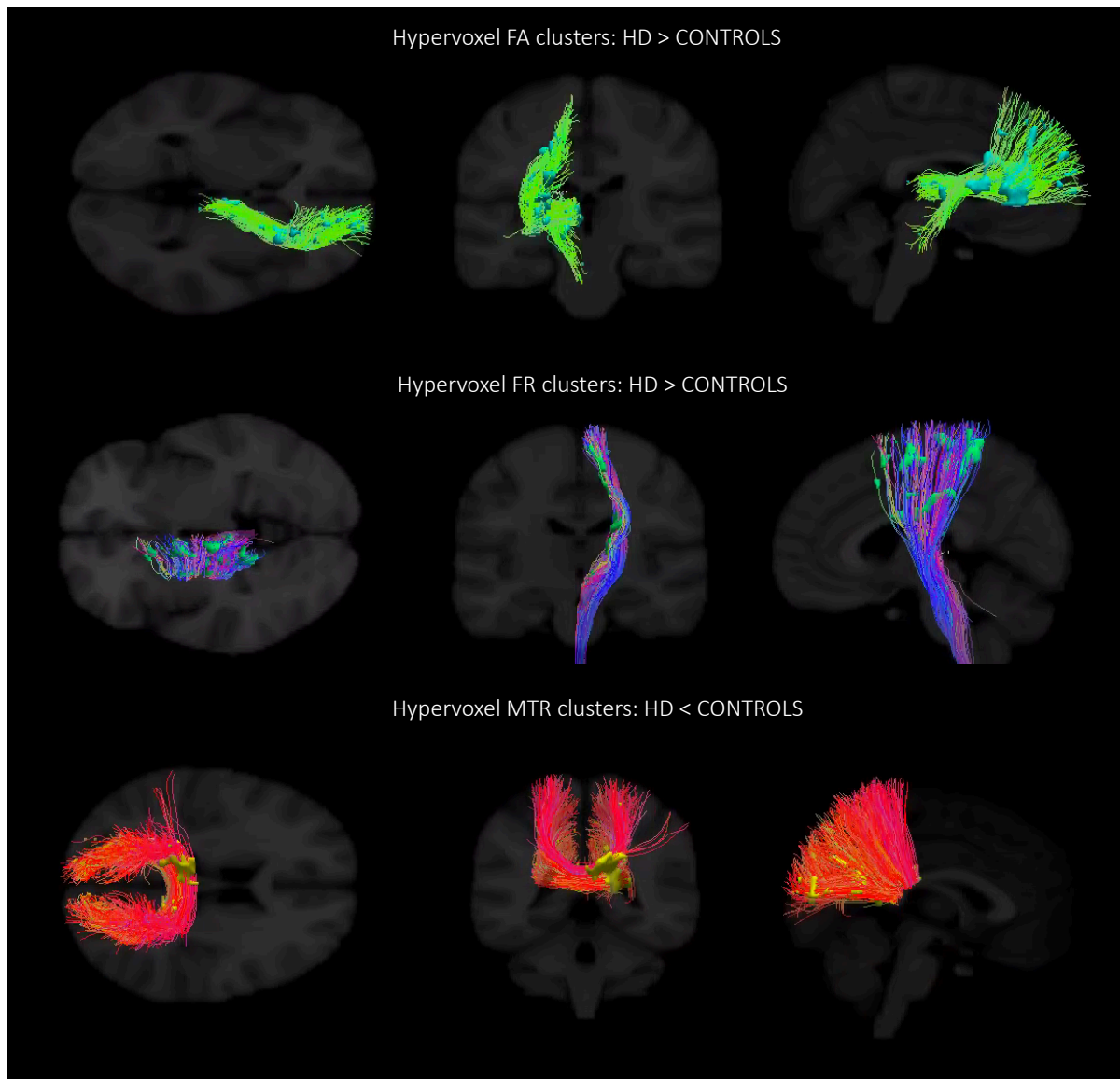


**Figure 21. Results of the cluster-analysis obtained with tract-based cluster analysis (TBCA) between patients and controls.**

*Cluster-level statistic: cluster mass (sum of t-score), family-wise error (FEW)  $p < 0.05$ . Microstructure alterations were detected in the posterior portion of the callosum, the left corticospinal tract and the right fronto-striatal projections. Abbreviations: FA: fractional anisotropy; FR: restricted volume fraction; MTR: magnetization transfer ratio.*

Figure 22 plots the relationship between significant microstructure clusters as detected with TBCA for HD patients. FR in the CST was significantly associated with MTR in the posterior CC ( $r = 0.498$ ,  $p = 0.011$ , corrected  $p = 0.033$ ), but not with FA in the right fronto-striatal projections ( $r = 0.328$ ,  $p = 0.110$ , corrected  $p = 0.327$ ). Additionally, MTR was not associated with FA ( $r = -0.218$ ,  $p = 0.294$ , corrected  $p = 0.882$ ).

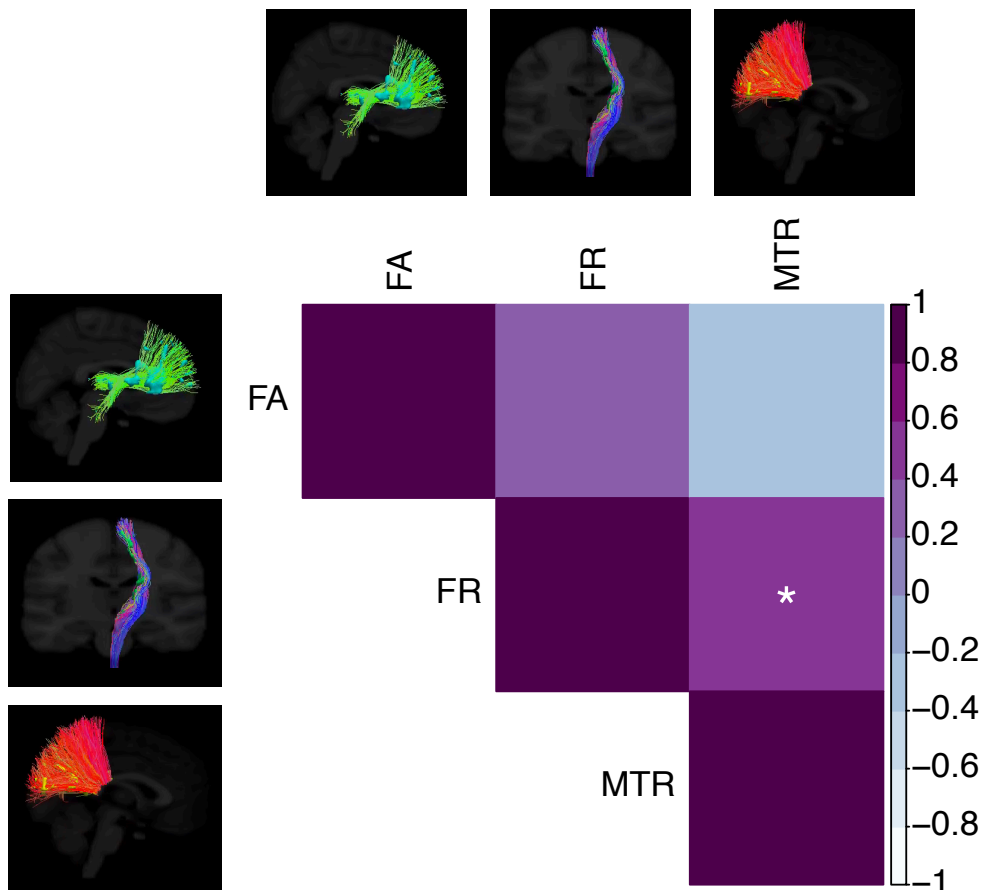


**Figure 22. Spearman correlations between significant tract based cluster analysis (TBCA) clusters in patients.**

Summary of significant clusters detected with TBCA and correlation matrix. Color intensity is proportional to the strength and direction of the correlation. \*  $p < 0.05$ , \*\*  $p < 0.01$ , \*\*\*  $p < 0.001$ , Bonferroni-corrected. Abbreviations: FA: fractional anisotropy; FR: restricted volume fraction; MTR: magnetization transfer ratio.

Table 14 summarizes results of the Spearman correlations of microstructural clusters with composite cognitive scores, striatal component scores, DBS and CAG. A trend for a positive association was detected between FR in the CST and cognitive performance ( $r = 0.561$ ,  $p = 0.019$ , corrected  $p = 0.057$ ). Additionally, consistent with the tractometry analysis, a trend for a positive association between MTR in the posterior CC and CAG repeat length was detected ( $r = 0.467$ ,  $p = 0.038$ , corrected  $p = 0.092$ ). The other correlations were not significant.

**Table 14. Correlations of significant clusters of microstructure metrics as detected with TBCA with cognitive component scores, striatal component scores, disease burden score (DBS) and CAG repeat length**

Correlation coefficients that were significant after Bonferroni correction are highlighted in bold. Trends, defined as correlations significant at the uncorrected level, are highlighted in italics. Abbreviations: FA: fractional anisotropy; FR: restricted volume fraction; MTR: magnetization transfer ratio. CAG: cytosine, adenine, and guanine repeat size.

<b>Composite cognitive scores</b>	
<b>FA</b>	$r = -0.221, p = 0.395, \text{corrected } p = 1$
<b>FR</b>	$r = 0.561, p = 0.019, \text{corrected } p = 0.057$
<b>MTR</b>	$r = 0.429, p = 0.086, \text{corrected } p = 0.2580$
<b>Striatal component scores</b>	
<b>FA</b>	$r = 0.017, p = 0.939, \text{corrected } p = 0.870$
<b>FR</b>	$r = 0.322, p = 0.125, \text{corrected } p = 0.966$
<b>MTR</b>	$r = 0.225, p = 0.290, \text{corrected } p = 0.375$
<b>DBS</b>	
<b>FA</b>	$r = -0.28, p = 0.896, \text{corrected } p = 1$
<b>FR</b>	$r = -0.328, p = 0.117, \text{corrected } p = 0.351$
<b>MTR</b>	$r = -0.215, p = 0.312, \text{corrected } p = 0.936$
<b>CAG</b>	
<b>FA</b>	$r = 0.073, p = 0.761, \text{corrected } p = 1$
<b>FR</b>	$r = 0.274, p = 0.243, \text{corrected } p = 0.721$
<b>MTR</b>	$r = 0.467, p = 0.038, \text{corrected } p = 0.091$

## 3.6. Discussion

The present study applied DTI, CHARMED and MTI in premanifest HD patients in order to disentangle the contribution of axon microstructure *versus* myelin to HD pathology. Results were examined alongside macrostructural GM changes and behavioural measures.

### 3.6.1. Premanifest HD patients present impairments in the encoding, temporary storage and updating of information

Patients performed significantly worse compared to controls in the 2-back task, while no significant difference in performance was detected between groups in the 1-back task, suggesting that abnormalities in the premanifest stage of HD may primarily affect more demanding tasks (Farrow et al., 2006; Klöppel et al., 2009). This may be due to recruitment of compensatory mechanisms that help to maintain function in the context of a slowly progressive neurodegeneration (Klöppel et al., 2009). Compensatory processes may also explain the lack of significant group differences in the tapping tasks. Additionally, these results suggest that executive deficits may precede the onset of bradykinesia in HD (Ca et al., 2014), consistent with previous work showing that routine motor behaviour remains largely unaffected in premanifest gene carriers (Campodonico et al., 1996; Giordani et al., 1995). Alternatively, it may be that the tapping task was not sensitive enough to pick up on motor deficits in the HD group. While this study assessed the mean number of taps, previous reports have demonstrated that the speeded tapping inter-tap interval may be more sensitive in detecting changes in premanifest HD (Scahill et al., 2013).

The lack of group differences in the digit span and the visual patterns tests may indicate that these tasks require a larger sample size to detect a group difference; alternatively, it might be that the well-established alterations in multi-tasking and executive functioning in HD (Mörkl et al., 2016; Papoutsi et al., 2014; Stout et al., 2016) are due to shortfalls in the executive

control and manipulation of information processing, rather than to a reduced capacity for storing information in working memory. Evidence for such a dissociation has been shown previously in manifest HD patients (Bourbon-Teles et al., 2019).

In this study, the HD group did not differ significantly from controls in performance in the emotion recognition task. While problems in the ability to recognize emotions have been widely shown in symptomatic HD over the last few decades (e.g. Bates et al. 2015; Dumas et al. 2013; Henley et al. 2012), evidence for the premanifest stage of the disease is more sparse and contrasting (Zarotti et al., 2018). Some smaller studies have reported no significant impairment (Kipps et al., 2007; Milders et al., 2003), while investigations in larger samples have detected a significant impairment of negative emotion specifically (Labuschagne et al., 2013; Scahill et al., 2013) – for a systematic review see Henley et al., 2012. Thus, it might be that our sample was too small to detect significant differences. Otherwise, inconsistencies in findings across studies might represent the variability inherent to HD, or the between-study differences in methodology (Henley et al., 2012). Importantly, though the Eyes test (Baron-Cohen et al., 2001) is used worldwide and has previously shown acceptable construct validity when compared to other emotion recognition tasks (Alaerts et al., 2011), as well as acceptable internal consistency (Voracek & Dressler, 2006), it was not possible with this task to focus specifically on the assessment of negative emotion recognition. The identification of negative emotions, in turn has been more consistently reported as impaired in premanifest HD (Henley et al., 2012).

### **3.6.2. Premanifest HD patients present atrophy in the striatum but not in the thalamus**

Consistent with previous studies, changes in subcortical GM, and specifically in the striatum, were detected in premanifest patients (Aylward et al., 2012; Paulsen et al., 2014a,

2014b; Tabrizi et al., 2012, 2013). Imaging evidence from PREDICT-HD, TRACK-HD and other studies, has shown that striatal atrophy is present in HD carriers as early as 15 years before clinical disease onset (Aylward et al., 2012; Paulsen et al., 2014a, 2014b; Tabrizi et al., 2012, 2013). Importantly, striatal changes have been shown to be the most sensitive and robust finding in MRI studies (Aylward, 2014; Ross et al., 2014), and have been proposed as a biomarker for future clinical trials (Georgiou-Karistianis et al., 2013b).

Worse cognitive performance was associated with greater striatal atrophy. However, the relationship was no longer significant after partialling out DBS, suggesting that disease burden is an important driver in this relationship. Accordingly, a significant negative relationship between scores on the striatal component and DBS indicated that increased proximity to disease onset is associated with greater striatal atrophy. These findings are consistent with evidence that proximity to clinical onset affects motor and cognitive performance in premanifest HD carriers (Farrow et al., 2006), and that striatal and cognitive changes are present across the disease course, into the manifest disease phase (Aylward et al., 2012; Paulsen et al., 2014a, 2014b; Tabrizi et al., 2012, 2013).

No significant group difference was detected on component scores for the thalamic component, suggesting that atrophy in the striatum precedes structural changes in the thalamus. HD is associated with a dysfunction of cortico-striatal circuits, and the thalamus presents widespread connectivity as part of the cortico-striatal loops (Cepeda et al., 2007; Furlong et al., 2020; Tekin & Cummings, 2002). However, little is known about the pathophysiologic role of this area and its relationship to cognitive, neuropsychiatric and motor dysfunction in HD (Furlong et al., 2020). While changes in thalamic structure have been detected in the symptomatic phase of the disease (Kassubek et al., 2004; van den Bogaard et al., 2011; Younes et al., 2014), neuroimaging and neuropathology studies have produced conflicting results with regards to the premanifest stage of HD (Furlong et al., 2020). A few studies have detected

reduced thalamic volumes (van den Bogaard et al., 2011) and a faster rate of change in thalamic volume over time (Aylward et al., 2011), while other studies have found no evidence of significant volumetric changes in premanifest patients (Majid et al., 2011; Younes et al., 2014). Accordingly, the present study suggests that striatal areas demonstrate atrophy prior to the thalamus (Aylward et al., 2011; Georgiou-Karistianis et al., 2013a).

Several explanations have been suggested to describe the process of spread of neuronal dysfunction in neurodegenerative diseases such as HD, for example an activity-dependant spreading of neurodegeneration in vulnerable brain networks via synaptic dysregulation (Fornito & Bullmore, 2015; Looi & Walterfang, 2013; Palop et al., 2006). Such neurodegenerative processes may explain evidence of thalamic atrophy later in disease progression, in symptomatic HD (Kassubek et al., 2004; van den Bogaard et al., 2011; Younes et al., 2014). Although this was beyond the scope of the present study, future research might prove useful in understanding the topographical and temporal sequence of changes in HD through longitudinal analysis of the thalamus, amongst other cortico-striatal components (Furlong et al., 2020).

### **3.6.3. Premanifest HD patients present alterations in callosal apparent myelin, which are associated with CAG repeat length, cognitive performance and striatal atrophy**

While callosal alterations have previously been shown in HD, even at the premanifest stage of the disease (Di Paola et al., 2012, 2014; Phillips et al., 2013; Rosas et al., 2006, 2010), the strength of the present study consisted in carrying out a comprehensive evaluation of the changes that take place regionally across the CC, by employing a tractometry approach (Bells et al., 2011; Jones et al., 2005, 2006). Crucially, by exploiting the very latest-in ultra-strong magnetic field gradient technology of the Connectom scanner (Setsompop et al., 2013; Jones et al., 2018), it was possible to better tease apart changes in myelin content from alterations in

axon microstructure, while maintaining reasonable echo times and thus sufficient SNR (Kleban et al. 2020).

The isthmus of the CC was found to be affected in the HD group. Specifically, decreased apparent myelin was detected in patients, in the absence of significant differences in axon density. This suggests the presence of demyelination in this portion of the CC. Previous evidence has shown microstructure changes in this callosal region in premanifest HD (Di Paola et al., 2014; Phillips et al., 2013), and implied the presence of demyelination because of increased RD and decreased FA, in the absence of AD changes (Di Paola et al., 2012). However, diffusion tensor indices do not allow the biophysical basis of any detected change to be inferred (Alexander et al., 2007; De Santis et al., 2014). In this study, the combination of standard tensor metrics with MTR and FR afforded a more biologically-meaningful interpretation of microstructure changes. Importantly, the present results are consistent with the Demyelination Hypothesis of HD, which argues that early- and heavily-myelinated fibres, such as those in the callosal isthmus are more susceptible to myelin breakdown in HD (Bartzokis et al., 2007).

More surprising is the finding that HD patients presented significantly higher scores compared to controls on the apparent myelin component in segment 1 and that, overall, scores on the apparent myelin component for the HD group were higher than controls in the more anterior portions of the CC, but lower than controls in the posterior portions.

It is possible that the HD mutation leads to excessive, rather than reduced, myelin production. Therefore, while earlier in disease progression the HD mutation may be associated with more myelin production, such increases in myelin content may lead to detrimental effects later in the disease because of oxidative stress (Bartzokis et al., 1999, 2007; Bartzokis & Tishler, 2000). This suggestion is consistent with the positive association detected between scores on the apparent myelin component in HD patients and CAG repeat length, with the

relationship becoming stronger after controlling for disease burden. This association indeed indicates that, rather than being linked to disease progression, such alterations in myelin content are a direct result of the disease mutation. Consistent with this, there was no significant association between apparent myelin and DBS in any of the segments. Critically, myelin content might go beyond optimal levels of myelination in early myelinating regions first, as myelination in these areas is greater and starts earlier in life (Martenson, 1992). This suggestion is in agreement with evidence that earlier myelinating regions are impaired first in the disease (Bartzokis et al., 2007), and with the finding of decreased apparent myelin in the posterior callosum in this study.

While excessive myelination has not been previously considered as a possible pathological process in HD, a previous study reported increases in MTR in the CC of children with autism, and suggested that this increase may reflect neurodevelopmental abnormalities (Gozzi et al., 2012). Similarly, the present findings are consistent with previous claims that brain development may contribute to the pathogenesis of HD, as a precursor to the more global neurodegeneration process (Barnat et al., 2020; Jin et al., 2015; Nopoulos et al., 2010; Phillips et al., 2014). Importantly, the fact that no atrophy or changes in axon density were detected in the CC, suggests that such an increase in MTR is likely due to actual changes in myelin rather than to an impairment in WM growth, which has previously been suggested as pathological mechanism in HD (Phillips et al., 2014).

Another possible explanation for this result is the presence of homeostatic remyelination in the HD brain. As the apparent myelin component presented high loadings on MTR, this interpretation is consistent with evidence that MTR decreases with acute demyelination and increases with remyelination (Deloire-Grassin et al., 2000; Dousset et al., 1992, 1995).

While compensatory increases in MRI proxies of myelin content have not been previously reported in HD, a study on Parkinson's disease patients reported increased myelin volume fraction in frontal and temporal WM and in the thalamus (Dean et al., 2016). Accordingly, the presence of a trend for positive associations between apparent myelin content and composite cognitive scores further indicates that the increases in apparent myelin might reflect a compensatory response to HD-associated myelin abnormalities, which in turn helps to maintain function. This is in accordance with what was observed in terms of cognitive changes in the HD sample (Klöppel et al., 2009).

Notably, although remyelination processes may successfully compensate for myelin loss during the premanifest HD stage, these may start failing in later years (Di Paola et al., 2014; Phillips et al., 2014), either because of oligodendrocyte dysfunction early in the disease course impairing remyelination (Bartzokis et al., 2007), or because the homeostatic increase in oligodendrocytes causes significant increases in ferritin iron content, in turn leading to oxidative stress (Bartzokis et al., 1999, 2007; Bartzokis & Tishler, 2000).

Both the proposal of homeostatic remyelination and of excessive myelin production in the early stages of HD are in agreement with the significant interaction effect detected between group and age on apparent myelin scores. This indeed suggests that while scores on this component are higher in younger patients, the opposite is true for older HD patients, which likely present increased disease burden. Additionally, both of these explanations are in agreement with findings from neuropathology showing increased density of oligodendrocytes in premanifest HD (Gómez-Tortosa et al., 2001) and that *mHTT* directly alters the proliferation property of cultured oligodendrocyte precursor cells (OPCs) with the degree of cell proliferation of OPCs increasing with pathological severity and increasing CAG repeat length (Jin et al., 2015).

However, the proposal of excessive myelination in HD is not consistent with histological findings from animal studies. For example, OPCs isolated from neonatal HD mouse brains and derivative oligodendrocytes show deficits in the levels of myelin-related genes (Teo et al., 2016). Similarly, HD mice present alterations in myelin sheaths which are paralleled by reduced expression of myelin-related genes (Blockx et al. 2012; Jin et al. 2015; Xiang et al. 2011). Finally, inactivation of *mHTT* within oligodendrocytes prevents myelin deficits in mouse models of HD, possibly due to improved cholesterol metabolism and increased transcription of myelin regulator factor (Bardile et al., 2019). Therefore, if considered in the context of the existing literature, the present findings are likely due to a dysregulation of the temporal profile of myelination and to deficient, rather than excessive, myelination as an important early pathogenic event in HD (Jin et al. 2015). Nevertheless, most experimental evidence about histological abnormalities in HD is based on mouse models (Xiang et al., 2011) and thus future studies following young premanifest subjects longitudinally should address the possibility of toxic myelin levels in the premanifest HD brain because of pathological CAG repeats size.

Overall, the above findings demonstrate measurable and significant differences in callosal apparent myelin before changes in proxy metrics of axon density can be detected. Additionally, these changes seem to be present before morphometric alterations, indicating that microstructural changes in the callosum are present prior to frank neurodegeneration and may instead reflect early neuronal dysfunction (Rosas et al., 2010) or a neurodevelopmental component to the pathogenesis of HD (Jin et al., 2015). Finally, they suggest that alterations in the callosum in HD follow both a topologically and temporally specific pattern of degeneration. Specifically, decreased apparent myelin in the most posterior areas, through which fibres from visual systems transverse, suggests that these regions are the first to be affected in the disease, either because of a failure in homeostatic responses to myelin impairment or because of toxicity

associated with increased myelin content. The visual system is functionally critical early in life and in this system myelination occurs early and progresses rapidly (Yakovlev, 1967). Additionally, this system is highly dynamic and is associated with big energetic demands. As metabolic dysfunction and alterations in energetics play important mechanistic roles in HD (Beal, 2005; Browne, 2008), these changes may contribute to the earlier myelin impairment in this callosal portion.

#### **3.6.4. Whole-brain analysis with TBCA reveals WM microstructure alterations in the posterior CC, the left CST and the right fronto-striatal projections**

Another strength of the present work consisted in moving beyond TBSS analysis and using TBCA to obtain the anatomical specificity required to disentangle distinct clusters belonging to different anatomical tracts (Luque Laguna, 2019). This approach was meaningful because of evidence showing widespread WM volume loss in HD (Aylward et al., 2011; Beglinger et al., 2007; Ciarmiello et al., 2006; Paulsen et al., 2008; Rosas et al., 2006; Tabrizi et al., 2009, 2011, 2012), and the concept of compensatory networks in response to neurodegeneration (Klöppel et al., 2009).

Consistent with the tractometry results, a significant decrease in MTR in the most posterior portion of the corpus callosum was detected in the HD group, lending support to a decrease in apparent myelin in this region in HD patients. Additionally, again in agreement with the tractometry analysis, a trend for a positive association between MTR in the posterior CC and CAG repeat length was detected. However, no increases in apparent myelin were found in the more anterior segments. This may be due to the increased power afforded by tractometry approaches in combination with PCA, compared to the much more stringent correction for multiple comparisons carried out in TBCA.

Clusters of significantly higher FA were detected in the HD group in the right fronto-striatal projections. In the previous literature, neurodegenerative disorders have normally been associated with decreased FA in major WM pathways, which has been attributed to WM degeneration, demyelination, reduced gliosis or axonal damage as a result of GM loss (Assaf, 2008; Concha et al., 2006). In this study, higher FA might reflect early compensatory mechanisms associated with increases in axonal density in this pathway. However, this explanation is unlikely, as no significant differences were detected in FR. Interestingly, a study on early HD patients showed that, despite the widely shown neuronal loss in this area, selective degeneration of specific WM tracts was reflected by higher anisotropy values and a paradoxical increase in microstructural organization, (Douaud et al., 2009). Results from the present study lend support to this suggestion and indicate that WM degeneration in this area is already present at the premanifest stage of the disease.

With TBCA, a significant increase in FR along most of the left CST was also detected. This tract is composed of descending WM tracts, with half of them arising from the primary motor cortex, and is anatomically linked to the basal ganglia (Kandel et al., 2000; Schultz, 2001). From a functional point of view, the CST conducts motor impulses from the brain to the spinal cord, and plays an essential role in voluntary movement (Kandel et al., 2000; Schultz, 2001). Even though the hallmark symptom of HD concerns purposeless, involuntary choreic movements (Folstein, 1989), alterations in voluntary movement are also present in premanifest HD patients, such as deficits in self-paced timing motor tasks (Rowe et al., 2010). This therefore stresses the connection between HD and the CST, and suggests that alterations in this tract may play an important role in the disease.

Previous studies have demonstrated reduced WM volume in the internal capsule, which forms part of the CST, of manifest HD patients (Fennema-Notestine et al., 2004; Nave et al., 2010). Accordingly, increases in FR detected in this study might reflect the loss of non-

neuronal cells, in turn leading to axons being pushed together (Rattray et al., 2013). Alternatively, such result might reflect axonal swelling (Marangoni et al., 2014). Consistent with this suggestion, previous evidence demonstrated increased iron levels in the left CST of premanifest HD patients (Phillips et al., 2015), interpreted as indicating an homeostatic increase in oligodendrocytes to repair myelin damage. In turn, myelin damage leads to axon swelling (Payne et al., 2012). It might also be that fibre bundles develop differently to start with because of the genetic mutation, and this is consistent with evidence of morphological alterations in the neurons of R6/2 HD mice, which present smaller diameter dendritic shafts, smaller somatic cross-sectional areas, and decreased diameter of the dendritic fields (Klapstein et al., 2001). Finally, increased FR might reflect the presence of a process of reorganization and compensatory pruning of axons in WM, such as pathologically-driven reduced collateral branching or morphological alterations of individual axons. Consistent with this suggestion, Zhang and colleagues (2018) revealed increased coherence of axonal organization in premanifest HD patients, as suggested by a smaller orientation dispersion index (OD), in tracts surrounding the basal ganglia and in the internal and external capsule.

Importantly, the finding of increased FR in the left CST is consistent with the leftward-biased GM loss present in the striatum of HD patients (Muhlau et al., 2007) and with the leftward asymmetry of brain iron in aging and motor disorders, which has been ascribed to motor lateralization (Langkammer et al., 2010; Xu et al., 2008). Nevertheless, future studies are needed to determine whether this is an important finding to understand HD pathology.

### **3.6.5. Methodological considerations**

It is important to note that the MTR is influenced by a complex combination of biological factors (including  $T_1$ ), making it difficult to separate the effects of reduced macromolecular density because of demyelination and/or axonal loss, or increased water

because of oedema and/or inflammation (Deloire-Grassin et al. 2000; Dousset et al. 1992, 1995; Gareau et al. 2000). As such, it is impossible to pinpoint which pathological processes are responsible for the decreased MTR observed in the isthmus of HD patients. Similarly, factors other than increased myelin content have been shown to affect MTR increases, such as non-myelin macromolecules (e.g. in neuroinflammation) (Bells 2012).

Previous research speculated that physical degradation of myelin early in Wallerian degradation may cause an increase in the available sites for magnetization transfer, thus contributing to the rise of MTR (Lexa et al., 1994). Other potential explanations include increases in axonal protein content or vesicle concentration from interruption of axoplasmic transport (Lexa et al., 1994). However, in this study no significant differences between patients and controls were detected in the axon density component. Overall, though an attempt was made to control for confounding elements by, for example, including FWF as a factor in the analyses, and complementing MTR with other microstructure-sensitive metrics, these results require replication in future studies; additionally, future investigations may benefit from utilising more quantitative measures such as qMT (Henkelman et al., 1993) to assess myelin alterations in the premanifest stage of HD.

Additionally, it is challenging to estimate the contribution of smaller axons to the diffusion signal (Drakesmith et al., 2019). Though this work utilised ultra-strong gradients (300 mT/m), therefore allowing the contribution of axons with a diameter as small as 3  $\mu\text{m}$  to be assessed (Drobnjak et al., 2016; Nilsson et al., 2017; Sepehrband et al., 2016), the majority of axons in the brain have a diameter smaller than 1  $\mu\text{m}$  (Aboitiz et al., 1992; Caminiti et al., 2013; Liewald et al., 2014; Sepehrband et al., 2016). Because of this, changes in later myelinating WM areas (such as the anterior portions of the CC), which are characterized by small and thinly myelinated axons, may have not been appropriately reflected by variation in FR. Hence, there is a possibility that increases in MTR observed in the anterior portions of the CC may have

reflected decreased axonal density in this area, rather than compensatory remyelination. However, the lack of significant changes in other measures, such as AD or RD, suggests the absence of significant axon changes in the HD sample.

Finally it has to be noted that, because of the way FR is computed, this measure is best described as the “T<sub>2</sub>-weighted restricted signal fraction”. This in turn implies that a change in T<sub>2</sub> relaxation (for example because of altered tissue water or myelin content) may be interpreted as a difference in FR when this measure was actually not altered.

Nevertheless, this is the first time that increases in this measure have been detected in premanifest HD patients, pointing to the potential of FR as *in vivo* MRI marker of HD-associated neural changes during the premanifest disease stage. Importantly, while the trend for a positive association between FR in the CST and cognitive performance suggests that this alteration may reflect a compensatory response, rather than a disease-related change, future studies are needed to clarify the neurobiological underpinning of this finding. For example, future research should investigate HD-associated changes in tract volume, axon diameter distribution and g-ratio in the CST, and the longitudinal evolution of changes in the HD brain.

## **Chapter 4**

# **Frequency difference mapping quantifies myelin breakdown in premanifest HD**

### **4.1. Chapter summary**

Frequency difference mapping (FDM) (Tendler & Bowtell, 2019; Wharton & Bowtell, 2013), an MRI-based phase-processing technique, has been shown to quantify myelin *in vivo*, therefore pointing to the potential of this technique for the study of WM myelin changes in health and disease (Li et al., 2016; Wisnieff et al., 2015). This study first characterized the reproducibility of FDM-based metrics across the CC in healthy participants, finding highest reproducibility in the posterior callosal segment. Subsequently, FDM was applied for the first time to investigate myelin breakdown *in vivo* in this callosal region in a sample of premanifest HD patients compared to age, sex and education matched healthy controls.

### **4.2. Declaration of collaborations**

The development of the FDM protocol and the processing of the data through the FDM pipeline were conducted in collaboration with Dr Elena Kleban (Cardiff University).

### **4.3. Introduction**

Quantitative MRI of myelin affords valuable insight into myelin alterations and is thus of particular interest in the study of myelin-related disorders. Most neuroimaging studies have used diffusion tensor magnetic resonance imaging (DT-MRI) to quantify WM tissue properties in HD (see Casella et al. 2020 for a review). However, while sensitive, DT-MRI measures are

not specific to WM sub-compartments, challenging the interpretation of any observed change in these indices (De Santis et al., 2014; Wheeler-Kingshott & Cercignani, 2009).

On the other hand, other MRI techniques have the promise to provide much more myelin-specific information (MacKay & Laule, 2016). For example, myelin water imaging (MWI) quantifies the fraction of the faster decaying signal from water trapped between myelin lipid bilayers (Mackay et al., 1994), the so-called myelin water fraction (MWF). MWF has a good correlation with histological measurements of myelin, demonstrating its potential as an *in vivo* biomarker of myelin content (Laule et al., 2006; 2004; Webb et al., 2003). MWI techniques are typically based on spin-echo (MacKay et al., 1994) or multi-echo gradient-recalled echo (mGRE) sequences (Du et al., 2007). Interestingly, mGRE enables further characterisation of the myelin sheath by exploring its interaction with the magnetic field  $B_0$ , which is suggestively dependent on the g-ratio (i.e. the ratio of the inner-to-outer diameter of a myelinated axon) (Wharton & Bowtell, 2012).

A plethora of studies have demonstrated the non-mono-exponential nature of mGRE signal evolution with echo time (TE) in WM (e.g. Sati et al. 2013; Wharton and Bowtell 2012, 2013), arising from sub-voxel microstructure, with distinct signal components originating from water confined to the myelin, intra-axonal and extra-axonal water pools (Cronin et al., 2017; Nam et al., 2015b; Nunes et al., 2017; Sati et al., 2013; Tendler & Bowtell, 2019; Thapaliya et al., 2017; Wharton & Bowtell, 2012). As a result of the rapid  $T_2^*$  decay of the myelin water signal, the frequency of the total signal changes with TE, producing a local, microstructure-dependent contribution to the signal phase. However, in order to uncover the specific effects of microstructure on phase signal evolution, it is necessary to remove TE-dependent signal inhomogeneities resulting from non-local field variation, together with other non-TE-dependent phase changes, such as those due to radiofrequency interaction with the tissue (Schweser et al., 2011).

For this purpose, FDM has recently been presented as phase-processing technique (Sati et al., 2013; Schweser et al., 2011; Tendler & Bowtell, 2019; van Gelderen et al., 2012; Wharton & Bowtell, 2013). FDM is performed by comparing frequency maps acquired at short and long TEs so as to yield local frequency difference values which depend solely upon the underlying tissue microstructure, and in particular upon the local nerve fibre orientation with respect to the applied magnetic field. Critically, since both compartmentalization and myelination are prerequisites for the generation of frequency differences, FDM has great potential for the study of myelin changes in WM (Li et al., 2016; Wisnieff et al., 2015).

The aim of the present study was to exploit, for the first time in the HD literature, the sensitivity of FDM to WM microstructure, and particularly to myelin content, to assess callosal myelin changes at the premanifest stage of the disease. Numerous studies have highlighted the importance of the CC in neurological and psychiatric disorders (Di Paola et al., 2012; Kim et al., 2008; Luders et al., 2007). Additionally, callosal fibers are coherently oriented perpendicular to the main magnetic field when the subject is inside the scanner, therefore generating the largest possible frequency offsets in the myelin and axonal compartments (Sati et al., 2013; Wharton & Bowtell, 2012; Yablonskiy et al., 2014). Importantly, scanning participants at high field strength constituted an advantage in terms of signal-to-noise ratio (SNR) and signal contrast (MacKay & Laule, 2016).

Specifically, this study sought to: i. establish the reliability of this method by investigating the anatomical variability in the reproducibility of FDM across the callosum at 7 Tesla; ii. compare two FDM-based myelin-related parameters between premanifest HD patients and healthy controls; and iii. assess brain-function relationships in patients by exploring correlations between myelin content and cognitive function, as well as proximity to disease onset. The two myelin-sensitive metrics assessed were: i. the myelin water signal fraction ( $f_m$ ) and ii. the difference in frequency offsets between myelin water pool and axonal

water pool ( $\Delta\omega$ ). The former is linked to the myelin volume fraction and may be used as a proxy for tissue myelin content (Laule et al., 2008; Li et al., 2015); the latter depends on the magnetic susceptibility difference and on the g-ratio (Wharton & Bowtell, 2012). Cognitive tests were selected in order to capture functioning across executive functions, working memory, social cognition and motor performance (Table 18), as these represent the earliest cognitive indicators of HD (Paulsen, 2011), and impaired performance in these domains has been associated with callosal microstructure (Kennedy & Raz, 2009; Lenzi et al., 2007; McDonald et al., 2018).

## **4.4. Materials and Methods**

### **4.4.1. Participants**

#### ***Reproducibility study***

To investigate the anatomical variability in the precision of FDM across the CC, six healthy subjects without known neurological or psychiatric conditions (3 female, 26-33 year-old) were scanned five times over a two-week period each. The study was approved by the Cardiff University School of Psychology Ethics Committee and written informed consent was obtained from all participants. To take part in the study, participants also had to be eligible for MRI scanning.

#### ***HD study***

For the assessment of callosal myelin content in premanifest HD, MRI scans and cognitive tests were performed on 19 premanifest HD patients and 21 age, sex, and education

matched healthy controls. Ethics, recruitment and consent procedures for this study matched the ones described for the study in Chapter 3. Of the 21 healthy controls assessed, 16 were recruited from Cardiff University and the School of Psychology community panel, while 5 were patients' spouses or family members. Of the participants assessed, 23 (N = 9 patients, N = 14 controls) took also part in the study described in Chapter 3.

Similarly to the study described in Chapter 3, patients recruited for this study had data available from their most recent assessment from their participation in the ENROLL-HD study, thus some of these data were used for this study. Table 15 summarizes information about demographic variables and performance in the MoCA (Nasreddine et al., 2005) and in the TOPF-UK for patients and controls. Although the two groups did not differ significantly in age, MoCA score, or TOPF-UK FSIQ, controls were on average slightly older and had a slightly higher IQ. Table 16 summarizes patients' demographic and background clinical characteristics. Based on TMS, all patients were at the premanifest disease stage. Based on diagnostic confidence level scores DCL, four patients presented some motor abnormalities, but none of them presented unequivocal motor signs of HD. Table 17 summarizes information about patients' medication.

**Table 15. Summary of participants' demographic and clinical background information.**

*Age is displayed in years. MoCA = Montreal Cognitive Assessment out of 30; the higher the score the better the performance. TOPF-UK IQ = verbal IQ estimate based on the Test of Premorbid Functioning, UK version.*

	<b>HD patients (n = 19)</b>	<b>Controls (n = 21)</b>	<b>p-value</b>
<b>Gender male/female (%)</b>	12(63.15)/7(36.85)	10(47.6)/11(52.4)	p > 0.05
<b>Mean age (SD, range)</b>	41.61 (13.1, 21-70)	45.14 (12.5, 27-71)	p > 0.05
<b>Mean TOPFUK FSIQ (SD, range)</b>	117.19 (11.58, 98-137.4)	123.42 (7.85, 109-131.9)	p > 0.05

<b>Mean MoCA score (SD, range)</b>	27.82 (2.29, 24-30)	28.16 (2.00, 26-30)	p > 0.05
--	------------------------	------------------------	----------

**Table 16. Background clinical information of the patients' cohort.**

CAG = cytosine, adenine, and guanine repeat size. Three individuals with CAG repeats of 37 (n = 1) and 38 (n = 2) were included in the current study. As mentioned in Chapter 3, although these individuals can be considered “affected”, they may have a lower risk of becoming symptomatic within their life span. DBS = disease burden score, a measure of proximity to clinical onset of the disease (Tabrizi et al., 2012), calculated as follows:  $DBS = age \times (CAG - 35.5)$ ; the higher the DBS, the closer the patient's proximity to disease onset. TMS = Total Motor Score out of 124 from the UHDRS Motor Diagnostic Confidence (Motor) – the higher the score stands for the higher the motor impairment. DCL = diagnostic confidence level, asks whether the participant “meets the operational definition of the unequivocal presence of an otherwise unexplained extrapyramidal movement disorder in a subject at risk for HD” (normal/no abnormalities = 0, non-specific motor abnormalities = 1, motor abnormalities that may be signs of HD = 2, motor abnormalities that are likely signs of HD = 3, motor abnormalities that are unequivocal signs of HD = 4).

<b>CAG (SD, range)</b>	<b>Mean DBS (SD, range)</b>	<b>Mean TMS (SD, range)</b>	<b>Mean DCL (SD, range)</b>
41.3 (2.14, 37-45)	236.15 (84.52, 80-450)	3.625 (5.11, 0-18)	0.875 (1.31, 0-3)

**Table 17. Information about patients' medication.**

Out of the 19 patients we assessed, 11 had been on stable medication for four weeks prior to taking part in the study.

<b>Patient</b>	<b>Medication</b>
1	Sumatriptan 10 mg, Albuterol 400 mg, Mirtazapine 15 mg
2	Zolmitriptan, Loratadine
3	Ethinyl Estradiol 30 mcg, Trimethoprim 400 mg
4	Ibuprofen 10g, Paracetamol 10g
5	Methylprednisolone with Lidocaine 40 mg/ml

6	Paracetamol 10 g, Mebeverine 405 mg, Prochlorperazine 15 mg
7	Formoterol 10 g, Albuterol 10 g, Prochlorperazine 10 g
8	Tamoxifen 20 mg, Venlafaxine 150 mg, Paracetamol and Codeine 10 g, Paracetamol 1000 mg, Bisoprolol 5 mg
9	Oxybutynin 1 mg, Desogestrel 10 g, Amitriptyline 10 mg
10	Budesonide and Formoterol 10 g, Medroxyprogesterone 10 mg
11	Citalopram 30 mg, Aspirin 75 mg, Mometasone spray, Topiramate 50 mg, Zopiclone 7.5 mg

#### 4.4.2. MRI data acquisition and processing

##### *Imaging protocol*

Complex mGRE data were acquired in a 7 Tesla MRI scanner (Siemens Healthineers, Erlangen, Germany), equipped with a 32-channel array-receive coil. A single mid-sagittal 5mm-thick slice was acquired, with in-plane field of view and resolution of  $256 \times 256 \text{mm}^2$  and  $1 \times 1 \text{mm}^2$ , respectively. Acquiring a relatively thick slice afforded higher SNR and greater robustness in terms of slice misalignments across scans. The first echo time, echo spacing, and repetition time were set to  $TE_1/\Delta TE/TR = 1.62/1.23/100 \text{ms}$ , the flip-angle of the RF excitation pulse was  $15^\circ$  and a total of 25 bipolar gradient echoes were acquired.

##### *Pre-processing steps*

The complex data were reconstructed per receive channel, followed by a complex multiplication of signals acquired with opposite read-gradient-polarities, in order to remove phase shift between adjacent echoes. Image-based coil-sensitivity-estimation was then used to perform coil combination. Frequency difference maps were calculated from the phase data to correct for linear non-local phase effects of the RF and  $B_0$  field inhomogeneities (Tendler & Bowtell, 2019). Finally, a 3<sup>rd</sup> degree spatial polynomial was fitted to the FDM data at each

echo to correct for the residual eddy current effects. Figure 23 summarises the pre-processing steps.



**Figure 23. Schematic representation of the processing pipeline.**

*Frequency difference mapping (FDM) allowed removal of the radio-frequency (RF)-related phase offsets and linear effect of large-length-scale field perturbations, without perturbing the local non-mono-exponential white matter signal.*

### **Signal analysis**

The corpus callosum was manually segmented from a magnitude mGRE image acquired at TE=15ms and further parcellated into anterior, middle and posterior portions as shown in Figure 24. Magnitude and FDM data were averaged over each callosal segment.

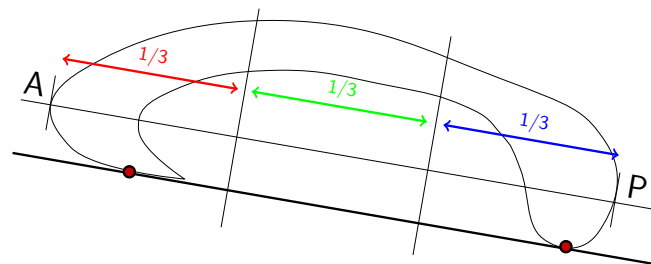


**Figure 24. Schematic representation of the callosal segmentation protocol.**

*The corpus callosum (CC) was segmented into three equal portions. Abbreviations: A = anterior; P = posterior.*

FDM and magnitude signal evolution from each callosal segment were modelled using a three-pool-model of complex signal evolution (Figure 8, Chapter 2), where myelin, intra-axonal and extra-axonal compartments each have different signal amplitudes, decay rates, and

frequency offsets (Cronin et al., 2017; Nam et al., 2015b; Nunes et al., 2017; Sati et al., 2013; Thapaliya et al., 2017):

$$S(t) = S_a(t) + S_e(t) + S_m(t) \sim f_a \cdot e^{\omega_a t} e^{-R_{2,a}^* t} + f_e \cdot e^{-R_{2,e}^* t} + f_m \cdot e^{\omega_m t} e^{-R_{2,m}^* t} .$$

Here, **a**, **e**, and **m** denote intra-, extra-axonal and myelin water and the complex mGRE signal **S(t)** is a superposition of their signals; **f** are the signal fractions, **ω** are the mean frequency offsets to the extra-axonal compartment, and **R<sub>2</sub><sup>\*</sup>** are the transverse relaxation rates. By including the frequency offset characteristics of the different water compartments (Sati et al., 2013; Wharton & Bowtell, 2012), this model offers reliable myelin water estimation (Nam et al., 2015b; Sati et al., 2013; van Gelderen et al., 2012).

**R<sub>2</sub><sup>\*</sup>**-values of the slow-decaying intra-axonal signal were constrained to 0 because of relatively low maximum TE (31ms). This constraint helped reducing the effect of the limited number of long TEs on the value estimation uncertainty at a cost of the potential under-/overestimation of the intra-/extra-axonal water signal fractions, respectively. Non-linear least-squares fitting was performed with initial parameter estimates and fitting boundaries based on previous literature (Sati et al., 2013; Tendler & Bowtell, 2019; Thapaliya et al., 2017; Wharton & Bowtell, 2012, 2013).

Pre-processing and signal analysis were performed in Matlab (Matlab, The Mathworks, Natick, MA).

#### 4.4.3. Cognitive tests

Cognitive performance was assessed in premanifest HD patients and age, sex and education matched healthy controls in the following tests: (1) the n-back task (Kirchner, 1958); (2) the digit span test from the Wechsler Adult Intelligence Scale-Revised (WAIS-R) (Wechsler,

1997); (3) the visual patterns test (Della Sala et al., 1997); (4) the Reading the Mind in the Eyes test (Baron-Cohen et al., 2001), hereafter referred to as the Eyes test; and (5) the speeded finger tapping task (Reitan & Wolfson, 2009). Tests (3) and (4) were administered as paper and pencil tests, tests (1), (2), (5), and (6) by using the computerized version provided by the Psychology Experiment Building Language (PEBL) Test Battery (Mueller & Piper, 2014). A description of each task's procedure has been provided in Chapter 3. In total, 6 cognitive outcome measures were obtained, which are summarised in Table 18.

**Table 18. Cognitive outcome variables employed to assess patient-control differences in cognition.**

*A short description of the task is provided, together with a list of outcome variables and cognitive domains assessed.*

<b>Task</b>	<b>Outcome variable</b>	<b>Cognitive process assessed</b>
N-back (Kirchner, 1958)	Percentage of correct responses in the 1) 1-back and 2) 2-back condition.	Encoding, temporary storage and updating of stored information with new upcoming information, inhibition of irrelevant items.
Digit span test from the WAIS-R (Wechsler, 1997)	Maximum span of digits recalled.	Verbal working-memory capacity.
Visual patterns test (Della Sala et al., 1997)	Maximum grid size recalled correctly.	Spatial working-memory capacity.
Eyes test (Baron-Cohen et al., 2001)	Number of emotional states correctly matched.	Social cognition and mentalising.
Speeded finger tapping task (Reitan & Wolfson, 2009)	Mean number of taps across 3 trials.	Motor speed.

#### 4.4.4. Statistical analysis

##### *Reproducibility study*

To assess the test-retest reproducibility of the data, the Fréchet distance (Fréchet, 1957) between FDM curves was obtained, to measure their similarity. This method takes into account the location and ordering of points along the curves. Specifically, given two curves, Q and P, the Fréchet distance is defined as the minimum cord-length sufficient to join a point traveling forward along P and one traveling forward along Q. Furthermore, the coefficients of variation (CVs, the ratio of the standard deviation to the mean) across the 5 visits were computed for  $f_m$ ,  $\omega_{a,m}$ , and  $\Delta\omega$  for each participant, for each segment. Finally, R package *cvequality* (Version 0.1.3, Marwick and Krishnamoorthy 2019) was used to compute the modified signed-likelihood ratio test for equality of CVs (Krishnamoorthy & Lee, 2014). This allowed to test for significant differences between the CVs across the three segments, for each metric.

##### *HD study*

As greater measurement reproducibility was detected in the posterior segment of the CC, this was chosen as area of interest for the assessment of patient-control differences in callosal myelin content. Age, but not TOPF-UK IQ, was found to be significantly correlated with both  $f_m$  and  $\Delta\omega$ , hence age was included as a covariate in the analysis of group effects.

Specifically, multiple regression analyses were run, assessing the effect of group, age, and a group-by-age interaction on  $f_m$  and  $\Delta\omega$ , in order to assess whether these metrics could disentangle age-related changes from pathologic HD-associated neurodegeneration. Regression diagnostics were performed and QQ plots and outlier profiles to detect any values above or below the upper/lower boundary of 95% confidence intervals of the slope of the regression line examined.

PCA was employed to reduce the complexity of the cognitive data and hence the problem of multiple comparisons, as well as to increase experimental power. The potential confounding effects of age or TOPF-UK IQ on the extracted components were examined. Age was included as a covariate in the model, which explored the effect of group, age, and a group-by-age interaction on the scores on the extracted components. Any significant effect was interpreted by referring to the variables with significant component loadings, as identified by values equal to or greater than 0.5 (Figure 29).

As a significant group effect was detected on  $f_m$ , Spearman rho correlation coefficients were calculated in patients between this metric, CAG, DBS, and scores on the first cognitive component (i.e. the component capturing the greatest amount of variability in the data), to assess disease-related brain-function relationships. Multiple comparisons correction was carried out with the Bonferroni correction with a family-wise alpha level of 5% (two-tailed). Significant correlations were further assessed with partial correlations to control for age as potentially mediating variable.

All statistical analyses were carried out in R Statistical Software (Foundation for Statistical Computing, Vienna, Austria) and Matlab (Matlab, The Mathworks, Natick, MA).

## **4.5. Results**

### **4.5.1. The precision of FDM in the corpus callosum is anatomically variable**

Figure 25 shows an example of FDM and magnitude signal evolution as a function of TE, for anterior/middle/posterior callosal segments, and the corresponding images at TE=15ms for five visits.

Analysis of curve similarity (Figure 26) and fitting parameter repeatability (Figure 27, Table 19) suggested greater reproducibility of measures in the posterior callosal portion as compared to the anterior sections. This is shown by generally lower Fréchet distance values and by overall low coefficients of variation calculated for the fitting parameters, which ranged between 3.72% and 12.02%, in this region (Table 19). The modified signed-likelihood ratio test for equality of CVs confirmed that CVs in the posterior callosal segment were significantly smaller across all measures [ $f_m$ :  $p = 0.021$ ;  $\omega_a/2\pi$  (Hz):  $p < 0.001$ ;  $\omega_m/2\pi$  (Hz):  $p < 0.001$ ;  $\Delta\omega/2\pi$  (Hz):  $p = 0.020$ ].

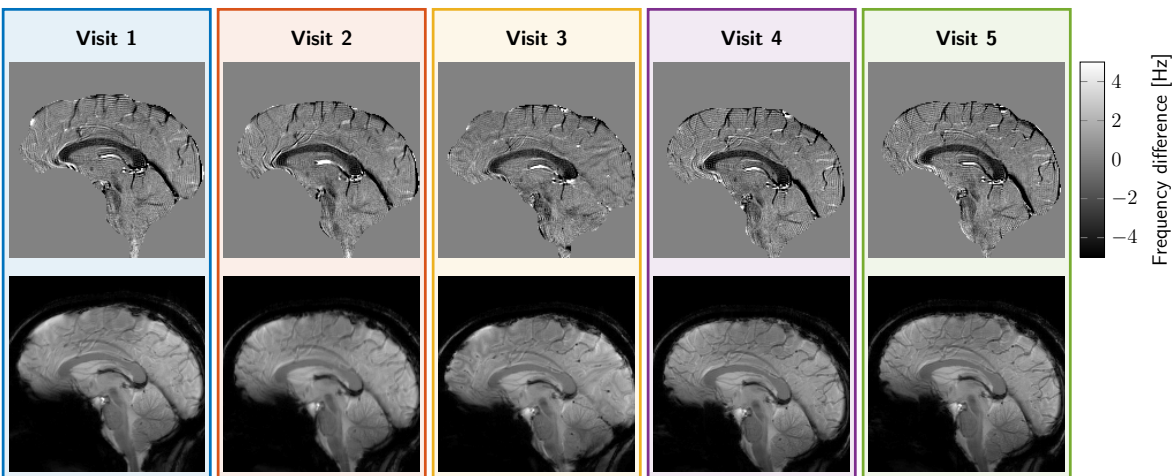
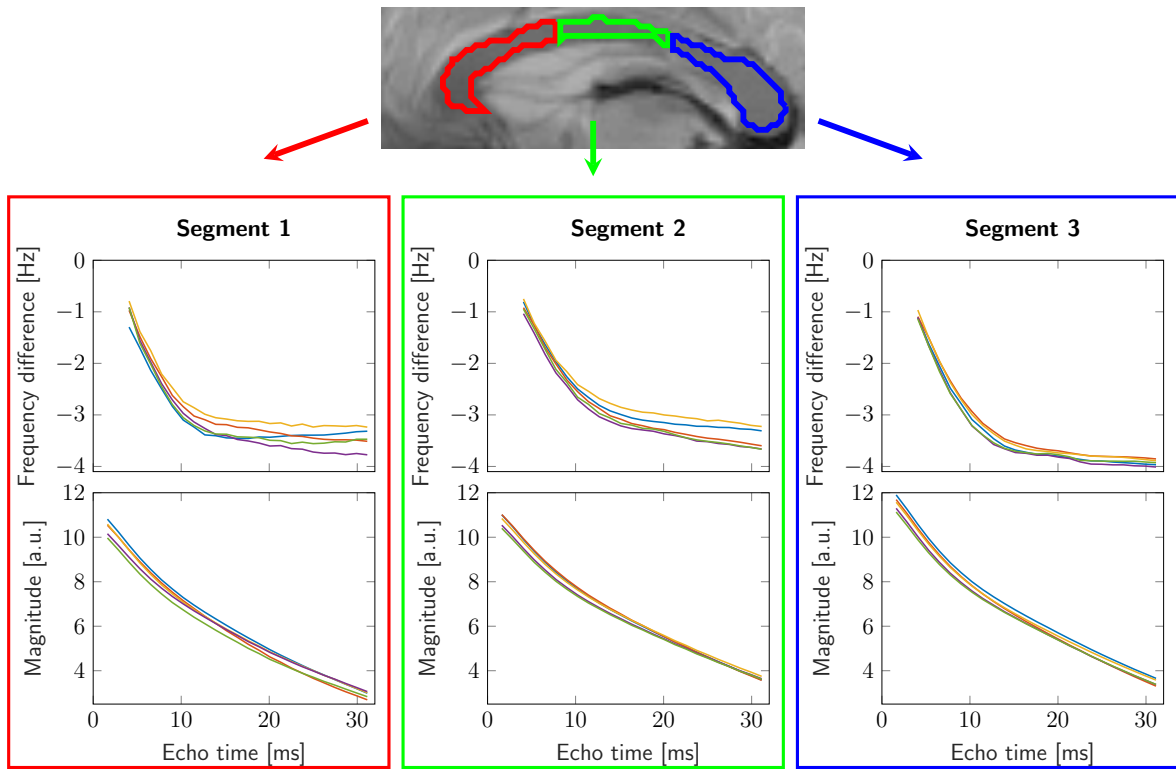


**Figure 25. Example reproducibility data from on representative subject.**

The top image shows callosal parcellation overlaid on a magnitude image; the plots show frequency difference and magnitude of signal as function of echo time (TE) for anterior/middle/posterior callosal segments; corresponding frequency difference and magnitude images at TE=15ms for five visits are shown at the bottom.

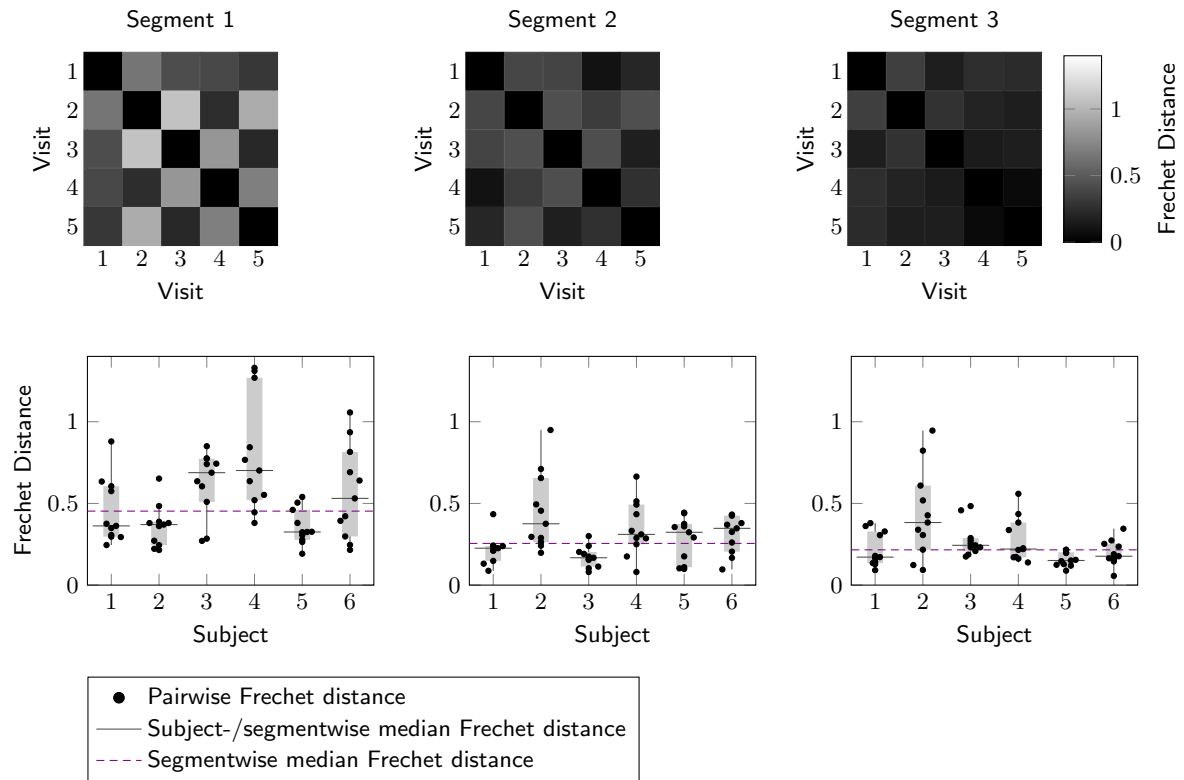


**Figure 26. Assessment of the similarity of frequency difference curves.**

*Top: Fréchet distance matrices from a representative participant for the three callosal segments. Bottom: Repeatability of frequency difference evolution across five visits for all subjects.*

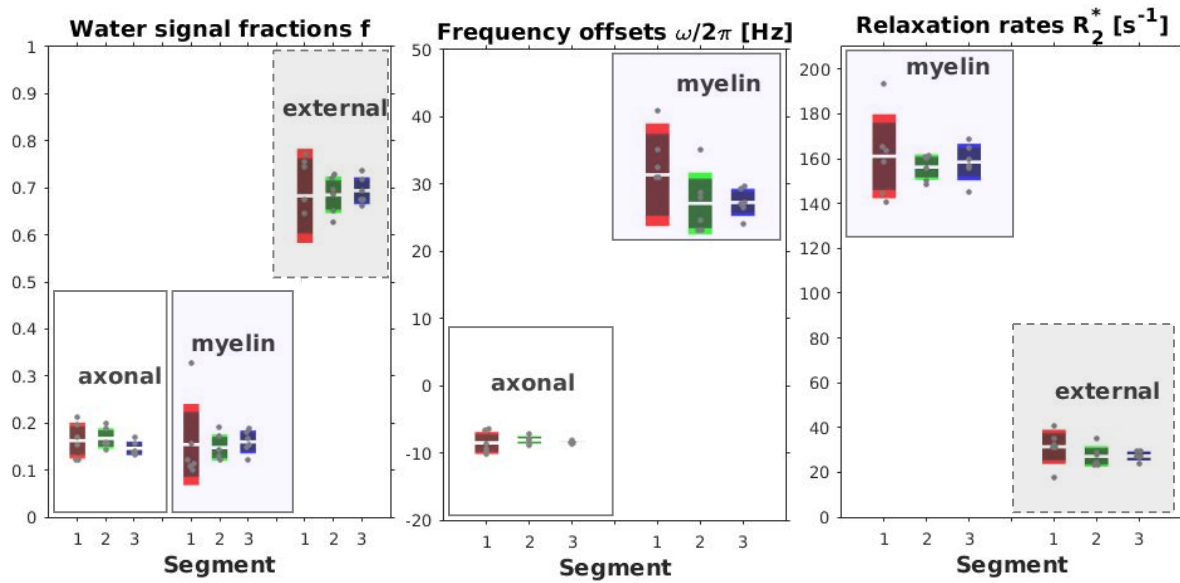


**Figure 27.** Fitting parameters estimated from the three-pool model, grouped for all subjects.

Colors represent the three callosal segments (red/green/blue for anterior/mid/posterior segments, respectively). The first plot shows signal fractions of myelin, intra-/extra-axonal water; the frequency offsets are displayed in the middle plot; the last plot shows the relation rates of myelin and extra-axonal water signals.

**Table 19. Coefficients of variation of the fitting parameters**

Reproducibility of myelin water signal fraction ( $f_m$ ), frequency offsets of axonal ( $\omega_a/2\pi$ ) and myelin ( $\omega_m/2\pi$ ) water pools, and difference in frequency offsets between myelin and axonal water pools ( $\Delta\omega/2\pi$ ). Means, standard deviation (SD) and coefficients of variation (CV) are reported for each value, across the different segments.

Metric	Callosal segment	Mean	SD	CV (%)
$f_m$	Segment 1	0.15	0.08	49.14
$\omega_a/2\pi$ (Hz)		-7.9	2.0	24.84
$\omega_m/2\pi$ (Hz)		27.1	10.2	37.01
$\Delta\omega/2\pi$ (Hz)		38.41	7.95	23.02
$f_m$	Segment 2	0.15	0.04	26.98
$\omega_a/2\pi$ (Hz)		-7.9	1.1	13.42
$\omega_m/2\pi$ (Hz)		27.1	4.4	16.60
$\Delta\omega/2\pi$ (Hz)		35.21	3.70	11.00
$f_m$	Segment 3	0.16	0.02	12.02
$\omega_a/2\pi$ (Hz)		-8.5	0.6	7.07
$\omega_m/2\pi$ (Hz)		27.3	2.1	7.61
$\Delta\omega/2\pi$ (Hz)		35.74	1.80	5.10

#### 4.5.2. FDM reveals HD-related myelin changes in the posterior segment of the CC

Figure 28 plots the relationship between age and  $f_m$ , and between age and  $\Delta\omega$ , split by group, in Segment 3 of the CC. Group and age explained 45% of the variance in  $f_m$  ( $R^2 = 0.45$ ,  $F(4, 35) = 7.18$ ,  $p < 0.001$ ). Specifically, it was found that group significantly predicted  $f_m$  values in this portion of the CC ( $\beta = -1.00$ ,  $p = 0.03$ ), as did age ( $\beta = -0.82$ ,  $p < 0.001$ ). However, no significant group-by-age interaction effect was detected ( $\beta = 0.82$ ,  $p = 0.08$ ). Overall, HD patients presented a flatter age-related variation in this metric, with values being overall lower, especially in younger subjects.

On the other hand, age and group explained 31% of the variance in  $\Delta\omega$  ( $R^2 = 0.31$ ,  $F(4, 35) = 3.87$ ,  $p = 0.01$ ). Age was found to be a significant predictor of variance in this metric ( $\beta = 0.55$ ,  $p = 0.009$ ), so that being older was associated with a greater  $\Delta\omega$  in this sample. However,

belonging to the patient or the control group did not have a significant effect on this measure ( $\beta = 0.13, p = 0.823$ ).

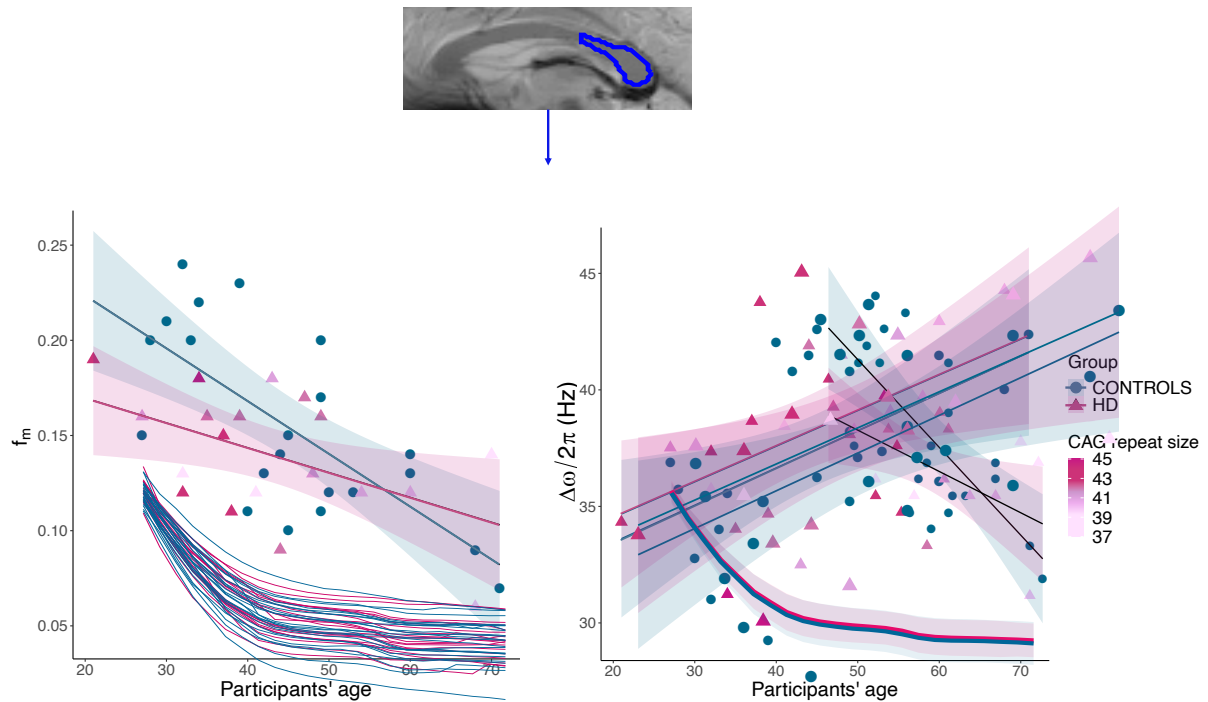


**Figure 28.** Relationship between age and the myelin water signal fraction ( $f_m$ ), and between age and the frequency offsets between myelin and axonal water pools ( $\Delta\omega$ ) in the posterior callosal segment, split by group.

*Top: Parcellation of segment 3 of the corpus callosum (CC) overlaid on a magnitude image; for parcellation, the same protocol as the one detailed in the reproducibility study section was utilized. Left: Regression plot showing the relationship between age and  $f_m$ , split by group. Both age and group were significant predictors of variance in  $f_m$ . No significant interaction effect was detected. Right: Regression plot showing the relationship between age and  $\Delta\omega$ , split by group. Age was a significant predictor in the model, while group did not significantly predict variance in this metric. No significant interaction effect was detected. HD data points are colored by cytosine-adenine-guanine (CAG) repeat size: older HD carriers presented shorter CAG repeat mutation and a trend for a greater overlap in  $f_m$  with values of age-matched healthy controls, indicating that CAG repeat size may directly affect myelin content in premanifest HD.*

### **4.5.3. Premanifest HD is associated with greater age-related decline in executive functions**

With PCA of cognitive test scores, three components were extracted that explained 77.7% of the variability in performance in the administered tests (Figure 29). The first component loaded positively on variables from the n-back task, and was therefore summarized as “executive function/updating” component. Principal component 2 (PC2) was summarised as “visuo-spatial motor function” component. Finally, PC3 was summarized as “verbal working memory capacity” component as this loaded mostly on the digit span task.

No significant main effect of group (although a trend was present) ( $\beta = 1.9$ ,  $p = 0.059$ ) or age ( $\beta = 0.004$ ,  $p = 0.815$ ) on the executive function/updating component was detected, but a significant interaction effect was present between group and age [ $\beta = -0.06$ ,  $p = 0.006$ ,  $R^2 = 0.52$ ,  $F(3,28) = 10.6$ ,  $p = 0.006$ ], indicating that while younger HD patients presented executive function scores which tended to overlap with those of healthy controls, the gap in performance between the two groups was significantly larger in older participants (Figure 30, left).

On the other hand, the main effects of group ( $\beta = -1.71$ ,  $p = 0.232$ ) and age ( $\beta = -0.036$ ,  $p = 0.142$ ), and the interaction effect between group and age ( $\beta = 0.03$ ,  $p = 0.311$ ) on the visuo-spatial motor function component were not significant [ $R^2 = 0.09$ ,  $F(3,28) = 0.94$ ,  $p = 0.432$ ]. Similarly, there was not a significant main effect of group ( $\beta = 0.03$ ,  $p = 0.821$ ) and age ( $\beta = 0.03$ ,  $p = 0.15$ ), nor a significant interaction effect between group and age ( $\beta = -0.003$ ,  $p = 0.911$ ) on the verbal working memory capacity component [ $R^2 = 0.14$ ,  $F(3,28) = 1.63$ ,  $p = 0.201$ ].

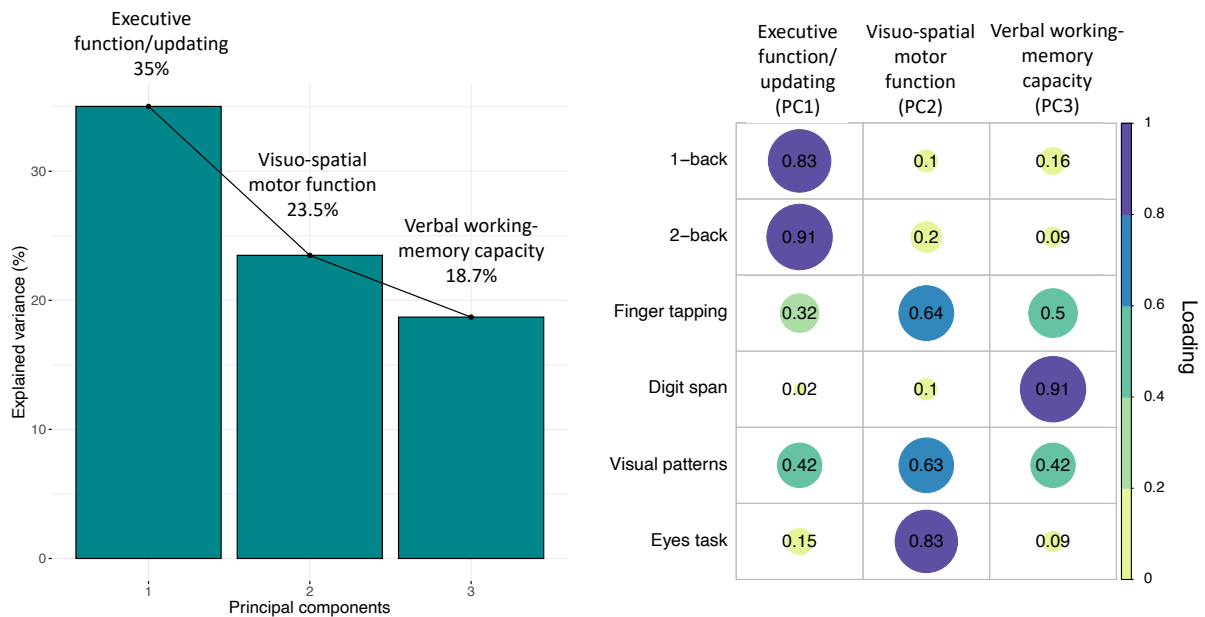


**Figure 29. Principal component analysis (PCA) of the cognitive data with varimax rotation.**

Left: PCA scree plot. Right: Plot summarizing how each variable is accounted for in every principal component (PC). The absolute correlation coefficient is plotted. Color intensity and the size of the circles are proportional to the loading. Three components explaining over 77% of the data variability were extracted. PC1 loaded on n-back task performance and was therefore summarized as “executive function” component; PC2 was summarized as “visuo-spatial motor function” component; PC3 loaded on digit span task performance and was therefore summarized as “working memory” component. 7 control cases did not complete all tests and were therefore excluded from the PCA. The final sample size for the PCA was  $n=19$  for the HD group and  $n=14$  for the control group.

#### 4.5.4. Interindividual differences in myelin content in the posterior callosum relate to executive function but not to proximity to disease onset in premanifest HD patients

There was a significant positive correlation between the patients’ inter-individual variation in  $f_m$  and their scores on the executive component ( $r = 0.54$ ,  $p = 0.011$ , corrected  $p = 0.041$ ) (Figure 30, right); although a positive trend remained, this relationship was no longer significant after partialling out age ( $r = 0.37$ ,  $p = 0.131$ ). Additionally, there was no association between inter-individual variation in  $f_m$  and proximity to disease onset as measured with DBS ( $r = -0.09$ ,  $p = 0.682$ , corrected  $p = 1$ ), nor inter-individual variation in  $f_m$  and CAG repeat size ( $r = 0.36$ ,  $p = 0.131$ , corrected  $p = 0.392$ ).

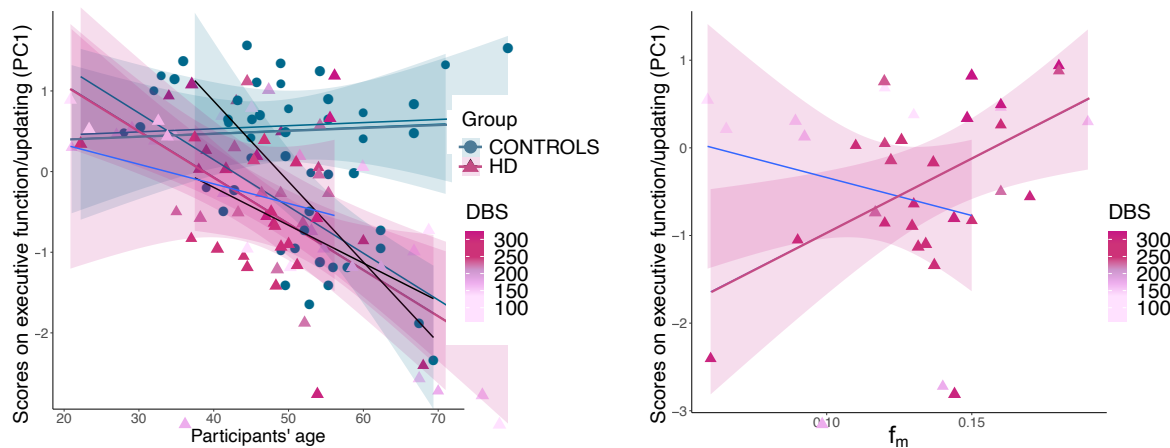


**Figure 30. Relationship of executive function with age and myelin water signal fraction ( $f_m$ ).**

*Left: Relationship between executive function scores and age, in patients and controls. A significant interaction effect between group and age was detected, suggesting that the group difference in executive function scores is larger at later ages. HD data points are colored by disease burden score (DBS). Older HD patients tend to be closer to disease onset, possibly confounding the effect of age on this measure. Right: Relationship between  $f_m$  and executive function scores in patients. Data points are colored by DBS. A significant positive correlation was found between  $f_m$  and executive function scores.*

## 4.6. Discussion

### 4.6.1. Reproducibility of the FDM signal across the CC

The reproducibility of FDM in the CC was found to be anatomically variable, and fitting parameters were shown to be more precise in the posterior callosal portion. Lower reproducibility of the data in the anterior portions of the CC could be attributed to in-flow artifacts from the anterior cerebral artery (Nam et al., 2015a; Tandler & Bowtell, 2019). Potential solutions and their limitations have been discussed in previous work, such as the application of flow saturation RF pulses to the inferior portion of the head (Nam et al., 2015a).

The estimated fitting parameters for the intra-axonal and myelin water frequency offsets ( -7.9 to -8.5 Hz and 27.1 to 37.4 Hz, respectively) and the myelin water signal fraction

(0.15 to 0.16) were consistent with previously reported values (Sati et al., 2013; Tendler & Bowtell, 2019; Thapaliya et al., 2017; Wharton & Bowtell, 2012). On the other hand, the relative signal fraction between intra- and extra-axonal compartments was lower than in other studies (Tendler & Bowtell, 2019). This could be attributed to the constraint placed on the intra-axonal water  $R_2^*$  when modelling the data, which was introduced in order to reduce the effect of the limited number of long TEs on the value estimation uncertainty.

#### **4.6.2. Application of FDM to assess myelin content in premanifest HD**

Significantly lower  $f_m$  values were observed in premanifest HD patients compared to healthy controls, suggesting the presence myelin impairment (Bartzokis et al., 2007). Previous animal studies have already shown a link between HD pathology and changes in myelin-associated biological processes at the cellular and molecular level (Bardile et al. 2018; Huang et al. 2015; Jin et al. 2015; Teo et al. 2016). Crucially, however, previous *in vivo* investigations of WM changes in HD have predominantly employed indices from DT-MRI (Pierpaoli and Basser 1996), or magnetization transfer ratio (MTR) imaging (Henkelman, Stanisz, and Graham 2001). These indices may be influenced by a multitude of processes affecting tissue microstructure and biochemistry (Beaulieu 2002; De Santis et al. 2014; Harsan et al. 2006; Wheeler-Kingshott and Cercignani 2009). In contrast, this study exploited FDM and a three-pool modelling of the mGRE signal to afford improved WM compartmental specificity, and estimate  $f_m$  as a marker of myelin content. Importantly, histological evidence shows that this metric is less sensitive to concomitant pathological processes such as inflammation (Gareau et al. 2000), suggesting that this may be a more specific measure of tissue myelination. These results highlight the potential of  $f_m$  in helping to better understand HD pathogenesis and progression, and gain further insight into the biological basis of WM microstructural changes in the HD brain. Additionally, they suggest the presence of demyelination of the posterior

callosum as an early feature of HD progression and are consistent with lower MTR values observed in this area in Chapter 3. Finally, these findings are consistent with evidence from a quantitative magnetisation transfer study (Bourbon-Teles et al., 2019), which demonstrated reductions in the macromolecular proton fraction - a myelin sensitive measure - in HD patients.

There was not a significant group effect on  $\Delta\omega$ , while this parameter was shown to significantly increase with age. Based on the model proposed by Wharton and Bowtell (2012), this might reflect two processes: i. the g-ratio decreases with age; ii. the magnetic susceptibility difference between the myelin sheath and the extra-axonal pool increases with age. The first suggestion contradicts previous studies showing increased g-ratio with age (Peters, 2009). However, as fibres with smaller diameters tend to have slightly lower g-ratios (Berthold et al., 1983), a selective loss of large-diameter axons would lead to an overall reduced voxel-averaged g-ratio (Cercignani et al., 2017). This scenario is a plausible explanation of the present finding, as fibres in the posterior portion of the CC are predominantly large and early myelinated (Aboitiz et al., 1992). Additionally, an increase in iron-containing glial cells in the surrounding extra-axonal space could result in the increase of the susceptibility difference between myelin sheath and the extra-axonal space. This is consistent with evidence showing that over the course of aging, iron accumulates in the brain (Connor et al., 1990; Dexter et al., 1991; Jellinger et al., 1990; Zecca et al., 2004).

With regards to the cognitive assessments, results from the present work indicate that executive functions, and specifically the updating of relevant information, tend to deteriorate to a larger extent with age in HD patients, compared to controls. Nevertheless, these results might have been confounded by stage of disease progression, as older participants presented a higher DBS. However, these results are consistent with the cognitive deficits detected in the study described in Chapter 3. Understanding the nature of cognitive deficits associated with HD pathogenesis and progression provide useful guidance for future research into the efficacy

of cognitive training and rehabilitation approaches in HD (Andrews et al., 2015). The present findings suggest that such approaches might be more effective early in the lifetime and in disease progression.

In the present study, it was also found that patients' inter-individual variability in  $f_m$  was positively associated with their scores on the executive/updating component. This is consistent with the positive association between apparent myelin and cognitive performance detected in Chapter 3. Although anterior, rather than posterior, callosal portions have been normally associated with frontal-lobe-mediated executive functions (e.g. Jokinen et al. 2007), posterior callosal fibres are connected to posterior parietal areas of the brain (Goldstein et al., 2020); these areas have been associated with top-down modulation during inhibition and attention processes (e.g. Erickson et al. 2009; Hopfinger, Buonocore, and Mangun 2000), which are recruited during maintenance and updating of relevant information. It is therefore plausible that microstructural variation in this callosal segment may impact performance in this cognitive domain. Additionally, although a positive trend remained, this relationship was no longer significant after partialling out age, stressing the important role of aging in both myelin content in the brain, and executive functioning (Grieve et al., 2007; Guttmann et al., 1998; Lintl & Braak, 1983; Pakkenberg et al., 2003).

Interestingly, no association was found between inter-individual variation in  $f_m$  and proximity to disease onset as measured with DBS. Again, this is consistent with the lack of association between apparent myelin variation in patients and DBS shown in Chapter 3. This suggests that myelin differences may precede the onset of clinical symptoms in HD, and may not directly relate to disease stages, pointing to a neurodevelopmental effect of the mutation on myelin content.

### 4.6.3. Conclusions, future directions and methodological considerations

In summary the present study exploited, for the first time in HD research, the sensitivity of FDM to quantify myelin changes in premanifest HD. Results stress the potential of this marker in helping to better understand HD pathogenesis and progression, and provide original *in vivo* evidence for reductions in  $f_m$ , a proxy MRI marker of myelin, in human premanifest HD. Expanding on evidence from pathology and animal studies, these results suggest that myelin breakdown is an early feature of HD progression.

The present findings were based on a relatively small sample size and warrant replication in larger samples. In addition, future studies should assess HD-related changes in  $f_m$  longitudinally rather than cross-sectionally, and investigate how these changes relate to clinical symptoms over time, to further understand the utility of this metric as a marker of early disease development and progression. Moreover, this study utilised a single-slice technique, and investigated a small portion of the CC, thus limiting the assessment of global diffuse tissue damage. Of special interest for future investigations might be to increase brain coverage and assess how  $f_m$  changes may differentially impact early and later myelinating regions in the premanifest HD brain. With regards to the observed increase of  $\Delta\omega$  with age, MR axon radius mapping using diffusion MRI and ultra-strong gradients (Veraart et al., 2020) may help elucidate whether a selective loss of large-diameter axons is producing this effect.

## **Chapter 5**

# **MRI assessment of WM microstructure in the R6/1 mouse model of HD: a high-resolution, *ex vivo* study**

### **5.1. Chapter summary**

The aim of this Chapter was to assess WM microstructure alterations in the transgenic R6/1 mouse model of HD. Processing and analyses methods similar to those used in the patient cohort in Chapter 3 were employed, to increase the translational validity of findings. Differences in the macromolecular proton fraction (MPF) from quantitative magnetization transfer (qMT) (Henkelman et al., 1993) as a proxy measure of myelin content, and the restricted volume fraction (FR) from CHARMED (Assaf & Basser, 2005) as a proxy marker of axon density (De Santis et al. 2014) were investigated *ex vivo* between R6/1 and age- and sex-matched WT littermates. Group differences in FA, AD and RD from DT-MRI (Pierpaoli and Basser 1996) were also assessed. A tractometry approach (Bells et al. 2011; Jones et al. 2005, 2006) was employed to investigate region-specific changes across the CC. Furthermore, voxel-based morphometry (VBM) and tract-based spatial statistics (TBSS) were used to explore brain-wise WM macro- and microstructure abnormalities in this model. Results were examined alongside transmission electron microscopy (TEM) results, with the aim to further elucidate the nature of WM alterations associated with this mouse line.

## 5.2. Declaration of collaborations

The development of the MRI protocol and the processing of the data was carried out with the support of Dr Greg Parker (Cardiff University). For the TEM analysis presented in this Chapter, the samples were processed and data were collected by Dr Christopher Von Ruhland at the Central Biotechnology Services in Cardiff University.

## 5.3. Introduction

The discovery of the mutation responsible for HD in 1993 (MacDonald et al., 1993) has allowed the generation of various animal models of this disease. Mice in particular, have been the mammal of choice for modelling disease-related phenotypes because of the skills we have acquired in manipulating their DNA. The study of animal models allows to move closer to a better understanding of the molecular and cellular mechanisms underlying disease pathogenesis and progression (Duty & Jenner, 2011). Critically, MRI studies on animal models enable greater translational validity through comparison of imaging findings in clinical populations and animal models of the respective disease (Hoyer et al., 2014), together with allowing validation of MR measurements with histological analysis.

This Chapter describes an MRI study of the R6/1 transgenic model of HD. The R6/1 and R6/2 mouse lines were the first transgenic mouse models developed to study HD. They both express *exon 1* of the human *HD* gene with approximately 115 and 150 CAG repeats, respectively (Mangiarini et al., 1996). Both R6/1 and R6/2 mice display a range of HD-like behavioural and regulatory changes that develop gradually. Any behavioural changes that occur in R6/2 mice seem to appear also in R6/1 mice, but the disease onset is delayed by several weeks in R6/1 mice, and there is a slower progression of the symptoms, due to shorter CAG

repeats and lower expression rate of the mutant transgene (31% *versus* 75%) (Mangiarini et al., 1996; Menalled, 2005).

R6/1 mice exhibit age-related progressive changes in both motor and cognitive performance from as early as 2-3 months of age (Brooks et al., 2012) and age-related GM brain atrophy and mutant huntingtin accumulation (Bayram-Weston et al., 2012). However, compared to the R6/2 line and other lines, fewer descriptions of the progressive pathologies exhibited by R6/1 mice exist, and the association between the molecular and cellular neuropathology with brain atrophy, and with the development of behavioural phenotypes, remains poorly understood in this model of HD. Crucially, despite evidence for GM pathology in R6/1 mice, no studies published so far have performed an MRI characterization WM microstructure alterations in this model. One previous study looking at gross volumetric changes in R6/1 mice, reported sparing of WM in this model, with no detectable differences in CC volume at either 9 or 17 weeks of age (Rattray et al., 2013). Hence, because of the lack of literature on pathological changes in brain structure in this model, findings in the present study will also be interpreted in light of previous findings from the R6/2 line.

The assessment of both macrostructural and microstructural changes in WM was performed *ex vivo* on the brains of 4 month old mice, to represent the early symptomatic stage of HD (Brooks et al., 2012; Rattray et al., 2013). *Post-mortem* imaging enabled longer scan times and limited the potential challenges commonly affecting live scanning, such as movement artefacts. This in turn allowed data to be acquired with higher resolution, signal-to-noise and contrast-to-noise ratio (Holmes et al., 2017). An effort was made to ensure that processing and analyses approaches were as similar as possible to those used in the patient cohort in Chapter 3, to increase the translational validity of findings.

Thus, WM microstructural differences in R6/1 mice were explored by combining FA, AD and RD from DT-MRI (Pierpaoli and Basser 1996), with MPF from qMT (Henkelman et al.,

1993) as a proxy measure of myelin, and FR from CHARMED (Assaf & Basser, 2005) as a proxy measure of axon density (De Santis et al. 2014), in an attempt to disentangle the contribution of changes in axon microstructure *versus* myelin to HD pathology. Importantly, MPF from qMT allowed improved sensitivity to myelin compared to MTR, which was measured in premanifest HD patients in Chapter 3 (Thiessen et al., 2013; Turati et al., 2015). Similar to the patient study, the analyses comprised tractometry assessments (Bells et al. 2011; Jones et al. 2005, 2006) of different segments of the CC and whole brain investigations of WM carried out with both VBM and TBSS approaches. Additionally, a strength of the present experimental work involved the ultrastructural characterization of axons in the CC using TEM, with the aim to complement the MRI assessment and to further elucidate WM alterations in this mouse model.

## **5.4. Materials and Methods**

### **5.4.1. Mice**

All experimental procedures in this study followed protocols in accordance with the United Kingdom Animals (Scientific Procedures) Act of 1986. All experimental procedures performed on mice were approved by Cardiff University Ethical Review Process Committee and carried out under Home Office License P49E8C976.

Twelve (12 weeks old) female hemizygous R6/1 mice were purchased from Jackson Laboratories (Jax®, Bar Harbour, Maine, U.S.A.) to be scanned at 16 weeks of age. This age-range was selected to represent the symptomatic stage of the disease. Twelve C57BL/6J female age-matched wild-type (WT) mice were purchased from Charles River.

Prior to the experiment, all animals were housed in age- and sex-matched groups of between 1 and 5 mice, with mixed genotype. Mice were subject to a 12-hour light:12-hour dark

cycle with controlled room temperature ( $21 \pm 3$  °C) and relative humidity ( $60 \pm 3\%$ ). Each cage contained modest environmental enrichment including play tunnels and nesting material. All animals were weighed on a weekly basis in order to monitor general health. A final sample of 7 WT and 8 R6/1 mice was examined in this study, due to fixation artifacts present in the other samples, which made them inadequate for quantitative data analysis (Cahill et al., 2012).

#### **5.4.2. Perfusion**

Mice were terminally anaesthetised *via* intraperitoneal injection of 0.3 ml Euthatal and then perfused through the left ventricle with approximately 60 ml of phosphate buffered saline (PBS). This was followed by infusion with about 150 ml of 4% paraformaldehyde (PFA) in PBS (pH 7.3) at a flow rate of 30 ml/min. The temperature of the perfusates was maintained at room temperature and the pH of the PFA was 7.2–7.4. After decapitation, the skulls were defleshed and post-fixed in 4% PFA in PBS overnight. They were then transferred to a 25% sucrose solution and stored at 4°.

#### **5.4.3. MRI tissue preparation**

Brains were scanned in-skull, in order to preserve neural structures. The skulls were soaked in chemical-grade PBS and washed daily for three days, to regain some signal due to tissue rehydration (Petiet et al., 2011). The skulls were then carefully wiped with tissue paper, and immersed in Galden, a proton-free susceptibility-matching fluid in a 15 ml syringe. The use of a syringe allowed any residual air bubbles to be pushed out, which might otherwise have affected MRI measurements. Immediately after scanning, skulls were returned to PBS and washed for three days, before being stored in a 25% sucrose - 0.1% sodium azide solution at 4°, to ensure tissue preservation.

#### 5.4.4. MRI data acquisition

MRI acquisition was conducted *ex vivo* on a 9.4 Tesla (20 cm) horizontal-bore animal system (Bruker Biospin, Germany). This was equipped with BGA12-S (12cm inner bore size, integrated shims) gradients. A transmit 1H 500 Watt echo-planar imaging (EPI) volume coil was used with a phased array 4-channel surface coil and Paravision software (version 6.1, Bruker Biospin) were used for data acquisition.

The magnetic field homogeneity was optimized with a localized shimming procedure (Fastmap, Bruker Biospin) on a volume of interest placed in the centre of the brain. A PRESS-waterline sequence (Bruker BioSpin) was used with outer volume suppression without water suppression to evaluate water line width (TR/TE = 2500/20 ms respectively) to assess the shim performance and the peak line width of the water signal. Iterations were repeated until all line widths < 40 Hz.

The acquisition protocol consisted of a T<sub>1</sub>-weighted FLASH sequence, a multi-shell dMRI acquisition for DTI and CHARMED, and an MT-weighted (MT-w) T<sub>1</sub> FLASH sequence. Additionally, the longitudinal relaxation rate of the system was estimated by acquiring T<sub>1</sub>-maps using T<sub>1</sub>-weighted FLASH images. A description of the acquisition parameters for each sequence is provided in Table 20.

**Table 20. Scan parameters.**

*All sequences were acquired at 9.4 Tesla. For each of the sequences, the main acquisition parameters are provided. MT: magnetization transfer; qMT: quantitative magnetization transfer. FoV: field of view; TE: echo time; TR: repetition time.*

<b>MRI acquisition parameters description</b>	
<b>Anatomical scan</b>	
<b>Pulse sequence</b>	FLASH (3D)
<b>Matrix size</b>	192×192×72
<b>FoV</b>	19.2×19.2×18

<b>Slice thickness (mm)</b>	-
<b>TE, TR (ms)</b>	4, 30
<b>Flip angle (°)</b>	36
<b>Acquisition duration</b>	20 min 44 s
<b>DTI/CHARMED</b>	
<b>Pulse sequence</b>	RARE
<b>Matrix size</b>	192×192
<b>FoV</b>	19.2×19.2
<b>b-values (s/mm<sup>2</sup>) – gradient directions</b>	0, 1200 – 50, 2400 – 50, 4000 – 50
<b>δ/Δ (ms)</b>	6.8/16.3
<b>Slice thickness (mm)</b>	0.4
<b>TE, TR (ms)</b>	31, 3000
<b>Flip angle (°)</b>	90
<b>Partial Fourier acceleration factor</b>	1
<b>Acquisition duration</b>	12h 14 min
<b>T<sub>1</sub> map</b>	
<b>Pulse sequence</b>	FLASH (3D)
<b>Matrix size</b>	192×192×72
<b>Fov</b>	19.2×19.2×18
<b>Slice thickness (mm)</b>	-
<b>TE, TR (ms)</b>	4, 30
<b>Flip angles (°)</b>	13, 17, 24, 36, 48
<b>Acquisition duration</b>	1 h 45 min
<b>MT/ qMT</b>	
<b>Pulse sequence</b>	FLASH 3D
<b>Matrix size</b>	192×192×72
<b>FoV</b>	19.2×19.2×18
<b>Slice thickness (mm)</b>	-
<b>TE, TR (ms)</b>	5, 47
<b>Off-resonance pulses (Hz/°)</b>	0/350, 1000/350, 1500/350, 3000/350, 6000/350, 12000/350, 24000/350, 1000/950, 1500/950, 3000/950, 6000/950, 12000/950, 24000/950
<b>Flip angles (°)</b>	5
<b>Acquisition duration</b>	9h 50 min

#### 5.4.5. Image processing

Skull stripping was performed using the Rodent Bet Brain Extraction Tool, a modified version of the Brain Extraction Tool (BET; FSL v5.0) that can process rodent brains (Wood et al., 2013).

### ***Anatomical data: T<sub>1</sub> volumes***

Processing of T<sub>1</sub> anatomical images was performed using SPM8 (Wellcome Trust Institute of Neurology, University College London, UK, [www.fil.ion.ucl.ac.uk/spm](http://www.fil.ion.ucl.ac.uk/spm)) with the SPMMouse toolbox (<http://spmmouse.org>) for animal brain morphometry (Sawiak et al., 2013). This toolbox extends SPM's functionality with affine registration priors for mouse and marmoset brains.

Specifically, a previously described mouse brain atlas (Sawiak et al., 2009) was used to register images from the brains of R6/1 mice with those of WT littermate controls. Following approximate manual registration using the SPM interface, images were bias-corrected and the affine priors supplied were used to register the images to the tissue probability maps. The registered images were then segmented to obtain GM, WM and CSF segmentations. The resulting WM segmentations were output in rigid template space and DARTEL (Ashburner, 2007) was used to create both non-linearly registered maps for each subject, and common templates for the cohort of animals. The warped WM portions for each mouse brain were modulated with the Jacobian determinant from the DARTEL registration fields to preserve tissue amounts, and smoothed with a Gaussian kernel of 400  $\mu\text{m}$  to produce maps for analysis (Gary et al., 2019).

### ***Diffusion data: FA, RD, AD and FR maps***

Pre-processing of DWI data was performed with various tools including FSL (Smith et al., 2004), MRtrix3 (Tournier et al., 2019), ExploreDTI (v.4.8.3) (Leemans et al., 2009), and ANTS (Avants et al., 2011). Each diffusion dataset was denoised (Veraart et al., 2016) and corrected for field distortion (Andersson et al., 2003) and Gibbs ringing artefacts (Kellner et al., 2016). Diffusion tensors were estimated using non-linearly weighted least squares (for  $b < 1500 \text{ s/mm}^2$  data) providing the following quantitative scalar measures: FA, AD and RD. Motion and distortion artefacts in the CHARMED data were corrected according to the

extrapolation method of Ben-Amitay, Jones, and Assaf (2012). FR maps (Assaf & Basser, 2005) were computed by fitting the CHARMED model to the DWI data, with an in-house software coded in MATLAB (The MathWorks, Natick, MA).

### ***Quantitative magnetization transfer: MPF maps***

MT-w images were corrected for Gibbs ringing artefacts (Kellner et al., 2016) and co-registered to the MT-w volume with the most contrast using an affine registration (FLIRT, 12 degrees of freedom, mutual information). Subsequently, the MT-w images and  $T_1$ -maps were modelled by the two-pool Ramani's pulsed MT approximation (Ramani et al., 2002). This provided MPF maps, which were nonlinearly registered to the  $b = 0$  s/mm<sup>2</sup> image using the MT-w volume with the most contrast as a reference, using FNIRT (Andersson et al., 2007). Accuracy of all registrations was confirmed by visual inspection.

### **5.4.6. Tractography of the CC**

Multi-shell, multi-tissue, constrained spherical deconvolution (MSMT-CSD) (Jeurissen et al., 2014) was applied to the pre-processed images to obtain voxel-wise estimates of fODFs (Descoteaux et al., 2008; Tournier et al., 2004, 2007) with maximal spherical harmonics order  $l_{max} = 8$ . The fODFs were generated using a set of 3-tissue group-averaged response functions (Dhollander et al., 2016). Seed points were positioned at the vertices of a  $0.2 \times 0.2 \times 0.2$  mm grid superimposed over the image. The tracking algorithm interpolated local fODF estimates at each seed point and then propagated 0.05 mm along orientations of each fODF lobe. This process was repeated until the minimally subtending peak magnitude fell below 0.05 or the change of direction between successive 0.05 mm steps exceeded an angle of  $40^\circ$ . Tracking was then repeated in the opposite direction from the initial seed point. Streamlines whose lengths were outside a range of 2 mm to 30 mm were discarded.

To assess regionally specific effect of HD on the CC, tractography was performed in three different callosal segments (genu, body and splenium). 3D fibre reconstructions were performed interactively in the native space of each mouse in FiberNavigator (Chamberland et al., 2014) (Figure 31), using a combination of include and exclude ROIs, according to the following protocols:

**Genu:** Two ROIs were placed anterolateral to the most rostral portion of the corpus callosum in each hemisphere. This approach was used to capture the anteriorly arching fibres of the genu (Catani and De Schotten, 2008). An exclusion ROI was used to exclude streamlines extending posteriorly to the genu on the sagittal plane, which make up the body of the CC.

**Body:** Two ROIs were placed ventral to the location of the cingulum and medial to the lateral ventricles (one in each hemisphere) (Catani and De Schotten, 2008). Exclusion ROIs were used to exclude the genu and splenium (i.e., the anterior and posterior sections of the CC, respectively).

**Splenium:** Two ROIs were placed posterolateral to the most caudal section on the CC in the left and right hemisphere (Catani and De Schotten, 2008). An exclusion ROI was used to remove streamlines extending anteriorly to the splenium.

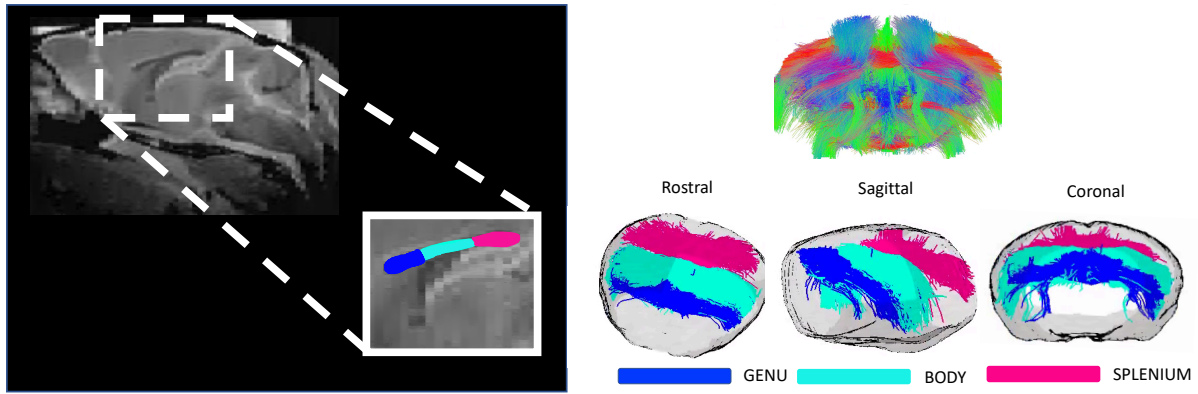


**Figure 31. Tractography of the corpus callosum (CC).**

*Left: Representative figure of manually delineated segments of the CC (genu, body, and splenium). Right: Coronal view of whole-brain tractography (top) and fibers travelling through the manually delineated region of interests (ROIs), in rostral, sagittal and coronal views (bottom).*

#### **5.4.7. Ultra-structural analysis of axons in the CC using TEM**

An ultra-structural analysis was conducted to look at axon diameter and g-ratio in R6/1 mice in the CC. The brains were embedded in TAAB embedding resin. Ultra-thin sections (50 nm) were stained with aqueous 4% uranyl acetate and lead citrate. The sections were visualised on a transmission electron microscope (CM12, Philips, the Netherlands). For quantification, images were taken using an on-axis 2048×2048 charge-coupled device camera (Proscan, Schering, Germany).

#### **5.4.8. Statistical analysis**

Statistical analyses were carried out using RStudio v1.1.456 (Team, 2015), MATLAB (The MathWorks, Natick, MA), SPSS version 20119 (Armonk, 2011), FSL (Smith et al., 2004) and the SPMMouse toolbox (<http://spmmouse.org>) for animal brain morphometry (Sawiak et al., 2013).

### ***Tractometry of the CC***

Microstructure differences were assessed in each of the three callosal segments. First, by taking each quantitative metric map (each registered to the  $b = 0$  s/mm<sup>2</sup> image during pre-processing), samples of each metric were obtained at each vertex of the reconstructed segments, and segment-specific medians were derived for FA, AD, RD, FR and MPF in MRtrix3 (Tournier, et al., 2019). Next, the overall mean was calculated, so that each dataset comprised 5 MRI-derived measures, mapped along 3 callosal segments.

### ***Investigation of group differences in callosal microstructure***

To assess group differences in callosal microstructure, the correlation of microstructure outcome measures with ICV was first tested to decide if this variable should be included as covariate in the analysis. As no Pearson's correlation coefficient greater than 0.3 was detected, this variable was not included in the analysis, and two-way mixed ANOVAs were run for each metric (i.e. FA, RD, AD, FR, MPF), with group as between-subject factor and segment as within-subject variable. The Tukey's Honest Significant Difference method was used to compute confidence intervals to further explore significant effects (Miller, 1981). Additionally, results were confirmed by running a robust mixed ANOVA, using the "bwtrim" R function from the WRS2 package (Mair & Wilcox, 2020). This implements robust methods for statistical estimation and therefore provides a good option to deal with data presenting small sample sizes, skewed distributions and outliers (Wilcox, 2011).

Across all analyses, outliers were first identified by examining box-and-whisker plots for each dependent variable, for WT and R6/1 mice separately. Outliers that were  $\pm 3$  standard deviations from the mean were then removed.

### ***Automatic evaluation of WM atrophy using VBM***

A general linear model to assess group differences in WM volume was evaluated using SPMMouse (Sawiak et al., 2013). For this analysis, ICV was included as a covariate of no interest as this was shown to improve estimation of volume differences in previous literature (Sawiak et al., 2013). Specifically, ICV was calculated as the sum of voxels identified as GM, WM and CSF in native space for each animal, to model out the effect of different brain sizes. The sum of the WM tissue probability maps was used as explicit mask in the analysis. An adjusted p-value was calculated to control the voxel-wise FDR (Benjamini and Hochberg, 1995).

### ***Assessment of brain-wise group differences in WM microstructure using TBSS***

In order to perform a whole-brain analysis of WM microstructure changes associated with HD, the TBSS protocol (Smith et al., 2006), modified for use in rodents (Sierra et al., 2011) was used. All FA maps were submitted to a free-search for a best registration target in order to minimize the image warping required for each brain volume. Specifically, each volume was first registered to every other volume, and the one requiring minimum transformation to be registered to other volumes was selected as the best registration target. This target was used as a template into which the registration was performed. Following registration, a mean FA map was calculated, thinned to represent a mean FA skeleton, and an optimal threshold of 0.2 was applied to the mean FA skeleton to create a binary WM skeleton mask. The application of such threshold allowed to exclude from further analysis areas of the brain of low FA, including peripheral small tracts, where there may be high between-subject variability and GM, and it is therefore unsafe to assume good tract correspondence across subjects (Smith et al., 2006).

The local FA-maximum was projected onto this WM skeleton. Subsequently, the voxel location of the local FA maximum was employed to project the respective AD, RD, FR and MPF values from that voxel onto the skeleton. Differences in microstructure measures between

the two groups were assessed using voxel-wise independent t-tests, where two +/- +/- different contrasts were used (WT > R6/1, and R6/1 > WT). The randomize function (part of FSL) was used, together with the TFCE algorithm (Smith & Nichols, 2009), generating cluster-size statistics based on 1000 random permutations. For multiple comparison correction, FWE correction was first used with a threshold of  $p < 0.05$ . Subsequently, in order to investigate more subtle changes, the analysis was repeated with the less conservative FDR correction (Benjamini and Hochberg, 1995), which has been previously used in rodent imaging data (Sagi et al., 2012; Sierra et al., 2011).

### ***Ultra-structural analysis of axons in the CC using transmission electron microscopy***

Five regions across genu and body of the CC were taken for quantification from randomly sampled 16.193  $\mu\text{m}^2$  electron micrographs (see Figure 36 for representative micrographs). The axon diameter of myelinated fibres and g-ratio (measure of myelin thickness relative to axon diameter) of myelinated axons were manually quantified using ImageJ (<https://imagej.net>) (Figure 32). Specifically, the inner and outer diameters were measured at the narrowest point of each axon, assuming them to be cylindrical, and thus having elliptical profiles. Where these were distorted, a best guess in the calculation was made. Two R6/1 brains were available for the analysis, and a total of 400 myelinated axons were analysed across these two samples.

As no samples from WT littermates were available for the analysis because of tissue degradation, measurements taken from R6/1 brains were compared to values for adult WT mice provided in the literature (West et al., 2015). Specifically, West and colleagues (2015) performed a quantitative analysis of the CC in WT mice and provided morphometric analysis of 72 electron microscopy images, with measures of axon diameter and g-ratio for the genu and the body of the CC. Here, the availability of the parameters of the  $\gamma$  -distribution [i.e.

characteristic shape ( $k$ ) and scale ( $\theta$ )] they utilised to describe both axon diameter and g-ratio distribution in their samples, as well as information about the mean and standard deviation for these two measures, was exploited to perform a statistical comparison with the values obtained from R6/1 brains.

First, it was tested whether the mean axon diameter and g-ratio for the two callosal areas obtained from R6/1 samples differed more than 2 times the standard deviation from the mean axon diameter and g-ratio reported in the study from West et al. (2015) [axon diameter: mean = 0.56  $\mu\text{m}$ , standard deviation = 0.32  $\mu\text{m}$  across all brains and image; g-ratio: mean = 0.82, standard deviation = 0.07]. This was chosen as cut-off based on the common practice to utilise such threshold to identify outliers in small samples. Subsequently, Kolmogorov-Smirnov (KS) tests were performed to assess whether the distributions of axon diameter and g-ratio values detected in this study were significantly different from the  $\gamma$ -distribution with shape ( $k$ ) and scale ( $\theta$ ) as defined in West et al. (2015) for each callosal region in WT brains [genu: axon diameter,  $k = 9.4$  and  $\theta = 0.059$ ; g-ratio,  $k = 305.1$  and  $\theta = 0.003$ ; body: axon diameter,  $k = 8.7$ ,  $\theta = 0.069$ ; g-ratio,  $k = 314.6$ ,  $\theta = 0.003$ ].

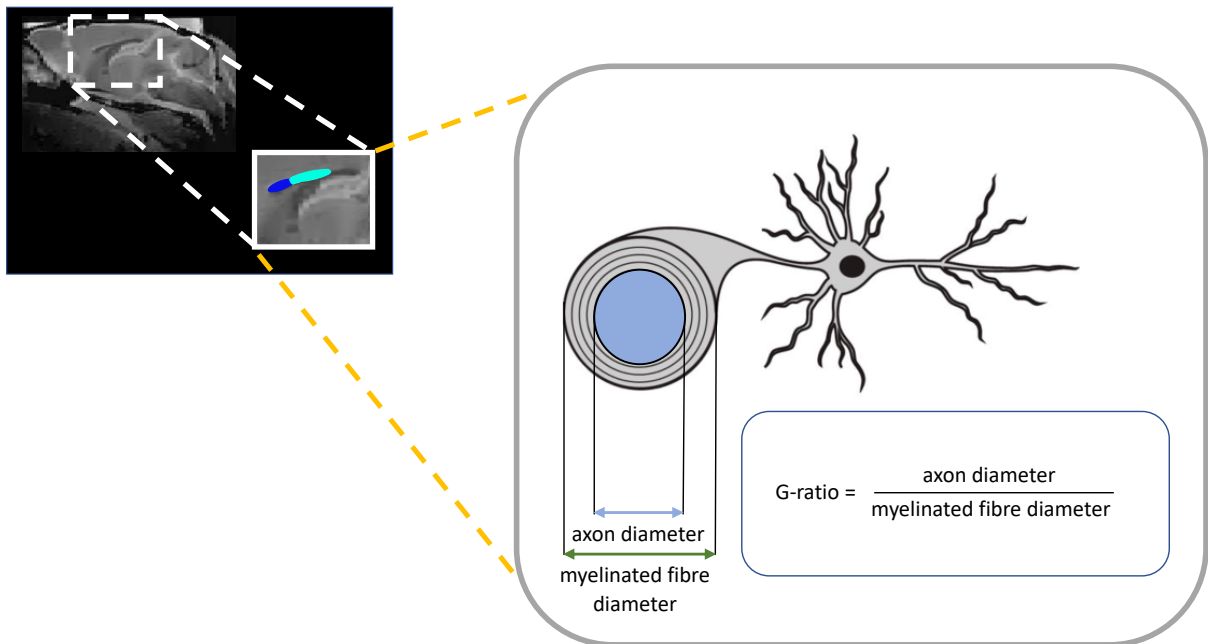


**Figure 32. Schematic illustration of the axon and myelin sheath, measurement of the axon diameter and g-ratio calculation.**

*A total of 400 myelinated axons from 2 R6/1 brains were analyzed.*

## 5.5. Results

### 5.5.1. R6/1 mice present alterations in apparent myelin and axon density across the CC

The mixed ANOVA for FA showed no significant effect of group [ $F(1, 39) = 0.123, p = 0.728$ ]. On the other hand, a significant effect of segment [ $F(2, 39) = 6.508, p = 0.004$ ] was detected, with the splenium showing significantly lower FA values compared to the genu ( $p = 0.04$ ) and body ( $p = 0.003$ ). No interaction effect between group and segment was present [ $F(2, 39) = 0.05, p = 0.952$ ]. Results from the robust mixed ANOVA were consistent with the above. Specifically, there was no effect of group ( $p = 0.592$ ) and no interaction ( $p = 0.991$ ), but a significant effect of segment ( $p = 0.023$ ).

The mixed ANOVA for RD showed no significant effect of group [ $F(1, 39) = 0.48, p = 0.491$ ], no significant effect of segment [ $F(2, 39) = 2.795, p = 0.072$ ], and no interaction effect between group and segment [ $F(2, 39) = 0.178, p = 0.838$ ]. The results from robust mixed ANOVA, however, showed a significant effect of segment ( $p = 0.003$ ), indicating higher RD values in the splenium compared to the body. No significant effect of group ( $p = 0.69$ ), nor a significant group-by-segment interaction ( $p = 0.750$ ) were detected.

The assessment of AD values did not show a significant effect of group [ $F(1, 39) = 0.487, p = 0.490$ ], segment [ $F(2, 39) = 1.695, p = 0.197$ ], or a group-by-segment interaction [ $F(2, 39) = 0.126, p = 0.882$ ]. The results from robust mixed ANOVA, however, showed a significant effect of segment ( $p = 0.012$ ), suggesting higher AD values in the splenium compared to the body. No significant effects of group ( $p = 0.732$ ), or group-by-segment interaction ( $p = 0.661$ ) were detected.

Significant main effects of group [ $F(1, 39) = 19.07, p < 0.001$ ] and segment [ $F(2, 39) = 11.05, p < 0.001$ ] on FR values were detected with the mixed ANOVA. Specifically, R6/1 mice presented overall higher FR values compared to WTs across all CC regions. The CC body presented lower FR values compared to the genu ( $p < 0.001$ ), and the splenium presented lower FR values compared to body ( $p = 0.006$ ). No significant group-by-segment interaction was detected [ $F(2, 39) = 0.328, p = 0.072$ ]. Consistent with these findings, the results from robust mixed ANOVA showed a significant effect of group ( $p = 0.032$ ) and segment ( $p < 0.001$ ), but not a significant group-by-segment interaction ( $p = 0.782$ ).

Finally, a significant effect of group on MPF was detected [ $F(1, 39) = 9.21, p = 0.004$ ], due to overall lower MPF values in R6/1 mice across the CC. No significant effect of segment was detected [ $F(2, 39) = 0.329, p = 0.722$ ], nor a significant group-by-segment interaction effect [ $F(2, 39) = 0.152, p = 0.861$ ]. The results from robust mixed ANOVA were consistent with the

findings by showing a significant effect of group ( $p = 0.052$ ), but no effect of segment ( $p = 0.171$ ), nor a significant group-by-segment interaction ( $p = 0.881$ ) (Figure 33).

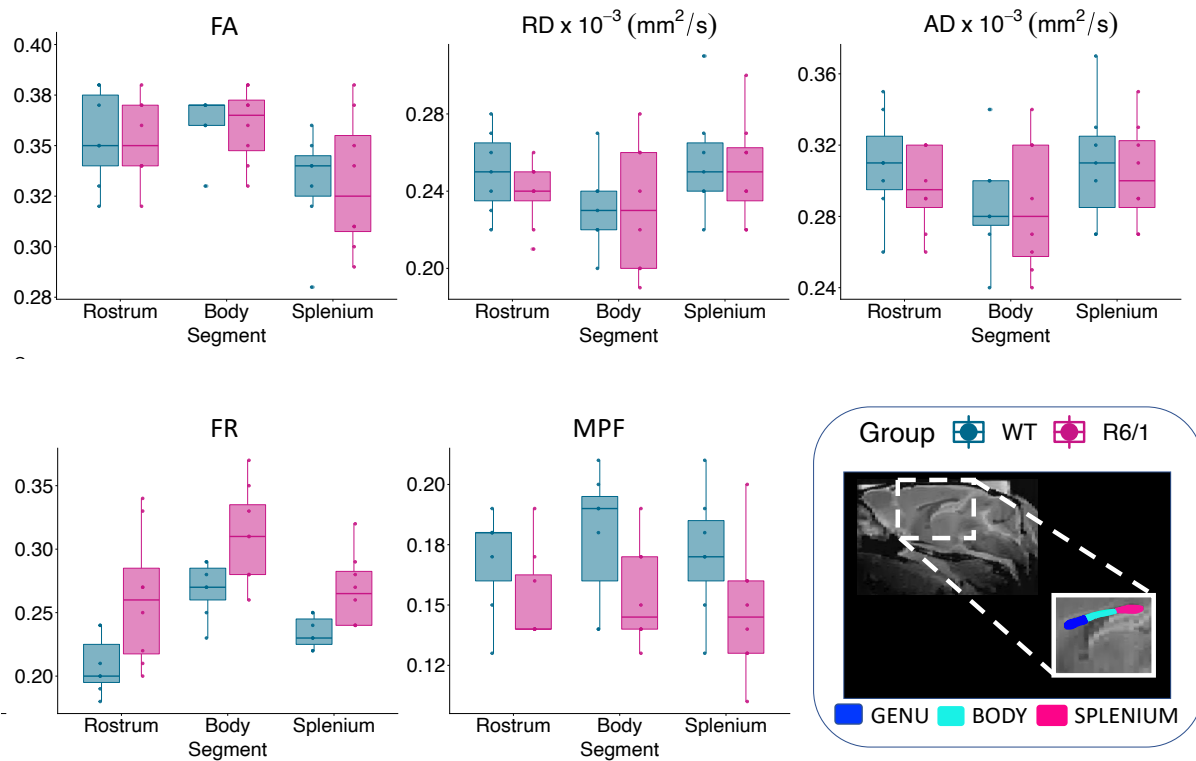


**Figure 33. Tractometry analysis of the corpus callosum (CC).**

Quantification of FA, RD, AD, FR, and MPF in the genu, body and splenium of the CC. FR values were significantly higher and MPF values significantly lower in the brain of R6/1 mice across the whole CC. No significant group effects were detected for the other measures. Abbreviations: FA: fractional anisotropy; RD: radial diffusivity; AD: axial diffusivity; FR: restricted volume fraction; MPF: macromolecular proton fraction.

### 5.5.2. R6/1 mice present areas of increased WM volume

Figure 34 shows regions where WM values were significantly higher in R6/1 brains than in WT controls ( $p < 0.05$ , FDR-corrected). Increased WM volume was detected in R6/1 mice in several areas such as the posterior callosum, external capsule and olfactory bulb.

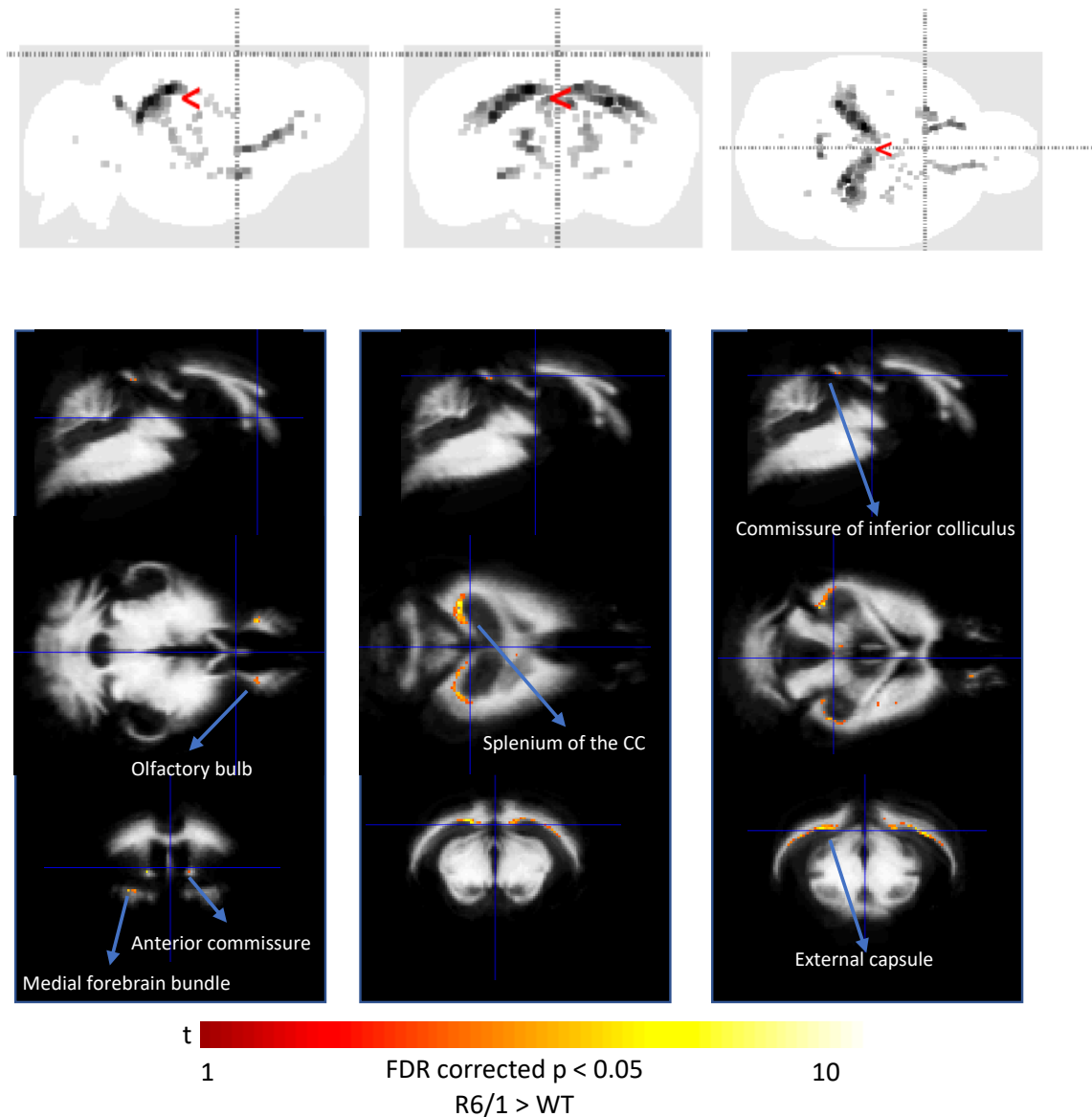


**Figure 34. Group-differences in white matter volume.**

*Top: Maximum intensity projections (MIPs). Bottom: Maps of the t-value (whole brain voxel analysis at  $p < 0.05$  False discovery rate-corrected for multiple comparisons) overlaid on template white matter map, demonstrating increased volume in several areas across the brain of R6/1 mice.*

### 5.5.3. TBSS reveals widespread increases in apparent axon density in R6/1 mice

At first, a highly conservative FWE correction method was used for the TBSS analysis. This approach showed widespread increases in FR in the WM of R6/1 mice (Figure 35, top). When the voxel-wise analysis was repeated using a less conservative FDR correction of 5%

(Benjamin and Hochberg, 1995), additional WM changes were detected, including more extended increases in FR and some decreases in MPF in R6/1 brains (Figure 35, bottom).

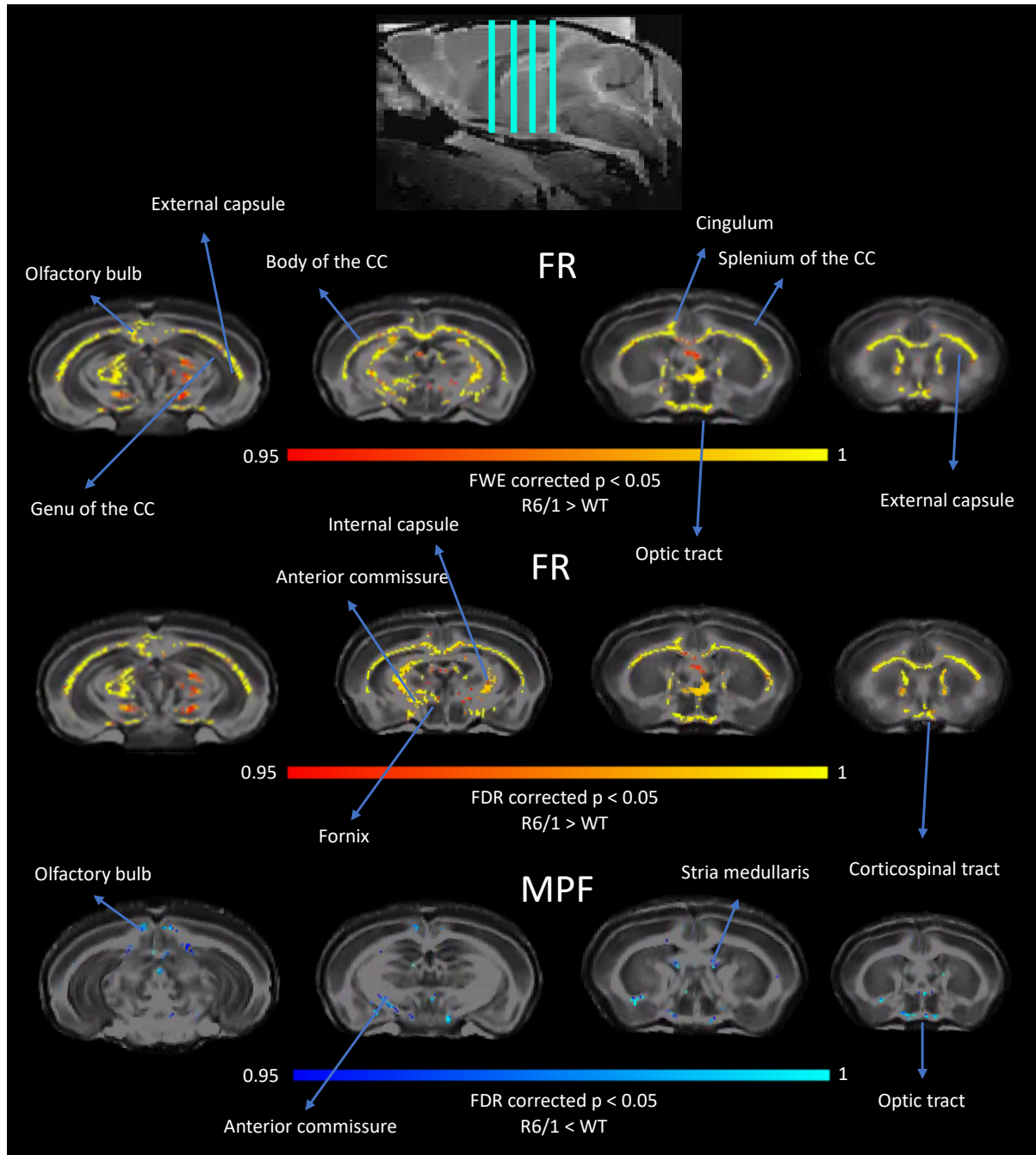


**Figure 35. Tract-based spatial statistics (TBSS) analysis of white matter microstructure in R6/1 mice.**

White matter microstructural alterations were detected across the brain of R6/1 mice. Family-wise error (FWE) multiple comparisons correction was applied first, revealing widespread increases in FR (top row). Subsequently, a less conservative false discovery rate (FDR) correction of 5% was used,

*again revealing widespread increases in FR and some areas of decreased MPF (middle and bottom rows). Abbreviations: FR: restricted volume fraction. MPF: macromolecular proton fraction.*

#### **5.5.4. The frequency distribution of myelinated axon diameters is skewed towards thinner axons in R6/1 mice**

In the present work, a mean axon diameter of 0.40  $\mu\text{m}$  was detected for both the genu (standard deviation = 0.15  $\mu\text{m}$ ) and the body (standard deviation = 0.14  $\mu\text{m}$ ). Additionally, the mean g-ratio was 0.74 both for the genu (standard deviation = 0.07  $\mu\text{m}$ ) and for the body (standard deviation = 0.08  $\mu\text{m}$ ). None of these values differed more than 2 standard deviations from the mean measurements obtained in WT mice in West et al. (2015). On the other hand, the K-S tests revealed that the distributions of values were significantly different from the ones of WT mice for both axon diameter [genu:  $D = 1$ ,  $p < 0.001$ ; body:  $D = 0.49$ ,  $p < 0.001$ ] and g-ratio [genu:  $D = 1$ ,  $p < 0.001$ ; body:  $D = 1$ ,  $p < 0.001$ ] (Figure 36), revealing that these distributions were left-skewed in R6/1 mice compared to WT mice. Additionally, the relationship between axon diameter and g-ratio exhibited a curved shape seen in previous studies (Little and Heath 1994; West et al. 2015).

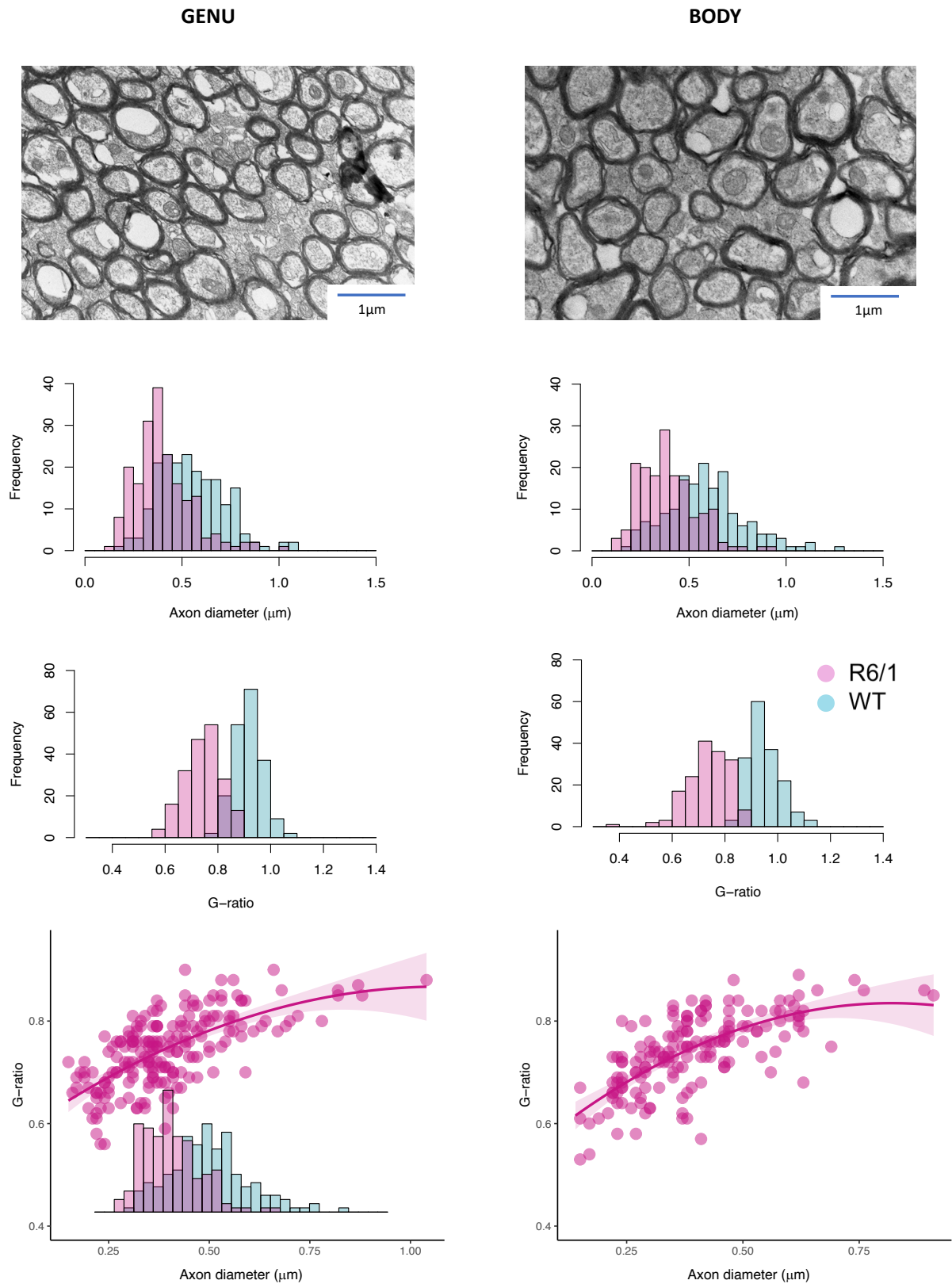


**Figure 36. Ultra-structural analysis of axons in the corpus callosum (CC) using transmission electron microscopy.**

Top: Representative electron micrographs of axons in the genu and body of R6/1 mice. Scale bars = 2 μm. Middle: Axon diameter and g-ratio distributions in the genu and body of R6/1 and wild-type (WT) mice. The data for WT mice was taken from West et al. (2015). For visualization, the function

“*rgamma*” from R was utilized to randomly generate the  $\gamma$ -distribution with characteristic shape ( $k$ ) and scale ( $\theta$ ), as provided in West et al. (2015). R6/1 mice presented a higher proportion of thinner axons and smaller  $g$ -ratio. Bottom:  $g$ -ratio versus axon diameter scatter plots from the genu and body of R6/1 mice. The relationship between axon diameter and  $g$ -ratio exhibited a curved shape seen in some previous studies (Little & Heath, 1994; West et al., 2015).

## 5.6. Discussion

The present Chapter describes a high-resolution *ex vivo* MRI assessment of 4 month old R6/1 mice and reports novel findings of WM alterations in this model of HD. While GM alterations, together with cognitive and behavioural deficits, have already been demonstrated and described (Bayram-Weston et al., 2012; Brooks et al., 2012; Rattray et al., 2013), this is the first study to characterize WM microstructure alterations in this HD model.

An initial assessment of WM microstructural changes across the CC using a tractometry approach (Bells et al. 2011; Jones et al. 2005, 2006) revealed increased FR and decreased MPF in R6/1 mice, compared to WT littermates, across the callosum. The subsequent brain-wise assessment of WM changes with VBM showed areas of increased WM volume in R6/1 mice. This was accompanied by widespread increases in FR, together with some regional decreases in MPF, as detected with TBSS. In order to explore the cellular causes underlying the imaging phenotype, brain tissue ultrastructure from the R6/1 mouse line was analysed using TEM. This analysis indicated that the frequency distribution of myelinated axon diameters was skewed towards thinner axons in R6/1 mice.

It is possible that shrinkage of the extra-axonal space in the absence of axonal loss led to an increase in apparent axon density in R6/1 brains. Accordingly, previous evidence has shown no cell death in R6/1 mice at 7.5 months of age, nor alterations in the density of the immunochemical staining for the NeuN protein (Fox-3, Rbfox3, or Hexaribonucleotide Binding Protein-3), considered to be a biomarker for neurons (Naver et al., 2003). Another

study demonstrated that R6/1 mice do not show neuronal loss before 19 weeks of age, and this loss predominantly affects male R6/1 mice (Ratray et al., 2013). Additionally, previous evidence has shown that, although the brains of 12 week old R6/2 mice weigh around 20% less than brains from WT controls, and the volume of the striatum is reduced by 17% in 18 week old R6/1 mice, this marked reduction in brain volume is not accompanied by cell death (Li et al., 2005). Furthermore, evidence from R6/2 mice (Ratray et al., 2013) demonstrated tissue atrophy, possibly caused by loss of microglia and extra-cellular matrix molecules (Ma et al., 2003; Ratray et al., 2013), in the absence of neuronal loss.

However, increased WM volume in areas partially overlapping with regions of increased FR was detected in R6/1 brains in this study. These findings indicate that WM atrophy is unlikely to explain the alterations in FR observed in R6/1 mice. Interestingly, the presence of brain oedema and tissue swelling, which occur in the disease (De Paepe et al., 2019), has been shown to bias brain atrophy measurements (Andravizou et al., 2019). Accordingly, swelling of glial cells and neurons may explain the widespread increases FR observed in R6/1 mice, by reducing extracellular fluid and thus causing reduced diffusion in the extra-axonal space (Arfanakis et al., 2002; Stidworthy et al., 2003). Consistent with this suggestion, previous studies have demonstrated a striking increase in axonal swelling in a knock-in model of HD, showing to precede cell body, dendrite, and synapse degeneration (Marangoni et al., 2014). Although Marangoni and colleagues (2014) only detected a non-significant trend in increased swellings in R6/2 mice, it might be that the slower progression of the disease in R6/1 mice allowed for morphologic signs of axonal degeneration to be detected in this study.

Alternatively, increased FR and WM volume may be a reflection of increased axon numbers. However, the decrease in MPF detected across the R6/1 brains suggests that, if it is true that R6/1 mice present increased axon number, such increase either concerns unmyelinated

axons or it is accompanied by pathological de-myelination. Additionally, based on the TEM results, neurons in R6/1 mice present an increased number of thinner axons compared to WT littermates. These results are consistent with previous evidence of morphological alterations in the neurons of symptomatic R6/2 mice, which present smaller diameter dendritic shafts, smaller somatic cross-sectional areas, and decreased diameter of the dendritic fields (Klapstein et al., 2001).

It might be that axons in this model develop normally but then shrink because of the disease process. However, it might also be that R6/1 mice present abnormalities in the postnatal development of axons and studies assessing axon microstructure in R6/1 mice earlier in development will be useful in assessing such possibility. Consistent with a developmental effect of the mutation, evidence shows that neurotypical development is associated with an increase in thick axons relative to thinner ones, which in turn tend to be present in a higher proportion early in life (Zikopoulos et al., 2018). Additionally, deficient myelination during the early postnatal period has previously been detected in the R6/2 mouse model of HD, suggesting that abnormalities in axon myelination occur very early in HD pathogenesis (Xiang et al., 2011). Critically, the observed decrease in MPF in the brain of R6/1 mice is consistent with evidence of myelin impairment in this model. This in turn suggests that the concomitant decreased g-ratio observed in R6/1 mice is not due to enhanced myelination. Rather, a skewed distribution towards smaller g-ratios might be due to an underrepresentation of large-calibre axons.

To summarize, the present findings suggest that: i. R6/1 mice present thinner myelinated axons, ii. R6/1 mice may present swelling of glial cells and/or neurons, and/or iii. R6/1 mice present increased density of axons. However, the latter likely concerns unmyelinated axons, because of the concomitant decreases in MPF observed in R6/1 mice. It is possible that these findings reflect the outcome of pathological processes associated with the mutation;

alternatively, they might reflect abnormalities in the development of WM. Although this cannot be determined from the here presented cross-sectional data, the idea that mutant huntingtin may affect development is not new (Mehler & Gokhan, 2000; Nguyen et al., 2013). Therefore, longitudinal studies on this model are needed to replicate such results, and to establish the time-course of these abnormalities in the disease process, together with their correlation with cellular and molecular changes, as well as behavioural impairments.

Critically, these results extend findings obtained from previous research and from the studies on premanifest HD patients described in Chapters 3 and 4, all of which demonstrate alterations in WM microstructure as a significant feature of HD. Importantly, such alterations seem to involve both axon microstructure and myelin in this mouse model of HD. Convergence of human and rodent findings, together with their importance in terms of a translational approach to the study of WM changes in HD are further considered in the General Discussion.

### **5.6.1. Methodological considerations**

The present data were obtained *ex vivo* from fixed tissue. As several factors, such as tissue fixation, sample temperature, and the acquisition scheme all have an effect on MRI measures, considerable care should be taken when extrapolating the present *ex vivo* findings to *in vivo* values (Antonsen et al., 2013). However, the observed group differences should be valid, since any bias in terms of methodology should have the same effect of the two groups compared. Furthermore, in the present study, several steps were taken with regards to the perfusion and tissue preparation protocols in order to obtain optimal tissue quality. Such procedures were based on previous literature (Cahill et al., 2012), and consisted in the utilisation of liquid, rather than powder, perfusates, as well as delivery of perfusate at a low flow rate, in order to avoid blockage of the capillary beds and vessels' rupture. Additionally, the storage of tissue in a sodium azide solution enabled improved tissue conservation.

A direct comparison of TEM data between R6/1 and WT mice could not be carried out in the present study. Instead, comparisons were performed based on data available from existing literature (West et al., 2015). Although processing and analysis of TEM data in this study was carried out following West and colleagues (2015) protocols as closely as possible (e.g. section thickness, measures assessed), it is plausible that between-studies differences may have affected the TEM findings. Therefore, these results require replication with an appropriate WT control sample.

It also has to be noted that, although FR has been referred to as a marker of apparent axon density in the literature (De Santis et al., 2014) and throughout this work, no formal link has actually been established between histological measures of axon density and FR. Additionally, as already mentioned in Chapter 3, the estimation of FR is affected by changes in  $T_2$  relaxation, meaning that a change in  $T_2$  relaxation (for example because of altered tissue water or myelin content) may be interpreted as a difference in FR when this measure was actually not altered. To gain a better insight into the axon microstructure changes observed in this study, future work could assess apparent fiber density changes at high diffusion-weightings, to increase suppression of the extra-axonal signal. This approach was recently shown to enable a better characterization of microstructural changes, because of the improved correspondence with intra-axonal properties (Genc et al., 2020; Kleban et al., 2020; McKinnon & Jensen, 2019).

# **Chapter 6**

## **Drumming motor sequence training induces apparent myelin remodelling in HD patients**

### **6.1. Chapter summary**

The aim of this final experimental Chapter was to investigate whether drumming training stimulates WM remodelling in manifest HD patients, and whether training-associated microstructural changes are related to improvements in motor and cognitive function. Patients with HD and age- and sex-matched controls undertook two months of drumming training exercises. WM microstructure, working memory and executive function were assessed before and after the training. Changes in WM microstructure were investigated with DT-MRI-based metrics (Basser & Jones, 2002; Pierpaoli & Basser, 1996), FR from CHARMED (Assaf & Basser, 2005) and MPF from qMT (Sled 2018). WM pathways linking the putamen and the supplementary motor area (SMA-Putamen), and three segments of the CC (CCI, CCII, CCIII) were studied using deterministic tractography. Baseline MPF differences between patients and controls were also assessed, using TBSS.

### **6.2. Declaration of collaborations**

The work described in this Chapter was part of a broader project funded by a Wellcome Trust Institutional Strategic Support Fund Award (ref: 506408) to Dr Claudia Metzler-Baddeley, Prof Anne Rosser, and Prof Derek K Jones. Recruitment of HD patients and matched healthy controls, as well as data collection for this study, were carried out by Dr Bourbon-Teles (Cardiff University). Dr Sonya Bells (Cardiff University) processed the qMT data.

### 6.3. Introduction

HD is caused by a single-gene and is therefore an ideal model to study neurodegeneration as a whole, and test for possible beneficial interventions that can slow or suppress disease onset. Despite this, and numerous clinical trials, at present no disease-modifying treatment is approved for patients with HD. Recent developments in gene therapy targeting *mHTT* expression have generated much excitement. However, these have yet to be proved to lead to measurable changes in disease progression (Barker & Mason, 2019). Furthermore, a number of questions linger, for example on the relative strength of different approaches, the importance of specifically targeting *mHTT* and the possible side effects of each therapy (Shannon, 2020). Importantly, these treatments aim to modify and not cure the disease, and while symptomatic therapies for HD are present, and are used for treating chorea and some of the psychiatric symptoms, their effectiveness varies between patients, and may lead to clinically significant side-effects (Barker & Mason, 2019). This stresses the need to develop better symptomatic therapies to aid patients and manage HD symptoms.

Environmental stimulation and behavioural interventions may have the potential to reduce disease progression and delay disease onset (Wood et al., 2011; Yhnell et al., 2016, 2018). Furthermore, previous studies have detected training-related changes in the WM of both healthy controls (Caeyenberghs et al., 2016) and clinical populations, including HD patients (Metzler-Baddeley et al., 2014). For example, DT MRI studies have shown microstructural WM changes following balance training in healthy (Taubert et al., 2011) and traumatic brain injury young adults (Drijkoningen et al., 2014). Other imaging studies have shown DT MRI changes as a result of juggling (Scholz et al., 2009), abacus training (Hu et al., 2011), extensive piano practice (Bengtsson et al., 2005; Han et al., 2009), working memory training (Takeuchi et al., 2010), reasoning training (Mackey et al., 2012), and meditation training (Tang et al., 2012).

Converging evidence implicates myelin plasticity as one of the routes by which experience shapes brain structure and function (Caeyenberghs et al., 2018; Gibson et al., 2014; Lakhani et al., 2016; Mensch et al., 2015; Sampaio-Baptista et al., 2013; Scholz et al., 2009). Plastic changes in myelination may be implicated in early adaptation and longer-term consolidation and improvement in motor tasks (Costa et al., 2004; Shmuelof & Krakauer, 2011; Steele et al., 2013; Yin et al., 2009). Changes in myelin-producing oligodendrocytes and in GM and WM microstructure have been reported within the first hours of skill acquisition (Sagi et al., 2012; Xiao et al., 2016), implying that experience can be quickly translated into adaptive changes in the brain.

This Chapter presents experimental work assessing whether two months of drumming training can trigger WM microstructure changes, and potentially myelin remodelling, in individuals with HD. The present training intervention was designed to exercise cognitive and motor functions, including sequence and reversal learning, response speed and multi-tasking (Metzler-Baddeley et al., 2014), all of which rely on healthy functioning of cortico-basal ganglia loops that are known to be impaired in HD (Han et al., 2010; Papoutsis et al., 2014). In brief, the intervention involves practising drumming patterns in ascending order of difficulty over a two-month period, and was previously found to induce WM changes in HD (Metzler-Baddeley et al., 2014). Based on reports of larger training-associated changes in structural MRI metrics in patient populations than in healthy subjects (Caeyenberghs et al., 2018), I hypothesised that changes in *microstructural* metrics would be more marked in patients than in healthy subjects.

Previous WM plasticity neuroimaging studies (Giacosa et al., 2016; Scholz et al., 2009) have predominantly employed indices from DT-MRI (Pierpaoli & Basser, 1996). To improve compartmental specificity beyond DT-MRI, the present study explored changes in the MPF from qMT (Sled, 2018) and FR from CHARMED (Assaf & Basser, 2005). FA and RD from

DT-MRI (Pierpaoli & Basser, 1996) were included for comparability with previous training studies (Lövdén et al., 2010; Scholz et al., 2009; Zatorre et al., 2012).

The MPF has been proposed as a proxy MRI marker of myelin (Serres et al., 2009). Accordingly, histology studies show that this measure reflects demyelination accurately in Shiverer mice (Ou et al., 2009), is sensitive to de-myelination in multiple sclerosis patients (Levesque et al., 2010) and reflects WM myelin content in post-mortem studies of multiple sclerosis brains (Schmierer et al., 2007). FR, on the other hand, represents the fraction of signal-attenuation that can be attributed to restricted diffusion, which is presumed to be predominantly intra-axonal, and therefore provides a proxy measure of axonal density (Barazany et al., 2009).

Training effects were investigated in WM pathways linking the putamen and the supplementary motor area (SMA-Putamen), and within three segments of the CC (CCI, CCII, CCIII). The SMA has efferent and afferent projections to the primary motor cortex and is involved in movement execution; previous work has reported altered DT-MRI metrics in the putamen-motor tracts of symptomatic HD patients (Poudel et al., 2014). The anterior and anterior-mid sections of the CC contain fibres connecting the motor, premotor and supplementary motor areas in each hemisphere (Hofer & Frahm, 2006). Previous work has demonstrated a thinning of the CC in post-mortem HD brains (Vonsattel & Difiglia, 1998), altered callosal DT-MRI metrics in both pre-symptomatic and symptomatic HD patients (Rosas et al., 2010; Phillips et al., 2013), and a correlation between these metrics and performance on motor function tests (Dumas et al., 2012).

Given previous reports of an effect of motor learning on myelin plasticity (Lakhani et al., 2016), changes following training were expected to be more marked in MPF, as compared to the other non-myelin sensitive metrics assessed in this study. Additionally, the relationship between training-associated changes in MRI measures, and changes in drumming performance and cognitive/executive function was also investigated. Finally, as previous evidence has

shown widespread reductions in MPF in premanifest and manifest HD patients (Bourbon-Teles et al., 2017), TBSS (Smith et al., 2006) was employed to investigate patient-control differences in MPF before training, across the whole brain; this aided the interpretation of the detected post-training microstructure changes.

## **6.4. Materials and Methods**

### **6.4.1. Participants**

Fifteen HD patients and thirteen age, sex, and education-matched healthy controls were recruited. The study was approved by the local National Health Service (NHS) Research Ethics Committee (Wales REC 1 13/WA/0326) and by the Cardiff University School of Psychology Ethics Committee, and procedures were carried out in accordance with the 1964 Helsinki declaration. HD patients were recruited from the Cardiff HD Research and Management clinic and the Bristol Brain Centre at Southmead Hospital. Healthy controls were recruited from Cardiff University, the School of Psychology community panel, and from patients' spouses or family members.

In order to be included in the study, subjects had to be drumming novices and to not have taken part in the previously-reported pilot study (Metzler-Baddeley et al., 2014). Additionally, they needed to have no history of head injury, stroke or cerebral haemorrhages, and to be eligible for MRI scanning i.e. to not present contraindications such as pacemakers, metal clips, stents or significant chorea which would have prevented them from lying still in the scanner. Control participants were excluded if they had a history of neurological or psychiatric conditions, and patients if they had a history of any other neurological condition.

Similar to the studies described in Chapters 3 and 4, consent was taken upon arrival at the imaging centre, where the information sheets were discussed and an opportunity to ask any further questions was provided, before participants were asked to read and sign the consent forms. Participants were informed of their right to withdraw from the study at any point without giving a reason, and were informed that they could request that their data be destroyed and not included in the study.

Of the recruited sample, two patients were not MRI compatible, four withdrew during the study and one patient's MRI data had to be excluded due to excessive motion. Therefore, while drumming performance and cognitive data from 11 patients were assessed, only 8 patients had a complete MRI dataset. One control participant was excluded due to an incidental MRI finding, two participants dropped out of the study and a fourth participant was not eligible for MRI. In total, drumming and cognitive tests performance was assessed in 8 controls, while MRI data from nine controls were available for analyses. Table 21 summarizes patients demographic and background clinical characteristics. Most patients were at early disease stages, however two were more advanced, as shown by their Total Motor Score (TMS; 69 and 40, respectively) and Functional Assessment Score (FAS; 18 and 17, respectively). Table 22 summarizes demographic variables and performance in the MoCA (Nasreddine et al., 2005) and the revised National Adult Reading Test (NART-R) (Nelson, 1991) for patients and controls. While the groups did not differ significantly in age, controls were on average slightly older, performed significantly better on the MoCA, and had a significantly higher NART-IQ than patients.

***Table 21. Demographics and background clinical information of the patients' cohort.***

*Based on TMS and FAS, most of the patients were at early disease stages, however two of them were more advanced. Abbreviations: CAG = cytosine-adenine-guanine; TMS = Total Motor Score out of 124 (the higher the scores the more impaired the performance); FAS = Functional Assessment Score out of 25 (the higher the scores the better the performance); SD = Standard Deviation.*

	<b>Age</b>	<b>CAG</b>	<b>TMS</b>	<b>FAS</b>
<b>Mean (Range)</b>	48.5 (22-68)	43.6 (40-51)	18.7 (0-69)	22.6 (17-25)
<b>SD</b>	15.6	3.5	24.7	3.3

**Table 22. Demographics and general cognitive profile of patients and controls.**

Both groups were matched for age, sex and years of education but the patient group had a lower NART-IQ and performed less well than the control group in the MoCA. Abbreviations: NART-IQ = verbal IQ estimate based on the National Adult Reading Test; MoCA = Montreal Cognitive Assessment score out of 30.

<b>Mean (SD, range)</b>	<b>Patients (n = 8)</b>	<b>Controls (n = 9)</b>	<b>p-value</b>
<b>Age</b>	48.5 (15.62, 22-68)	52.6 (14.56, 22-68)	p > 0.5
<b>NART-IQ</b>	106.3 (13.13, 94-123)	121.22 4.32, 117-128	p = 0.006
<b>MoCA</b>	23 (5.6, 14-29)	27.67 (1, 26-29)	p = 0.036

#### **6.4.2. Training intervention: Drumming-based rhythm exercises**

The rhythm exercise and drumming training described previously in Metzler-Baddeley et al. (2014) was applied. Participants were provided with twenty-two 15 min training sessions on CDs, a pair of Bongo drums and a drumming diary and could practise at home. They were asked to exercise for 15 min per day, 5 times per week, for 2 months and to record the date and time of each exercise in their diary. Each training session introduced a drumming pattern based on one of the following rhythms: Brazilian samba, Spanish rumba, West-African kuku and Cuban son. After a brief warm up, trainees were encouraged to drum along with the instructor, initially with each hand separately and then with both hands alternating, starting with the dominant hand first and then reversing the order of the hands. The first exercises were based on very simple, slow, and regular patterns but the level of complexity and speed increased over the training sessions.

Importantly, each individual progressed through the training adaptively at their own pace i.e., as long as they exercised for the specified time, they could repeat each session as often as they felt necessary to master it. To maintain engagement and motivation, the training incorporated pieces of music based on rhythms participants had learned and could drum along to. The researcher (Dr Bourbon-Teles) supervised the first training sessions and then remained in regular telephone contact (at least once a week) with each participant throughout the intervention. Whenever possible, carers and/or spouses were involved in the study to support the training. Control participants started with Session 3 since the first two exercises were built on a very low level of complexity, with slow, regular patterns of movement required, and were therefore designed for patients

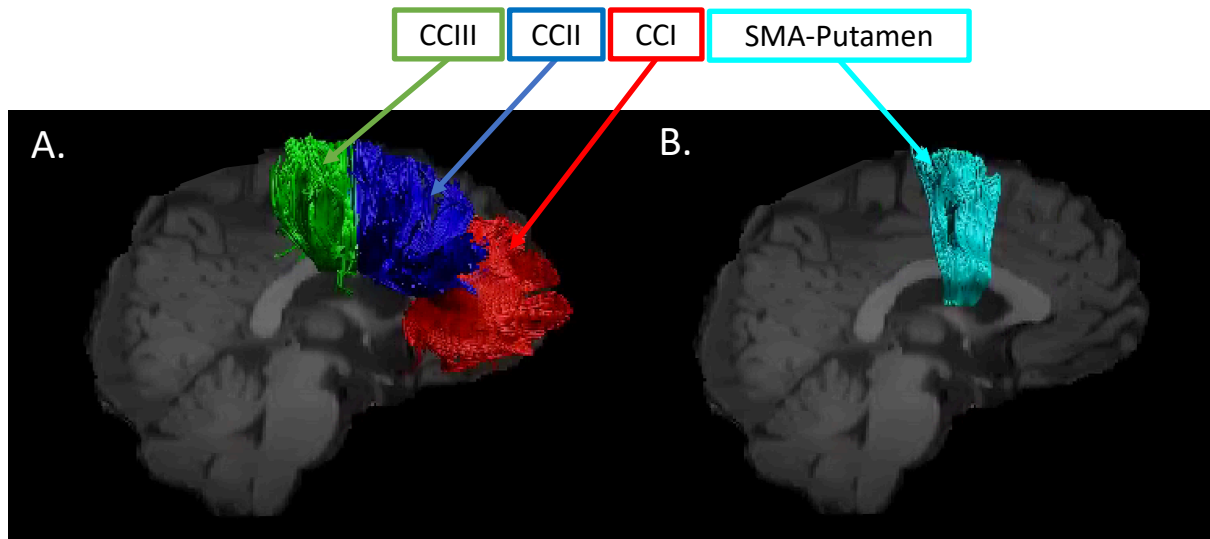


**Figure 37. White matter pathway regions of interest.**

*Sagittal views of the reconstructed white matter pathways displayed on a  $T_1$ -weighted image for one control participant. (A) CCI, CCII, and CCIII (Hofer and Frahm, 2006): CCI is the most anterior portion of the CC and maintains prefrontal connections between both hemispheres; CCII is the portion that maintains connections between premotor and supplementary motor areas of both hemispheres. CCIII maintains connections between primary motor cortices of both hemispheres. (B) Supplementary motor area (SMA)-putamen pathway: this pathway has efferent and afferent projections to the primary motor cortex and is involved in movement execution.*

### 6.4.3. Drumming assessment

Progress in drumming ability was assessed by digitally recording participants' drumming performance for three patterns of ascending levels of difficulty (easy, medium and hard), which were not part of the training sessions, at baseline and after the training. Each recording was judged by an independent rater, blind to group and time, according to an adopted version of the Trinity College London marking criteria for percussion (2016) ([www.trinitycollege.com](http://www.trinitycollege.com)).

### 6.4.4. Cognitive assessments

Different aspects of cognition and executive function were assessed before and after the training as described in Metzler-Baddeley et al. (2014). Multi-tasking was assessed with a dual task requiring simultaneous box crossing and digit-sequences repetition (Baddeley, 1996).

Attention switching was assessed with the trails test (VT) requiring the verbal generation of letter and digit sequences in alternate order relative to a baseline condition of generating letter or digit sequences only (Baddeley, 1996). Distractor suppression was tested with the Stroop task involving the naming of incongruent ink colours of colour words (Trenerry et al., 1989). Verbal and category fluency were tested using the letter cues “F”, “A”, “S” and “M”, “C”, “R” as well as the categories of “animals” and “boys’ names” and “supermarket items” and “girls’ names” respectively (Baldo et al., 2001). In total, 7 outcome variables were assessed (Table 23), and percentage change scores in performance were computed for each of these variables.

**Table 23. Cognitive outcome variables assessed in this study.**

*Tests were carried out before and after the training, and a percentage change score was computed for each variable.*

<b>Task</b>	<b>Outcome variables</b>	<b>Description</b>
Simultaneous box crossing and digit sequences repetition (Baddeley, 1996)	Correct digits recalled under single task condition; correct digits recalled under dual task conditions; boxes identified under dual task condition.	Correct number of recalled digits in a standard digit span test; correct number of recalled digits in the dual condition; number of boxes identified in the dual condition.
Stroop test (Trenerry et al., 1989)	Stroop interference score.	Calculated by subtracting the number of errors from the total number of items presented in the test.
Trials test (Baddeley, 1996)	Trail test switching.	Performance accuracy: reflects the ability of moving flexibly from one set of rules to another in response to changing task requirements.
Verbal and category fluency test (Delis et al., 2001)	Verbal and category fluency.	Number of generated words starting with the following letters: “F”, “A”, “S” and “M”, “C”, “R”; number of generated words belonging to the following categories: “animals” and “boys’ names” and “supermarket items” and “girls’ names”.

#### 6.4.5. MRI data acquisition

MRI data were acquired on a 3 Tesla General Electric HDx MRI system (GE Medical Systems, Milwaukee) using an eight channel receive-only head RF coil at the Cardiff University Brain Research Imaging Centre (CUBRIC). The MRI protocol comprised the following images sequences: a high-resolution fast spoiled gradient echo (FSPGR) T<sub>1</sub>-weighted (T<sub>1</sub>-w) sequence for registration; a diffusion-weighted spin-echo echo-planar sequence (SE\EPI) with 60 uniformly distributed directions ( $b = 1200 \text{ s/mm}^2$ ), according to an optimized gradient vector scheme (Jones et al., 1999); a CHARMED acquisition with 45 gradient orientations distributed on 8 shells (maximum b-value =  $8700 \text{ s/mm}^2$ ) (Assaf and Basser, 2005); and a 3D MT-weighted fast spoiled gradient recalled-echo (FSPGR) sequence (Cercignani and Alexander, 2006). The acquisition parameters of all scan sequences are reported in Table 24. Diffusion data acquisition was peripherally gated to the cardiac cycle. The off-resonance irradiation frequencies ( $\Theta$ ) and their corresponding saturation pulse amplitude ( $\Delta\text{SAT}$ ) for the 11 Magnetization transfer (MT) weighted images were optimized using Cramer-Rao lower bound optimization (Cercignani & Alexander, 2006).

**Table 24. Scan-parameters.**

All sequences were acquired at 3T. For each of the sequences, the main acquisition parameters are provided.  $T_1$ -w:  $T_1$ -weighted; MT-w: MT-weighted; FSPGR: fast spoiled gradient echo; SE: spin-echo; EPI: echo-planar imaging; SPGR: spoiled gradient recalled-echo; FoV: field of view; TE: echo time; TR: repetition time.

	$T_1$ -w	DTI	CHARMED	$T_1$ map	MT-w	$B_0$ map
Pulse sequence	FSPGR	SE\SE PI	SE\EPI	SPGR (3D)	FSPGR (3D)	SPGR (3D)
Matrix size	256×256	96×96 6	96×96	96×96×6 0	96×96×60	128×128 8
FoV (mm)	230	230	230	240	240	220
Slices	172	60	60	-	-	-
Slice thickness (mm)	1	2.4	2.4	-	-	-
TE,TR (ms)	7.8, 2.9	87, 1600 0	126, 17000	6.85, 1.2	2.18, 25.82	TE: 9 & 7 TR: 20
Off-resonance pulses (Hz/°)	-	-	-	-	1000/332, 1000/333, 12062/628,47185/628, 56363/332,2751/628, 1000/628, 1000/628, 2768/628, 2791/628, 2887/628	-
Flip angles (°)	20	90	90	15, 7, 3	5	90

#### 6.4.6. MRI data processing

The diffusion-weighted data were corrected for distortions induced by the diffusion-weighted gradients, artefacts due to head motion and EPI-induced geometrical distortions by registering each image volume to the  $T_1$ -w anatomical images (Irfanoglu et al., 2012), with appropriate reorientation of the encoding vectors (Leemans & Jones, 2009), all done in ExploreDTI (Version 4.8.3) (Leemans, Jeurissen, Sijbers, & Jones, 2009). A two-compartment

model was fitted to derive maps of FA and RD in each voxel (Pasternak et al., 2009). CHARMED data were corrected for motion and distortion artefacts according to the extrapolation method of Ben-Amitay, Jones, and Assaf (2012). The number of distinct fiber populations (1, 2, or 3) in each voxel was obtained using a model selection approach (De Santis et al., 2014) and FR was calculated per voxel with an in-house software (De Santis et al., 2014) coded in MATLAB (The MathWorks, Natick, MA). MT-weighted SPGR volumes for each participant were co-registered to the MT-volume with the most contrast using an affine (12 degrees of freedom, mutual information) registration to correct for inter-scan motion using Elastix (Klein et al., 2010). The 11 MT-weighted SPGR images and T<sub>1</sub> map were modelled by the two pool Ramani's pulsed MT approximation (Henkelman et al., 1993; Ramani et al., 2002), which included corrections for amplitude of B<sub>0</sub> field inhomogeneities. This approximation provided MPF maps, which were nonlinearly warped to the T<sub>1</sub>-w images using the MT-volume with the most contrast as a reference using Elastix (normalized mutual information cost function) (Klein et al., 2010).

#### **6.4.7. Deterministic Tractography**

Training-related changes in FA, RD, FR, and MPF were quantified using a tractography approach in pathways interconnecting the putamen and the supplementary motor area bilaterally (SMA-Putamen), and within three segments of the corpus callosum (CCI, CCII and CCIII) (Hofer & Frahm, 2006) (Figure 37).

Whole brain tractography was performed for each participant in their native space using the damped Richardson-Lucy algorithm (Dell'acqua et al., 2010), which allows the recovery of multiple fiber orientations within each voxel including those affected by partial volume. The tracking algorithm estimated peaks in the fiber orientation density function (fODF) by selecting seed points at the vertices of a 2×2×2 mm grid superimposed over the image and propagated

in 0.5-mm steps along these axes re-estimating the fODF peaks at each new location (Jeurissen et al., 2011). Tracks were terminated if the fODF threshold fell below 0.05 or the direction of pathways changed through an angle greater than 45° between successive 0.5 mm steps. This procedure was then repeated by tracking in the opposite direction from the initial seed-points.

The WM tracts of interest were extracted from the whole-brain tractograms by applying way-point regions of interest (ROI) (Catani et al., 2002). These were drawn manually by one operator (Dr Bourbon-Teles) blind to the identity of each dataset on color-coded fiber orientation maps in native space guided by the following anatomical landmark protocols (Figure 38).

### ***Corpus callosum:***

Reconstruction of the CC segments followed the protocol of Hofer and Frahm (Hofer & Frahm, 2006) as illustrated in Figure 38 A. Segment reconstructions were visually inspected and, if necessary, additional gates were placed to exclude streamlines inconsistent with the known anatomy of the CC.

### ***SMA-putamen pathway:***

One axial way-point ROI was placed around the putamen and one axial ROI around the supplementary motor cortex (Leh et al., 2007) (Figure 38 B). A way-point gate to exclude fibres projecting to the brain stem was placed inferior to the putamen.

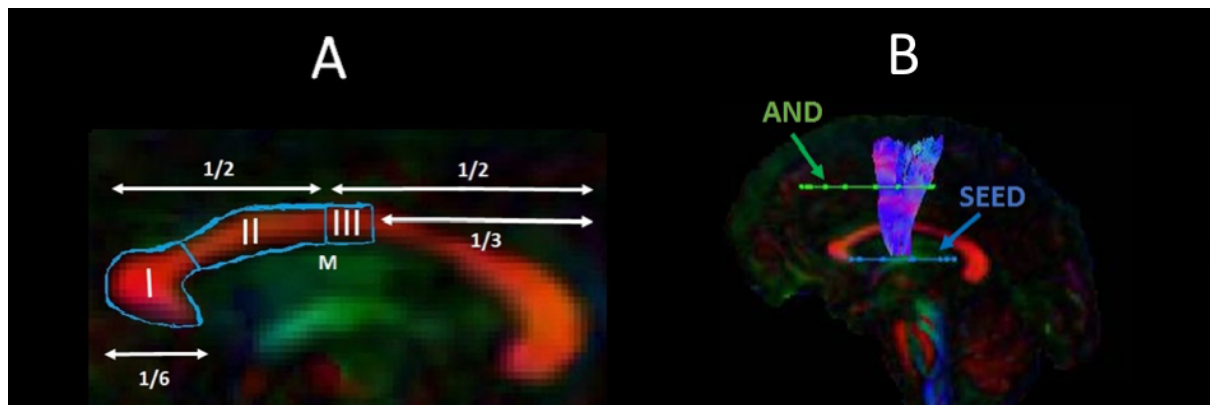


**Figure 38. Sagittal views of the tractography protocols.**

(A) CCI, CCII and CCIII (B) SMA - putamen pathway. Boolean logic OR waypoint regions of interest gates are illustrated in blue; AND gates in green. M = Midline. Abbreviations: CC: corpus callosum; SMA: supplementary motor area.

#### 6.4.8. Statistical analyses

Statistical analyses were carried out in R Statistical Software (Foundation for Statistical Computing, Vienna, Austria).

#### *Assessment of training effects on drumming performance*

Improvements in drumming performance were analysed with a two-way mixed ANOVA testing for the effects of group (HD/controls), time of assessment (before/after the training) and group by time interaction effects. Furthermore, results were compared to the ones obtained by running a robust mixed ANOVA, using the bwtrim R function from the WRS2 package (Mair & Wilcox, 2020). This implements robust methods for statistical estimation and therefore provides a good option to deal with data presenting small sample sizes, skewed distributions and outliers (Wilcox, 2011). Significant effects were further explored with post-hoc paired and independent t-tests. The reliability of the post-hoc analyses was assessed with bootstrap analysis based on 1000 samples and the 95% confidence interval (CI) of the mean difference is provided for each significant comparison.

### ***Assessment of group differences in the effect of training on cognitive performance***

Performance measures in executive function tasks have been shown to share underlying cognitive structures (Testa et al., 2012). Therefore, PCA was employed to reduce the complexity of the cognitive data and hence the problem of multiple comparisons as well as to increase experimental power. PCA was run on change scores for all participants across both groups. Due to the relatively small sample size, the suitability of the data for PCA was first confirmed with the Kaiser-Meyer-Olkin (KMO) test. Subsequently, guidelines were followed to limit the number of extracted components (Preacher & MacCallum, 2002; Winter, Dodou, & Wieringa, 2009), as follows: first, the Kaiser criterion of including all components with an eigenvalue greater than 1 was employed; second, the Cattell scree plot (Cattell, 1966) was inspected to identify the minimal number of components that accounted for most variability in the data; third, each component's interpretability was assessed. A PCA procedure with orthogonal Varimax rotation of the component matrix was used. Loadings of  $\geq 0.5$  were considered significant.

Next, group differences in the component scores were assessed with permutation analyses, to understand whether the training had differentially affected HD patients as compared to controls. Significant group differences were tested using 5,000 permutations. Permutation testing relies only on minimal assumptions and can therefore be applied when the assumptions of a parametric approach are untenable such as in the case of small sample sizes. Because of the small sample size, multiple comparison correction was based on a 5% false discovery rate (FDR) using the Benjamini-Hochberg procedure (Benjamini & Hochberg, 1995), a less conservative method compared to the Bonferroni procedure.

### ***Training effects on WM microstructure***

Median measures of FA, RD, FR and MPF were derived for each of the reconstructed tracts in ExploreDTI (Leemans et al., 2009)). A percentage change score in these measures between

baseline and post-training was calculated in each tract (CCI, CCII, CCIII, left and right SMA-Putamen).

Previous research has shown that variation in the microstructural properties of WM may represent a global effect, rather than being specific to individual tracts, and that WM measures are highly correlated across WM areas (Lövdén et al., 2010; Penke et al., 2010; Wahl et al., 2010). Therefore, inspection of the inter-tract correlation for each of microstructural metric was carried out, revealing that MPF values were highly correlated, whereas this was not true for the other metrics. Hence, percentage change scores in MPF across the different tracts were transformed with PCA to extract meaningful anatomical properties, following the procedure described above for the PCA of cognitive change scores. PC scores for each participant were then used as dependent variables in a permutation-based analysis using 5,000 permutations to assess group differences in training associated changes in MPF. Finally, as a post-hoc exploration, between-groups differences in MPF changes in the individual tracts were tested using 5000 permutations.

Training-associated changes in FA, FR and RD were investigated with permutation analyses separately for each tract. Significant group differences in these measures were tested using 5,000 permutations. Multiple comparison correction was based on a 5% FDR using the Benjamini-Hochberg procedure (Benjamini & Hochberg, 1995).

### ***Baseline differences in WM microstructure***

TBSS (Smith et al., 2006) was carried out to investigate baseline differences in MPF between HD subjects and healthy controls, to gain a better insight into differences in training-associated changes. To produce significance maps, a voxel-wise analysis was performed on the MPF projected 4D data for all voxels with  $FA \geq 0.20$  to exclude peripheral tracts where significant inter-subject variability exists. Inference based on permutations (5,000

permutations) and threshold-free-cluster-enhancement was used. The significance level was set at  $p < 0.05$  and corrected by multiple comparisons (family-wise error, FWE).

### ***Relationship between changes in MRI measures and changes in drumming and cognitive performance***

Percentage change scores for the drumming performance were computed in the same way as cognitive change scores were calculated. Scores were computed for the easy test pattern in patients and for the medium test pattern in controls, as these training patterns showed a significant improvement in the two groups, respectively. Spearman correlation coefficients were calculated between drumming and cognitive performance, and microstructural components that showed significant group differences, to assess whether microstructural changes were related to any drumming and/or cognitive benefits of the training.

## **6.5. Results**

### **6.5.1. Training effects on drumming performance**

The mixed ANOVA of drumming performance for the easy and medium test pattern showed a significant effect of group [easy:  $F(1,17) = 22.3$ ,  $p < 0.001$ ; medium:  $F(1,17) = 13.1$ ,  $p = 0.002$ ] and time [easy:  $F(1,17) = 12.83$ ,  $p = 0.004$ ; medium:  $F(1,17) = 13.4$ ,  $p = 0.002$ ] but no interaction (easy:  $p = 0.825$ ; medium:  $p = 0.305$ ). For the hard test pattern there was only a significant effect of group [ $F(1,17) = 9.95$ ,  $p = 0.006$ ] but not of time ( $p = 0.123$ ) and there was no interaction ( $p = 0.432$ ). Results from the robust mixed ANOVA were largely consistent with the above. Specifically, the easy and medium test patterns showed a significant effect of group (easy:  $p = 0.002$ ; medium:  $p = 0.021$ ) and time (easy:  $p = 0.041$ ; medium:  $p = 0.049$ ) but no interaction (easy:  $p = 0.452$ ; medium:  $p = 0.691$ ). The hard test pattern showed a significant effect of group ( $p = 0.021$ ) but not of time ( $p = 0.222$ ) and no interaction ( $p = 0.811$ ). Figure

39 summarises the average drumming performance per group and time point. Overall patients' drumming performance was poorer than controls. Patients improved their drumming performance significantly for the easy pattern [ $t(10) = 2.7, p = 0.022$ ; 95% CI of mean difference: 1.5 – 7.8] and controls for the medium pattern [ $t(7) = 3.8, p = 0.01$ ; 95% CI of mean difference: 2.8 – 8.5].

### **6.5.2. Group differences in the effect of training on cognitive performance**

Three components, accounting for 79% of the variance in performance improvement in the cognitive tests were extracted. The first component loaded highly on performance changes in the dual task (total number of boxes identified under dual task condition), the Stroop task (Stroop interference score), and the trails making task (Trail test switching). Since these variables all measure executive functions including focused attention and distractor suppression, the first component was labelled “executive” component. The second component loaded on variables reflecting the ability to correctly recall digits sequences (i.e. number of correct digits recalled under single and dual task condition) and was therefore labelled “working memory capacity” component. Finally, the third extracted component loaded highly on verbal and category fluency and was therefore labelled “fluency” component (Table 25).

Differences between the two groups in terms of post-training cognition changes were tested by running permutation analyses on the individual scores for the three extracted components. The two groups differed in the executive component,  $t = -1.03, p = 0.008$ , FDR-corrected  $p = 0.024$ . However, no significant group differences were detected in the other two components (Working Memory capacity:  $t = -0.22, p = 0.329$ , FDR-corrected  $p = 0.329$ ; Fluency:  $t = -0.39, p = 0.242$  FDR corrected  $p = 0.329$ ).

### 6.5.3. Training effects on WM microstructure

Table 26 reports a summary of the training associated changes in FA, RD, FR and MPF, across the different tracts.

#### *Training-associated group differences in FA*

Permutation analyses of FA changes across the different tracts revealed no significant differences between HD and control groups [CCI:  $t = 1.22$ ,  $p = 0.912$  (FDR-corrected); CCII:  $t = 2.65$ ,  $p = 0.912$  (FDR-corrected); CCIII:  $t = 0.325$ ,  $p = 0.131$  (FDR-corrected); right SMA-Putamen:  $t = -9.54$ ,  $p = 0.101$  (FDR-corrected); left SMA-Putamen:  $t = 5.16$ ,  $p = 0.772$  (FDR-corrected)].

#### *Training-associated group differences in RD*

There were no significant differences in RD changes following training between HD patients and controls [CCI:  $t = -0.48$ ,  $p = 0.452$  (FDR-corrected); CCII:  $t = -1.29$ ,  $p = 0.451$  (FDR-corrected); CCIII:  $t = -1.04$ ,  $p = 0.452$  (FDR-corrected); right SMA-Putamen,  $t = 4.01$ ,  $p = 0.811$  (FDR-corrected); left SMA-Putamen,  $t = -3.68$ ,  $p = 0.391$  (FDR-corrected)].

#### *Training-associated group differences in FR*

Permutation analyses of FR changes across the different tracts revealed no significant differences between HD and control groups [CCI:  $t = 3.39$ ,  $p = 0.821$  (FDR-corrected); CCII:  $t = -0.17$ ,  $p = 0.821$  (FDR-corrected); CCIII:  $t = 3.08$ ,  $p = 0.821$  (FDR-corrected); right SMA-Putamen:  $t = -5.24$ ,  $p = 0.821$  (FDR-corrected); left SMA-Putamen:  $t = 1.05$ ,  $p = 0.821$  (FDR-corrected)].

### ***Training-associated group differences in MPF***

PCA of change scores in MPF revealed one single component explaining 70.2% of the variance. This component presented high loadings from all the tracts investigated. A significant group difference was found for the MPF change-score component, indicating that HD patients presented significantly greater MPF changes in response to training, as compared to controls [t(14) = -1.743, p = 0.032].

Finally, I found a significant difference in mean MPF change scores between the two groups for CCII [t(14) = -20.72, p = 0.042], CCIII [t(14) = -25.87, p = 0.042], and the right SMA-putamen pathway [t(14) = -25.48, p = 0.042] after FDR correction, therefore indicating that there was a differential group effect of training on MPF within these tracts (Figure 40).

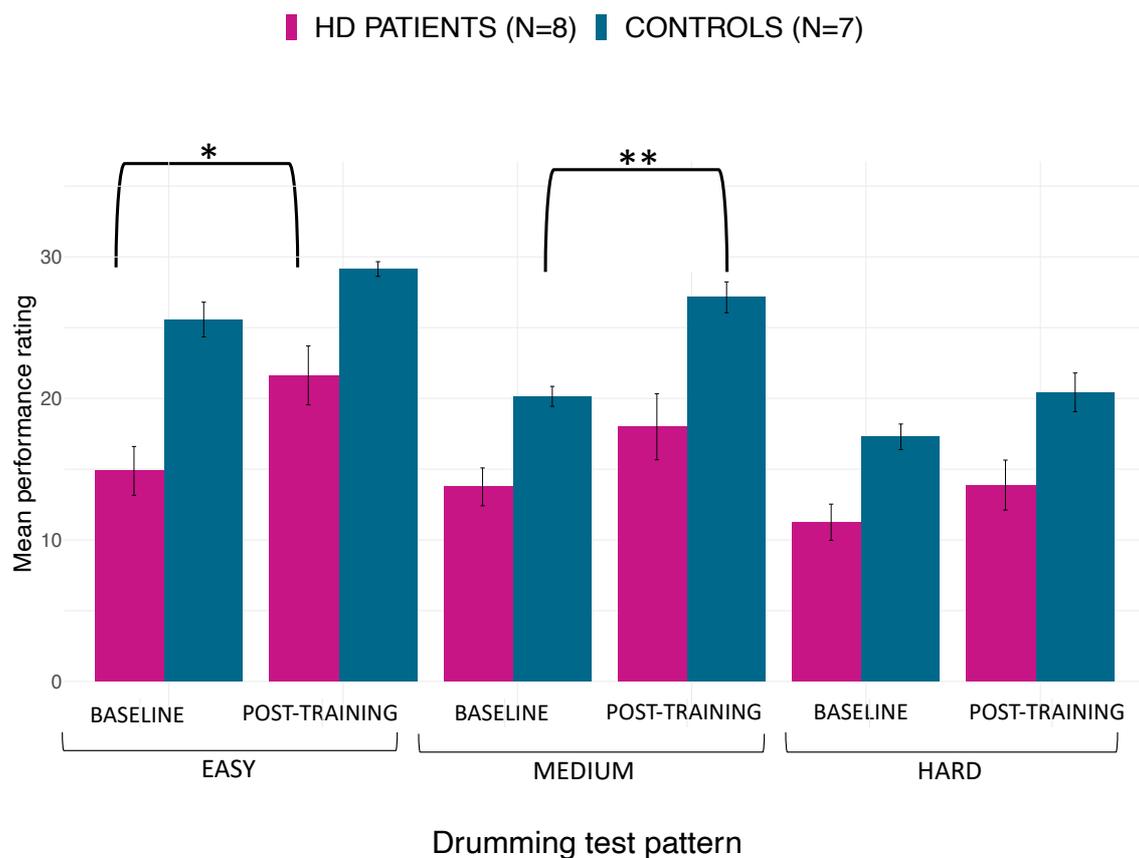


***Figure 39. Mean ratings for drumming performance.***

*Drumming performance scores according to the Trinity College London marking criteria for percussion (2016) as a function of group and time point. Patients improved their drumming*

performance significantly for the easy test pattern and controls for the medium difficult test pattern. \*  $p < 0.05$ , \*\*  $p < 0.01$ , bootstrapping based on 1000 samples.

#### 6.5.4. Changes in microstructure do not correlate with improvement in drumming performance

No significant association was found between the MPF component scores and improvement in drumming performance ( $r = -0.14$ ,  $p = 0.079$ ). Moreover, although no significant correlation was observed between the Executive and the MPF component scores, a positive trend was present ( $r = 0.348$ ,  $p = 0.171$ ).

#### 6.5.5. HD patients present reductions in apparent myelin before training

Baseline MPF was reduced in the HD group compared to controls, in the midbody of the CC ( $t = 3.13$ ,  $p = 0.052$ , FWE corrected). Figure 41 shows the areas with reduced MPF in HD patients, in blue.

*Table 25. Rotated component loadings on change in the cognitive benchmark tests.*

*Significant loadings ( $>0.5$ ) are highlighted in bold.*

% Change	Executive	Working memory capacity	Fluency
Total box (dual)	<b>0.864</b>	0.022	0.419
Stroop interference score	<b>0.811</b>	-0.270	-0.267
Trail test switching	<b>0.731</b>	-0.470	0.162
Correct digits under single task condition	0.201	<b>0.904</b>	0.129
Correct digits under dual task condition	-0.193	<b>0.855</b>	-0.018

---

<b>Category fluency</b>	-0.070	-0.138	<b>0.817</b>
<b>Verbal fluency</b>	-0.026	-0.232	<b>-0.799</b>

---

**Table 26. Summary statistics for the permutation analysis of training effects on FA, RD, FR and MPF, across the investigated tracts. Abbreviations: FA: fractional anisotropy; RD: radial diffusivity; FR: restricted volume fraction; MPF: macromolecular proton fraction.**

<b>FA</b>	<b>t</b>	<b>p</b>	<b>FDR corrected p</b>
CCI	1.220	0.91	0.91
CCII	2.650	0.91	0.91
CCIII	0.320	0.48	0.91
Left SMA-Putamen	5.160	0.77	0.91
Right SMA-Putamen	-9.54	0.02	0.11
<b>RD</b>			
CCI	-0.48	0.35	0.45
CCII	-1.29	0.22	0.45
CCIII	-1.04	0.30	0.45
Left SMA-Putamen	-3.68	0.08	0.39
Right SMA-Putamen	4.010	0.80	0.80
<b>FR</b>			
CCI	0.033	0.81	0.82
CCII	-0.001	0.49	0.82
CCIII	0.03	0.82	0.82
Left SMA-Putamen	0.01	0.58	0.82
Right SMA-Putamen	-0.052	0.29	0.82
<b>MPF</b>			
CCI	-12.06	0.08	0.10
CCII	-20.72	<b>0.03</b>	<b>0.05</b>
CCIII	-25.87	<b>0.02</b>	<b>0.05</b>
Left SMA-Putamen	-4.34	0.38	0.38
Right SMA-Putamen	-25.48	<b>0.02</b>	<b>0.05</b>

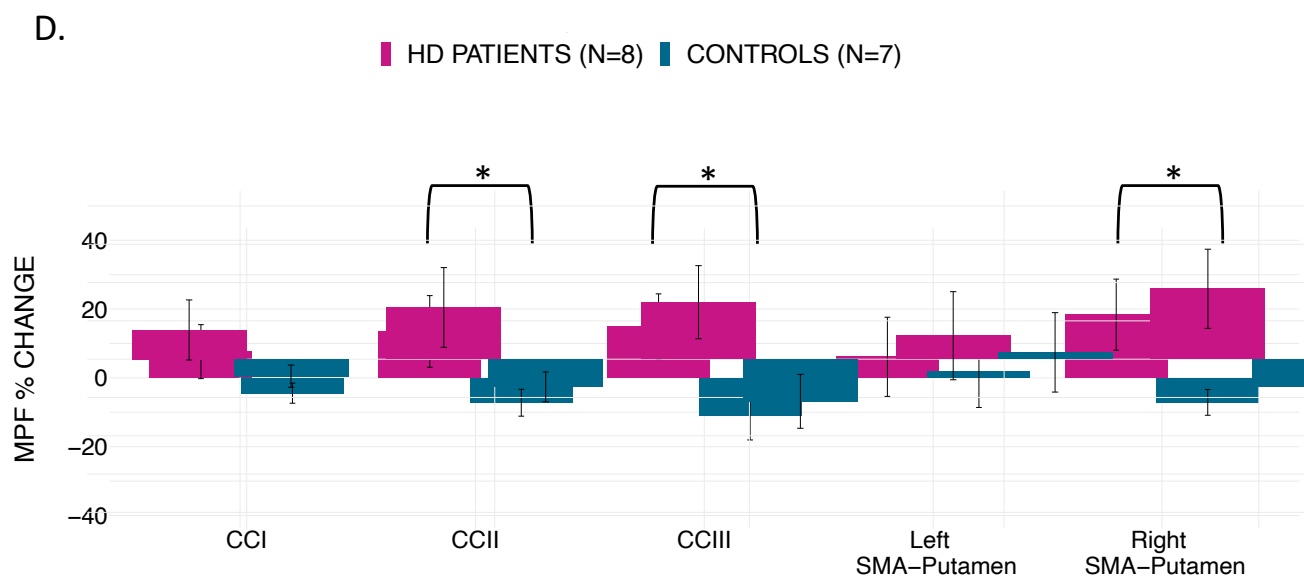
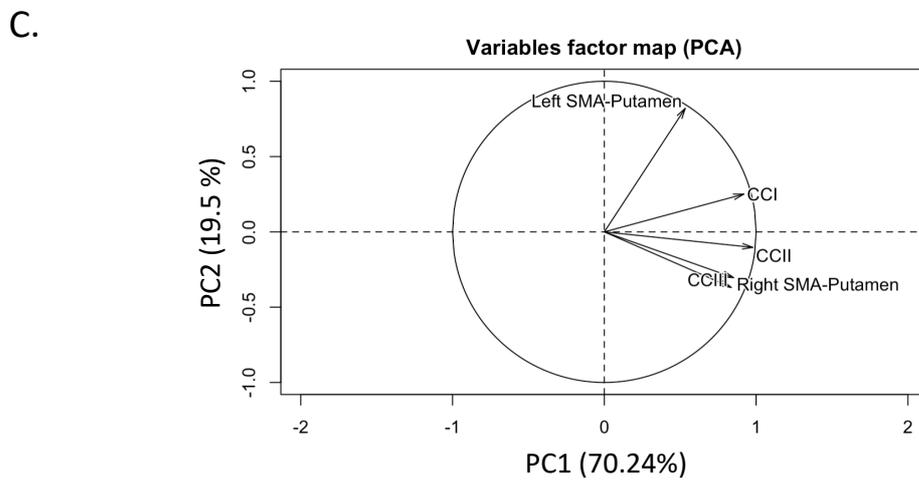
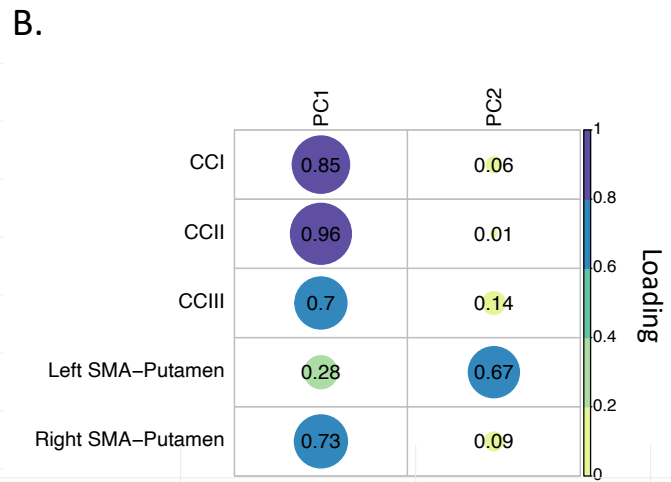
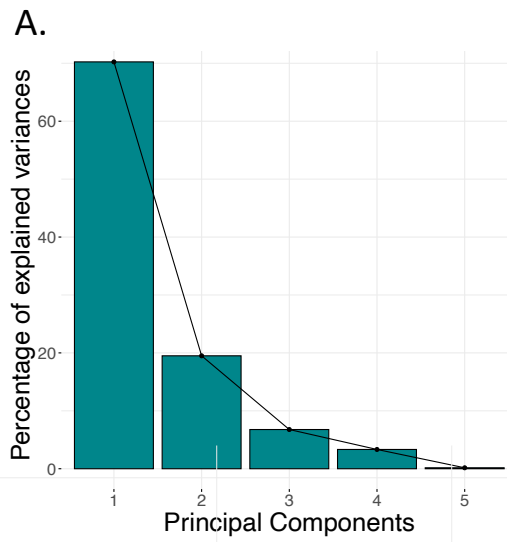


**Figure 40. Training-associated macromolecular proton fraction (MPF) changes.**

Principal component analysis (PCA) scree plot (A); plot summarizing how each variable is accounted for in every principal component (PC) - color intensity and the size of the circles are proportional to the loading: PC1 loads on CCI, CCII, CCIII and right SMA-Putamen, while PC2 loads mostly on the left SMA-Putamen; the absolute correlation coefficient is plotted (B); correlation circle, interpreted as follows: 1) positively correlated variables are grouped together, 2) negatively correlated variables are positioned on opposite sides of the plot origin (opposite quadrants), 3) the distance between variables and the origin measures the quality of the variable on the factor map. Variables that are away from the origin are well represented on the factor map (C); Bar graph of the percentage change in MPF across the inspected tracts; Error bars represent the standard error; training was associated with a significantly greater change in MPF in CCII, CCIII, and right SMA-Putamen; \* ( $p < 0.05$ ), results corrected for multiple comparisons with false discovery rate (FDR) (D).

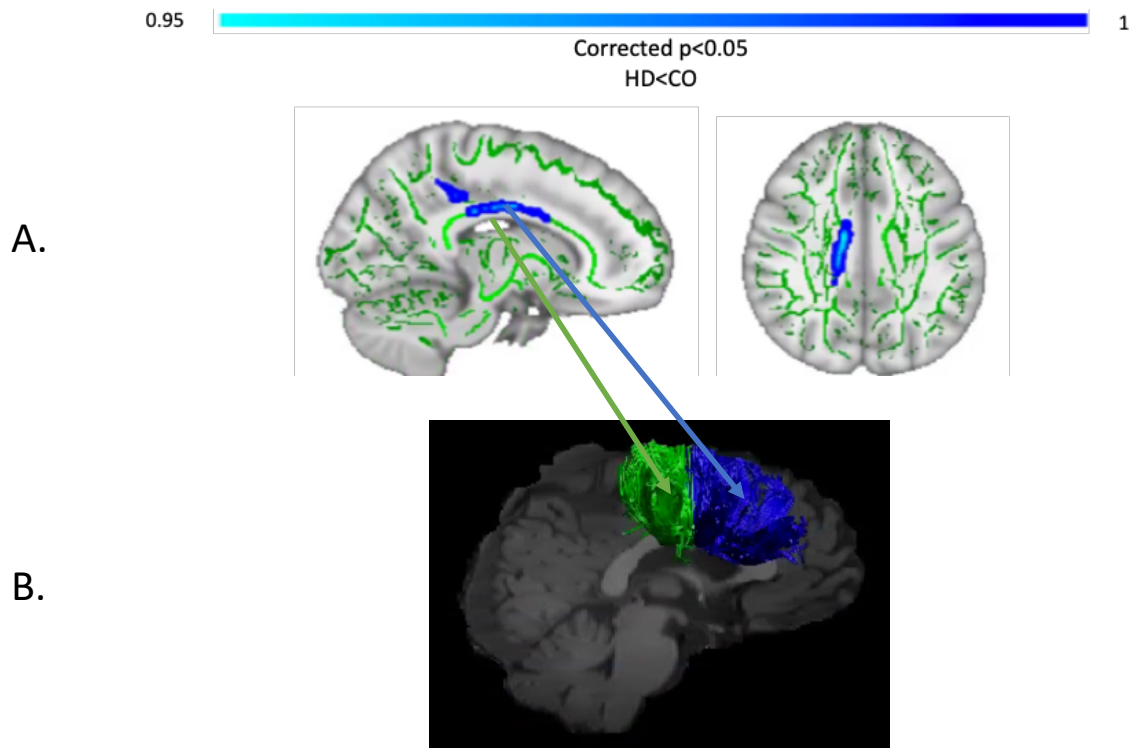


**Figure 41. Tract-based spatial statistics (TBSS) analysis of baseline macromolecular proton fraction (MPF) values.**

(A). Light blue areas show a significant reduction of MPF in patients with HD compared to controls ( $p < 0.05$ , FWE corrected). The midbody of the corpus callosum (CC) was mostly found to be affected, which carries connections to the premotor, supplementary motor and motor areas of the brain. Tracts showing significantly greater MPF changes in HD patients post-training as compared to controls (B). Areas showing significant MPF reductions at baseline overlap with tracts showing significant changes post-training (i.e. CCII and CCIII).

## 6.6. Discussion

Based on evidence that myelin impairment contributes to WM damage in HD (Bartzokis et al., 2007), and the suggestion that myelin plasticity underlies the learning of new motor skills (Lakhani et al., 2016; Scholz et al., 2009), the present study explored whether two months of drumming training would result in changes in WM microstructure in HD patients. Specifically, greater changes in MPF, as marker of WM myelin plasticity, were expected in HD patients relative to healthy controls.

Firstly, a behavioural effect of the training was demonstrated by showing a significant improvement in drumming performance in patients (easy test pattern) and controls (medium test pattern). No group differences in training-associated changes were detected in the diffusion based indices of FA, RD and FR. However, as hypothesised, a group difference in training-induced changes in the MPF PCA component was found. Specifically, HD patients showed significantly higher increases in MPF relative to controls. Furthermore, through exploratory post-hoc investigations, significantly higher training-induced MPF changes within the CCII, CCIII and the right SMA-putamen pathway were shown in patients relative to controls. Additionally, TBSS analysis of baseline differences in MPF suggested a partial overlap of WM areas showing significant MPF reductions at baseline with areas showing changes post-training (i.e. CCII and CCIII).

MPF can be affected by inflammation (Henkelman, Stanisiz, & Graham, 2001) and in advanced HD it is likely that inflammation goes hand-in-hand with myelin breakdown (Rocha et al., 2016). However, a recent CSF biomarker study found no evidence of neuro-inflammation in early-manifest HD (Vinther-Jensen et al., 2016). Furthermore, recent evidence shows that this measure may be inconsistent when investigated in relatively small WM areas, presumably because of the effect of spatial heterogeneity in myelin thickness (Wang et al., 2020). Nevertheless, the within-subjects design employed in the present study should have helped to

minimise noise due to the spatial inconsistency of this measure. Therefore, though preliminary and based on a small sample size, these findings suggest that two months of drumming and rhythm exercises may result in myelin remodelling in patients with early HD.

It is plausible that this group difference arose due to WM microstructural differences between patients and controls before the training. Accordingly, the HD group showed a significantly lower baseline MPF, consistent with lower myelin content (Bartzokis et al., 2007). Furthermore, previous studies have reported that training-associated percentage changes in MRI measures tend to be higher in patients than in healthy subjects (Caeyenberghs et al., 2018). One possibility is that in the healthy brain, neural networks may be optimally myelinated, and further increasing myelin may not improve performance (Chomiak & Hu, 2009; Kaller et al., 2017; Rushton, 1951). Hence, the MPF changes in patients relative to controls might depict mainly a “catch-up effect” to the better baseline status of the control group. However, disentangling the impact of prior WM microstructural differences on microstructural plasticity during learning is beyond the scope of the current work.

Notably, the behavioral effect of drumming training and cognition differed between patients and controls. Specifically, patients improved in the easy drumming test pattern, and controls improved in the medium test pattern. Furthermore, consistent with evidence from our pilot study (Metzler-Baddeley et al., 2014), patients showed increases in the executive function components whilst control participants did not show improvements in their cognition. Therefore, inter-group differences in microstructural changes might not only be due to baseline WM microstructural differences, but also to a different behavioral effect of the task between HD subjects and controls. For instance, control participants performed close to ceiling in the easy test pattern, and as the training was tailored to patients’ needs, some of the earlier practice sessions may not have optimally challenged them. The fact that the training seemed more taxing for patients than controls may also explain why improvements in executive functions

and changes in MPF were only observed for the patients.

A critical question relevant to all training studies concerns the functional significance of any observed neural changes. If, and to what degree adaptive alterations in myelin content can facilitate behavioural change, remains poorly understood (Kaller et al., 2017). In the present study, no significant relationships between changes in MRI measures and changes in drumming proficiency or performance in cognitive tests were found. This might have been due to non-specific training-related neural responses. Specifically, while the training exercise might have triggered changes in brain structure, training-induced changes may not necessarily co-vary with improvements in performance. Alternatively, it might be that the study was insufficiently powered to detect brain-function correlations. The minimum sample size required to detect a correlation was calculated to be 64 people ( $\alpha = 0.05$ ; 80% power; medium effect size; GPower 3 software). Interestingly, a positive trend was detected between changes in the MPF component and those in the Executive component, both of which showed significant differences between HD patients and controls. Therefore, these results need replication in larger samples. A lack of correlation between structural and functional changes after training has been reported in other studies (including well-powered studies) and may suggest that these processes follow different time courses and/or may occur in different brain regions (Valkanova et al., 2014).

It is important to note that this study did not include a non-intervention patient group. Within the 12 month time period of this study it was not possible to recruit a sufficiently large number of well-matched patient controls. Therefore, the effects of the training on WM microstructure cannot be disentangled from HD-associated pathological changes. However, given that HD is a progressive neurodegenerative disease associated with demyelination (Bartzokis et al., 2007), it is unlikely that increases in MPF observed in the patient group were due to the disease itself. Finally, while the majority of training studies assess brain structural

changes between baseline and post-training (Caeyenberghs et al., 2018), presumably on account of cost and participant compliance, it is suggested that acquiring intermittent scans during the training period could have helped to better capture and understand changes in WM microstructure observed in this study. Accordingly, future studies and more advanced statistical analyses might be able to give greater insights into the complex nonlinear relationships between structural changes and behaviour (Thomas & Baker, 2013).

A final important point to note is the high drop-out rate observed during the training, with 4 patients and 2 controls withdrawing from the study. From the patients' feedback it was clear that sometimes the training was too hard and sometimes too easy. The high drop-out rate is therefore likely to be due to a combination of Huntington's disease with symptoms of apathy, low motivation and depression, and possibility of worsening of symptoms, and the fact that the training was not always optimally targeted to participants' abilities. Thus, future studies may improve the training by digitising it, hence enabling the implementation of an adaptive staircase procedure to ensure that everyone is practising at their optimally challenging level of about 75% success rate. This in turn would help to avoid boredom and/or overchallenge/frustration. Digitisation would also allow objective assessment of adherence and training progress.

To conclude, this study showed that two months of drumming and rhythm exercises result in a significantly greater change in a proxy MRI measure of myelin in patients with HD relative to healthy controls. Whilst the current results require replication in a larger patient group with an appropriately matched patient control group, they suggest that behavioural stimulation may result in neural benefits in HD that could be exploited for future therapeutics aiming to delay disease progression.



# Chapter 7

## General Discussion

### 7.1. Thesis overview

The fact that HD arises from a known single genetic mutation means that we can investigate HD-associated brain changes from the earliest, premanifest stages of the disease. Subtle and progressive WM alterations (Dayalu & Albin, 2015) have been observed early in HD progression, before the onset of motor symptoms (Aylward et al., 2011; Ciarmiello et al., 2006; Paulsen et al., 2008; Ruocco et al., 2008; Tabrizi et al., 2009), implying that WM disturbances might independently contribute to HD pathogenesis (Aylward et al. 2011; Bartzokis et al. 2007; Tabrizi et al. 2009). However, the aetiology of WM degeneration and its role in disease pathogenesis remain unclear. The assessment of early WM microstructural changes in the HD brain is therefore of fundamental importance. Understanding such changes might prove useful for the identification of disease-related biomarkers and in measuring responsiveness to pharmaceutical and other therapeutic approaches, such as environmental stimulation and behavioural interventions. Importantly, new MRI methods provide in-depth information about tissue integrity and organization at the microstructural and biochemical levels. Thus, the primary aim of this work was to exploit both ultra-strong gradients (300 mT/m) and ultra-high field (7 Tesla, 9.4 Tesla) to assess WM microstructural changes in HD, using a variety of MRI techniques in premanifest and manifest HD patients, as well as a mouse model of the disease.

This Thesis moved beyond the diffusion tensor framework for the investigation of WM, with the application of advanced microstructural imaging, including high b-value measurements of restricted diffusion, high-field assessments of susceptibility with frequency difference mapping, along with magnetization transfer measurements of apparent myelin.

Using these advanced MR techniques I was able to provide a comprehensive and detailed characterisation of WM microstructural differences in the HD brain. Specifically, I was able to better tease apart changes in apparent myelin content from alterations in axon microstructure allowing novel insights into HD-related WM differences that were not possible with standard DTI.

Additionally, studying both human patients and a mouse model of HD with these advanced MRI techniques allowed for direct cross-species comparisons and bi-directional translation of results. This is important for gaining novel insights into human HD neuropathology, affording the foundation for translational research in the R6/1 mouse model, and for increased biological specificity of the work in the HD model that informs knowledge and research in the human condition.

Finally, I was able to apply the improved compartmental specificity obtained by complementing standard DTI metrics with measurements from qMT and CHARMED, to study the effects of two months of a novel drumming training on WM plasticity in patients with manifest HD. This in turn allowed to assess whether tailored cognitive-motor stimulation may lead to neural benefits in early HD, that could be exploited for delaying disease progression.

In the following sections, I will first reiterate the major findings of this Thesis; I will then discuss their broader significance in the context of the current understanding of WM pathology in HD and in light of the Demyelination Hypothesis (Bartzokis et al., 2007). Subsequently, I will evaluate the translation of findings between patients and the R6/1 model, and consider the methodological limitations along with potential future directions that could provide greater understanding of WM pathological changes in HD.

## 7.2. Summary of findings

Findings from this Thesis replicated evidence on HD already present in the literature. For example, they showed that premanifest patients present striatal atrophy (Aylward et al., 2012; Paulsen et al., 2014a, 2014b; Tabrizi et al., 2012, 2013), which does not seem to extend to the thalamus (Furlong et al., 2020), and dysexecutive deficits (Mörkl et al., 2016; Papoutsis et al., 2014; Stout et al., 2016), which likely reflect impairments in the executive control and manipulation of information processing (Bourbon-Teles et al., 2019).

Additionally, a range of significant changes in WM as detected with MRI were observed in premanifest and manifest HD patients, as well as in HD mice (Bartzokis et al. 2007; Jin et al. 2015; Meng et al. 2017; Rosas et al. 2018; Rosas et al. 2006; Tabrizi et al. 2009, 2011). However, the present experimental work also made novel contributions to understanding the effect of HD on WM microstructure, by disentangling the contribution of changes in axon microstructure *versus* myelin to HD pathology, and demonstrating significant differences in both apparent myelin and axon microstructure across the brain and the disease course. Importantly, in the premanifest stage of the disease these changes were present before morphometric alterations in WM could be detected, indicating that microstructural changes precede frank neurodegeneration and may reflect early neuronal dysfunction (Rosas et al., 2010) or a neurodevelopmental component to the pathogenesis of HD (Jin et al., 2015).

In Chapter 3, I first assessed cognition and subcortical GM and found deficits in the executive control and manipulation of information processing, as well as atrophy in the striatum, in premanifest HD patients. I then investigated region-specific changes across the CC using a tractometry approach (Bells et al., 2011; Jones et al., 2005b, 2006), as well as WM microstructural abnormalities across the whole brain with TBCA (Luque Laguna, 2019). Results from both approaches showed lower MTR in the posterior callosum of premanifest patients, in turn suggesting lower apparent myelin in this region. On the other hand,

premanifest HD patients presented significantly higher apparent myelin in the more anterior portions of the CC. Importantly, there was a positive association between apparent myelin and cognitive performance, as well as between apparent myelin and CAG repeat length in patients. On the other hand, no association of apparent myelin in the CC with disease burden was detected, indicating that such changes in myelin might be a direct result of the disease mutation. With TBCA, I also detected clusters of significantly higher FA in the right fronto-striatal projections, and increased FR in the left CST in premanifest patients, indicating that WM changes in premanifest HD extend beyond the callosum. FR in the CST was significantly associated with MTR in the posterior CC and a trend was present for a positive association with cognitive performance, possibly reflecting compensation to myelin loss.

In Chapter 4, I first showed that the executive updating of relevant information tends to deteriorate to a larger extent with age in premanifest HD patients, consistent with the cognitive deficits demonstrated in Chapter 3. I then validated the potential of a novel phase-processing approach, FDM, and three-pool modelling of the mGRE signal, in gaining further insight into the biological basis of WM microstructural changes in the HD brain. Specifically, I estimated  $f_m$  as a marker of myelin in the posterior callosum and observed significantly lower  $f_m$  values in this area in premanifest HD patients compared to controls, suggesting, consistent with findings from Chapter 3, the presence of myelin impairment in this callosal segment. Interestingly, I also found that patients' inter-individual variability in  $f_m$  was positively associated with their executive performance, but detected no association between inter-individual variation in  $f_m$  and proximity to disease onset as measured with DBS. Both of these results are consistent with findings of Chapter 3 and suggest that myelin differences may precede the onset of clinical symptoms in HD and may not directly relate to disease stages.

In Chapter 5 I performed an MRI characterization of WM microstructure in the transgenic R6/1 mouse model of HD. Such assessment was performed *ex vivo* on the brains of

4 month old mice, to represent the early symptomatic stage of HD. Processing and analyses methods similar to those used in the patient cohort in Chapter 3 were employed, in the attempt to increase the translational validity of findings. An initial assessment of WM microstructural changes across the CC using a tractometry approach revealed increased FR and decreased MPF in R6/1 mice, compared to WT littermates, across this tract. The subsequent assessment of WM microstructural abnormalities across the whole brain with VBM showed areas of greater WM volume in R6/1 mice. This was accompanied by widespread higher FR, together with some decreases in MPF, as detected with TBSS. Importantly, decreased apparent myelin and increased FR are both consistent with what I observed in Chapter 3 in premanifest patients, although changes were more widespread in R6/1 mice, possibly because of differences in disease progression stages. Finally, brain tissue ultrastructure from the R6/1 mouse line was analysed using TEM, indicating that the frequency distribution of myelinated axon diameters was skewed towards thinner axons in R6/1 mice.

Lastly, in Chapter 6 I investigated whether drumming training stimulates WM remodelling in manifest HD patients, and whether training-associated microstructural changes are related to improvements in motor and cognitive function. Firstly, I demonstrated a behavioural effect of the training by showing a significant improvement in drumming performance in patients and controls. I also found significantly higher training-associated MPF changes within the mid-anterior portion of the CC and the right SMA-putamen pathway in patients relative to controls. Additionally, TBSS analysis of baseline differences in MPF suggested a decrease in apparent myelin in the callosum of manifest HD patients, consistent with what observed in premanifest patients and R6/1 mice in the previous chapters. Importantly, I detected a partial overlap of WM areas showing significant MPF reductions at baseline with areas showing changes post-training, suggesting the presence of a training-associated myelin remodelling in these areas.

## **7.3. Bringing it all together**

In this section I will be discussing the most interesting findings of this Thesis in the broader context of the existing literature, and I will explore how this experimental work has furthered our understanding of WM pathology in HD and stimulated further research.

### **7.3.1. Myelin pathology in HD: excessive myelin or myelin breakdown?**

The work described in this Thesis provides supporting evidence to the suggestion that WM in HD is subject to alterations in myelin-associated biological processes (Bartzokis et al., 2007; Gómez-Tortosa et al., 2001; Myers et al., 1991; Teo et al., 2016). In Chapters 3 and 4, decreased apparent myelin in the posterior portion of the CC was found in premanifest HD patients. Furthermore, findings from R6/1 mice, tested at 4 months of age to represent the early symptomatic stage of the disease, indicate that demyelination later in disease progression may be more widespread. Consistent with findings from HD mice, in Chapter 6 decreases in apparent myelin in symptomatic HD patients extended across the mid-anterior portions of the callosum, as well as the superior longitudinal fasciculus.

The suggestion of a progressive spread of demyelination across the HD brain and of myelin impairment first starting in posterior, early myelinating areas of the brain is consistent with previous findings from human neuroimaging studies (Di Paola et al., 2012; Lee, 2016; Tabrizi et al., 2012). However, while previous suggestions have been based on DTI measures, which are inherently non-specific to subcomponents of WM microstructure (Alexander et al., 2007; De Santis et al., 2014), the combination of standard tensor metrics with MTR and FR from ultra-strong gradient scanning, and  $f_m$  from ultra-high field susceptibility measurements afforded in this work a more biologically-meaningful interpretation of microstructure changes. Accordingly, the present results indicate that changes in DTI measures observed in previous

studies in posterior WM areas of premanifest patients are indeed likely to be due to myelin alterations.

Importantly, the present results are consistent with the Demyelination Hypothesis of HD (Bartzokis et al. 2007), and the suggestion that *mHTT* leads to premature myelin breakdown in HD. Consistent with findings from this Thesis, the Demyelination Hypothesis argues that early- and heavily-myelinated fibres, such as those in the callosal isthmus, are more susceptible to myelin breakdown in HD, and are thus affected first in the disease (Bartzokis et al., 2007), possibly because of metabolic dysfunction and alterations in energetics (Beal, 2005; Browne, 2008). The spatial pattern of pathology is in contrast with the “last-in-first-out hypothesis” that was proposed for degenerative processes of normal brain aging (Raz, 2000), which postulates that later-myelinating fibres are more vulnerable to insult in later life, as compared to earlier-myelinating ones.

Unexpected was the detection of higher apparent myelin in premanifest HD patients compared to controls in anterior portions of the CC (Chapter 3). To explain such finding, I suggested two possible mechanisms: the first concerns the presence of toxic myelination levels in the premanifest HD brain because of pathologically-increased CAG repeat size; the second proposes the presence of homeostatic remyelination in response to the myelin breakdown associated with the mutation.

The proposal of excessive myelination in HD is not consistent with previous histological findings from animal studies (Bardile et al., 2019; Blockx et al., 2012; Jin et al., 2015; Teo et al., 2016; Xiang et al., 2011). Therefore, if considered in the context of the existing animal literature, findings of increased apparent myelin in the anterior callosum of premanifest HD patients are likely due to a dysregulation of the temporal profile of myelination and to deficient, rather than excessive, myelination as an important early pathogenic event in HD (Jin et al. 2015). However, most experimental evidence about histological abnormalities in HD is

based on mouse models (Xiang et al., 2011). Therefore, investigating WM microstructure in neurodegeneration *in vivo* through neuroimaging will be critical to better understanding myelin alterations in the premanifest stage of HD.

### **7.3.2. Axon pathology in HD: pathologically driven morphological alterations?**

In Chapter 3, a significant increase in FR was detected along most of the left CST in premanifest HD patients. Interestingly, the assessment of WM microstructural changes in the R6/1 mouse model of HD in Chapter 5 revealed widespread increases in FR across the brain. Though these findings need to be interpreted with caution as they are based on a mouse model rather than symptomatic HD patients, they suggest that, similarly to the alterations in apparent myelin, later in disease progression changes in axon density are more widespread, thus pointing to a progressive spread of alterations across the HD brain as the disease progresses.

While FR from CHARMED can provide maps of the signal fraction of intra-cellular space (Assaf & Basser, 2005), this model represents axons as parallel cylinders and thus cannot recover the effect of axonal-orientation dispersion due to bending and fanning of axon bundles widespread throughout the brain (Bürgel et al., 2006). By relaxing this constraint, more recent models such as the neurite orientation dispersion and density imaging (NODDI) model (Zhang et al., 2012) support a more realistic description of WM beyond the most coherently-oriented structures and provide an estimate of orientation dispersion (OD).

It is therefore plausible that the increases in FR observed in the present work both in premanifest patients and in R6/1 mice reflect a process of reorganization or selective pruning of fibres, such as pathologically-driven reduced collateral branching or morphological alterations of individual axons, rather than an actual increase in axon density. In agreement with this suggestion, Zhang and colleagues (2018) revealed increased coherence of axonal

organization in premanifest HD patients, as suggested by smaller OD, in tracts surrounding the basal ganglia and in the internal and external capsule, which form part of the CST. This in turn indicates the presence of compensatory pruning of axons in WM regions. Additionally, such suggestion is consistent with previous evidence of morphological alterations in the neurons of R6/2 mice, which present smaller diameter dendritic shafts, smaller somatic cross-sectional areas, and decreased diameter of the dendritic fields (Klapstein et al., 2001). TEM results in Chapter 5 indicated that neurons in R6/1 mice present an increased number of thinner axons compared to WT littermates, thus lending further support to the presence of a process of morphological alteration of fibres.

Alternatively, increases in FR may reflect the presence of tissue swelling in the HD brain. This suggestion is supported by the animal work described in Chapter 5, which showed increased WM volume in areas partially overlapping with regions of increased FR. The presence of brain oedema and tissue swelling, which occur in the disease (De Paepe et al., 2019), have indeed been shown to bias brain atrophy measurements (Andravizou et al., 2019). Accordingly, swelling of glial cells and axons may lead to increased FR by reducing extracellular fluid and thus causing reduced diffusion in the extra-axonal space (Arfanakis et al., 2002; Stidworthy et al., 2003).

Accordingly, previous evidence demonstrated increased iron levels in the left CST of premanifest HD patients (Phillips et al., 2015), proposed to reflect an homeostatic increase in oligodendrocytes to repair myelin damage. In turn, myelin breakdown leads to axon swelling (Payne et al., 2012). Additionally, previous studies have demonstrated a striking increase in axonal swelling in mouse models of HD, that were shown to precede cell body, dendrite, and synapse degeneration (Marangoni et al., 2014). Overall, the presence of axon swelling due to myelin breakdown is consistent with the Demyelination Hypothesis of HD, and with the idea

that the premanifest HD brain is continually trying to remyelinate in a losing attempt to compensate for the disease-related myelin loss (Bartzokis et al., 2007).

Generally, these findings indicate the presence of axonal alterations in the HD brain. It is possible that axons in HD develop normally but then undergo alterations associated with the disease process, or that such abnormalities arise in the postnatal development of axons. The trend for a positive association between FR in the CST and cognitive performance observed in premanifest patients suggests that, at least at the premanifest of the disease these alterations reflect a compensatory response rather than a disease-related change. However, findings of increased WM volume in R6/1 mice suggest the presence of axonal swelling, and thus of a disease-related response. Therefore, future studies are needed to clarify the neurobiological underpinning of these findings and how such changes relate to each other within the time course of HD and its clinical symptoms.

### **7.3.3. FR from CHARMED and $f_m$ from FDM: novel HD imaging biomarkers?**

For the first time in the HD literature, I have observed increased FR in the WM of premanifest HD patients. Crucially, findings from the R6/1 mouse model provided cross-species convergence in also showing an increase in this measure. This points to the potential of FR as a novel MRI biomarker of HD-associated changes in WM microstructure.

Biomarkers constitute the most important tool of translational science in medicine, thus the development of biomarkers that are useful and accessible in both animal models and humans affords improved translation of animal findings into humans and, likewise, the back-translation of imaging methods from humans to animal models (Wendler & Wehling, 2010). Therefore, while inherent differences between species remain, and though the study on R6/1

mice was carried out *ex vivo*, the present findings may represent an important preliminary step in the establishment of FR as a novel *in vivo* imaging biomarker of WM pathology in HD.

As well as FR's potential for aiding understanding of HD pathogenesis and progression, and as a possible biomarker for clinical trials, the promise of  $f_m$  from FDM for the *in vivo* quantification of myelin breakdown in HD was demonstrated in Chapter 4. Importantly, results obtained with  $f_m$  converged with the MTR findings in Chapter 3 in suggesting a reduction in myelin content in the posterior callosum of premanifest HD patients.

Quantitative MRI of myelin affords valuable insight into myelin alterations and is thus of particular interest for the evaluation of myelin changes in the HD brain. While previous *in vivo* investigations of WM changes in HD have predominantly employed indices from DT-MRI (Pierpaoli and Basser 1996), or magnetization transfer ratio (MTR) imaging (Henkelman, Stanisz, and Graham 2001), these indices may be influenced by a multitude of processes affecting tissue microstructure and biochemistry (Beaulieu 2002; De Santis et al. 2014; Harsan et al. 2006; Wheeler-Kingshott and Cercignani 2009). On the other hand, FDM and the three-pool modelling of the mGRE signal afford improved WM compartmental specificity, and estimate  $f_m$  as a marker of myelin content. Notably, histological evidence shows that this metric is less sensitive to concomitant pathological processes such as inflammation (Gareau et al. 2000), suggesting that this may be a more specific measure of tissue myelination. This in turn stresses the strong potential of this method for better understanding HD-associated alterations in WM myelin.

#### **7.3.4. Drumming rhythm training: possible therapeutic approach to symptomatic HD?**

Another important finding of this Thesis consisted in demonstrating the potential of two months of drumming and rhythm exercises to result in WM microstructural benefits in

HD, as indicated by a significantly greater training-associated change in apparent myelin in patients with HD relative to healthy controls. Whilst the current results require replication in a larger patient group with an appropriately matched patient control group, they suggest that that cognitive-motor stimulation may be exploited for future therapeutics aiming to delay disease progression.

The development of symptomatic therapies to aid patients in managing their symptoms is of fundamental importance even in an era in which developments in gene therapy targeting *mHTT* expression have generated much excitement. Such approaches have indeed yet to be proven to lead to measurable changes in disease progression (Barker & Mason, 2019), with many doubts still lingering, for example on the relative strength of different approaches and the possible side effects of each therapy (Shannon, 2020). Crucially, these treatments aim to modify and not cure the disease, and while symptomatic therapies for HD exist, their effectiveness varies between patients and may lead to clinically significant side-effects (Barker & Mason, 2019). On the other hand, cognitive and motor training has no significant side-effects and could be used in combination with gene modifying, drug or transplant therapies.

### **7.3.5. The importance of a translational neuroimaging approach**

Findings from animal models of HD need to be considered while keeping in mind the inherent differences between these animal models and human patients. Specifically, the equivalent and divergent features of the brain for different species need to be understood to ensure that data extrapolation is performed rationally. Additionally, mouse models are simply models of disease, as demonstrated by the differences in neuropathology and phenotype across different models (Steventon, 2014). This in turn implies that results seen in HD patients might not be evident in, or relevant, in mouse models of the disease.

Nevertheless, work using HD mouse models does have translational potential. In this context, especially useful are techniques that do not require invasive procedures to be measured, and can be applied sequentially; this in turn reduces the sample size needed for conclusions to be drawn (Wendler & Wehling, 2010), and is therefore in good accordance with the 3Rs in preclinical research: refine, reduce and replace (Flecknell, 2002). Accordingly, small-animal preclinical imaging affords non-invasive, longitudinal studies, which in turn are associated with reduced biological variability and enable a substantial decrease in the number of animals without losing statistical power (Cunha et al., 2014; Koo et al., 2006). Additionally, preclinical imaging studies use almost the same technologies in terms of hardware and software settings as for human patients and hence, might result in a more rapid translation.

In the present experimental work, an effort was made to ensure the pulse sequences were as similar as possible between HD patients and R6/1 mice in order for comparisons to be drawn. As shown in the above sections, a number of common findings emerged in patients and R6/1 mice, supporting the view that the HD gene affects WM microstructure at different stages in the disease course. This stresses the usefulness of examining consistencies across species with regards to the effects of the mutation, to then probe the biophysical basis of imaging results with *in vitro* techniques not possible in most human studies. Additionally, as most experimental evidence about histological alterations in HD is based on mouse models (Xiang et al., 2011), the ability to investigate WM microstructure in HD *in vivo* through neuroimaging is critical to understanding HD pathogenesis and progression (Estevez-Fraga et al., 2021).

### **7.3.6. Conclusions and future directions**

The conclusions of this Thesis can be summarized as follows:

- Measurable and significant differences in callosal microstructure are present in the premanifest HD brain, likely reflecting myelin alterations.
- Callosal changes are present before alterations in proxy metrics of axon density can be detected in this tract, thus suggesting that WM impairment in HD unlikely reflects solely Wallerian degeneration or a secondary result of neuronal cell death in GM, and may instead represent an independent factor to HD pathology.
- Results are broadly consistent with the Demyelination Hypothesis of HD (Bartzokis et al. 2007), and the suggestion that *mHTT* leads to premature myelin breakdown in HD, affecting early- and heavily-myelinated fibres, such as those in the callosal isthmus, first (Bartzokis et al., 2007).
- Myelin alterations likely reflect a dysregulation of the temporal profile of myelination and are probably a direct result of the mutation, rather than just being a result of disease progression.
- Outside the callosum, other alterations can be detected, likely reflecting axonal alterations such as axonal swelling and/or a process of compensatory reorganization or selective pruning of fibres, such as pathologically-driven reduced collateral branching or morphological alterations of individual axons.
- Later in disease progression, WM microstructure changes seem more widespread, thus pointing to a progressive spread of alterations across the HD brain as the disease progresses. This finding is in agreement with the Demyelination Hypothesis (Bartzokis et al. 2007).
- These changes may reflect early neuronal dysfunction (Rosas et al., 2010) and/or a neurodevelopmental component to the pathogenesis of HD, as precursor to the more global neurodegeneration process (Barnat et al., 2020; Jin et al., 2015; Nopoulos et al., 2010; Phillips et al., 2014).

- Behavioural stimulation may be exploited for future therapeutics aiming to delay disease progression or as symptomatic therapy.

Future studies could investigate the longitudinal evolution of changes in FR in the HD brain, to further understand axon microstructure changes in this disease. Following young premanifest subjects longitudinally will also help addressing the possibility of toxic myelin levels in the premanifest HD brain because of pathological CAG repeats size. Finally, future studies should attempt to apply  $f_m$  to anterior callosal portions to clarify the finding of MTR in premanifest patients in this work.

Overall, findings from this Thesis suggest that an enhanced understanding of the mechanisms underlying WM abnormalities could shed light on new therapeutic approaches for HD. Therefore, intervention strategies should be expanded from the current neuro-centric focus of most therapeutic strategies to include oligodendroglial targets (Bardile et al., 2019). Indeed, these data suggest that directly targeting WM pathology could be beneficial for HD. In many neurodegenerative diseases such as Alzheimer's and Parkinson's disease, WM disturbance starts before other pathological changes are evident (Bartzokis et al., 2007, 2010).

Similarly, this work demonstrated that in HD, critical pathogenic events are present prior to clinical onset of the disease, and there might therefore be a decades-long period in which therapeutic intervention could change the course of the disease. Notably, though much of our understanding of HD pathology will increasingly rely on advanced neuroimaging techniques, this reliance also stresses the importance to remember and address the shortcomings of these approaches.

# Appendix 1

## Solutions

### A1.1. Chemical-grade Phosphate Buffer Saline (PBS)

- 950 ml Distilled water
- 9.5 ml Sodium Phosphate Monobasic Dihydrate 0.2 M 31.2 g / l (Sigma) 40.5 ml Sodium Phosphate Monobasic Dihydrate 0.2 M 28.4 g / l (Sigma) 8.0 g Sodium Chloride (Sigma)
- 0.2 g Potassium Chloride (Sigma)
- pH 7.4

### A.1.2. Paraformaldehyde solution (PFA)

- 40g PFA (4%)
- 1 L Prewash buffer
- Heat to dissolve
- pH 7.3 (orthophosphoric acid)

### A.1.3. Sucrose solution

- 25 g sucrose (Fisher Scientific)
- 100 ml phosphate buffered saline (Sigma)

## References

- Abe, O., Takao, H., Gono, W., Sasaki, H., Murakami, M., Kabasawa, H., Kawaguchi, H., Goto, M., Yamada, H., & Yamasue, H. (2010). Voxel-based analysis of the diffusion tensor. *Neuroradiology*, *52*(8), 699–710.
- Aboitiz, F., Scheibel, A. B., Fisher, R. S., & Zaidel, E. (1992). Fiber composition of the human corpus callosum. *Brain Research*, *598*(1–2), 143–153.
- Adjeroud, N., Besnard, J., El Massioui, N., Verny, C., Prudean, A., Scherer, C., Gohier, B., Bonneau, D., & Allain, P. (2016). Theory of mind and empathy in preclinical and clinical Huntington's disease. *Social Cognitive and Affective Neuroscience*, *11*(1), 89–99. <https://doi.org/10.1093/scan/nsv093>
- Alaerts, K., Nackaerts, E., Meyns, P., Swinnen, S. P., & Wenderoth, N. (2011). Action and Emotion Recognition from Point Light Displays: An Investigation of Gender Differences. *PLOS ONE*, *6*(6), e20989. <https://doi.org/10.1371/journal.pone.0020989>
- Albin, R. L., Qin, Y., Young, A. B., Penney, J. B., & Chesselet, M. F. (1991). Preproenkephalin messenger RNA-containing neurons in striatum of patients with symptomatic and presymptomatic Huntington's disease: An in situ hybridization study. *Annals of Neurology*, *30*(4), 542–549. <https://doi.org/10.1002/ana.410300406>
- Albin, R. L., Reiner, A., Anderson, K. D., Dure, L. S., Handelin, B., Balfour, R., Whetsell, W. O., Penney, J. B., & Young, A. B. (1992). Preferential loss of striato-external pallidal projection neurons in presymptomatic Huntington's disease. *Annals of Neurology*, *31*(4), 425–430. <https://doi.org/10.1002/ana.410310412>
- Albin, R. L., Young, A. B., Penney, J. B., Handelin, B., Balfour, R., Anderson, K. D., Markel, D. S., Tourtellotte, W. W., & Reiner, A. (1990). Abnormalities of striatal projection neurons and N-methyl-D-aspartate receptors in presymptomatic

- Huntington's disease. *The New England Journal of Medicine*, 322(18), 1293–1298.  
<https://doi.org/10.1056/NEJM199005033221807>
- Alexander, A. L., Hasan, K. M., Lazar, M., Tsuruda, J. S., & Parker, D. L. (2001). Analysis of partial volume effects in diffusion-tensor MRI. *Magnetic Resonance in Medicine: An Official Journal of the International Society for Magnetic Resonance in Medicine*, 45(5), 770–780.
- Alexander, A. L., Hurley, S. A., Samsonov, A. A., Adluru, N., Hosseinbor, A. P., Mossahebi, P., Tromp, D. P. M., Zakszewski, E., & Field, A. S. (2011). Characterization of Cerebral White Matter Properties Using Quantitative Magnetic Resonance Imaging Stains. *Brain Connectivity*, 1(6), 423–446. <https://doi.org/10.1089/brain.2011.0071>
- Alexander, A. L., Lee, J. E., Lazar, M., & Field, A. S. (2007). Diffusion Tensor Imaging of the Brain. *Neurotherapeutics: The Journal of the American Society for Experimental NeuroTherapeutics*, 4(3), 316–329. <https://doi.org/10.1016/j.nurt.2007.05.011>
- Alexander, D. C., Zikic, D., Ghosh, A., Tanno, R., Wottschel, V., Zhang, J., Kaden, E., Dyrby, T. B., Sotiropoulos, S. N., Zhang, H., & Criminisi, A. (2017). Image quality transfer and applications in diffusion MRI. *NeuroImage*, 152, 283–298.  
<https://doi.org/10.1016/j.neuroimage.2017.02.089>
- Alexander, D. C., Zikic, D., Zhang, J., Zhang, H., & Criminisi, A. (2014). Image quality transfer via random forest regression: Applications in diffusion MRI. *Medical Image Computing and Computer-Assisted Intervention: MICCAI ... International Conference on Medical Image Computing and Computer-Assisted Intervention*, 17(Pt 3), 225–232. [https://doi.org/10.1007/978-3-319-10443-0\\_29](https://doi.org/10.1007/978-3-319-10443-0_29)
- Allain, P., Havet-Thomassin, V., Verny, C., Gohier, B., Lancelot, C., Besnard, J., Fasotti, L., & Le Gall, D. (2011). Evidence for deficits on different components of theory of mind

in Huntington's disease. *Neuropsychology*, 25(6), 741–751.

<https://doi.org/10.1037/a0024408>

Andersson, J. L., Jenkinson, M., & Smith, S. (2007). Non-linear registration, aka spatial normalisation. *FMRIB Technical Report TR07JA2*, 22.

Andersson, J. L. R., Skare, S., & Ashburner, J. (2003). How to correct susceptibility distortions in spin-echo echo-planar images: Application to diffusion tensor imaging. *NeuroImage*, 20(2), 870–888. [https://doi.org/10.1016/S1053-8119\(03\)00336-7](https://doi.org/10.1016/S1053-8119(03)00336-7)

Andersson, J. L. R., & Sotiropoulos, S. N. (2016). An integrated approach to correction for off-resonance effects and subject movement in diffusion MR imaging. *NeuroImage*, 125, 1063–1078. <https://doi.org/10.1016/j.neuroimage.2015.10.019>

Andravizou, A., Dardiotis, E., Artemiadis, A., Sokratous, M., Siokas, V., Tsouris, Z., Aloizou, A.-M., Nikolaidis, I., Bakirtzis, C., Tsivgoulis, G., Deretzi, G., Grigoriadis, N., Bogdanos, D. P., & Hadjigeorgiou, G. M. (2019). Brain atrophy in multiple sclerosis: Mechanisms, clinical relevance and treatment options. *Autoimmunity Highlights*, 10(1), 7. <https://doi.org/10.1186/s13317-019-0117-5>

Andrews, S. C., Domínguez, J. F., Mercieca, E.-C., Georgiou-Karistianis, N., & Stout, J. C. (2015). Cognitive interventions to enhance neural compensation in Huntington's disease. *Neurodegenerative Disease Management*, 5(2), 155–164.

Antonsen, B. T., Jiang, Y., Veraart, J., Qu, H., Nguyen, H. P., Sijbers, J., von Hörsten, S., Johnson, G. A., & Leergaard, T. B. (2013). Altered diffusion tensor imaging measurements in aged transgenic Huntington disease rats. *Brain Structure & Function*, 218(3), 767–778. <https://doi.org/10.1007/s00429-012-0427-0>

Arfanakis, K., Haughton, V. M., Carew, J. D., Rogers, B. P., Dempsey, R. J., & Meyerand, M. E. (2002). Diffusion tensor MR imaging in diffuse axonal injury. *AJNR. American Journal of Neuroradiology*, 23(5), 794–802.

- Armonk, N. (2011). *IBM Corp. SPSS Statistics for windows, Version 20.0.*
- Arrasate, M., & Finkbeiner, S. (2012). Protein aggregates in Huntington's disease. *Experimental Neurology*, *238*(1), 1–11.  
<https://doi.org/10.1016/j.expneurol.2011.12.013>
- Arrasate, M., Mitra, S., Schweitzer, E. S., Segal, M. R., & Finkbeiner, S. (2004). Inclusion body formation reduces levels of mutant huntingtin and the risk of neuronal death. *Nature*, *431*(7010), 805–810. <https://doi.org/10.1038/nature02998>
- Ashburner, J., & Friston, K. J. (2000). Voxel-based morphometry—The methods. *NeuroImage*, *11*(6 Pt 1), 805–821. <https://doi.org/10.1006/nimg.2000.0582>
- Assaf, Y. (2008). Can we use diffusion MRI as a bio-marker of neurodegenerative processes? *Bioessays*, *30*(11-12), 1235–1245.
- Assaf, Y., & Basser, P. J. (2005). Composite hindered and restricted model of diffusion (CHARMED) MR imaging of the human brain. *NeuroImage*, *27*(1), 48–58.  
<https://doi.org/10.1016/j.neuroimage.2005.03.042>
- Avants, B. B., Tustison, N. J., Song, G., Cook, P. A., Klein, A., & Gee, J. C. (2011). A reproducible evaluation of ANTs similarity metric performance in brain image registration. *NeuroImage*, *54*(3), 2033–2044.  
<https://doi.org/10.1016/j.neuroimage.2010.09.025>
- Aylward, E. H. (2014). Magnetic resonance imaging striatal volumes: A biomarker for clinical trials in Huntington's disease. *Movement Disorders: Official Journal of the Movement Disorder Society*, *29*(11), 1429–1433. <https://doi.org/10.1002/mds.26013>
- Aylward, E. H., Harrington, D. L., Mills, J. A., Nopoulos, P. C., Ross, C. A., Long, J. D., Liu, D., Westervelt, H. K., & Paulsen, J. S. (2013). Regional Atrophy Associated with Cognitive and Motor Function in Prodromal Huntington Disease. *Journal of Huntington's Disease*, *2*(4), 477–489. <https://doi.org/10.3233/JHD-130076>

- Aylward, E. H., Liu, D., Nopoulos, P. C., Ross, C. A., Pierson, R. K., Mills, J. A., Long, J. D., Paulsen, J. S., & PREDICT-HD Investigators and Coordinators of the Huntington Study Group. (2012). Striatal volume contributes to the prediction of onset of Huntington disease in incident cases. *Biological Psychiatry, 71*(9), 822–828.  
<https://doi.org/10.1016/j.biopsych.2011.07.030>
- Aylward, E. H., Nopoulos, P. C., Ross, C. A., Langbehn, D. R., Pierson, R. K., Mills, J. A., Johnson, H. J., Magnotta, V. A., Juhl, A. R., Paulsen, J. S., & PREDICT-HD Investigators and Coordinators of Huntington Study Group. (2011). Longitudinal change in regional brain volumes in prodromal Huntington disease. *Journal of Neurology, Neurosurgery, and Psychiatry, 82*(4), 405–410.  
<https://doi.org/10.1136/jnnp.2010.208264>
- Bach, M., Laun, F. B., Leemans, A., Tax, C. M. W., Biessels, G. J., Stieltjes, B., & Maier-Hein, K. H. (2014). Methodological considerations on tract-based spatial statistics (TBSS). *NeuroImage, 100*, 358–369.  
<https://doi.org/10.1016/j.neuroimage.2014.06.021>
- Baddeley, A. (n.d.). *Exploring the Central Executive*. 24.
- Baldo, J. V., Shimamura, A. P., Delis, D. C., Kramer, J., & Kaplan, E. (2001). Verbal and design fluency in patients with frontal lobe lesions. *Journal of the International Neuropsychological Society, 7*(5), 586–596.  
<https://doi.org/10.1017/S1355617701755063>
- Barazany, D., Basser, P. J., & Assaf, Y. (2009). In vivo measurement of axon diameter distribution in the corpus callosum of rat brain. *Brain, 132*(5), 1210–1220.  
<https://doi.org/10.1093/brain/awp042>
- Bardile, C. F., Garcia-Miralles, M., Caron, N. S., Rayan, N. A., Langley, S. R., Harmston, N., Rondelli, A. M., Teo, R. T. Y., Walth, S., & Anderson, L. M. (2019). Intrinsic mutant

- HTT-mediated defects in oligodendroglia cause myelination deficits and behavioral abnormalities in Huntington disease. *Proceedings of the National Academy of Sciences*, 116(19), 9622–9627.
- Barker, R., & Mason, S. L. (2019). The hunt for better treatments for Huntington’s disease. *The Lancet Neurology*, 18(2), 131–133. [https://doi.org/10.1016/S1474-4422\(18\)30448-4](https://doi.org/10.1016/S1474-4422(18)30448-4)
- Barkhof, F. (1999). MRI in multiple sclerosis: Correlation with expanded disability status scale (EDSS). *Multiple Sclerosis Journal*, 5(4), 283–286.
- Barnat, M., Capizzi, M., Aparicio, E., Boluda, S., Wennagel, D., Kacher, R., Kassem, R., Lenoir, S., Agasse, F., Braz, B. Y., Liu, J.-P., Ighil, J., Tessier, A., Zeitlin, S. O., Duyckaerts, C., Dommergues, M., Durr, A., & Humbert, S. (2020). Huntington’s disease alters human neurodevelopment. *Science*, 369(6505), 787–793. <https://doi.org/10.1126/science.aax3338>
- Baron-Cohen, S., Wheelwright, S., Hill, J., Raste, Y., & Plumb, I. (2001). The “Reading the Mind in the Eyes” Test Revised Version: A Study with Normal Adults, and Adults with Asperger Syndrome or High-functioning Autism. *Journal of Child Psychology and Psychiatry*, 42(2), 241–251. <https://doi.org/10.1111/1469-7610.00715>
- Barrett, R. L., Dawson, M., Dyrby, T. B., Krug, K., Ptito, M., D’Arceuil, H., Croxson, P. L., Johnson, P. J., Howells, H., & Forkel, S. J. (2020). Differences in frontal network anatomy across primate species. *Journal of Neuroscience*, 40(10), 2094–2107.
- Bartzokis, G. (2012). Neuroglialpharmacology: Myelination As A Shared Mechanism of Action of Psychotropic Treatments. *Neuropharmacology*, 62(7), 2137–2153. <https://doi.org/10.1016/j.neuropharm.2012.01.015>
- Bartzokis, G., Cummings, J., Perlman, S., Hance, D. B., & Mintz, J. (1999). Increased basal ganglia iron levels in Huntington disease. *Archives of Neurology*, 56(5), 569–574.

- Bartzokis, G., Lu, P. H., Tingus, K., Mendez, M. F., Richard, A., Peters, D. G., Oluwadara, B., Barrall, K. A., Finn, J. P., Villablanca, P., Thompson, P. M., & Mintz, J. (2010). Lifespan trajectory of myelin integrity and maximum motor speed. *Neurobiology of Aging*, *31*(9), 1554–1562. <https://doi.org/10.1016/j.neurobiolaging.2008.08.015>
- Bartzokis, G., Lu, P. H., Tishler, T. A., Fong, S. M., Oluwadara, B., Finn, J. P., Huang, D., Bordelon, Y., Mintz, J., & Perlman, S. (2007). Myelin breakdown and iron changes in Huntington's disease: Pathogenesis and treatment implications. *Neurochemical Research*, *32*(10), 1655–1664. <https://doi.org/10.1007/s11064-007-9352-7>
- Bartzokis, G., & Tishler, T. A. (2000). MRI evaluation of basal ganglia ferritin iron and neurotoxicity in Alzheimer's and Huntington's disease. *Cellular and Molecular Biology (Noisy-Le-Grand, France)*, *46*(4), 821–833.
- Basser, P. J. (1995). Inferring microstructural features and the physiological state of tissues from diffusion-weighted images. *NMR in Biomedicine*, *8*(7), 333–344.
- Basser, P. J., & Jones, D. K. (2002). Diffusion-tensor MRI: theory, experimental design and data analysis—a technical review. *NMR in Biomedicine: An International Journal Devoted to the Development and Application of Magnetic Resonance In Vivo*, *15*(7-8), 456–467.
- Basser, P. J., Mattiello, J., & LeBihan, D. (1994). MR diffusion tensor spectroscopy and imaging. *Biophysical Journal*, *66*(1), 259–267.
- Basser, P. J., Pajevic, S., Pierpaoli, C., Duda, J., & Aldroubi, A. (2000). In vivo fiber tractography using DT-MRI data. *Magnetic Resonance in Medicine*, *44*(4), 625–632. [https://doi.org/10.1002/1522-2594\(200010\)44:4<625::AID-MRM17>3.0.CO;2-O](https://doi.org/10.1002/1522-2594(200010)44:4<625::AID-MRM17>3.0.CO;2-O)
- Bastiani, M., Shah, N. J., Goebel, R., & Roebroek, A. (2012). Human cortical connectome reconstruction from diffusion weighted MRI: the effect of tractography algorithm. *Neuroimage*, *62*(3), 1732–1749.

- Bates, G. P., Dorsey, R., Gusella, J. F., Hayden, M. R., Kay, C., Leavitt, B. R., Nance, M., Ross, C. A., Scahill, R. I., Wetzel, R., Wild, E. J., & Tabrizi, S. J. (2015). Huntington disease. *Nature Reviews Disease Primers*, *1*(1), 1–21.  
<https://doi.org/10.1038/nrdp.2015.5>
- Baxa, M., Hruska-Plochan, M., Juhas, S., Vodicka, P., Pavlok, A., Juhasova, J., Miyanochara, A., Nejime, T., Klima, J., & Macakova, M. (2013). A transgenic minipig model of Huntington's Disease. *Journal of Huntington's Disease*, *2*(1), 47–68.
- Bayram-Weston, Z., Jones, L., Dunnett, S. B., & Brooks, S. P. (2012). Light and electron microscopic characterization of the evolution of cellular pathology in the R6/1 Huntington's disease transgenic mice. *Brain Research Bulletin*, *88*(2–3), 104–112.  
<https://doi.org/10.1016/j.brainresbull.2011.07.009>
- Beal, M. F. (2005). Mitochondria take center stage in aging and neurodegeneration. *Annals of Neurology: Official Journal of the American Neurological Association and the Child Neurology Society*, *58*(4), 495–505.
- Beaulieu, C. (2002). The basis of anisotropic water diffusion in the nervous system—A technical review. *NMR in Biomedicine*, *15*(7–8), 435–455.  
<https://doi.org/10.1002/nbm.782>
- Beglinger, L. J., Prest, L., Mills, J. A., Paulsen, J. S., Smith, M. M., Gonzalez-Alegre, P., Rowe, K. C., Nopoulos, P., & Uc, E. Y. (2012). Clinical predictors of driving status in Huntington disease. *Movement Disorders: Official Journal of the Movement Disorder Society*, *27*(9), 1146–1152. <https://doi.org/10.1002/mds.25101>
- Behrens, T. E. J., Berg, H. J., Jbabdi, S., Rushworth, M. F. S., & Woolrich, M. W. (2007). Probabilistic diffusion tractography with multiple fibre orientations: What can we gain? *NeuroImage*, *34*(1), 144–155. <https://doi.org/10.1016/j.neuroimage.2006.09.018>

- Behrens, T. E. J., Woolrich, M. W., Jenkinson, M., Johansen-Berg, H., Nunes, R. G., Clare, S., Matthews, P. M., Brady, J. M., & Smith, S. M. (2003). Characterization and propagation of uncertainty in diffusion-weighted MR imaging. *Magnetic Resonance in Medicine: An Official Journal of the International Society for Magnetic Resonance in Medicine*, *50*(5), 1077–1088.
- Bells, S., Cercignani, M., Deoni, S., Assaf, Y., Pasternak, O., Evans, C., Leemans, A., & Jones, D. (2011). *Tractometry—comprehensive multi-modal quantitative assessment of white matter along specific tracts*. *678*, 1.
- Ben-Amitay, S., Jones, D. K., & Assaf, Y. (2012). Motion correction and registration of high b-value diffusion weighted images. *Magnetic Resonance in Medicine*, *67*(6), 1694–1702. <https://doi.org/10.1002/mrm.23186>
- Bengtsson, S. L., Nagy, Z., Skare, S., Forsman, L., Forssberg, H., & Ullén, F. (2005). Extensive piano practicing has regionally specific effects on white matter development. *Nature Neuroscience*, *8*(9), 1148–1150. <https://doi.org/10.1038/nn1516>
- Benjamini, Y., & Hochberg, Y. (1995). Controlling the False Discovery Rate: A Practical and Powerful Approach to Multiple Testing. *Journal of the Royal Statistical Society. Series B (Methodological)*, *57*(1), 289–300. JSTOR.
- Berthold, C.-H., Nilsson, I., & Rydmark, M. (1983). Axon diameter and myelin sheath thickness in nerve fibres of the ventral spinal root of the seventh lumbar nerve of the adult and developing cat. *Journal of Anatomy*, *136*(Pt 3), 483.
- Bhide, P. G., Day, M., Sapp, E., Schwarz, C., Sheth, A., Kim, J., Young, A. B., Penney, J., Golden, J., Aronin, N., & DiFiglia, M. (1996). Expression of Normal and Mutant Huntingtin in the Developing Brain. *The Journal of Neuroscience*, *16*(17), 5523–5535. <https://doi.org/10.1523/JNEUROSCI.16-17-05523.1996>

- Blezer, E. L., Bauer, J., Brok, H. P., Nicolay, K., & 't Hart, B. A. (2007). Quantitative MRI-pathology correlations of brain white matter lesions developing in a non-human primate model of multiple sclerosis. *NMR in Biomedicine: An International Journal Devoted to the Development and Application of Magnetic Resonance In Vivo*, *20*(2), 90–103.
- Blockx, I., Van Camp, N., Verhoye, M., Boisgard, R., Dubois, A., Jego, B., Jonckers, E., Raber, K., Siquier, K., Kuhnast, B., Dollé, F., Nguyen, H. P., Von Hörsten, S., Tavitian, B., & Van der Linden, A. (2011). Genotype specific age related changes in a transgenic rat model of Huntington's disease. *NeuroImage*, *58*(4), 1006–1016. <https://doi.org/10.1016/j.neuroimage.2011.07.007>
- Blockx, I., Verhoye, M., Van Audekerke, J., Bergwerf, I., Kane, J. X., Delgado Y Palacios, R., Veraart, J., Jeurissen, B., Raber, K., von Hörsten, S., Ponsaerts, P., Sijbers, J., Leergaard, T. B., & Van der Linden, A. (2012). Identification and characterization of Huntington related pathology: An in vivo DKI imaging study. *NeuroImage*, *63*(2), 653–662. <https://doi.org/10.1016/j.neuroimage.2012.06.032>
- Bodini, B., & Ciccarelli, O. (2014). Chapter 11—Diffusion MRI in Neurological Disorders. In H. Johansen-Berg & T. E. J. Behrens (Eds.), *Diffusion MRI (Second Edition)* (pp. 241–255). Academic Press. <https://doi.org/10.1016/B978-0-12-396460-1.00011-1>
- Borlongan, C. V., Koutouzis, T. K., & Sanberg, P. R. (1997). 3-Nitropropionic acid animal model and Huntington's disease. *Neuroscience & Biobehavioral Reviews*, *21*(3), 289–293. [https://doi.org/10.1016/S0149-7634\(96\)00027-9](https://doi.org/10.1016/S0149-7634(96)00027-9)
- Bourbon-Teles, J., Bells, S., Jones, D. K., Coulthard, E., Rosser, A., & Metzler-Baddeley, C. (2017). Myelin breakdown in human Huntington's disease: Multi-modal evidence from diffusion MRI and quantitative magnetization transfer. *Neuroscience*. <https://doi.org/10.1016/j.neuroscience.2017.05.042>

- Bourbon-Teles, J., Bells, S., Jones, D. K., Coulthard, E., Rosser, A., & Metzler-Baddeley, C. (2019). Myelin Breakdown in Human Huntington's Disease: Multi-Modal Evidence from Diffusion MRI and Quantitative Magnetization Transfer. *Non-Invasive MRI Windows on Brain Inflammation*, 403, 79–92.  
<https://doi.org/10.1016/j.neuroscience.2017.05.042>
- Brochet, B., & Dousset, V. (1999). Pathological correlates of magnetization transfer imaging abnormalities in animal models and humans with multiple sclerosis. *Neurology*, 53(5 Suppl 3), S12-7.
- Brooks, S. P., Janghra, N., Workman, V. L., Bayram-Weston, Z., Jones, L., & Dunnett, S. B. (2012). Longitudinal analysis of the behavioural phenotype in R6/1 (C57BL/6J) Huntington's disease transgenic mice. *Brain Research Bulletin*, 88(2–3), 94–103.  
<https://doi.org/10.1016/j.brainresbull.2011.01.010>
- Brouillet, E., Jenkins, B. G., Hyman, B. T., Ferrante, R. J., Kowall, N. W., Srivastava, R., Roy, D. S., Rosen, B. R., & Beal, M. F. (1993). Age-dependent vulnerability of the striatum to the mitochondrial toxin 3-nitropropionic acid. *Journal of Neurochemistry*, 60(1), 356–359. <https://doi.org/10.1111/j.1471-4159.1993.tb05859.x>
- Browne, S. E. (2008). Mitochondria and Huntington's disease pathogenesis: Insight from genetic and chemical models. *Annals of the New York Academy of Sciences*, 1147(1), 358–382.
- Brundin, P., Melki, R., & Kopito, R. (2010). Prion-like transmission of protein aggregates in neurodegenerative diseases. *Nature Reviews. Molecular Cell Biology*, 11(4), 301–307.  
<https://doi.org/10.1038/nrm2873>
- Brüne, M., Blank, K., Witthaus, H., & Saft, C. (2011). “Theory of mind” is impaired in Huntington's disease. *Movement Disorders*, 26(4), 671–678.  
<https://doi.org/10.1002/mds.23494>

- Bürgel, U., Amunts, K., Hoemke, L., Mohlberg, H., Gilsbach, J. M., & Zilles, K. (2006). White matter fiber tracts of the human brain: Three-dimensional mapping at microscopic resolution, topography and intersubject variability. *Neuroimage*, *29*(4), 1092–1105.
- Ca, R., A, P., J, K., & J, B. (2014). Determinants of functional disability in Huntington's disease: Role of cognitive and motor dysfunction. *Movement Disorders : Official Journal of the Movement Disorder Society*, *29*(11), 1351–1358.  
<https://doi.org/10.1002/mds.26012>
- Caeyenberghs, K., Clemente, A., Imms, P., Egan, G., Hocking, D. R., Leemans, A., Metzler-Baddeley, C., Jones, D. K., & Wilson, P. H. (2018). Evidence for Training-Dependent Structural Neuroplasticity in Brain-Injured Patients: A Critical Review. *Neurorehabilitation and Neural Repair*, *32*(2), 99–114.  
<https://doi.org/10.1177/1545968317753076>
- Caeyenberghs, K., Metzler-Baddeley, C., Foley, S., & Jones, D. K. (2016). Dynamics of the Human Structural Connectome Underlying Working Memory Training. *The Journal of Neuroscience: The Official Journal of the Society for Neuroscience*, *36*(14), 4056–4066. <https://doi.org/10.1523/JNEUROSCI.1973-15.2016>
- Cahill, L. S., Laliberté, C. L., Ellegood, J., Spring, S., Gleave, J. A., van Eede, M. C., Lerch, J. P., & Henkelman, R. M. (2012). Preparation of fixed mouse brains for MRI. *Neuroimage*, *60*(2), 933–939.
- Calabrese, E., Badea, A., Cofer, G., Qi, Y., & Johnson, G. A. (2015). A diffusion MRI tractography connectome of the mouse brain and comparison with neuronal tracer data. *Cerebral Cortex*, *25*(11), 4628–4637.
- Calder, A. J., Keane, J., Young, A. W., Lawrence, A. D., Mason, S., & Barker, R. A. (2010). The relation between anger and different forms of disgust: Implications for emotion

- recognition impairments in Huntington's disease. *Neuropsychologia*, 48(9), 2719–2729. <https://doi.org/10.1016/j.neuropsychologia.2010.05.019>
- Caminiti, R., Carducci, F., Piervincenzi, C., Battaglia-Mayer, A., Confalone, G., Visco-Comandini, F., Pantano, P., & Innocenti, G. M. (2013). Diameter, length, speed, and conduction delay of callosal axons in macaque monkeys and humans: Comparing data from histology and magnetic resonance imaging diffusion tractography. *Journal of Neuroscience*, 33(36), 14501–14511.
- Campononico, J. R., Codori, A. M., & Brandt, J. (1996). Neuropsychological stability over two years in asymptomatic carriers of the Huntington's disease mutation. *Journal of Neurology, Neurosurgery & Psychiatry*, 61(6), 621–624.
- Carroll, J. B., Lerch, J. P., Franciosi, S., Spreuw, A., Bissada, N., Henkelman, R. M., & Hayden, M. R. (2011). Natural history of disease in the YAC128 mouse reveals a discrete signature of pathology in Huntington disease. *Neurobiology of Disease*, 43(1), 257–265. <https://doi.org/10.1016/j.nbd.2011.03.018>
- Carter, R. J., Lione, L. A., Humby, T., Mangiarini, L., Mahal, A., Bates, G. P., Dunnett, S. B., & Morton, A. J. (1999). Characterization of progressive motor deficits in mice transgenic for the human Huntington's disease mutation. *The Journal of Neuroscience: The Official Journal of the Society for Neuroscience*, 19(8), 3248–3257.
- Catani, M., Howard, R. J., Pajevic, S., & Jones, D. K. (2002). Virtual in vivo interactive dissection of white matter fasciculi in the human brain. *NeuroImage*, 17(1), 77–94. <https://doi.org/10.1006/nimg.2002.1136>
- Cattell, R. B. (1966). The Scree Test For The Number Of Factors. *Multivariate Behavioral Research*, 1(2), 245–276. [https://doi.org/10.1207/s15327906mbr0102\\_10](https://doi.org/10.1207/s15327906mbr0102_10)

- Cepeda, C., Wu, N., André, V. M., Cummings, D. M., & Levine, M. S. (2007). The corticostriatal pathway in Huntington's disease. *Progress in Neurobiology*, *81*(5), 253–271. <https://doi.org/10.1016/j.pneurobio.2006.11.001>
- Cercignani, M., Giulietti, G., Dowell, N. G., Gabel, M., Broad, R., Leigh, P. N., Harrison, N. A., & Bozzali, M. (2017). Characterizing axonal myelination within the healthy population: A tract-by-tract mapping of effects of age and gender on the fiber g-ratio. *Neurobiology of Aging*, *49*, 109–118. <https://doi.org/10.1016/j.neurobiolaging.2016.09.016>
- Chamberland, M., Whittingstall, K., Fortin, D., Mathieu, D., & Descoteaux, M. (2014). Real-time multi-peak tractography for instantaneous connectivity display. *Frontiers in Neuroinformatics*, *8*. <https://doi.org/10.3389/fninf.2014.00059>
- Chan, J. C. S., Stout, J. C., & Vogel, A. P. (2019). Speech in prodromal and symptomatic Huntington's disease as a model of measuring onset and progression in dominantly inherited neurodegenerative diseases. *Neuroscience & Biobehavioral Reviews*, *107*, 450–460. <https://doi.org/10.1016/j.neubiorev.2019.08.009>
- Chomiak, T., & Hu, B. (2009). What Is the Optimal Value of the g-Ratio for Myelinated Fibers in the Rat CNS? A Theoretical Approach. *PLOS ONE*, *4*(11), e7754. <https://doi.org/10.1371/journal.pone.0007754>
- Ciarmiello, A., Cannella, M., Lastoria, S., Simonelli, M., Frati, L., Rubinsztein, D. C., & Squitieri, F. (2006). Brain white-matter volume loss and glucose hypometabolism precede the clinical symptoms of Huntington's disease. *Journal of Nuclear Medicine: Official Publication, Society of Nuclear Medicine*, *47*(2), 215–222.
- Ciarochi, J. A., Calhoun, V. D., Lourens, S., Long, J. D., Johnson, H. J., Bockholt, H. J., Liu, J., Plis, S. M., Paulsen, J. S., Turner, J. A., & PREDICT-HD Investigators and Coordinators of the Huntington Study Group. (2016). Patterns of Co-Occurring Gray

- Matter Concentration Loss across the Huntington Disease Prodrome. *Frontiers in Neurology*, 7, 147. <https://doi.org/10.3389/fneur.2016.00147>
- Concha, L., Gross, D. W., Wheatley, B. M., & Beaulieu, C. (2006). Diffusion tensor imaging of time-dependent axonal and myelin degradation after corpus callosotomy in epilepsy patients. *Neuroimage*, 32(3), 1090–1099.
- Connor, J., Menzies, S., Martin, S. S., & Mufson, E. (1990). Cellular distribution of transferrin, ferritin, and iron in normal and aged human brains. *Journal of Neuroscience Research*, 27(4), 595–611.
- Conturo, T. E., Lori, N. F., Cull, T. S., Akbudak, E., Snyder, A. Z., Shimony, J. S., McKinstry, R. C., Burton, H., & Raichle, M. E. (1999). Tracking neuronal fiber pathways in the living human brain. *Proceedings of the National Academy of Sciences*, 96(18), 10422–10427. <https://doi.org/10.1073/pnas.96.18.10422>
- Cook, L. L., Foster, P. J., Mitchell, J. R., & Karlik, S. J. (2004). In vivo 4.0-T magnetic resonance investigation of spinal cord inflammation, demyelination, and axonal damage in chronic-progressive experimental allergic encephalomyelitis. *Journal of Magnetic Resonance Imaging: An Official Journal of the International Society for Magnetic Resonance in Medicine*, 20(4), 563–571.
- Costa, R. M., Cohen, D., & Nicolelis, M. A. L. (2004). Differential corticostriatal plasticity during fast and slow motor skill learning in mice. *Current Biology: CB*, 14(13), 1124–1134. <https://doi.org/10.1016/j.cub.2004.06.053>
- Cronin, M. J., Wang, N., Decker, K. S., Wei, H., Zhu, W.-Z., & Liu, C. (2017). Exploring the origins of echo-time-dependent quantitative susceptibility mapping (QSM) measurements in healthy tissue and cerebral microbleeds. *Neuroimage*, 149, 98–113.

- Cunha, L., Horvath, I., Ferreira, S., Lemos, J., Costa, P., Vieira, D., Veres, D. S., Szigeti, K., Summavielle, T., & Máthé, D. (2014). Preclinical imaging: An essential ally in modern biosciences. *Molecular Diagnosis & Therapy*, *18*(2), 153–173.
- Davids, M., Guérin, B., Malzacher, M., Schad, L. R., & Wald, L. L. (2017). Predicting Magnetostimulation Thresholds in the Peripheral Nervous System using Realistic Body Models. *Scientific Reports*, *7*(1), 5316. <https://doi.org/10.1038/s41598-017-05493-9>
- Davies, S. W., Turmaine, M., Cozens, B. A., DiFiglia, M., Sharp, A. H., Ross, C. A., Scherzinger, E., Wanker, E. E., Mangiarini, L., & Bates, G. P. (1997). Formation of Neuronal Intranuclear Inclusions Underlies the Neurological Dysfunction in Mice Transgenic for the HD Mutation. *Cell*, *90*(3), 537–548. [https://doi.org/10.1016/S0092-8674\(00\)80513-9](https://doi.org/10.1016/S0092-8674(00)80513-9)
- Dayalu, P., & Albin, R. L. (2015). Huntington disease: Pathogenesis and treatment. *Neurologic Clinics*, *33*(1), 101–114.
- de la Monte, S. M., Vonsattel, J. P., & Richardson, E. P. (1988). Morphometric demonstration of atrophic changes in the cerebral cortex, white matter, and neostriatum in Huntington's disease. *Journal of Neuropathology and Experimental Neurology*, *47*(5), 516–525.
- De Paepe, A. E., Sierpowska, J., Garcia-Gorro, C., Martinez-Horta, S., Perez-Perez, J., Kulisevsky, J., Rodriguez-Dechicha, N., Vaquer, I., Subira, S., Calopa, M., Muñoz, E., Santacruz, P., Ruiz-Idiago, J., Mareca, C., de Diego-Balaguer, R., & Camara, E. (2019). White matter cortico-striatal tracts predict apathy subtypes in Huntington's disease. *NeuroImage: Clinical*, *24*, 101965. <https://doi.org/10.1016/j.nicl.2019.101965>

- De Santis, S., Drakesmith, M., Bells, S., Assaf, Y., & Jones, D. K. (2014). Why diffusion tensor MRI does well only some of the time: Variance and covariance of white matter tissue microstructure attributes in the living human brain. *Neuroimage*, *89*(100), 35–44. <https://doi.org/10.1016/j.neuroimage.2013.12.003>
- Dean, D. C., Sojkova, J., Hurley, S., Kecskemeti, S., Okonkwo, O., Bendlin, B. B., Theisen, F., Johnson, S. C., Alexander, A. L., & Gallagher, C. L. (2016). Alterations of Myelin Content in Parkinson's Disease: A Cross-Sectional Neuroimaging Study. *PloS One*, *11*(10), e0163774. <https://doi.org/10.1371/journal.pone.0163774>
- Della Sala, S., Gray, C., Baddeley, A., & Wilson, L. (1997). Visual Patterns Test: A test of short-term visual recall. *Thames Valley Test Company*, *40*.
- Dell'acqua, F., Scifo, P., Rizzo, G., Catani, M., Simmons, A., Scotti, G., & Fazio, F. (2010). A modified damped Richardson-Lucy algorithm to reduce isotropic background effects in spherical deconvolution. *NeuroImage*, *49*(2), 1446–1458. <https://doi.org/10.1016/j.neuroimage.2009.09.033>
- Deloire-Grassin, M., Brochet, B., Quesson, B., Delalande, C., Dousset, V., Canioni, P., & Petry, K. (2000). In vivo evaluation of remyelination in rat brain by magnetization transfer imaging. *Journal of the Neurological Sciences*, *178*(1), 10–16.
- Descoteaux, M., Deriche, R., Knosche, T. R., & Anwander, A. (2008). Deterministic and probabilistic tractography based on complex fibre orientation distributions. *IEEE Transactions on Medical Imaging*, *28*(2), 269–286.
- Dexter, D. T., Carayon, A., Javoy-Agid, F., Agid, Y., Wells, F. R., Daniel, S. E., Lees, A. J., Jenner, P., & Marsden, C. D. (1991). Alterations in the levels of iron, ferritin and other trace metals in Parkinson's disease and other neurodegenerative diseases affecting the basal ganglia. *Brain: A Journal of Neurology*, *114* ( Pt 4), 1953–1975.

- Dhollander, T., Raffelt, D., & Connelly, A. (2016). *Unsupervised 3-tissue response function estimation from single-shell or multi-shell diffusion MR data without a co-registered T1 image*. 5, 5.
- Di Paola, M., Luders, E., Cherubini, A., Sanchez-Castaneda, C., Thompson, P. M., Toga, A. W., Caltagirone, C., Orobello, S., Elifani, F., Squitieri, F., & Sabatini, U. (2012). Multimodal MRI analysis of the corpus callosum reveals white matter differences in presymptomatic and early Huntington's disease. *Cerebral Cortex (New York, N.Y.: 1991)*, 22(12), 2858–2866. <https://doi.org/10.1093/cercor/bhr360>
- Di Paola, M., Phillips, O. R., Sanchez-Castaneda, C., Di Pardo, A., Maglione, V., Caltagirone, C., Sabatini, U., & Squitieri, F. (2014). MRI measures of corpus callosum iron and myelin in early Huntington's disease. *Human Brain Mapping*, 35(7), 3143–3151. <https://doi.org/10.1002/hbm.22391>
- Diana Rosas, H., Lee, S. Y., Bender, A., Zaleta, A. K., Vange, M., Yu, P., Fischl, B., Pappu, V., Cha, J.-H., Salat, D. H., & Hersch, S. M. (2010). Altered White Matter Microstructure in the Corpus Callosum in Huntington's Disease: Implications for cortical "disconnection." *NeuroImage*, 49(4), 2995–3004. <https://doi.org/10.1016/j.neuroimage.2009.10.015>
- DiFiglia, M., Sapp, E., Chase, K. O., Davies, S. W., Bates, G. P., Vonsattel, J. P., & Aronin, N. (1997). Aggregation of huntingtin in neuronal intranuclear inclusions and dystrophic neurites in brain. *Science (New York, N.Y.)*, 277(5334), 1990–1993.
- Donahue, C. J., Sotiropoulos, S. N., Jbabdi, S., Hernandez-Fernandez, M., Behrens, T. E., Dyrby, T. B., Coalson, T., Kennedy, H., Knoblauch, K., & Van Essen, D. C. (2016). Using diffusion tractography to predict cortical connection strength and distance: A quantitative comparison with tracers in the monkey. *Journal of Neuroscience*, 36(25), 6758–6770.

- Douaud, G., Behrens, T. E., Poupon, C., Cointepas, Y., Jbabdi, S., Gaura, V., Golestani, N., Krystkowiak, P., Verny, C., Damier, P., Bachoud-Lévi, A.-C., Hantraye, P., & Remy, P. (2009). In vivo evidence for the selective subcortical degeneration in Huntington's disease. *NeuroImage*, *46*(4), 958–966.  
<https://doi.org/10.1016/j.neuroimage.2009.03.044>
- Douaud, G., Gaura, V., Ribeiro, M.-J., Lethimonnier, F., Maroy, R., Verny, C., Krystkowiak, P., Damier, P., Bachoud-Levi, A.-C., Hantraye, P., & Remy, P. (2006). Distribution of grey matter atrophy in Huntington's disease patients: A combined ROI-based and voxel-based morphometric study. *NeuroImage*, *32*(4), 1562–1575.  
<https://doi.org/10.1016/j.neuroimage.2006.05.057>
- Dousset, V., Brochet, B., Vital, A., Gross, C., Benazzouz, A., Boullerne, A., Bidabe, A.-M., Gin, A.-M., & Caille, J.-M. (1995). Lysolecithin-induced demyelination in primates: Preliminary in vivo study with MR and magnetization transfer. *American Journal of Neuroradiology*, *16*(2), 225–231.
- Dousset, V., Grossman, R. I., Ramer, K. N., Schnall, M. D., Young, L. H., Gonzalez-Scarano, F., Lavi, E., & Cohen, J. A. (1992). Experimental allergic encephalomyelitis and multiple sclerosis: Lesion characterization with magnetization transfer imaging. *Radiology*, *182*(2), 483–491.
- Drakesmith, M., Harms, R., Rudrapatna, S. U., Parker, G. D., Evans, C. J., & Jones, D. K. (2019). Estimating axon conduction velocity in vivo from microstructural MRI. *NeuroImage*, *203*, 116186.
- Drijkoningen, D., Caeyenberghs, K., Leunissen, I., Vander Linden, C., Leemans, A., Sunaert, S., Duysens, J., & Swinnen, S. P. (2014). Training-induced improvements in postural control are accompanied by alterations in cerebellar white matter in brain injured

patients. *NeuroImage : Clinical*, 7, 240–251.

<https://doi.org/10.1016/j.nicl.2014.12.006>

Drobnjak, I., Zhang, H., Ianuş, A., Kaden, E., & Alexander, D. C. (2016). PGSE, OGSE, and sensitivity to axon diameter in diffusion MRI: insight from a simulation study.

*Magnetic Resonance in Medicine*, 75(2), 688–700.

Du, Y. P., Chu, R., Hwang, D., Brown, M. S., Kleinschmidt-DeMasters, B. K., Singel, D., & Simon, J. H. (2007). Fast multislice mapping of the myelin water fraction using multicompartment analysis of T decay at 3T: A preliminary postmortem study.

*Magnetic Resonance in Medicine: An Official Journal of the International Society for Magnetic Resonance in Medicine*, 58(5), 865–870.

Duff, K., Paulsen, J., Mills, J., Beglinger, L. J., Moser, D. J., Smith, M. M., Langbehn, D., Stout, J., Queller, S., Harrington, D. L., & PREDICT-HD Investigators and Coordinators of the Huntington Study Group. (2010). Mild cognitive impairment in prediagnosed Huntington disease. *Neurology*, 75(6), 500–507.

<https://doi.org/10.1212/WNL.0b013e3181eccfa2>

Dumas, E. M., van den Bogaard, S. J. A., Middelkoop, H. A. M., & Roos, R. A. C. (2013). A review of cognition in Huntington's disease. *Frontiers in Bioscience (Scholar Edition)*, 5, 1–18. <https://doi.org/10.2741/s355>

Dumas, E. M., van den Bogaard, S. J. A., Ruber, M. E., Reilman, R. R., Stout, J. C., Craufurd, D., Hicks, S. L., Kennard, C., Tabrizi, S. J., van Buchem, M. A., van der Grond, J., & Roos, R. A. C. (2012). Early changes in white matter pathways of the sensorimotor cortex in premanifest Huntington's disease. *Human Brain Mapping*, 33(1), 203–212. <https://doi.org/10.1002/hbm.21205>

Dunnett, S. B., & Rosser, A. E. (2004). Cell Therapy in Huntington's Disease. *NeuroRx*, 1(4), 394–405.

- Duty, S., & Jenner, P. (2011). Animal models of Parkinson's disease: A source of novel treatments and clues to the cause of the disease. *British Journal of Pharmacology*, *164*(4), 1357–1391. <https://doi.org/10.1111/j.1476-5381.2011.01426.x>
- Duyao, M. P., Auerbach, A. B., Ryan, A., Persichetti, F., Barnes, G. T., McNeil, S. M., Ge, P., Vonsattel, J.-P., Gusella, J. F., Joyner, A. L., & MacDonald, M. E. (1995). Inactivation of the mouse Huntington's disease gene homolog Hdh. *Science*, *269*(5222), 407–410. <https://doi.org/10.1126/science.7618107>
- Duyn, J. H. (2010). Study of Brain Anatomy with High Field MRI: Recent Progress. *Magnetic Resonance Imaging*, *28*(8), 1210–1215. <https://doi.org/10.1016/j.mri.2010.02.007>
- Duyn, J. H. (2012). The future of ultra-high field MRI and fMRI for study of the human brain. *Neuroimage*, *62*(2), 1241–1248. <https://doi.org/10.1016/j.neuroimage.2011.10.065>
- Duyn, J. H. (2018). Studying brain microstructure with magnetic susceptibility contrast at high-field. *NeuroImage*, *168*, 152–161. <https://doi.org/10.1016/j.neuroimage.2017.02.046>
- Duyn, J. H., & Schenck, J. (2017). CONTRIBUTIONS TO MAGNETIC SUSCEPTIBILITY OF BRAIN TISSUE. *NMR in Biomedicine*, *30*(4). <https://doi.org/10.1002/nbm.3546>
- Duyn, J. H., van Gelderen, P., Li, T.-Q., de Zwart, J. A., Koretsky, A. P., & Fukunaga, M. (2007). High-field MRI of brain cortical substructure based on signal phase. *Proceedings of the National Academy of Sciences of the United States of America*, *104*(28), 11796–11801. <https://doi.org/10.1073/pnas.0610821104>
- Edden, R. A., & Jones, D. K. (2011). Spatial and orientational heterogeneity in the statistical sensitivity of skeleton-based analyses of diffusion tensor MR imaging data. *Journal of*

*Neuroscience Methods*, 201(1), 213–219.

<https://doi.org/10.1016/j.jneumeth.2011.07.025>

Eddy, C. M., & Rickards, H. E. (2015). Cognitive deficits predict poorer functional capacity in Huntington's disease: But what is being measured? *Neuropsychology*, 29(2), 268–273. <https://doi.org/10.1037/neu0000134>

Eddy, C. M., Sira Mahalingappa, S., & Rickards, H. E. (2012). Is Huntington's disease associated with deficits in theory of mind? *Acta Neurologica Scandinavica*, 126(6), 376–383. <https://doi.org/10.1111/j.1600-0404.2012.01659.x>

Erickson, K. I., Prakash, R. S., Kim, J. S., Sutton, B. P., Colcombe, S. J., & Kramer, A. F. (2009). Top-down attentional control in spatially coincident stimuli enhances activity in both task-relevant and task-irrelevant regions of cortex. *Behavioural Brain Research*, 197(1), 186–197.

Estevez-Fraga, C., Scahill, R., Rees, G., Tabrizi, S. J., & Gregory, S. (2021). Diffusion imaging in Huntington's disease: Comprehensive review. *Journal of Neurology, Neurosurgery & Psychiatry*, 92(1), 62–69. <https://doi.org/10.1136/jnnp-2020-324377>

Faber, P. W., Voisine, C., King, D. C., Bates, E. A., & Hart, A. C. (2002). Glutamine/proline-rich PQE-1 proteins protect *Caenorhabditis elegans* neurons from huntingtin polyglutamine neurotoxicity. *Proceedings of the National Academy of Sciences of the United States of America*, 99(26), 17131–17136.

<https://doi.org/10.1073/pnas.262544899>

Faria, A. V., Ratnanather, J. T., Tward, D. J., Lee, D. S., van den Noort, F., Wu, D., Brown, T., Johnson, H., Paulsen, J. S., Ross, C. A., Younes, L., & Miller, M. I. (2016). Linking white matter and deep gray matter alterations in premanifest Huntington disease. *NeuroImage: Clinical*, 11, 450–460.

<https://doi.org/10.1016/j.nicl.2016.02.014>

- Farrow, M., Chua, P., Churchyard, A., Bradshaw, J. L., Chiu, E., & Georgiou-Karistianis, N. (2006). Proximity to Clinical Onset Influences Motor and Cognitive Performance in Presymptomatic Huntington Disease Gene Carriers. *Cognitive and Behavioral Neurology, 19*(4), 208–216. <https://doi.org/10.1097/01.wnn.0000213914.64772.b6>
- Fazio, P., Paucar, M., Svenningsson, P., & Varrone, A. (2018). Novel Imaging Biomarkers for Huntington's Disease and Other Hereditary Chorea. *Current Neurology and Neuroscience Reports, 18*(12), 85. <https://doi.org/10.1007/s11910-018-0890-y>
- Fennema-Notestine, C., Archibald, S., Jacobson, M., Corey-Bloom, J., Paulsen, J., Peavy, G., Gamst, A., Hamilton, J., Salmon, D., & Jernigan, T. L. (2004). In vivo evidence of cerebellar atrophy and cerebral white matter loss in Huntington disease. *Neurology, 63*(6), 989–995.
- Filimonenko, M., Isakson, P., Finley, K. D., Anderson, M., Jeong, H., Melia, T. J., Bartlett, B. J., Myers, K. M., Birkeland, H. C. G., Lamark, T., Krainc, D., Brech, A., Stenmark, H., Simonsen, A., & Yamamoto, A. (2010). The selective macroautophagic degradation of aggregated proteins requires the PI3P-binding protein Alfy. *Molecular Cell, 38*(2), 265–279. <https://doi.org/10.1016/j.molcel.2010.04.007>
- Fischer, H. W., Haverbeke, Y. V., Schmitz-Feuerhake, I., & Muller, R. N. (1989). The uncommon longitudinal relaxation dispersion of human brain white matter. *Magnetic Resonance in Medicine, 9*(3), 441–446. <https://doi.org/10.1002/mrm.1910090319>
- Fischer, H. W., Rinck, P. A., Van Haverbeke, Y., & Muller, R. N. (1990). Nuclear relaxation of human brain gray and white matter: Analysis of field dependence and implications for MRI. *Magnetic Resonance in Medicine, 16*(2), 317–334. <https://doi.org/10.1002/mrm.1910160212>
- Fischl, B., Salat, D. H., Busa, E., Albert, M., Dieterich, M., Haselgrove, C., van der Kouwe, A., Killiany, R., Kennedy, D., Klaveness, S., Montillo, A., Makris, N., Rosen, B., &

- Dale, A. M. (2002). Whole brain segmentation: Automated labeling of neuroanatomical structures in the human brain. *Neuron*, 33(3), 341–355.  
[https://doi.org/10.1016/s0896-6273\(02\)00569-x](https://doi.org/10.1016/s0896-6273(02)00569-x)
- Flecknell, P. (2002). Replacement, reduction, refinement. *ALTEX-Alternatives to Animal Experimentation*, 19(2), 73–78.
- Folstein, S. E. (1989). *Huntington's disease: A disorder of families*. Johns Hopkins University Press.
- Fornito, A., & Bullmore, E. T. (2015). Connectomics: A new paradigm for understanding brain disease. *European Neuropsychopharmacology*, 25(5), 733–748.  
<https://doi.org/10.1016/j.euroneuro.2014.02.011>
- Fréchet, M. (1957). Sur la distance de deux lois de probabilité. *COMPTES RENDUS HEBDOMADAIRES DES SEANCES DE L ACADEMIE DES SCIENCES*, 244(6), 689–692.
- Freeman, G. L. (1940). The relationship between performance level and bodily activity level. *Journal of Experimental Psychology*, 26(6), 602–608.  
<https://doi.org/10.1037/h0056767>
- Furlong, L. S., Jakabek, D., Power, B. D., Owens-Walton, C., Wilkes, F. A., Walterfang, M., Velakoulis, D., Egan, G., Looi, J. C., & Georgiou-Karistianis, N. (2020). Morphometric in vivo evidence of thalamic atrophy correlated with cognitive and motor dysfunction in Huntington's disease: The IMAGE-HD study. *Psychiatry Research. Neuroimaging*, 298, 111048.  
<https://doi.org/10.1016/j.psychresns.2020.111048>
- Gareau, P. J., Rutt, B. K., Karlik, S. J., & Mitchell, J. R. (2000). Magnetization transfer and multicomponent T2 relaxation measurements with histopathologic correlation in an experimental model of MS. *Journal of Magnetic Resonance Imaging: An Official*

*Journal of the International Society for Magnetic Resonance in Medicine*, 11(6), 586–595.

Gary, C., Lam, S., Hérard, A.-S., Koch, J. E., Petit, F., Gipchtein, P., Sawiak, S. J., Caillierez, R., Eddarkaoui, S., Colin, M., Aujard, F., Deslys, J.-P., Duyckaerts, C., Sazdovitch, V., Leclère-Turbant, S., Artaud-Botté, M.-C., Vital, A., Chapon, F., Kemeny, J.-L., ... French Neuropathology Network. (2019). Encephalopathy induced by Alzheimer brain inoculation in a non-human primate. *Acta Neuropathologica Communications*, 7(1), 126. <https://doi.org/10.1186/s40478-019-0771-x>

Gauthier, L. R., Charrin, B. C., Borrell-Pagès, M., Dompierre, J. P., Rangone, H., Cordelières, F. P., De Mey, J., MacDonald, M. E., Lessmann, V., Humbert, S., & Saudou, F. (2004). Huntingtin controls neurotrophic support and survival of neurons by enhancing BDNF vesicular transport along microtubules. *Cell*, 118(1), 127–138. <https://doi.org/10.1016/j.cell.2004.06.018>

Genc, S., Tax, C. M. W., Raven, E. P., Chamberland, M., Parker, G. D., & Jones, D. K. (2020). Impact of b-value on estimates of apparent fibre density. *Human Brain Mapping*, 41(10), 2583–2595. <https://doi.org/10.1002/hbm.24964>

Georgiou-Karistianis, Gray, M., Dymowski, A., Bohanna, I., Johnston, L., Churchyard, A., Chua, P., Stout, J., & Egan, G. (2013a). Automated differentiation of pre-diagnosis Huntington's disease from healthy control individuals based on quadratic discriminant analysis of the basal ganglia: The IMAGE-HD study. *Neurobiology of Disease*, 51, 82–92.

Georgiou-Karistianis, Scahill, R., Tabrizi, S. J., Squitieri, F., & Aylward, E. (2013b). Structural MRI in Huntington's disease and recommendations for its potential use in clinical trials. *Neuroscience and Biobehavioral Reviews*, 37(3), 480–490. <https://doi.org/10.1016/j.neubiorev.2013.01.022>

- Giacosa, C., Karpati, F. J., Foster, N. E. V., Penhune, V. B., & Hyde, K. L. (2016). Dance and music training have different effects on white matter diffusivity in sensorimotor pathways. *NeuroImage*, *135*, 273–286.  
<https://doi.org/10.1016/j.neuroimage.2016.04.048>
- Gibson, E. M., Purger, D., Mount, C. W., Goldstein, A. K., Lin, G. L., Wood, L. S., Inema, I., Miller, S. E., Bieri, G., Zuchero, J. B., Barres, B. A., Woo, P. J., Vogel, H., & Monje, M. (2014). Neuronal Activity Promotes Oligodendrogenesis and Adaptive Myelination in the Mammalian Brain. *Science (New York, N.Y.)*, *344*(6183), 1252304.  
<https://doi.org/10.1126/science.1252304>
- Giordani, B., Berent, S., Boivin, M. J., Penney, J. B., Lehtinen, S., Markel, D. S., Hollingsworth, Z., Butterbaugh, G., Hichwa, R. D., & Gusella, J. F. (1995). Longitudinal neuropsychological and genetic linkage analysis of persons at risk for Huntington's disease. *Archives of Neurology*, *52*(1), 59–64.
- Glasser, M. F., Sotiropoulos, S. N., Wilson, J. A., Coalson, T. S., Fischl, B., Andersson, J. L., Xu, J., Jbabdi, S., Webster, M., Polimeni, J. R., Van Essen, D. C., Jenkinson, M., & WU-Minn HCP Consortium. (2013). The minimal preprocessing pipelines for the Human Connectome Project. *NeuroImage*, *80*, 105–124.  
<https://doi.org/10.1016/j.neuroimage.2013.04.127>
- Goldstein, A., Covington, B. P., Mahabadi, N., & Mesfin, F. B. (2020). Neuroanatomy, Corpus Callosum. In *StatPearls*. StatPearls Publishing.  
<http://www.ncbi.nlm.nih.gov/books/NBK448209/>
- Gómez-Tortosa, E., MacDonald, M. E., Friend, J. C., Taylor, S. A., Weiler, L. J., Cupples, L. A., Srinidhi, J., Gusella, J. F., Bird, E. D., Vonsattel, J. P., & Myers, R. H. (2001). Quantitative neuropathological changes in presymptomatic Huntington's disease. *Annals of Neurology*, *49*(1), 29–34.

- Gozzi, M., Nielson, D. M., Lenroot, R. K., Ostuni, J. L., Luckenbaugh, D. A., Thurm, A. E., Giedd, J. N., & Swedo, S. E. (2012). A magnetization transfer imaging study of corpus callosum myelination in young children with autism. *Biological Psychiatry*, *72*(3), 215–220. <https://doi.org/10.1016/j.biopsych.2012.01.026>
- Graybiel, A. M. (1990). Neurotransmitters and neuromodulators in the basal ganglia. *Trends in Neurosciences*, *13*(7), 244–254. [https://doi.org/10.1016/0166-2236\(90\)90104-I](https://doi.org/10.1016/0166-2236(90)90104-I)
- Grieve, S. M., Williams, L. M., Paul, R. H., Clark, C. R., & Gordon, E. (2007). Cognitive Aging, Executive Function, and Fractional Anisotropy: A Diffusion Tensor MR Imaging Study. *American Journal of Neuroradiology*, *28*(2), 226–235.
- Grussu, F., Schneider, T., Tur, C., Yates, R. L., Tachrount, M., Ianuș, A., Yiannakas, M. C., Newcombe, J., Zhang, H., Alexander, D. C., DeLuca, G. C., & Gandini Wheeler-Kingshott, C. A. M. (2017). Neurite dispersion: A new marker of multiple sclerosis spinal cord pathology? *Annals of Clinical and Translational Neurology*, *4*(9), 663–679. <https://doi.org/10.1002/acn3.445>
- Gutkunst, C. A., Li, S. H., Yi, H., Mulroy, J. S., Kuemmerle, S., Jones, R., Rye, D., Ferrante, R. J., Hersch, S. M., & Li, X. J. (1999). Nuclear and neuropil aggregates in Huntington's disease: Relationship to neuropathology. *The Journal of Neuroscience: The Official Journal of the Society for Neuroscience*, *19*(7), 2522–2534.
- Guttmann, C. R., Jolesz, F. A., Kikinis, R., Killiany, R. J., Moss, M. B., Sandor, T., & Albert, M. S. (1998). White matter changes with normal aging. *Neurology*, *50*(4), 972–978.
- Hamilton, J. M., Salmon, D. P., Corey-Bloom, J., Gamst, A., Paulsen, J. S., Jerkins, S., Jacobson, M. W., & Peavy, G. (2003). Behavioural abnormalities contribute to functional decline in Huntington's disease. *Journal of Neurology, Neurosurgery, and Psychiatry*, *74*(1), 120–122. <https://doi.org/10.1136/jnnp.74.1.120>

- Han, I., You, Y., Kordower, J. H., Brady, S. T., & Morfini, G. A. (2010). Differential vulnerability of neurons in Huntington's disease: The role of cell type-specific features. *Journal of Neurochemistry*, *113*(5), 1073–1091.  
<https://doi.org/10.1111/j.1471-4159.2010.06672.x>
- Han, Y., Yang, H., Lv, Y.-T., Zhu, C.-Z., He, Y., Tang, H.-H., Gong, Q.-Y., Luo, Y.-J., Zang, Y.-F., & Dong, Q. (2009). Gray matter density and white matter integrity in pianists' brain: A combined structural and diffusion tensor MRI study. *Neuroscience Letters*, *459*(1), 3–6. <https://doi.org/10.1016/j.neulet.2008.07.056>
- Harrington, D. L., Long, J. D., Durgerian, S., Mourany, L., Koenig, K., Bonner-Jackson, A., Paulsen, J. S., PREDICT-HD Investigators of the Huntington Study Group, & Rao, S. M. (2016). Cross-sectional and longitudinal multimodal structural imaging in prodromal Huntington's disease. *Movement Disorders: Official Journal of the Movement Disorder Society*, *31*(11), 1664–1675. <https://doi.org/10.1002/mds.26803>
- Hayes, A. F. (2017). *Introduction to mediation, moderation, and conditional process analysis: A regression-based approach*. Guilford publications.
- Heath, F., Hurley, S. A., Johansen-Berg, H., & Sampaio-Baptista, C. (2018). Advances in noninvasive myelin imaging. *Developmental Neurobiology*, *78*(2), 136–151.  
<https://doi.org/10.1002/dneu.22552>
- Hebb, M. O., Denovan-Wright, E. M., & Robertson, H. A. (1999). Expression of the Huntington's disease gene is regulated in astrocytes in the arcuate nucleus of the hypothalamus of postpartum rats. *FASEB Journal: Official Publication of the Federation of American Societies for Experimental Biology*, *13*(9), 1099–1106.  
<https://doi.org/10.1096/fasebj.13.9.1099>

- Heinsen, H., Strik, M., Bauer, M., Luther, K., Ulmar, G., Gangnus, D., Jungkunz, G., Eisenmengers, W., & Götz, M. (1994). Cortical and striatal neurone number in Huntington's disease. *Acta Neuropathologica*, *88*(4), 320–333.
- Henkelman, R. M., Huang, X., Xiang, Q. S., Stanisz, G. J., Swanson, S. D., & Bronskill, M. J. (1993). Quantitative interpretation of magnetization transfer. *Magnetic Resonance in Medicine*, *29*(6), 759–766.
- Henkelman, R. M., Stanisz, G. J., & Graham, S. J. (2001). Magnetization transfer in MRI: A review. *NMR in Biomedicine*, *14*(2), 57–64. <https://doi.org/10.1002/nbm.683>
- Henley, S. M. D., Novak, M. J. U., Frost, C., King, J., Tabrizi, S. J., & Warren, J. D. (2012). Emotion recognition in Huntington's disease: A systematic review. *Neuroscience & Biobehavioral Reviews*, *36*(1), 237–253.  
<https://doi.org/10.1016/j.neubiorev.2011.06.002>
- Hofer, S., & Frahm, J. (2006). Topography of the human corpus callosum revisited—Comprehensive fiber tractography using diffusion tensor magnetic resonance imaging. *NeuroImage*, *32*(3), 989–994.  
<https://doi.org/10.1016/j.neuroimage.2006.05.044>
- Holmes, H. E., Powell, N. M., Ma, D., Ismail, O., Harrison, I. F., Wells, J. A., Colgan, N., O'Callaghan, J. M., Johnson, R. A., Murray, T. K., Ahmed, Z., Heggenes, M., Fisher, A., Cardoso, M. J., Modat, M., O'Neill, M. J., Collins, E. C., Fisher, E. M. C., Ourselin, S., & Lythgoe, M. F. (2017). Comparison of In Vivo and Ex Vivo MRI for the Detection of Structural Abnormalities in a Mouse Model of Tauopathy. *Frontiers in Neuroinformatics*, *11*. <https://doi.org/10.3389/fninf.2017.00020>
- Hopfinger, J. B., Buonocore, M. H., & Mangun, G. R. (2000). The neural mechanisms of top-down attentional control. *Nature Neuroscience*, *3*(3), 284–291.

- Horsfield, M. A. (2005). Magnetization transfer imaging in multiple sclerosis. *Journal of Neuroimaging*, *15*, 58S-67S.
- Hoyer, C., Gass, N., Weber-Fahr, W., & Sartorius, A. (2014). Advantages and Challenges of Small Animal Magnetic Resonance Imaging as a Translational Tool. *Neuropsychobiology*, *69*(4), 187–201. <https://doi.org/10.1159/000360859>
- Hu, Y., Geng, F., Tao, L., Hu, N., Du, F., Fu, K., & Chen, F. (2011). Enhanced white matter tracts integrity in children with abacus training. *Human Brain Mapping*, *32*(1), 10–21. <https://doi.org/10.1002/hbm.20996>
- Huntington, G. (1967). ON CHOREA. *Archives of Neurology*, *17*(3), 332–333. <https://doi.org/10.1001/archneur.1967.00470270110014>
- Irfanoglu, M. O., Walker, L., Sarlls, J., Marenco, S., & Pierpaoli, C. (2012). Effects of image distortions originating from susceptibility variations and concomitant fields on diffusion MRI tractography results. *NeuroImage*, *61*(1), 275–288. <https://doi.org/10.1016/j.neuroimage.2012.02.054>
- Ishiguro, H., Yamada, K., Sawada, H., Nishii, K., Ichino, N., Sawada, M., Kurosawa, Y., Matsushita, N., Kobayashi, K., Goto, J., Hashida, H., Masuda, N., Kanazawa, I., & Nagatsu, T. (2001). Age-dependent and tissue-specific CAG repeat instability occurs in mouse knock-in for a mutant Huntington's disease gene. *Journal of Neuroscience Research*, *65*(4), 289–297. <https://doi.org/10.1002/jnr.1153>
- Jacobsen, J. C., Bawden, C. S., Rudiger, S. R., McLaughlan, C. J., Reid, S. J., Waldvogel, H. J., MacDonald, M. E., Gusella, J. F., Walker, S. K., Kelly, J. M., Webb, G. C., Faull, R. L. M., Rees, M. I., & Snell, R. G. (2010). An ovine transgenic Huntington's disease model. *Human Molecular Genetics*, *19*(10), 1873–1882. <https://doi.org/10.1093/hmg/ddq063>

- Jelescu, I. O., Veraart, J., Fieremans, E., & Novikov, D. S. (2016). Degeneracy in model parameter estimation for multi-compartmental diffusion in neuronal tissue. *NMR in Biomedicine*, *29*(1), 33–47. <https://doi.org/10.1002/nbm.3450>
- Jellinger, K., Paulus, W., Grundke-Iqbal, I., Riederer, P., & Youdim, M. (1990). Brain iron and ferritin in Parkinson's and Alzheimer's diseases. *Journal of Neural Transmission-Parkinson's Disease and Dementia Section*, *2*(4), 327–340.
- Jeurissen, B., Leemans, A., Jones, D. K., Tournier, J.-D., & Sijbers, J. (2011). Probabilistic fiber tracking using the residual bootstrap with constrained spherical deconvolution. *Human Brain Mapping*, *32*(3), 461–479. <https://doi.org/10.1002/hbm.21032>
- Jeurissen, B., Tournier, J.-D., Dhollander, T., Connelly, A., & Sijbers, J. (2014). Multi-tissue constrained spherical deconvolution for improved analysis of multi-shell diffusion MRI data. *NeuroImage*, *103*, 411–426.
- Jin, J., Peng, Q., Hou, Z., Jiang, M., Wang, X., Langseth, A. J., Tao, M., Barker, P. B., Mori, S., Bergles, D. E., Ross, C. A., Detloff, P. J., Zhang, J., & Duan, W. (2015). Early white matter abnormalities, progressive brain pathology and motor deficits in a novel knock-in mouse model of Huntington's disease. *Human Molecular Genetics*, *24*(9), 2508–2527. <https://doi.org/10.1093/hmg/ddv016>
- Johansen-Berg, H., & Behrens, T. E. J. (2006). Just pretty pictures? What diffusion tractography can add in clinical neuroscience. *Current Opinion in Neurology*, *19*(4), 379–385. <https://doi.org/10.1097/01.wco.0000236618.82086.01>
- Jokinen, H., Ryberg, C., Kalska, H., Ylikoski, R., Rostrup, E., Stegmann, M. B., Waldemar, G., Madureira, S., Ferro, J. M., van Straaten, E. C. W., Scheltens, P., Barkhof, F., Fazekas, F., Schmidt, R., Carlucci, G., Pantoni, L., Inzitari, D., & Erkinjuntti, T. (2007). Corpus callosum atrophy is associated with mental slowing and executive deficits in subjects with age-related white matter hyperintensities: The LADIS Study.

*Journal of Neurology, Neurosurgery, and Psychiatry*, 78(5), 491–496.

<https://doi.org/10.1136/jnnp.2006.096792>

- Jones, D. K. (2004). The effect of gradient sampling schemes on measures derived from diffusion tensor MRI: a Monte Carlo study. *Magnetic Resonance in Medicine: An Official Journal of the International Society for Magnetic Resonance in Medicine*, 51(4), 807–815.
- Jones, D. K., Alexander, D. C., Bowtell, R., Cercignani, M., Dell'Acqua, F., McHugh, D. J., Miller, K. L., Palombo, M., Parker, G. J. M., Rudrapatna, U. S., & Tax, C. M. W. (2018). Microstructural imaging of the human brain with a 'super-scanner': 10 key advantages of ultra-strong gradients for diffusion MRI. *NeuroImage*, 182, 8–38.  
<https://doi.org/10.1016/j.neuroimage.2018.05.047>
- Jones, D. K., Catani, M., Pierpaoli, C., Reeves, S. J., Shergill, S. S., O'Sullivan, M., Golesworthy, P., McGuire, P., Horsfield, M. A., & Simmons, A. (2006). Age effects on diffusion tensor magnetic resonance imaging tractography measures of frontal cortex connections in schizophrenia. *Human Brain Mapping*, 27(3), 230–238.
- Jones, D. K., & Cercignani, M. (2010). Twenty-five pitfalls in the analysis of diffusion MRI data. *NMR in Biomedicine*, 23(7), 803–820. <https://doi.org/10.1002/nbm.1543>
- Jones, D. K., & Pierpaoli, C. (2005). Confidence mapping in diffusion tensor magnetic resonance imaging tractography using a bootstrap approach. *Magnetic Resonance in Medicine: An Official Journal of the International Society for Magnetic Resonance in Medicine*, 53(5), 1143–1149.
- Jones, D. K., Symms, M. R., Cercignani, M., & Howard, R. J. (2005a). The effect of filter size on VBM analyses of DT-MRI data. *NeuroImage*, 26(2), 546–554.  
<https://doi.org/10.1016/j.neuroimage.2005.02.013>

- Jones, D. K., Travis, A. R., Eden, G., Pierpaoli, C., & Basser, P. J. (2005b). PASTA: pointwise assessment of streamline tractography attributes. *Magnetic Resonance in Medicine: An Official Journal of the International Society for Magnetic Resonance in Medicine*, 53(6), 1462–1467.
- Jurgens, C. K., Jasinschi, R., Ekin, A., Witjes-Ané, M.-N. W., van der Grond, J., Middelkoop, H., & Roos, R. A. C. (2010). MRI T2 Hypointensities in basal ganglia of premanifest Huntington's disease. *PLoS Currents*, 2.  
<https://doi.org/10.1371/currents.RRN1173>
- Kaller, M. S., Lazari, A., Blanco-Duque, C., Sampaio-Baptista, C., & Johansen-Berg, H. (2017). Myelin plasticity and behaviour—Connecting the dots. *Current Opinion in Neurobiology*, 47, 86–92. <https://doi.org/10.1016/j.conb.2017.09.014>
- Kandel, E. R., Schwartz, J. H., Jessell, T. M., Department of Biochemistry and Molecular Biophysics Thomas Jessell, Siegelbaum, S., & Hudspeth, A. (2000). *Principles of neural science* (Vol. 4). McGraw-hill New York.
- Kassubek, J., Juengling, F. D., Kioschies, T., Henkel, K., Karitzky, J., Kramer, B., Ecker, D., Andrich, J., Saft, C., Kraus, P., Aschoff, A. J., Ludolph, A. C., & Landwehrmeyer, G. B. (2004). Topography of cerebral atrophy in early Huntington's disease: A voxel based morphometric MRI study. *Journal of Neurology, Neurosurgery, and Psychiatry*, 75(2), 213–220.
- Kay, C., Skotte, N. H., Southwell, A. L., & Hayden, M. R. (2014). Personalized gene silencing therapeutics for Huntington disease. *Clinical Genetics*, 86(1), 29–36.  
<https://doi.org/10.1111/cge.12385>
- Keihaninejad, S., Ryan, N. S., Malone, I. B., Modat, M., Cash, D., Ridgway, G. R., Zhang, H., Fox, N. C., & Ourselin, S. (2012). The importance of group-wise registration in

- tract based spatial statistics study of neurodegeneration: A simulation study in Alzheimer's disease. *PloS One*, 7(11), e45996.
- Kellner, E., Dhital, B., Kiselev, V. G., & Reisert, M. (2016). Gibbs-ringing artifact removal based on local subvoxel-shifts. *Magnetic Resonance in Medicine*, 76(5), 1574–1581. <https://doi.org/10.1002/mrm.26054>
- Kennedy, K. M., & Raz, N. (2009). Aging White Matter and Cognition: Differential Effects of Regional Variations in Diffusion Properties on Memory, Executive Functions, and Speed. *Neuropsychologia*, 47(3), 916–927. <https://doi.org/10.1016/j.neuropsychologia.2009.01.001>
- Kieburz, K., MacDonald, M., Shih, C., Feigin, A., Steinberg, K., Bordwell, K., Zimmerman, C., Srinidhi, J., Sotack, J., & Gusella, J. (1994). Trinucleotide repeat length and progression of illness in Huntington's disease. *Journal of Medical Genetics*, 31(11), 872–874.
- Kieburz, K., Penney, J. B., Corno, P., Ranen, N., Shoulson, I., Feigin, A., Abwender, D., Greenarnyre, J. T., Higgins, D., & Marshall, F. J. (2001). Unified Huntington's disease rating scale: Reliability and consistency. *Neurology*, 11(2), 136–142.
- Kim, S., & Kim, K.-T. (2014). Therapeutic Approaches for Inhibition of Protein Aggregation in Huntington's Disease. *Experimental Neurobiology*, 23(1), 36–44. <https://doi.org/10.5607/en.2014.23.1.36>
- Kipps, C., Duggins, A., McCusker, E., & Calder, A. (2007). Disgust and happiness recognition correlate with anteroventral insula and amygdala volume respectively in preclinical Huntington's disease. *Journal of Cognitive Neuroscience*, 19(7), 1206–1217.
- Kirchner, W. K. (1958). Age differences in short-term retention of rapidly changing information. *Journal of Experimental Psychology*, 55(4), 352.

- Kirk, R. G. W. (2018). Recovering The Principles of Humane Experimental Technique. *Science, Technology & Human Values*, 43(4), 622–648.  
<https://doi.org/10.1177/0162243917726579>
- Klapstein, G. J., Fisher, R. S., Zanjani, H., Cepeda, C., Jokel, E. S., Chesselet, M.-F., & Levine, M. S. (2001). Electrophysiological and morphological changes in striatal spiny neurons in R6/2 Huntington's disease transgenic mice. *Journal of Neurophysiology*, 86(6), 2667–2677.
- Kleban, E., Tax, C. M. W., Rudrapatna, U. S., Jones, D. K., & Bowtell, R. (2020). Strong diffusion gradients allow the separation of intra- and extra-axonal gradient-echo signals in the human brain. *NeuroImage*, 217, 116793.  
<https://doi.org/10.1016/j.neuroimage.2020.116793>
- Klein, S., Staring, M., Murphy, K., Viergever, M. A., & Pluim, J. P. W. (2010). elastix: A toolbox for intensity-based medical image registration. *IEEE Transactions on Medical Imaging*, 29(1), 196–205. <https://doi.org/10.1109/TMI.2009.2035616>
- Klement, I. A., Skinner, P. J., Kaytor, M. D., Yi, H., Hersch, S. M., Clark, H. B., Zoghbi, H. Y., & Orr, H. T. (1998). Ataxin-1 nuclear localization and aggregation: Role in polyglutamine-induced disease in SCA1 transgenic mice. *Cell*, 95(1), 41–53.  
[https://doi.org/10.1016/s0092-8674\(00\)81781-x](https://doi.org/10.1016/s0092-8674(00)81781-x)
- Klöppel, S., Draganski, B., Siebner, H. R., Tabrizi, S. J., Weiller, C., & Frackowiak, R. S. J. (2009). Functional compensation of motor function in pre-symptomatic Huntington's disease. *Brain*, 132(6), 1624–1632. <https://doi.org/10.1093/brain/awp081>
- Koo, V., Hamilton, P., & Williamson, K. (2006). Non-invasive in vivo imaging in small animal research. *Analytical Cellular Pathology*, 28(4), 127–139.

- Kosior, N., & Leavitt, B. R. (2018). Murine Models of Huntington's Disease for Evaluating Therapeutics. In S. V. Precious, A. E. Rosser, & S. B. Dunnett (Eds.), *Huntington's Disease* (pp. 179–207). Springer. [https://doi.org/10.1007/978-1-4939-7825-0\\_10](https://doi.org/10.1007/978-1-4939-7825-0_10)
- Krishnamoorthy, K., & Lee, M. (2014). Improved tests for the equality of normal coefficients of variation. *Computational Statistics*, *29*(1), 215–232. <https://doi.org/10.1007/s00180-013-0445-2>
- Krüger, G., Kastrup, A., & Glover, G. H. (2001). Neuroimaging at 1.5 T and 3.0 T: Comparison of oxygenation-sensitive magnetic resonance imaging. *Magnetic Resonance in Medicine*, *45*(4), 595–604. <https://doi.org/10.1002/mrm.1081>
- Labuschagne, I., Jones, R., Callaghan, J., Whitehead, D., Dumas, E. M., Say, M. J., Hart, E. P., Justo, D., Coleman, A., Dar Santos, R. C., Frost, C., Craufurd, D., Tabrizi, S. J., Stout, J. C., & TRACK-HD Investigators. (2013). Emotional face recognition deficits and medication effects in pre-manifest through stage-II Huntington's disease. *Psychiatry Research*, *207*(1–2), 118–126. <https://doi.org/10.1016/j.psychres.2012.09.022>
- Ladd, M. E., Bachert, P., Meyerspeer, M., Moser, E., Nagel, A. M., Norris, D. G., Schmitter, S., Speck, O., Straub, S., & Zaiss, M. (2018). Pros and cons of ultra-high-field MRI/MRS for human application. *Progress in Nuclear Magnetic Resonance Spectroscopy*, *109*, 1–50. <https://doi.org/10.1016/j.pnmrs.2018.06.001>
- Lakhani, B., Borich, M. R., Jackson, J. N., Wadden, K. P., Peters, S., Villamayor, A., MacKay, A. L., Vavasour, I. M., Rauscher, A., & Boyd, L. A. (2016). *Motor Skill Acquisition Promotes Human Brain Myelin Plasticity* [Research article]. *Neural Plasticity*. <https://doi.org/10.1155/2016/7526135>
- Landwehrmeyer, G. B., Fitzer-Attas, C. J., Giuliano, J. D., Gonçalves, N., Anderson, K. E., Cardoso, F., Ferreira, J. J., Mestre, T. A., Stout, J. C., & Sampaio, C. (2017). Data

- analytics from Enroll-HD, a global clinical research platform for Huntington's disease. *Movement Disorders Clinical Practice*, 4(2), 212–224.
- Landwehrmeyer, G. B., McNeil, S. M., Dure, L. S., Ge, P., Aizawa, H., Huang, Q., Ambrose, C. M., Duyao, M. P., Bird, E. D., & Bonilla, E. (1995). Huntington's disease gene: Regional and cellular expression in brain of normal and affected individuals. *Annals of Neurology*, 37(2), 218–230. <https://doi.org/10.1002/ana.410370213>
- Langkammer, C., Krebs, N., Goessler, W., Scheurer, E., Ebner, F., Yen, K., Fazekas, F., & Ropele, S. (2010). Quantitative MR imaging of brain iron: A postmortem validation study. *Radiology*, 257(2), 455–462.
- Langkammer, C., Schweser, F., Krebs, N., Deistung, A., Goessler, W., Scheurer, E., Sommer, K., Reishofer, G., Yen, K., Fazekas, F., Ropele, S., & Reichenbach, J. R. (2012). Quantitative susceptibility mapping (QSM) as a means to measure brain iron? A post mortem validation study. *NeuroImage*, 62(3), 1593–1599. <https://doi.org/10.1016/j.neuroimage.2012.05.049>
- Lansbury, P. T. (1997). Structural neurology: Are seeds at the root of neuronal degeneration? *Neuron*, 19(6), 1151–1154. [https://doi.org/10.1016/s0896-6273\(00\)80406-7](https://doi.org/10.1016/s0896-6273(00)80406-7)
- Lanska, D. J. (2000). George Huntington (1850-1916) and hereditary chorea. *Journal of the History of the Neurosciences*, 9(1), 76–89. [https://doi.org/10.1076/0964-704X\(200004\)9:1;1-2;FT076](https://doi.org/10.1076/0964-704X(200004)9:1;1-2;FT076)
- Larmor, J. (1897). LXIII. On the theory of the magnetic influence on spectra; and on the radiation from moving ions. *The London, Edinburgh, and Dublin Philosophical Magazine and Journal of Science*, 44(271), 503–512.
- Laule, C., Kozlowski, P., Leung, E., Li, D. K. B., Mackay, A. L., & Moore, G. R. W. (2008). Myelin water imaging of multiple sclerosis at 7 T: Correlations with histopathology. *NeuroImage*, 40(4), 1575–1580. <https://doi.org/10.1016/j.neuroimage.2007.12.008>

- Lawrence, A. D., Hodges, J. R., Rosser, A. E., Kershaw, A., ffrench-Constant, C., Rubinsztein, D. C., Robbins, T. W., & Sahakian, B. J. (1998a). Evidence for specific cognitive deficits in preclinical Huntington's disease. *Brain: A Journal of Neurology*, *121* ( Pt 7), 1329–1341. <https://doi.org/10.1093/brain/121.7.1329>
- Lawrence, A. D., Sahakian, B. J., Hodges, J. R., Rosser, A. E., Lange, K. W., & Robbins, T. W. (1996). Executive and mnemonic functions in early Huntington's disease. *Brain: A Journal of Neurology*, *119* ( Pt 5), 1633–1645. <https://doi.org/10.1093/brain/119.5.1633>
- Lawrence, A. D., Weeks, R. A., Brooks, D. J., Andrews, T. C., Watkins, L. H., Harding, A. E., Robbins, T. W., & Sahakian, B. J. (1998b). The relationship between striatal dopamine receptor binding and cognitive performance in Huntington's disease. *Brain: A Journal of Neurology*, *121* ( Pt 7), 1343–1355. <https://doi.org/10.1093/brain/121.7.1343>
- Lazar, M., & Alexander, A. L. (2005). Bootstrap white matter tractography (BOOT-TRAC). *NeuroImage*, *24*(2), 524–532.
- Lee, J. K., Mathews, K., Schlaggar, B., Perlmutter, J., Paulsen, J. S., Epping, E., Burmeister, L., & Nopoulos, P. (2012). Measures of growth in children at risk for Huntington disease. *Neurology*, *79*(7), 668–674. <https://doi.org/10.1212/WNL.0b013e3182648b65>
- Lee, J., Shmueli, K., Fukunaga, M., van Gelderen, P., Merkle, H., Silva, A. C., & Duyn, J. H. (2010). Sensitivity of MRI resonance frequency to the orientation of brain tissue microstructure. *Proceedings of the National Academy of Sciences of the United States of America*, *107*(11), 5130–5135. <https://doi.org/10.1073/pnas.0910222107>
- Lee, Q. (2016). *Fronto-striatal circuitry in children at risk for Huntington's disease* [PhD, University of Iowa]. <https://doi.org/10.17077/etd.2uix1txf>

- Leemans, A., Jeurissen, B., Sijbers, J., & Jones, D. (2009). ExploreDTI: a graphical toolbox for processing, analyzing, and visualizing diffusion MR data. *Proc Intl Soc Mag Reson Med*, *17*(1).
- Leemans, A., Jeurissen, B., Sijbers, J., & Jones, D. K. (n.d.). *ExploreDTI: a graphical toolbox for processing, analyzing, and visualizing diffusion MR data*. 1.
- Leemans, A., & Jones, D. K. (2009). The B-matrix must be rotated when correcting for subject motion in DTI data. *Magnetic Resonance in Medicine*, *61*(6), 1336–1349. <https://doi.org/10.1002/mrm.21890>
- Leh, S. E., Ptito, A., Chakravarty, M. M., & Strafella, A. P. (2007). Fronto-striatal connections in the human brain: A probabilistic diffusion tractography study. *Neuroscience Letters*, *419*(2), 113–118. <https://doi.org/10.1016/j.neulet.2007.04.049>
- Lenzi, D., Conte, A., Mainero, C., Frasca, V., Fubelli, F., Totaro, P., Caramia, F., Inghilleri, M., Pozzilli, C., & Pantano, P. (2007). Effect of corpus callosum damage on ipsilateral motor activation in patients with multiple sclerosis: A functional and anatomical study. *Human Brain Mapping*, *28*(7), 636–644.
- Levesque, I. R., Giacomini, P. S., Narayanan, S., Ribeiro, L. T., Sled, J. G., Arnold, D. L., & Pike, G. B. (2010). Quantitative magnetization transfer and myelin water imaging of the evolution of acute multiple sclerosis lesions. *Magnetic Resonance in Medicine*, *63*(3), 633–640. <https://doi.org/10.1002/mrm.22244>
- Lexa, F. J., Grossman, R., & Rosenquist, A. (1994). Dyke Award paper. MR of wallerian degeneration in the feline visual system: Characterization by magnetization transfer rate with histopathologic correlation. *American Journal of Neuroradiology*, *15*(2), 201–212.

- Li, J. Y., Popovic, N., & Brundin, P. (2005). The use of the R6 transgenic mouse models of Huntington's disease in attempts to develop novel therapeutic strategies. *NeuroRx*, 2(3), 447–464.
- Li, S. H., Schilling, G., Young, W. S., Li, X., Margolis, R. L., Stine, O. C., Wagster, M. V., Abbott, M. H., Franz, M. L., Ranen, N. G., Folstein, S. E., Hedreen, J. C., & Ross, C. A. (1993). Huntington's disease gene (IT15) is widely expressed in human and rat tissues. *Neuron*, 11(5), 985–993. [https://doi.org/10.1016/0896-6273\(93\)90127-D](https://doi.org/10.1016/0896-6273(93)90127-D)
- Li, T.-Q., van Gelderen, P., Merkle, H., Talagala, L., Koretsky, A. P., & Duyn, J. (2006). Extensive heterogeneity in white matter intensity in high-resolution T2\*-weighted MRI of the human brain at 7.0 T. *NeuroImage*, 32(3), 1032–1040. <https://doi.org/10.1016/j.neuroimage.2006.05.053>
- Li, X., Harrison, D. M., Liu, H., Jones, C. K., Oh, J., Calabresi, P. A., & van Zijl, P. C. (2016). Magnetic susceptibility contrast variations in multiple sclerosis lesions. *Journal of Magnetic Resonance Imaging*, 43(2), 463–473.
- Li, X., van Gelderen, P., Sati, P., de Zwart, J. A., Reich, D. S., & Duyn, J. H. (2015). Detection of demyelination in multiple sclerosis by analysis of [Formula: See text] relaxation at 7 T. *NeuroImage. Clinical*, 7, 709–714. PubMed. <https://doi.org/10.1016/j.nicl.2015.02.021>
- Liewald, D., Miller, R., Logothetis, N., Wagner, H.-J., & Schüz, A. (2014). Distribution of axon diameters in cortical white matter: An electron-microscopic study on three human brains and a macaque. *Biological Cybernetics*, 108(5), 541–557.
- Lim, K. O., & Helpert, J. A. (2002). Neuropsychiatric applications of DTI - a review. *NMR in Biomedicine*, 15(7–8), 587–593. <https://doi.org/10.1002/nbm.789>
- Lin, C.-H., Tallaksen-Greene, S., Chien, W.-M., Cearley, J. A., Jackson, W. S., Crouse, A. B., Ren, S., Li, X.-J., Albin, R. L., & Detloff, P. J. (2001). Neurological abnormalities

- in a knock-in mouse model of Huntington's disease. *Human Molecular Genetics*, 10(2), 137–144. <https://doi.org/10.1093/hmg/10.2.137>
- Lintl, P., & Braak, H. (1983). Loss of intracortical myelinated fibers: A distinctive age-related alteration in the human striate area. *Acta Neuropathologica*, 61(3–4), 178–182.
- Little, G. J., & Heath, J. W. (1994). Morphometric analysis of axons myelinated during adult life in the mouse superior cervical ganglion. *Journal of Anatomy*, 184(Pt 2), 387–398.
- Liu, W., Yang, J., Burgunder, J., Cheng, B., & Shang, H. (2016). Diffusion imaging studies of Huntington's disease: A meta-analysis. *Parkinsonism & Related Disorders*, 32, 94–101.
- Loi, S. M., Walterfang, M., Velakoulis, D., & Looi, J. C. (2018). Huntington's disease: Managing neuropsychiatric symptoms in Huntington's disease. *Australasian Psychiatry*, 26(4), 376–380. <https://doi.org/10.1177/1039856218766120>
- Looi, J. C. L., & Walterfang, M. (2013). Striatal morphology as a biomarker in neurodegenerative disease. *Molecular Psychiatry*, 18(4), 417–424. <https://doi.org/10.1038/mp.2012.54>
- Lövdén, M., Bodammer, N. C., Kühn, S., Kaufmann, J., Schütze, H., Tempelmann, C., Heinze, H.-J., Düzel, E., Schmiedek, F., & Lindenberger, U. (2010). Experience-dependent plasticity of white-matter microstructure extends into old age. *Neuropsychologia*, 48(13), 3878–3883. <https://doi.org/10.1016/j.neuropsychologia.2010.08.026>
- Luque Laguna, P. A. (2019). *Neuroanatomy-based strategies for the statistical analysis of brain imaging and tractography data*.
- Ma, L., Morton, A. J., & Nicholson, L. F. (2003). Microglia density decreases with age in a mouse model of Huntington's disease. *Glia*, 43(3), 274–280.

- MacKay, A. L., & Laule, C. (2016). Magnetic resonance of myelin water: An in vivo marker for myelin. *Brain Plasticity*, 2(1), 71–91.
- MacKay, A., Whittall, K., Adler, J., Li, D., Paty, D., & Graeb, D. (1994). In vivo visualization of myelin water in brain by magnetic resonance. *Magnetic Resonance in Medicine*, 31(6), 673–677. <https://doi.org/10.1002/mrm.1910310614>
- Mackey, A. P., Whitaker, K. J., & Bunge, S. A. (2012). Experience-dependent plasticity in white matter microstructure: Reasoning training alters structural connectivity. *Frontiers in Neuroanatomy*, 6. <https://doi.org/10.3389/fnana.2012.00032>
- Maier-Hein, K. H., Neher, P. F., Houde, J.-C., Côté, M.-A., Garyfallidis, E., Zhong, J., Chamberland, M., Yeh, F.-C., Lin, Y.-C., Ji, Q., Reddick, W. E., Glass, J. O., Chen, D. Q., Feng, Y., Gao, C., Wu, Y., Ma, J., He, R., Li, Q., ... Descoteaux, M. (2017). The challenge of mapping the human connectome based on diffusion tractography. *Nature Communications*, 8(1), 1349. <https://doi.org/10.1038/s41467-017-01285-x>
- Mair, P., & Wilcox, R. (2020). Robust statistical methods in R using the WRS2 package. *Behavior Research Methods*, 52(2), 464–488. <https://doi.org/10.3758/s13428-019-01246-w>
- Majid, D. S. A., Aron, A. R., Thompson, W., Sheldon, S., Hamza, S., Stoffers, D., Holland, D., Goldstein, J., Corey-Bloom, J., & Dale, A. M. (2011). Basal ganglia atrophy in prodromal Huntington’s disease is detectable over one year using automated segmentation. *Movement Disorders: Official Journal of the Movement Disorder Society*, 26(14), 2544–2551. <https://doi.org/10.1002/mds.23912>
- Mangiarini, L., Sathasivam, K., Seller, M., Cozens, B., Harper, A., Hetherington, C., Lawton, M., Trottier, Y., Lehrach, H., Davies, S. W., & Bates, G. P. (1996). Exon 1 of the HD gene with an expanded CAG repeat is sufficient to cause a progressive neurological

- phenotype in transgenic mice. *Cell*, 87(3), 493–506. [https://doi.org/10.1016/s0092-8674\(00\)81369-0](https://doi.org/10.1016/s0092-8674(00)81369-0)
- Mann, D. M., Oliver, R., & Snowden, J. S. (1993). The topographic distribution of brain atrophy in Huntington's disease and progressive supranuclear palsy. *Acta Neuropathologica*, 85(5), 553–559. <https://doi.org/10.1007/BF00230496>
- Marangoni, M., Adalbert, R., Janeckova, L., Patrick, J., Kohli, J., Coleman, M. P., & Conforti, L. (2014). Age-related axonal swellings precede other neuropathological hallmarks in a knock-in mouse model of Huntington's disease. *Neurobiology of Aging*, 35(10), 2382–2393. <https://doi.org/10.1016/j.neurobiolaging.2014.04.024>
- Marder, K., Sandler, S., Lechich, A., Klager, J., & Albert, S. M. (2002). Relationship between CAG repeat length and late-stage outcomes in Huntington's disease. *Neurology*, 59(10), 1622–1624. <https://doi.org/10.1212/01.wnl.0000035627.16789.23>
- Maroof, D. A., Gross, A. L., & Brandt, J. (2011). Modeling longitudinal change in motor and cognitive processing speed in presymptomatic Huntington's disease. *Journal of Clinical and Experimental Neuropsychology*, 33(8), 901–909. <https://doi.org/10.1080/13803395.2011.574606>
- Martenson, R. E. (1992). *Myelin*. CRC Press.
- Marwick, B., & Krishnamoorthy, K. (2019). cvequality: Tests for the equality of coefficients of variation from multiple groups. *R Package Version 0.1*, 3.
- McColgan, P., & Tabrizi, S. J. (2018). Huntington's disease: A clinical review. *European Journal of Neurology*, 25(1), 24–34. <https://doi.org/10.1111/ene.13413>
- McDonald, S., Rushby, J. A., Dalton, K. I., Allen, S. K., & Parks, N. (2018). The role of abnormalities in the corpus callosum in social cognition deficits after Traumatic Brain Injury. *Social Neuroscience*, 13(4), 471–479. <https://doi.org/10.1080/17470919.2017.1356370>

- McKinnon, E. T., & Jensen, J. H. (2019). Measuring intra-axonal T2 in white matter with direction-averaged diffusion MRI. *Magnetic Resonance in Medicine*, *81*(5), 2985–2994. <https://doi.org/10.1002/mrm.27617>
- Mehler, M. F., & Gokhan, S. (2000). Mechanisms underlying neural cell death in neurodegenerative diseases: Alterations of a developmentally-mediated cellular rheostat. *Trends in Neurosciences*, *23*(12), 599–605.
- Menalled, L. B. (2005). Knock-In Mouse Models of Huntington’s Disease. *NeuroRx*, *2*(3), 465–470.
- Meng, Y., Jiang, J., Bachevalier, J., Zhang, X., & Chan, A. W. S. (2017). Developmental Whole Brain White Matter Alterations in Transgenic Huntington’s Disease Monkey. *Scientific Reports*, *7*. <https://doi.org/10.1038/s41598-017-00381-8>
- Mensch, S., Baraban, M., Almeida, R., Czopka, T., Ausborn, J., El Manira, A., & Lyons, D. A. (2015). Synaptic vesicle release regulates myelin sheath number of individual oligodendrocytes in vivo. *Nature Neuroscience*, *18*(5), 628–630. <https://doi.org/10.1038/nn.3991>
- Metzler-Baddeley, C., Cantera, J., Coulthard, E., Rosser, A., Jones, D. K., & Baddeley, R. J. (2014). Improved Executive Function and Callosal White Matter Microstructure after Rhythm Exercise in Huntington’s Disease. *Journal of Huntington’s Disease*, *3*(3), 273–283. <https://doi.org/10.3233/JHD-140113>
- Metzler-Baddeley, C., Foley, S., de Santis, S., Charron, C., Hampshire, A., Caeyenberghs, K., & Jones, D. K. (2017). Dynamics of White Matter Plasticity Underlying Working Memory Training: Multimodal Evidence from Diffusion MRI and Relaxometry. *Journal of Cognitive Neuroscience*, *29*(9), 1509–1520. [https://doi.org/10.1162/jocn\\_a\\_01127](https://doi.org/10.1162/jocn_a_01127)

- Milders, M., Crawford, J. R., Lamb, A., & Simpson, S. A. (2003). Differential deficits in expression recognition in gene-carriers and patients with Huntington's disease. *Neuropsychologia*, *41*(11), 1484–1492. [https://doi.org/10.1016/s0028-3932\(03\)00079-4](https://doi.org/10.1016/s0028-3932(03)00079-4)
- Miller, R. G. (1981). Normal univariate techniques. In *Simultaneous statistical inference* (pp. 37–108). Springer.
- Mitchell, I. J., Cooper, A. J., & Griffiths, M. R. (1999). The selective vulnerability of striatopallidal neurons. *Progress in Neurobiology*, *59*(6), 691–719. [https://doi.org/10.1016/S0301-0082\(99\)00019-2](https://doi.org/10.1016/S0301-0082(99)00019-2)
- Monoranu, C. M., Apfelbacher, M., Grünblatt, E., Puppe, B., Alafuzoff, I., Ferrer, I., Al-Saraj, S., Keyvani, K., Schmitt, A., Falkai, P., Schittenhelm, J., Halliday, G., Kril, J., Harper, C., McLean, C., Riederer, P., & Roggendorf, W. (2009). pH measurement as quality control on human post mortem brain tissue: A study of the BrainNet Europe consortium. *Neuropathology and Applied Neurobiology*, *35*(3), 329–337. <https://doi.org/10.1111/j.1365-2990.2008.01003a.x>
- Montoya, A., Pelletier, M., Menear, M., Duplessis, E., Richer, F., & Lepage, M. (2006). Episodic memory impairment in Huntington's disease: A meta-analysis. *Neuropsychologia*, *44*(10), 1984–1994. <https://doi.org/10.1016/j.neuropsychologia.2006.01.015>
- Mori, S., Crain, B. J., Chacko, V. P., & Zijl, P. C. M. V. (1999). Three-dimensional tracking of axonal projections in the brain by magnetic resonance imaging. *Annals of Neurology*, *45*(2), 265–269. [https://doi.org/10.1002/1531-8249\(199902\)45:2<265::AID-ANA21>3.0.CO;2-3](https://doi.org/10.1002/1531-8249(199902)45:2<265::AID-ANA21>3.0.CO;2-3)
- Mörkl, S., Müller, N. J., Blesl, C., Wilkinson, L., Tmava, A., Wurm, W., Holl, A. K., & Painold, A. (2016). Problem solving, impulse control and planning in patients with

- early-and late-stage Huntington's disease. *European Archives of Psychiatry and Clinical Neuroscience*, 266(7), 663–671.
- Moser, E., Stahlberg, F., Ladd, M. E., & Tractnig, S. (2012). 7-T MR—from research to clinical applications? *NMR in Biomedicine*, 25(5), 695–716.  
<https://doi.org/10.1002/nbm.1794>
- Mueller, S. T., & Piper, B. J. (2014). The psychology experiment building language (PEBL) and PEBL test battery. *Journal of Neuroscience Methods*, 222, 250–259.
- Muhlau, M., Gaser, C., & Wohlschager, A. (2007). *Striatal atrophy in Huntington's disease is leftward biased*. 120.
- Myers, R. H., Vonsattel, J. P., Paskevich, P. A., Kiely, D. K., Stevens, T. J., Cupples, L. A., Richardson, E. P., & Bird, E. D. (1991). Decreased Neuronal and Increased Oligodendroglial Densities in Huntington's Disease Caudate Nucleus. *Journal of Neuropathology & Experimental Neurology*, 50(6), 729–742.  
<https://doi.org/10.1097/00005072-199111000-00005>
- Nair, G., Tanahashi, Y., Low, H. P., Billings-Gagliardi, S., Schwartz, W. J., & Duong, T. Q. (2005). Myelination and long diffusion times alter diffusion-tensor-imaging contrast in myelin-deficient shiverer mice. *NeuroImage*, 28(1), 165–174.  
<https://doi.org/10.1016/j.neuroimage.2005.05.049>
- Nam, Y., Kim, D.-H., & Lee, J. (2015a). Physiological noise compensation in gradient-echo myelin water imaging. *NeuroImage*, 120, 345–349.  
<https://doi.org/10.1016/j.neuroimage.2015.07.014>
- Nam, Y., Lee, J., Hwang, D., & Kim, D.-H. (2015b). Improved estimation of myelin water fraction using complex model fitting. *NeuroImage*, 116, 214–221.  
<https://doi.org/10.1016/j.neuroimage.2015.03.081>

- Nance, M. A., Mathias-Hagen, V., Breningstall, G., Wick, M. J., & McGlennen, R. C. (1999). Analysis of a very large trinucleotide repeat in a patient with juvenile Huntington's disease. *Neurology*, *52*(2), 392–394.  
<https://doi.org/10.1212/wnl.52.2.392>
- Nasir, J., Floresco, S. B., O'Kusky, J. R., Diewert, V. M., Richman, J. M., Zeisler, J., Borowski, A., Marth, J. D., Phillips, A. G., & Hayden, M. R. (1995). Targeted disruption of the Huntington's disease gene results in embryonic lethality and behavioral and morphological changes in heterozygotes. *Cell*, *81*(5), 811–823.  
[https://doi.org/10.1016/0092-8674\(95\)90542-1](https://doi.org/10.1016/0092-8674(95)90542-1)
- Nasreddine, Z. S., Phillips, N. A., Bédirian, V., Charbonneau, S., Whitehead, V., Collin, I., Cummings, J. L., & Chertkow, H. (2005). The Montreal Cognitive Assessment, MoCA: A Brief Screening Tool For Mild Cognitive Impairment. *Journal of the American Geriatrics Society*, *53*(4), 695–699. <https://doi.org/10.1111/j.1532-5415.2005.53221.x>
- Nave, R. D., Ginestroni, A., Tessa, C., Giannelli, M., Piacentini, S., Filippi, M., & Mascalchi, M. (2010). Regional Distribution and Clinical Correlates of White Matter Structural Damage in Huntington Disease: A Tract-Based Spatial Statistics Study. *American Journal of Neuroradiology*, *31*(9), 1675–1681. <https://doi.org/10.3174/ajnr.A2128>
- Naver, B., Stub, C., Møller, M., Fenger, K., Hansen, A. K., Hasholt, L., & Sørensen, S. A. (2003). Molecular and behavioral analysis of the R6/1 Huntington's disease transgenic mouse. *Neuroscience*, *122*(4), 1049–1057.  
<https://doi.org/10.1016/j.neuroscience.2003.08.053>
- Neema, M., Goldberg-Zimring, D., Guss, Z. D., Healy, B. C., Guttmann, C. R. G., Houtchens, M. K., Weiner, H. L., Horsfield, M. A., Hackney, D. B., Alsop, D. C., & Bakshi, R. (2009). 3T MRI relaxometry detects T2 prolongation in the cerebral

- normal-appearing white matter in multiple sclerosis. *NeuroImage*, 46(3), 633–641.  
<https://doi.org/10.1016/j.neuroimage.2009.03.001>
- Nehl, C., Paulsen, J. S., & Huntington Study Group. (2004). Cognitive and psychiatric aspects of Huntington disease contribute to functional capacity. *The Journal of Nervous and Mental Disease*, 192(1), 72–74.  
<https://doi.org/10.1097/01.nmd.0000106004.67587.57>
- Nguyen, G. D., Gokhan, S., Molero, A. E., & Mehler, M. F. (2013). Selective roles of normal and mutant huntingtin in neural induction and early neurogenesis. *PloS One*, 8(5), e64368. <https://doi.org/10.1371/journal.pone.0064368>
- Nichols, T., & Holmes, A. (2014). *SnPM-Statistical NonParametric Mapping: A Toolbox for SPM*.
- Nilsson, M., Lasič, S., Drobňak, I., Topgaard, D., & Westin, C. (2017). Resolution limit of cylinder diameter estimation by diffusion MRI: The impact of gradient waveform and orientation dispersion. *NMR in Biomedicine*, 30(7), e3711.
- Ning, L., Bonet-Carne, E., Grussu, F., Seppehrband, F., Kaden, E., Veraart, J., Blumberg, S. B., Khoo, C. S., Palombo, M., & Coll-Font, J. (2019). *Muti-shell diffusion MRI harmonisation and enhancement challenge (MUSHAC): Progress and results*. 217–224.
- Nopoulos, P. C. (2016). Huntington disease: A single-gene degenerative disorder of the striatum. *Dialogues in Clinical Neuroscience*, 18(1), 91–98.
- Nopoulos, P. C., Aylward, E. H., Ross, C. A., Johnson, H. J., Magnotta, V. A., Juhl, A. R., Pierson, R. K., Mills, J., Langbehn, D. R., & Paulsen, J. S. (2010). Cerebral cortex structure in prodromal Huntington disease. *Neurobiology of Disease*, 40(3), 544–554.
- Norris, D. G. (2003). High field human imaging. *Journal of Magnetic Resonance Imaging*, 18(5), 519–529. <https://doi.org/10.1002/jmri.10390>

- Novikov, D. S., Fieremans, E., Jespersen, S. N., & Kiselev, V. G. (2019). Quantifying brain microstructure with diffusion MRI: Theory and parameter estimation. *NMR in Biomedicine*, 32(4), e3998. <https://doi.org/10.1002/nbm.3998>
- Nunes, D., Cruz, T. L., Jespersen, S. N., & Shemesh, N. (2017). Mapping axonal density and average diameter using non-monotonic time-dependent gradient-echo MRI. *Journal of Magnetic Resonance*, 277, 117–130.
- Odrobina, E. E., Lam, T. Y. J., Pun, T., Midha, R., & Stanisz, G. J. (2005). MR properties of excised neural tissue following experimentally induced demyelination. *NMR in Biomedicine*, 18(5), 277–284. <https://doi.org/10.1002/nbm.951>
- O'Rourke, J. J. F., Adams, W. H., Duff, K., Byars, J., Nopoulos, P., Paulsen, J. S., & Beglinger, L. J. (2011). Estimating Premorbid Functioning in Huntington's Disease: The Relationship between Disease Progression and the Wide Range Achievement Test Reading Subtest. *Archives of Clinical Neuropsychology*, 26(1), 59–66. <https://doi.org/10.1093/arclin/acq088>
- Orr, H. T., & Zoghbi, H. Y. (2007). Trinucleotide Repeat Disorders. *Annual Review of Neuroscience*, 30(1), 575–621. <https://doi.org/10.1146/annurev.neuro.29.051605.113042>
- Ou, X., Sun, S.-W., Liang, H.-F., Song, S.-K., & Gochberg, D. F. (2009). The MT pool size ratio and the DTI radial diffusivity may reflect the myelination in shiverer and control mice. *NMR in Biomedicine*, 22(5), 480–487. <https://doi.org/10.1002/nbm.1358>
- Pakkenberg, B., Pelvig, D., Marner, L., Bundgaard, M. J., Gundersen, H. J. G., Nyengaard, J. R., & Regeur, L. (2003). Aging and the human neocortex. *Experimental Gerontology*, 38(1–2), 95–99.

- Palop, J. J., Chin, J., & Mucke, L. (2006). A network dysfunction perspective on neurodegenerative diseases. *Nature*, *443*(7113), 768–773.  
<https://doi.org/10.1038/nature05289>
- Papadakis, N. G., Murrills, C. D., Hall, L. D., Huang, C. L.-H., & Carpenter, T. A. (2000). Minimal gradient encoding for robust estimation of diffusion anisotropy☆. *Magnetic Resonance Imaging*, *18*(6), 671–679.
- Papoutsis, M., Labuschagne, I., Tabrizi, S. J., & Stout, J. C. (2014). The cognitive burden in Huntington’s disease: Pathology, phenotype, and mechanisms of compensation. *Movement Disorders*, *29*(5), 673–683. <https://doi.org/10.1002/mds.25864>
- Papp, K. V., Kaplan, R. F., & Snyder, P. J. (2011). Biological markers of cognition in prodromal Huntington’s disease: A review. *Brain and Cognition*, *77*(2), 280–291.  
<https://doi.org/10.1016/j.bandc.2011.07.009>
- Parker, G. (2014). *Robust processing of diffusion weighted image data* [Phd, Cardiff University]. <http://orca.cf.ac.uk/61622/>
- Pasternak, O., Sochen, N., Gur, Y., Intrator, N., & Assaf, Y. (2009). Free water elimination and mapping from diffusion MRI. *Magnetic Resonance in Medicine*, *62*(3), 717–730.  
<https://doi.org/10.1002/mrm.22055>
- Paulsen, J. S. (2011). Cognitive Impairment in Huntington Disease: Diagnosis and Treatment. *Current Neurology and Neuroscience Reports*, *11*(5), 474–483.  
<https://doi.org/10.1007/s11910-011-0215-x>
- Paulsen, J. S., Hayden, M., Stout, J. C., Langbehn, D. R., Aylward, E., Ross, C. A., Guttman, M., Nance, M., Kiebertz, K., Oakes, D., Shoulson, I., Kayson, E., Johnson, S., Penziner, E., & Predict-HD Investigators of the Huntington Study Group. (2006). Preparing for preventive clinical trials: The Predict-HD study. *Archives of Neurology*, *63*(6), 883–890. <https://doi.org/10.1001/archneur.63.6.883>

- Paulsen, J. S., Langbehn, D. R., Stout, J. C., Aylward, E., Ross, C. A., Nance, M., Guttman, M., Johnson, S., MacDonald, M., Beglinger, L. J., Duff, K., Kayson, E., Biglan, K., Shoulson, I., Oakes, D., Hayden, M., & Predict-HD Investigators and Coordinators of the Huntington Study Group. (2008). Detection of Huntington's disease decades before diagnosis: The Predict-HD study. *Journal of Neurology, Neurosurgery, and Psychiatry*, 79(8), 874–880. <https://doi.org/10.1136/jnnp.2007.128728>
- Paulsen, J. S., Long, J. D., Johnson, H. J., Aylward, E. H., Ross, C. A., Williams, J. K., Nance, M. A., Erwin, C. J., Westervelt, H. J., Harrington, D. L., Bockholt, H. J., Zhang, Y., McCusker, E. A., Chiu, E. M., Panegyres, P. K., & PREDICT-HD Investigators and Coordinators of the Huntington Study Group. (2014a). Clinical and Biomarker Changes in Premanifest Huntington Disease Show Trial Feasibility: A Decade of the PREDICT-HD Study. *Frontiers in Aging Neuroscience*, 6, 78. <https://doi.org/10.3389/fnagi.2014.00078>
- Paulsen, J. S., Long, J. D., Ross, C. A., Harrington, D. L., Erwin, C. J., Williams, J. K., Westervelt, H. J., Johnson, H. J., Aylward, E. H., Zhang, Y., Bockholt, H. J., Barker, R. A., & PREDICT-HD Investigators and Coordinators of the Huntington Study Group. (2014b). Prediction of manifest Huntington's disease with clinical and imaging measures: A prospective observational study. *The Lancet. Neurology*, 13(12), 1193–1201. [https://doi.org/10.1016/S1474-4422\(14\)70238-8](https://doi.org/10.1016/S1474-4422(14)70238-8)
- Paulsen, J. S., Miller, A. C., Hayes, T., & Shaw, E. (2017). Chapter 6—Cognitive and behavioral changes in Huntington disease before diagnosis. In A. S. Feigin & K. E. Anderson (Eds.), *Handbook of Clinical Neurology* (Vol. 144, pp. 69–91). Elsevier. <https://doi.org/10.1016/B978-0-12-801893-4.00006-7>
- Paulson, H. L., & Albin, R. L. (2011). Huntington's Disease: Clinical Features and Routes to Therapy. In D. C. Lo & R. E. Hughes (Eds.), *Neurobiology of Huntington's Disease:*

*Applications to Drug Discovery*. CRC Press/Taylor & Francis.

<http://www.ncbi.nlm.nih.gov/books/NBK56000/>

- Payne, S. C., Bartlett, C. A., Harvey, A. R., Dunlop, S. A., & Fitzgerald, M. (2012). Myelin Sheath Decompaction, Axon Swelling, and Functional Loss during Chronic Secondary Degeneration in Rat Optic Nerve. *Investigative Ophthalmology & Visual Science*, 53(10), 6093–6101. <https://doi.org/10.1167/iovs.12-10080>
- Penke, L., Maniega, S. M., Murray, C., Gow, A. J., Hernández, M. C. V., Clayden, J. D., Starr, J. M., Wardlaw, J. M., Bastin, M. E., & Deary, I. J. (2010). A General Factor of Brain White Matter Integrity Predicts Information Processing Speed in Healthy Older People. *Journal of Neuroscience*, 30(22), 7569–7574. <https://doi.org/10.1523/JNEUROSCI.1553-10.2010>
- Peters, A. (2009). The effects of normal aging on myelinated nerve fibers in monkey central nervous system. *Frontiers in Neuroanatomy*, 3, 11.
- Petiet, A., Delatour, B., & Dhenain, M. (2011). Models of Neurodegenerative Disease – Alzheimer’s Anatomical and Amyloid Plaque Imaging. In L. Schröder & C. Faber (Eds.), *In vivo NMR Imaging* (Vol. 771, pp. 293–308). Humana Press. [https://doi.org/10.1007/978-1-61779-219-9\\_16](https://doi.org/10.1007/978-1-61779-219-9_16)
- Pflanz, C. P., Charquero-Ballester, M., Majid, D. S. A., Winkler, A. M., Vallée, E., Aron, A. R., Jenkinson, M., & Douaud, G. (2019). One-year changes in brain microstructure differentiate preclinical Huntington’s disease stages. *NeuroImage : Clinical*, 25. <https://doi.org/10.1016/j.nicl.2019.102099>
- Phillips, O., Sanchez-Castaneda, C., Elifani, F., Maglione, V., Pardo, A. D., Caltagirone, C., Squitieri, F., Sabatini, U., & Paola, M. D. (2013). Tractography of the Corpus Callosum in Huntington’s Disease. *PLOS ONE*, 8(9), e73280. <https://doi.org/10.1371/journal.pone.0073280>

- Phillips, O., Squitieri, F., Sanchez-Castaneda, C., Elifani, F., Caltagirone, C., Sabatini, U., & Paola, M. D. (2014). Deep White Matter in Huntington's Disease. *PLOS ONE*, *9*(10), e109676. <https://doi.org/10.1371/journal.pone.0109676>
- Phillips, O., Squitieri, F., Sanchez-Castaneda, C., Elifani, F., Griguoli, A., Maglione, V., Caltagirone, C., Sabatini, U., & Di Paola, M. (2015). The Corticospinal Tract in Huntington's Disease. *Cerebral Cortex*, *25*(9), 2670–2682. <https://doi.org/10.1093/cercor/bhu065>
- Pierpaoli, C., & Basser, P. J. (1996). Toward a quantitative assessment of diffusion anisotropy. *Magnetic Resonance in Medicine*, *36*(6), 893–906.
- Pirogovsky, E., Goldstein, J., Peavy, G., Jacobson, M. W., Corey-Bloom, J., & Gilbert, P. E. (2009). Temporal order memory deficits prior to clinical diagnosis in Huntington's disease. *Journal of the International Neuropsychological Society: JINS*, *15*(5), 662.
- Poudel, G. R., Stout, J. C., Domínguez D, J. F., Salmon, L., Churchyard, A., Chua, P., Georgiou-Karistianis, N., & Egan, G. F. (2014). White matter connectivity reflects clinical and cognitive status in Huntington's disease. *Neurobiology of Disease*, *65*, 180–187. <https://doi.org/10.1016/j.nbd.2014.01.013>
- Pouladi, M. A., Morton, A. J., & Hayden, M. R. (2013). Choosing an animal model for the study of Huntington's disease. *Nature Reviews Neuroscience*, *14*(10), 708–721. <https://doi.org/10.1038/nrn3570>
- Poupon, C., Clark, C. A., Frouin, V., Regis, J., Bloch, I., Le Bihan, D., & Mangin, J.-F. (2000). Regularization of diffusion-based direction maps for the tracking of brain white matter fascicles. *Neuroimage*, *12*(2), 184–195.
- Preacher, K. J., & MacCallum, R. C. (2002). Exploratory Factor Analysis in Behavior Genetics Research: Factor Recovery with Small Sample Sizes. *Behavior Genetics*, *32*(2), 153–161. <https://doi.org/10.1023/A:1015210025234>

- Pringsheim, T., Wiltshire, K., Day, L., Dykeman, J., Steeves, T., & Jette, N. (2012). The incidence and prevalence of Huntington's disease: A systematic review and meta-analysis. *Movement Disorders: Official Journal of the Movement Disorder Society*, 27(9), 1083–1091. <https://doi.org/10.1002/mds.25075>
- Ramani, A., Dalton, C., Miller, D. H., Tofts, P. S., & Barker, G. J. (2002). Precise estimate of fundamental in-vivo MT parameters in human brain in clinically feasible times. *Magnetic Resonance Imaging*, 20(10), 721–731. [https://doi.org/10.1016/S0730-725X\(02\)00598-2](https://doi.org/10.1016/S0730-725X(02)00598-2)
- Ramaswamy, S., & Kordower, J. H. (2012). Gene therapy for Huntington's disease. *Neurobiology of Disease*. <https://doi.org/10.1016/j.nbd.2011.12.030>
- Rattray, I., Smith, E. J., Crum, W. R., Walker, T. A., Gale, R., Bates, G. P., & Modo, M. (2013). Correlations of Behavioral Deficits with Brain Pathology Assessed through Longitudinal MRI and Histopathology in the R6/1 Mouse Model of Huntington's Disease. *PLOS ONE*, 8(12), e84726. <https://doi.org/10.1371/journal.pone.0084726>
- Reitan, R. M., & Wolfson, D. (2009). The Halstead–Reitan neuropsychological test battery for adults—Theoretical, methodological, and validation bases. *Neuropsychological Assessment of Neuropsychiatric and Neuromedical Disorders*, 1, 36.
- Reveley, C., Seth, A. K., Pierpaoli, C., Silva, A. C., Yu, D., Saunders, R. C., Leopold, D. A., & Frank, Q. Y. (2015). Superficial white matter fiber systems impede detection of long-range cortical connections in diffusion MR tractography. *Proceedings of the National Academy of Sciences*, 112(21), E2820–E2828.
- Robins Wahlin, T.-B., Luszcz, M. A., Wahlin, Å., & Byrne, G. J. (2015). Non-Verbal and Verbal Fluency in Prodromal Huntington's Disease. *Dementia and Geriatric Cognitive Disorders EXTRA*, 5(3), 517–529. <https://doi.org/10.1159/000441942>

- Rocha, N. P., Ribeiro, F. M., Furr-Stimming, E., & Teixeira, A. L. (2016). Neuroimmunology of Huntington's Disease: Revisiting Evidence from Human Studies. *Mediators of Inflammation*, 2016. <https://doi.org/10.1155/2016/8653132>
- Rohrer, D., Salmon, D. P., Wixted, J. T., & Paulsen, J. S. (1999). The disparate effects of Alzheimer's disease and Huntington's disease on semantic memory. *Neuropsychology*, 13(3), 381–388. <https://doi.org/10.1037/0894-4105.13.3.381>
- Roos, R. A. C. (2010). Huntington's disease: A clinical review. *Orphanet Journal of Rare Diseases*, 5, 40. <https://doi.org/10.1186/1750-1172-5-40>
- Rosas, H. D., Goodman, J., Chen, Y. I., Jenkins, B. G., Kennedy, D. N., Makris, N., Patti, M., Seidman, L. J., Beal, M. F., & Koroshetz, W. J. (2001). Striatal volume loss in HD as measured by MRI and the influence of CAG repeat. *Neurology*, 57(6), 1025–1028.
- Rosas, H. D., Hevelone, N. D., Zaleta, A. K., Greve, D. N., Salat, D. H., & Fischl, B. (2005). Regional cortical thinning in preclinical Huntington disease and its relationship to cognition. *Neurology*, 65(5), 745–747. <https://doi.org/10.1212/01.wnl.0000174432.87383.87>
- Rosas, H. D., Lee, S. Y., Bender, A. C., Zaleta, A. K., Vangel, M., Yu, P., Fischl, B., Pappu, V., Onorato, C., & Cha, J.-H. (2010). Altered white matter microstructure in the corpus callosum in Huntington's disease: Implications for cortical “disconnection.” *Neuroimage*, 49(4), 2995–3004.
- Rosas, H. D., Liu, A. K., Hersch, S., Glessner, M., Ferrante, R. J., Salat, D. H., van der Kouwe, A., Jenkins, B. G., Dale, A. M., & Fischl, B. (2002). Regional and progressive thinning of the cortical ribbon in Huntington's disease. *Neurology*, 58(5), 695–701.
- Rosas, H. D., Tuch, D. S., Hevelone, N. D., Zaleta, A. K., Vangel, M., Hersch, S. M., & Salat, D. H. (2006). Diffusion tensor imaging in presymptomatic and early

- Huntington's disease: Selective white matter pathology and its relationship to clinical measures. *Movement Disorders: Official Journal of the Movement Disorder Society*, 21(9), 1317–1325. <https://doi.org/10.1002/mds.20979>
- Rosas, H. D., Wilkens, P., Salat, D. H., Mercaldo, N. D., Vangel, M., Yendiki, A. Y., & Hersch, S. M. (2018). Complex spatial and temporally defined myelin and axonal degeneration in Huntington disease. *NeuroImage: Clinical*, 20, 236–242. <https://doi.org/10.1016/j.nicl.2018.01.029>
- Rosenblatt, A., Kumar, B. V., Mo, A., Welsh, C. S., Margolis, R. L., & Ross, C. A. (2012). Age, CAG repeat length, and clinical progression in Huntington's disease. *Movement Disorders: Official Journal of the Movement Disorder Society*, 27(2), 272–276. <https://doi.org/10.1002/mds.24024>
- Rosenblatt, A., Liang, K.-Y., Zhou, H., Abbott, M. H., Gourley, L. M., Margolis, R. L., Brandt, J., & Ross, C. A. (2006). The association of CAG repeat length with clinical progression in Huntington disease. *Neurology*, 66(7), 1016–1020. <https://doi.org/10.1212/01.wnl.0000204230.16619.d9>
- Ross, C. A., Aylward, E. H., Wild, E. J., Langbehn, D. R., Long, J. D., Warner, J. H., Scahill, R. I., Leavitt, B. R., Stout, J. C., Paulsen, J. S., Reilmann, R., Unschuld, P. G., Wexler, A., Margolis, R. L., & Tabrizi, S. J. (2014). Huntington disease: Natural history, biomarkers and prospects for therapeutics. *Nature Reviews Neurology*, 10(4), 204–216. <https://doi.org/10.1038/nrneurol.2014.24>
- Rovira, À., Auger, C., & Alonso, J. (2013). Magnetic resonance monitoring of lesion evolution in multiple sclerosis. *Therapeutic Advances in Neurological Disorders*, 6(5), 298–310. <https://doi.org/10.1177/1756285613484079>

- Rowe, K. C., Paulsen, J. S., Langbehn, D. R., Duff, K., Beglinger, L. J., Wang, C., O'Rourke, J. J., Stout, J. C., & Moser, D. J. (2010). Self-paced timing detects and tracks change in prodromal Huntington disease. *Neuropsychology*, *24*(4), 435.
- Rüb, U., Seidel, K., Heinsen, H., Vonsattel, J. P., den Dunnen, W. F., & Korf, H. W. (2016). Huntington's disease (HD): The neuropathology of a multisystem neurodegenerative disorder of the human brain. *Brain Pathology (Zurich, Switzerland)*, *26*(6), 726–740. <https://doi.org/10.1111/bpa.12426>
- Rüb, U., Vonsattel, J. P. V., Heinsen, H., & Korf, H.-W. (2015). The Neuropathology of Huntington's disease: Classical findings, recent developments and correlation to functional neuroanatomy. *Advances in Anatomy, Embryology, and Cell Biology*, *217*, 1–146.
- Rudrapatna, U., Parker, G. D., Roberts, J., & Jones, D. K. (2021a). A comparative study of gradient nonlinearity correction strategies for processing diffusion data obtained with ultra-strong gradient MRI scanners. *Magnetic Resonance in Medicine*, *85*(2), 1104–1113. <https://doi.org/10.1002/mrm.28464>
- Rudrapatna, U., Parker, G. D., Roberts, J., & Jones, D. K. (2021b). A comparative study of gradient nonlinearity correction strategies for processing diffusion data obtained with ultra-strong gradient MRI scanners. *Magnetic Resonance in Medicine*, *85*(2), 1104–1113. <https://doi.org/10.1002/mrm.28464>
- Ruocco, H. H., Bonilha, L., Li, L. M., Lopes-Cendes, I., & Cendes, F. (2008). Longitudinal analysis of regional grey matter loss in Huntington disease: Effects of the length of the expanded CAG repeat. *Journal of Neurology, Neurosurgery, and Psychiatry*, *79*(2), 130–135. <https://doi.org/10.1136/jnnp.2007.116244>
- Rushton, W. A. H. (1951). A theory of the effects of fibre size in medullated nerve. *The Journal of Physiology*, *115*(1), 101–122.

- Saba, R. A., Yared, J. H., Doring, T. M., Borges, V., & Ferraz, H. B. (2017). Diffusion tensor imaging of brain white matter in Huntington gene mutation individuals. *Arquivos de Neuro-Psiquiatria*, *75*(8), 503–508.
- Sagi, Y., Tavor, I., Hofstetter, S., Tzur-Moryosef, S., Blumenfeld-Katzir, T., & Assaf, Y. (2012). Learning in the Fast Lane: New Insights into Neuroplasticity. *Neuron*, *73*(6), 1195–1203. <https://doi.org/10.1016/j.neuron.2012.01.025>
- Sairanen, V., Leemans, A., & Tax, C. M. W. (2018). Fast and accurate Slicewise OutLier Detection (SOLID) with informed model estimation for diffusion MRI data. *NeuroImage*, *181*, 331–346. <https://doi.org/10.1016/j.neuroimage.2018.07.003>
- Sampaio-Baptista, C., Khrapitchev, A. A., Foxley, S., Schlagheck, T., Scholz, J., Jbabdi, S., DeLuca, G. C., Miller, K. L., Taylor, A., Thomas, N., Kleim, J., Sibson, N. R., Bannerman, D., & Johansen-Berg, H. (2013). Motor Skill Learning Induces Changes in White Matter Microstructure and Myelination. *The Journal of Neuroscience*, *33*(50), 19499–19503. <https://doi.org/10.1523/JNEUROSCI.3048-13.2013>
- Sánchez, I., Mahlke, C., & Yuan, J. (2003). Pivotal role of oligomerization in expanded polyglutamine neurodegenerative disorders. *Nature*, *421*(6921), 373–379. <https://doi.org/10.1038/nature01301>
- Sati, P., van Gelderen, P., Silva, A. C., Reich, D. S., Merkle, H., de Zwart, J. A., & Duyn, J. H. (2013). Micro-compartment specific T2\* relaxation in the brain. *NeuroImage*, *77*, 268–278. <https://doi.org/10.1016/j.neuroimage.2013.03.005>
- Saudou, F., Finkbeiner, S., Devys, D., & Greenberg, M. E. (1998). Huntingtin Acts in the Nucleus to Induce Apoptosis but Death Does Not Correlate with the Formation of Intranuclear Inclusions. *Cell*, *95*(1), 55–66. [https://doi.org/10.1016/S0092-8674\(00\)81782-1](https://doi.org/10.1016/S0092-8674(00)81782-1)

- Saudou, F., & Humbert, S. (2016). The Biology of Huntingtin. *Neuron*, *89*(5), 910–926.  
<https://doi.org/10.1016/j.neuron.2016.02.003>
- Sawiak, S., Wood, N., Williams, G., Morton, A., & Carpenter, T. (2009). *SPMMouse: A new toolbox for SPM in the animal brain*. 18–24.
- Sawiak, Wood, N. I., Williams, G. B., Morton, A. J., & Carpenter, T. A. (2013). Voxel-based morphometry with templates and validation in a mouse model of Huntington’s disease. *Magnetic Resonance Imaging*, *31*(9), 1522–1531.
- Scahill, R. I., Hobbs, N. Z., Say, M. J., Bechtel, N., Henley, S. M. D., Hyare, H., Langbehn, D. R., Jones, R., Leavitt, B. R., Roos, R. A. C., Durr, A., Johnson, H., Lehericy, S., Craufurd, D., Kennard, C., Hicks, S. L., Stout, J. C., Reilmann, R., Tabrizi, S. J., & TRACK-HD investigators. (2013). Clinical impairment in premanifest and early Huntington’s disease is associated with regionally specific atrophy. *Human Brain Mapping*, *34*(3), 519–529. <https://doi.org/10.1002/hbm.21449>
- Scahill, R. I., Zeun, P., Osborne-Crowley, K., Johnson, E. B., Gregory, S., Parker, C., Lowe, J., Nair, A., O’Callaghan, C., Langley, C., Papoutsis, M., McColgan, P., Estevez-Fraga, C., Fayer, K., Wellington, H., Rodrigues, F. B., Byrne, L. M., Heselgrave, A., Hyare, H., ... Tabrizi, S. J. (2020). Biological and clinical characteristics of gene carriers far from predicted onset in the Huntington’s disease Young Adult Study (HD-YAS): A cross-sectional analysis. *The Lancet Neurology*, *19*(6), 502–512.  
[https://doi.org/10.1016/S1474-4422\(20\)30143-5](https://doi.org/10.1016/S1474-4422(20)30143-5)
- Schäfer, A., Wharton, S., Gowland, P., & Bowtell, R. (2009). Using magnetic field simulation to study susceptibility-related phase contrast in gradient echo MRI. *NeuroImage*, *48*(1), 126–137. <https://doi.org/10.1016/j.neuroimage.2009.05.093>

- Schenck, J. F. (1996). The role of magnetic susceptibility in magnetic resonance imaging: MRI magnetic compatibility of the first and second kinds. *Medical Physics*, 23(6), 815–850. <https://doi.org/10.1118/1.597854>
- Schiffer, N. W., Broadley, S. A., Hirschberger, T., Tavan, P., Kretzschmar, H. A., Giese, A., Haass, C., Hartl, F. U., & Schmid, B. (2007). Identification of anti-prion compounds as efficient inhibitors of polyglutamine protein aggregation in a zebrafish model. *The Journal of Biological Chemistry*, 282(12), 9195–9203. <https://doi.org/10.1074/jbc.M607865200>
- Schmierer, K., Tozer, D. J., Scaravilli, F., Altmann, D. R., Barker, G. J., Tofts, P. S., & Miller, D. H. (2007). Quantitative Magnetization Transfer Imaging in Postmortem Multiple Sclerosis Brain. *Journal of Magnetic Resonance Imaging : JMRI*, 26(1), 41–51. <https://doi.org/10.1002/jmri.20984>
- Scholz, J., Klein, M. C., Behrens, T. E. J., & Johansen-Berg, H. (2009). Training induces changes in white matter architecture. *Nature Neuroscience*, 12(11), 1370–1371. <https://doi.org/10.1038/nn.2412>
- Schulte, J., & Littleton, J. T. (2011). The biological function of the Huntingtin protein and its relevance to Huntington's Disease pathology. *Current Trends in Neurology*, 5, 65–78.
- Schultz, S. K. (2001). Principles of neural science. *American Journal of Psychiatry*, 158(4), 662–662.
- Schwarcz, R., Whetsell, W. O., & Mangano, R. M. (1983). Quinolinic acid: An endogenous metabolite that produces axon-sparing lesions in rat brain. *Science (New York, N.Y.)*, 219(4582), 316–318. <https://doi.org/10.1126/science.6849138>
- Schweser, F., Deistung, A., Lehr, B. W., & Reichenbach, J. R. (2011). Quantitative imaging of intrinsic magnetic tissue properties using MRI signal phase: An approach to in vivo brain iron metabolism? *Neuroimage*, 54(4), 2789–2807.

- Selemon, L. D., Rajkowska, G., & Goldman-Rakic, P. S. (2004). Evidence for progression in frontal cortical pathology in late-stage Huntington's disease. *The Journal of Comparative Neurology*, *468*(2), 190–204. <https://doi.org/10.1002/cne.10938>
- Sellers, J., Ridner, S. H., & Claassen, D. O. (2020). A Systematic Review of Neuropsychiatric Symptoms and Functional Capacity in Huntington's Disease. *The Journal of Neuropsychiatry and Clinical Neurosciences*, *32*(2), 109–124. <https://doi.org/10.1176/appi.neuropsych.18120319>
- Sepehrband, F., Alexander, D. C., Kurniawan, N. D., Reutens, D. C., & Yang, Z. (2016). Towards higher sensitivity and stability of axon diameter estimation with diffusion-weighted MRI. *NMR in Biomedicine*, *29*(3), 293–308.
- Serres, S., Anthony, D. C., Jiang, Y., Campbell, S. J., Broom, K. A., Khrapitchev, A., & Sibson, N. R. (2009). Comparison of MRI signatures in pattern I and II multiple sclerosis models. *NMR in Biomedicine*, *22*(10), 1014–1024. <https://doi.org/10.1002/nbm.1404>
- Setsompop, K., Kimmlingen, R., Eberlein, E., Witzel, T., Cohen-Adad, J., McNab, J. A., Keil, B., Tisdall, M. D., Hoecht, P., Dietz, P., Cauley, S. F., Tountcheva, V., Matschl, V., Lenz, V. H., Heberlein, K., Potthast, A., Thein, H., Van Horn, J., Toga, A., ... Wald, L. L. (2013). Pushing the limits of in vivo diffusion MRI for the Human Connectome Project. *NeuroImage*, *80*, 220–233. <https://doi.org/10.1016/j.neuroimage.2013.05.078>
- Shannon, K. M. (2020). Recent Advances in the Treatment of Huntington's Disease: Targeting DNA and RNA. *CNS Drugs*, *34*(3), 219–228. <https://doi.org/10.1007/s40263-019-00695-3>
- Shishegar, R., Rajapakse, S., & Georgiou-Karistianis, N. (2019). Altered Cortical Morphometry in Pre-manifest Huntington's Disease: Cross-sectional Data from the

- IMAGE-HD Study. *Conference Proceedings: ... Annual International Conference of the IEEE Engineering in Medicine and Biology Society. IEEE Engineering in Medicine and Biology Society. Annual Conference, 2019*, 2844–2847.  
<https://doi.org/10.1109/EMBC.2019.8857240>
- Shmuelof, L., & Krakauer, J. W. (2011). Are we ready for a natural history of motor learning? *Neuron*, 72(3), 469–476. <https://doi.org/10.1016/j.neuron.2011.10.017>
- Sierra, A., Laitinen, T., Lehtimäki, K., Rieppo, L., Pitkänen, A., & Gröhn, O. (2011). Diffusion tensor MRI with tract-based spatial statistics and histology reveals undiscovered lesioned areas in kainate model of epilepsy in rat. *Brain Structure and Function*, 216(2), 123–135.
- Siesling, S., Van Vugt, J. P., Zwinderman, K. A., Kieburz, K., & Roos, R. A. (1998). Unified Huntington's disease rating scale: A follow up. *Movement Disorders: Official Journal of the Movement Disorder Society*, 13(6), 915–919.
- Simmons, D. A., Casale, M., Alcon, B., Pham, N., Narayan, N., & Lynch, G. (2007). Ferritin accumulation in dystrophic microglia is an early event in the development of Huntington's disease. *Glia*, 55(10), 1074–1084.
- Simpson, J. A., Lovecky, D., Kogan, J., Vetter, L. A., & Yohrling, G. J. (2016). Survey of the Huntington's Disease Patient and Caregiver Community Reveals Most Impactful Symptoms and Treatment Needs. *Journal of Huntington's Disease*, 5(4), 395–403.  
<https://doi.org/10.3233/JHD-160228>
- Sitek, E. J., Sołtan, W., Wiczorek, D., Schinwelski, M., Robowski, P., Reilmann, R., Guzińska, K., Harciarek, M., Krysa, W., & Sławek, J. (2011). Self-awareness of motor dysfunction in patients with Huntington's disease in comparison to Parkinson's disease and cervical dystonia. *Journal of the International Neuropsychological Society: JINS*, 17(5), 788–795. <https://doi.org/10.1017/S1355617711000725>

- Skare, S., Hedehus, M., Moseley, M. E., & Li, T.-Q. (2000). Condition number as a measure of noise performance of diffusion tensor data acquisition schemes with MRI. *Journal of Magnetic Resonance*, *147*(2), 340–352.
- Sled, J. G. (2018). Modelling and interpretation of magnetization transfer imaging in the brain. *NeuroImage*, *182*, 128–135. <https://doi.org/10.1016/j.neuroimage.2017.11.065>
- Slow, E. J., van Raamsdonk, J., Rogers, D., Coleman, S. H., Graham, R. K., Deng, Y., Oh, R., Bissada, N., Hossain, S. M., Yang, Y.-Z., Li, X.-J., Simpson, E. M., Gutekunst, C.-A., Leavitt, B. R., & Hayden, M. R. (2003). Selective striatal neuronal loss in a YAC128 mouse model of Huntington disease. *Human Molecular Genetics*, *12*(13), 1555–1567. <https://doi.org/10.1093/hmg/ddg169>
- Smith, S. M., Jenkinson, M., Johansen-Berg, H., Rueckert, D., Nichols, T. E., Mackay, C. E., Watkins, K. E., Ciccarelli, O., Cader, M. Z., Matthews, P. M., & Behrens, T. E. J. (2006). Tract-based spatial statistics: Voxelwise analysis of multi-subject diffusion data. *NeuroImage*, *31*(4), 1487–1505. <https://doi.org/10.1016/j.neuroimage.2006.02.024>
- Smith, S. M., Jenkinson, M., Woolrich, M. W., Beckmann, C. F., Behrens, T. E. J., Johansen-Berg, H., Bannister, P. R., De Luca, M., Drobnjak, I., Flitney, D. E., Niazy, R. K., Saunders, J., Vickers, J., Zhang, Y., De Stefano, N., Brady, J. M., & Matthews, P. M. (2004). Advances in functional and structural MR image analysis and implementation as FSL. *NeuroImage*, *23 Suppl 1*, S208-219. <https://doi.org/10.1016/j.neuroimage.2004.07.051>
- Smith, S. M., & Nichols, T. E. (2009). Threshold-free cluster enhancement: Addressing problems of smoothing, threshold dependence and localisation in cluster inference. *NeuroImage*, *44*(1), 83–98. <https://doi.org/10.1016/j.neuroimage.2008.03.061>

- Snowden, J. S. (2017). The Neuropsychology of Huntington's Disease. *Archives of Clinical Neuropsychology*, 32(7), 876–887. <https://doi.org/10.1093/arclin/acx086>
- Snowden, J. S., Austin, N. A., Sembi, S., Thompson, J. C., Craufurd, D., & Neary, D. (2008). Emotion recognition in Huntington's disease and frontotemporal dementia. *Neuropsychologia*, 46(11), 2638–2649. <https://doi.org/10.1016/j.neuropsychologia.2008.04.018>
- Snowden, J. S., Craufurd, D., Thompson, J., & Neary, D. (2002). Psychomotor, executive, and memory function in preclinical Huntington's disease. *Journal of Clinical and Experimental Neuropsychology*, 24(2), 133–145. <https://doi.org/10.1076/jcen.24.2.133.998>
- Snowden, J. S., Gibbons, Z. C., Blackshaw, A., Doubleday, E., Thompson, J., Craufurd, D., Foster, J., Happé, F., & Neary, D. (2003). Social cognition in frontotemporal dementia and Huntington's disease. *Neuropsychologia*, 41(6), 688–701. [https://doi.org/10.1016/s0028-3932\(02\)00221-x](https://doi.org/10.1016/s0028-3932(02)00221-x)
- Snyder, J. M., Hagan, C. E., Bolon, B., & Keene, C. D. (2018). 20—Nervous System. In P. M. Treuting, S. M. Dintzis, & K. S. Montine (Eds.), *Comparative Anatomy and Histology (Second Edition)* (pp. 403–444). Academic Press. <https://doi.org/10.1016/B978-0-12-802900-8.00020-8>
- Song, S.-K., Sun, S.-W., Ramsbottom, M. J., Chang, C., Russell, J., & Cross, A. H. (2002). Demyelination revealed through MRI as increased radial (but unchanged axial) diffusion of water. *NeuroImage*, 17(3), 1429–1436.
- Song, S.-K., Yoshino, J., Le, T. Q., Lin, S.-J., Sun, S.-W., Cross, A. H., & Armstrong, R. C. (2005). Demyelination increases radial diffusivity in corpus callosum of mouse brain. *NeuroImage*, 26(1), 132–140. <https://doi.org/10.1016/j.neuroimage.2005.01.028>

- Sporns, O., Tononi, G., & Kötter, R. (2005). The human connectome: A structural description of the human brain. *PLoS Comput Biol*, *1*(4), e42.
- Sprengelmeyer, R., Young, A. W., Calder, A. J., Karnat, A., Lange, H., Hömberg, V., Perrett, D. I., & Rowland, D. (1996). Loss of disgust. Perception of faces and emotions in Huntington's disease. *Brain: A Journal of Neurology*, *119* ( Pt 5), 1647–1665.  
<https://doi.org/10.1093/brain/119.5.1647>
- Squitieri, F., Cannella, M., Simonelli, M., Sassone, J., Martino, T., Venditti, E., Ciammola, A., Colonnese, C., Frati, L., & Ciarmiello, A. (2009). Distinct Brain Volume Changes Correlating with Clinical Stage, Disease Progression Rate, Mutation Size, and Age at Onset Prediction as Early Biomarkers of Brain Atrophy in Huntington's Disease. *CNS Neuroscience & Therapeutics*, *15*(1), 1–11. <https://doi.org/10.1111/j.1755-5949.2008.00068.x>
- Stanisz, G. J., Webb, S., Munro, C. A., Pun, T., & Midha, R. (2004). MR properties of excised neural tissue following experimentally induced inflammation. *Magnetic Resonance in Medicine*, *51*(3), 473–479. <https://doi.org/10.1002/mrm.20008>
- Steele, C. J., Bailey, J. A., Zatorre, R. J., & Penhune, V. B. (2013). Early musical training and white-matter plasticity in the corpus callosum: Evidence for a sensitive period. *The Journal of Neuroscience: The Official Journal of the Society for Neuroscience*, *33*(3), 1282–1290. <https://doi.org/10.1523/JNEUROSCI.3578-12.2013>
- Stejskal, E. O., & Tanner, J. E. (1965). Spin diffusion measurements: Spin echoes in the presence of a time-dependent field gradient. *The Journal of Chemical Physics*, *42*(1), 288–292.
- Steventon, J. (2014). *Characterising the structural brain changes in Huntington's disease using translational neuroimaging* [Phd, Cardiff University].  
<http://orca.cf.ac.uk/71204/>

- Stidworthy, M. F., Genoud, S., Suter, U., Mantei, N., & Franklin, R. J. M. (2003). Quantifying the early stages of remyelination following cuprizone-induced demyelination. *Brain Pathology (Zurich, Switzerland)*, *13*(3), 329–339. <https://doi.org/10.1111/j.1750-3639.2003.tb00032.x>
- Stout, J. C., Glikmann-Johnston, Y., & Andrews, S. C. (2016). Cognitive assessment strategies in Huntington’s disease research. *Journal of Neuroscience Methods*, *265*, 19–24.
- Stout, J. C., Jones, R., Labuschagne, I., O’Regan, A. M., Say, M. J., Dumas, E. M., Queller, S., Justo, D., Santos, R. D., Coleman, A., Hart, E. P., Dürr, A., Leavitt, B. R., Roos, R. A., Langbehn, D. R., Tabrizi, S. J., & Frost, C. (2012). Evaluation of longitudinal 12 and 24 month cognitive outcomes in premanifest and early Huntington’s disease. *Journal of Neurology, Neurosurgery & Psychiatry*, *83*(7), 687–694. <https://doi.org/10.1136/jnnp-2011-301940>
- Stout, J. C., Paulsen, J. S., Queller, S., Solomon, A. C., Whitlock, K. B., Campbell, J. C., Carlozzi, N., Duff, K., Beglinger, L. J., Langbehn, D. R., Johnson, S. A., Biglan, K. M., & Aylward, E. H. (2011). Neurocognitive signs in prodromal Huntington disease. *Neuropsychology*, *25*(1), 1–14. <https://doi.org/10.1037/a0020937>
- Strong, T. V., Tagle, D. A., Valdes, J. M., Elmer, L. W., Boehm, K., Swaroop, M., Kaatz, K. W., Collins, F. S., & Albin, R. L. (1993). Widespread expression of the human and rat Huntington’s disease gene in brain and nonneural tissues. *Nature Genetics*, *5*(3), 259–265. <https://doi.org/10.1038/ng1193-259>
- Tabrizi, S. J., Langbehn, D. R., Leavitt, B. R., Roos, R. A., Durr, A., Craufurd, D., Kennard, C., Hicks, S. L., Fox, N. C., Scahill, R. I., Borowsky, B., Tobin, A. J., Rosas, H. D., Johnson, H., Reilmann, R., Landwehrmeyer, B., Stout, J. C., & TRACK-HD investigators. (2009). Biological and clinical manifestations of Huntington’s disease

- in the longitudinal TRACK-HD study: Cross-sectional analysis of baseline data. *The Lancet. Neurology*, 8(9), 791–801. [https://doi.org/10.1016/S1474-4422\(09\)70170-X](https://doi.org/10.1016/S1474-4422(09)70170-X)
- Tabrizi, S. J., Leavitt, B. R., Landwehrmeyer, G. B., Wild, E. J., Saft, C., Barker, R. A., Blair, N. F., Craufurd, D., Priller, J., Rickards, H., Rosser, A., Kordasiewicz, H. B., Czech, C., Swayze, E. E., Norris, D. A., Baumann, T., Gerlach, I., Schobel, S. A., Paz, E., ... Lane, R. M. (2019). Targeting Huntingtin Expression in Patients with Huntington's Disease. *New England Journal of Medicine*, 380(24), 2307–2316. <https://doi.org/10.1056/NEJMoa1900907>
- Tabrizi, S. J., Reilmann, R., Roos, R. A. C., Durr, A., Leavitt, B., Owen, G., Jones, R., Johnson, H., Craufurd, D., Hicks, S. L., Kennard, C., Landwehrmeyer, B., Stout, J. C., Borowsky, B., Scahill, R. I., Frost, C., Langbehn, D. R., & TRACK-HD investigators. (2012). Potential endpoints for clinical trials in premanifest and early Huntington's disease in the TRACK-HD study: Analysis of 24 month observational data. *The Lancet. Neurology*, 11(1), 42–53. [https://doi.org/10.1016/S1474-4422\(11\)70263-0](https://doi.org/10.1016/S1474-4422(11)70263-0)
- Tabrizi, S. J., Scahill, R. I., Durr, A., Roos, R. A., Leavitt, B. R., Jones, R., Landwehrmeyer, G. B., Fox, N. C., Johnson, H., Hicks, S. L., Kennard, C., Craufurd, D., Frost, C., Langbehn, D. R., Reilmann, R., Stout, J. C., & TRACK-HD Investigators. (2011). Biological and clinical changes in premanifest and early stage Huntington's disease in the TRACK-HD study: The 12-month longitudinal analysis. *The Lancet. Neurology*, 10(1), 31–42. [https://doi.org/10.1016/S1474-4422\(10\)70276-3](https://doi.org/10.1016/S1474-4422(10)70276-3)
- Tabrizi, S. J., Scahill, R. I., Owen, G., Durr, A., Leavitt, B. R., Roos, R. A., Borowsky, B., Landwehrmeyer, B., Frost, C., Johnson, H., Craufurd, D., Reilmann, R., Stout, J. C., & Langbehn, D. R. (2013). Predictors of phenotypic progression and disease onset in premanifest and early-stage Huntington's disease in the TRACK-HD study: Analysis

of 36-month observational data. *The Lancet Neurology*, *12*(7), 637–649.

[https://doi.org/10.1016/S1474-4422\(13\)70088-7](https://doi.org/10.1016/S1474-4422(13)70088-7)

Takeuchi, H., Sekiguchi, A., Taki, Y., Yokoyama, S., Yomogida, Y., Komuro, N., Yamanouchi, T., Suzuki, S., & Kawashima, R. (2010). Training of working memory impacts structural connectivity. *The Journal of Neuroscience: The Official Journal of the Society for Neuroscience*, *30*(9), 3297–3303.

<https://doi.org/10.1523/JNEUROSCI.4611-09.2010>

Tanaka, M., Machida, Y., Niu, S., Ikeda, T., Jana, N. R., Doi, H., Kurosawa, M., Nekooki, M., & Nukina, N. (2004). Trehalose alleviates polyglutamine-mediated pathology in a mouse model of Huntington disease. *Nature Medicine*, *10*(2), 148–154.

<https://doi.org/10.1038/nm985>

Tang, Y.-Y., Lu, Q., Fan, M., Yang, Y., & Posner, M. I. (2012). Mechanisms of white matter changes induced by meditation. *Proceedings of the National Academy of Sciences*,

*109*(26), 10570–10574. <https://doi.org/10.1073/pnas.1207817109>

Taubert, M., Lohmann, G., Margulies, D. S., Villringer, A., & Ragert, P. (2011). Long-term effects of motor training on resting-state networks and underlying brain structure.

*NeuroImage*, *57*(4), 1492–1498. <https://doi.org/10.1016/j.neuroimage.2011.05.078>

Tavor, I., Hofstetter, S., Ben-Amitay, S., & Assaf, Y. (2011). *Investigation tissue micro-structure changes in short term neuro-plasticity with diffusion MRI*. Proceedings of the 19th Annual Scientific Meeting of the International Society for Magnetic Resonance in Medicine, Montreal, Quebec, Canada.

Team, Rs. (2015). RStudio: Integrated development for R. *RStudio, Inc., Boston, MA URL* <Http://Www.Rstudio.Com>, *42*, 14.

- Tekin, S., & Cummings, J. L. (2002). Frontal–subcortical neuronal circuits and clinical neuropsychiatry: An update. *Journal of Psychosomatic Research*, *53*(2), 647–654. [https://doi.org/10.1016/S0022-3999\(02\)00428-2](https://doi.org/10.1016/S0022-3999(02)00428-2)
- Tendler, B. C., & Bowtell, R. (2019). Frequency difference mapping applied to the corpus callosum at 7T. *Magnetic Resonance in Medicine*, *81*(5), 3017–3031. <https://doi.org/10.1002/mrm.27626>
- Teo, R. T. Y., Hong, X., Yu-Taeger, L., Huang, Y., Tan, L. J., Xie, Y., To, X. V., Guo, L., Rajendran, R., Novati, A., Calaminus, C., Riess, O., Hayden, M. R., Nguyen, H. P., Chuang, K.-H., & Pouladi, M. A. (2016). Structural and molecular myelination deficits occur prior to neuronal loss in the YAC128 and BACHD models of Huntington disease. *Human Molecular Genetics*, *25*(13), 2621–2632. <https://doi.org/10.1093/hmg/ddw122>
- Testa, R., Bennett, P., & Ponsford, J. (2012). Factor analysis of nineteen executive function tests in a healthy adult population. *Archives of Clinical Neuropsychology: The Official Journal of the National Academy of Neuropsychologists*, *27*(2), 213–224. <https://doi.org/10.1093/arclin/acr112>
- Thapaliya, K., Vegh, V., Bollmann, S., & Barth, M. (2017). Assessment of microstructural signal compartments across the corpus callosum using multi-echo gradient recalled echo at 7 T. *NeuroImage*. <https://doi.org/10.1016/j.neuroimage.2017.11.029>
- Thiessen, J. D., Zhang, Y., Zhang, H., Wang, L., Buist, R., Del Bigio, M. R., Kong, J., Li, X., & Martin, M. (2013). Quantitative MRI and ultrastructural examination of the cuprizone mouse model of demyelination. *NMR in Biomedicine*, *26*(11), 1562–1581.
- Thomas, C., & Baker, C. I. (2013). Teaching an adult brain new tricks: A critical review of evidence for training-dependent structural plasticity in humans. *NeuroImage*, *73*, 225–236. <https://doi.org/10.1016/j.neuroimage.2012.03.069>

- Thompson, J. C., Harris, J., Sollom, A. C., Stopford, C. L., Howard, E., Snowden, J. S., & Craufurd, D. (2012). Longitudinal Evaluation of Neuropsychiatric Symptoms in Huntington's Disease. *J Neuropsychiatry Clin Neurosci*, 8.
- Tournier, J.-D., Calamante, F., & Connelly, A. (2007). Robust determination of the fibre orientation distribution in diffusion MRI: non-negativity constrained super-resolved spherical deconvolution. *Neuroimage*, 35(4), 1459–1472.
- Tournier, J.-D., Calamante, F., Gadian, D. G., & Connelly, A. (2004). Direct estimation of the fiber orientation density function from diffusion-weighted MRI data using spherical deconvolution. *Neuroimage*, 23(3), 1176–1185.
- Tournier, J.-D., Smith, R., Raffelt, D., Tabbara, R., Dhollander, T., Pietsch, M., Christiaens, D., Jeurissen, B., Yeh, C.-H., & Connelly, A. (2019). MRtrix3: A fast, flexible and open software framework for medical image processing and visualisation. *NeuroImage*, 202, 116137. <https://doi.org/10.1016/j.neuroimage.2019.116137>
- Trinkler, I., Cleret de Langavant, L., & Bachoud-Lévi, A.-C. (2013). Joint recognition-expression impairment of facial emotions in Huntington's disease despite intact understanding of feelings. *Cortex; a Journal Devoted to the Study of the Nervous System and Behavior*, 49(2), 549–558. <https://doi.org/10.1016/j.cortex.2011.12.003>
- Turati, L., Moscatelli, M., Mastropietro, A., Dowell, N. G., Zucca, I., Erbetta, A., Cordiglieri, C., Brenna, G., Bianchi, B., & Mantegazza, R. (2015). In vivo quantitative magnetization transfer imaging correlates with histology during de- and remyelination in cuprizone-treated mice. *NMR in Biomedicine*, 28(3), 327–337.
- Tustison, N. J., Avants, B. B., Cook, P. A., Zheng, Y., Egan, A., Yushkevich, P. A., & Gee, J. C. (2010). N4ITK: Improved N3 bias correction. *IEEE Transactions on Medical Imaging*, 29(6), 1310–1320. <https://doi.org/10.1109/TMI.2010.2046908>

- Unified Huntington's disease rating scale: Reliability and consistency. (1996). *Movement Disorders*, 11(2), 136–142. <https://doi.org/10.1002/mds.870110204>
- Valkanova, V., Eguia Rodriguez, R., & Ebmeier, K. P. (2014). Mind over matter—What do we know about neuroplasticity in adults? *International Psychogeriatrics*, 26(6), 891–909. <https://doi.org/10.1017/S1041610213002482>
- van den Bogaard, S. J. A., Dumas, E. M., Acharya, T. P., Johnson, H., Langbehn, D. R., Scahill, R. I., Tabrizi, S. J., van Buchem, M. A., van der Grond, J., Roos, R. A. C., & TRACK-HD Investigator Group. (2011). Early atrophy of pallidum and accumbens nucleus in Huntington's disease. *Journal of Neurology*, 258(3), 412–420. <https://doi.org/10.1007/s00415-010-5768-0>
- van Dijk, J. G., van der Velde, E. A., Roos, R. A., & Bruyn, G. W. (1986). Juvenile Huntington disease. *Human Genetics*, 73(3), 235–239. <https://doi.org/10.1007/BF00401235>
- van Gelderen, P., de Zwart, J. A., Lee, J., Sati, P., Reich, D. S., & Duyn, J. H. (2012). Non-exponential T2\* decay in White Matter. *Magnetic Resonance in Medicine*, 67(1), 110–117. <https://doi.org/10.1002/mrm.22990>
- Van Hecke, W., Leemans, A., De Backer, S., Jeurissen, B., Parizel, P. M., & Sijbers, J. (2010). Comparing isotropic and anisotropic smoothing for voxel-based DTI analyses: A simulation study. *Human Brain Mapping*, 31(1), 98–114.
- Vaughan, J. T., Garwood, M., Collins, C. M., Liu, W., DelaBarre, L., Adriany, G., Andersen, P., Merkle, H., Goebel, R., Smith, M. B., & Ugurbil, K. (2001). 7T vs. 4T: RF power, homogeneity, and signal-to-noise comparison in head images. *Magnetic Resonance in Medicine*, 46(1), 24–30. <https://doi.org/10.1002/mrm.1156>

- Veraart, J., Fieremans, E., & Novikov, D. S. (2016). Diffusion MRI noise mapping using random matrix theory. *Magnetic Resonance in Medicine*, 76(5), 1582–1593.  
<https://doi.org/10.1002/mrm.26059>
- Veraart, J., Nunes, D., Rudrapatna, U., Fieremans, E., Jones, D. K., Novikov, D. S., & Shemesh, N. (2020). Noninvasive quantification of axon radii using diffusion MRI. *ELife*, 9, e49855. <https://doi.org/10.7554/eLife.49855>
- Vinther-Jensen, T., Simonsen, A., Budtz-Jørgensen, E., Hjermand, L., & Nielsen, J. E. (2015). Ubiquitin: A potential cerebrospinal fluid progression marker in Huntington's disease. *European Journal of Neurology*, 22(10), 1378–1384.
- Vinther-Jensen, T., Simonsen, A. H., Budtz-Jørgensen, E., Hjermand, L. E., & Nielsen, J. E. (n.d.). Ubiquitin: A potential cerebrospinal fluid progression marker in Huntington's disease. *European Journal of Neurology*, 22(10), 1378–1384.  
<https://doi.org/10.1111/ene.12750>
- von Hörsten, S., Schmitt, I., Nguyen, H. P., Holzmann, C., Schmidt, T., Walther, T., Bader, M., Pabst, R., Kobbe, P., Krotova, J., Stiller, D., Kask, A., Vaarmann, A., Rathke-Hartlieb, S., Schulz, J. B., Grasshoff, U., Bauer, I., Vieira-Saecker, A. M. M., Paul, M., ... Riess, O. (2003). Transgenic rat model of Huntington's disease. *Human Molecular Genetics*, 12(6), 617–624. <https://doi.org/10.1093/hmg/ddg075>
- Vonsattel, J. P. G., & Difiglia, M. (1998). Huntington Disease. *Journal of Neuropathology & Experimental Neurology*, 57(5), 369–384. <https://doi.org/10.1097/00005072-199805000-00001>
- Vonsattel, J.-P., Myers, R. H., Stevens, T. J., Ferrante, R. J., Bird, E. D., & Richardson, E. P. (1985). Neuropathological Classification of Huntington's Disease. *Journal of Neuropathology & Experimental Neurology*, 44(6), 559–577.  
<https://doi.org/10.1097/00005072-198511000-00003>

- Voracek, M., & Dressler, S. G. (2006). Lack of correlation between digit ratio (2D:4D) and Baron-Cohen's "Reading the Mind in the Eyes" test, empathy, systemising, and autism-spectrum quotients in a general population sample. *Personality and Individual Differences, 41*(8), 1481–1491. <https://doi.org/10.1016/j.paid.2006.06.009>
- Vos, S. B., Tax, C. M. W., Luijten, P. R., Ourselin, S., Leemans, A., & Froeling, M. (2017). The importance of correcting for signal drift in diffusion MRI. *Magnetic Resonance in Medicine, 77*(1), 285–299. <https://doi.org/10.1002/mrm.26124>
- Wahl, M., Li, Y.-O., Ng, J., Lahue, S. C., Cooper, S. R., Sherr, E. H., & Mukherjee, P. (2010). Microstructural correlations of white matter tracts in the human brain. *NeuroImage, 51*(2), 531–541. <https://doi.org/10.1016/j.neuroimage.2010.02.072>
- Wang, Y., van Gelderen, P., de Zwart, J. A., & Duyn, J. H. (2020). B0-field dependence of MRI T1 relaxation in human brain. *NeuroImage, 213*, 116700. <https://doi.org/10.1016/j.neuroimage.2020.116700>
- Wanker, E. E. (2000). Protein aggregation in Huntington's and Parkinson's disease: Implications for therapy. *Molecular Medicine Today, 6*(10), 387–391. [https://doi.org/10.1016/S1357-4310\(00\)01761-5](https://doi.org/10.1016/S1357-4310(00)01761-5)
- Warrick, J. M., Paulson, H. L., Gray-Board, G. L., Bui, Q. T., Fischbeck, K. H., Pittman, R. N., & Bonini, N. M. (1998). Expanded polyglutamine protein forms nuclear inclusions and causes neural degeneration in *Drosophila*. *Cell, 93*(6), 939–949. [https://doi.org/10.1016/s0092-8674\(00\)81200-3](https://doi.org/10.1016/s0092-8674(00)81200-3)
- Wasserthal, J., Neher, P., & Maier-Hein, K. H. (2018). TractSeg—Fast and accurate white matter tract segmentation. *NeuroImage, 183*, 239–253. <https://doi.org/10.1016/j.neuroimage.2018.07.070>

- Weaver, K. E., Richards, T. L., Liang, O., Laurino, M. Y., Samii, A., & Aylward, E. H. (2009). Longitudinal diffusion tensor imaging in Huntington's Disease. *Experimental Neurology*, 216(2), 525–529. <https://doi.org/10.1016/j.expneurol.2008.12.026>
- Wechsler, D. (1997). Wechsler Adult Intelligence Scale—Revised UK. *New York: Psychological Corporation*;
- Wechsler, D. (2011). Test of premorbid functioning. UK version (TOPF UK). *UK: Pearson Corporation*.
- Wendler, A., & Wehling, M. (2010). The translatability of animal models for clinical development: Biomarkers and disease models. *Current Opinion in Pharmacology*, 10(5), 601–606. <https://doi.org/10.1016/j.coph.2010.05.009>
- West, K. L., Kelm, N. D., Carson, R. P., & Does, M. D. (2015). Quantitative analysis of mouse corpus callosum from electron microscopy images. *Data in Brief*, 5, 124–128.
- Wharton, S., & Bowtell, R. (2012). Fiber orientation-dependent white matter contrast in gradient echo MRI. *Proceedings of the National Academy of Sciences of the United States of America*, 109(45), 18559–18564. <https://doi.org/10.1073/pnas.1211075109>
- Wharton, S., & Bowtell, R. (2013). Gradient echo based fiber orientation mapping using R2\* and frequency difference measurements. *NeuroImage*, 83, 1011–1023. <https://doi.org/10.1016/j.neuroimage.2013.07.054>
- Wheeler, V. C., Persichetti, F., McNeil, S. M., Mysore, J. S., Mysore, S. S., MacDonald, M. E., Myers, R. H., Gusella, J. F., & Wexler, N. S. (2007). Factors associated with HD CAG repeat instability in Huntington disease. *Journal of Medical Genetics*, 44(11), 695–701. <https://doi.org/10.1136/jmg.2007.050930>
- Wheeler-Kingshott, C. A. M., & Cercignani, M. (2009). About “axial” and “radial” diffusivities. *Magnetic Resonance in Medicine*, 61(5), 1255–1260. <https://doi.org/10.1002/mrm.21965>

- Wickham, H. (2014). Tidy data. *Journal of Statistical Software*, 59(10), 1–23.
- Wilcox, R. R. (2011). *Introduction to Robust Estimation and Hypothesis Testing*. Academic Press.
- Wild, E. J., & Tabrizi, S. J. (2019). One decade ago, one decade ahead in huntington's disease. *Movement Disorders*, 34(10), 1434–1439. <https://doi.org/10.1002/mds.27849>
- Williams, J. K., Barnette, J. J., Reed, D., Sousa, V. D., Schutte, D. L., McGonigal-Kenney, M., Jarmon, L., Phillips, E., Tripp-Reimer, T., & Paulsen, J. S. (2010). Development of the Huntington Disease Family Concerns and Strategies Survey From Focus Group Data. *Journal of Nursing Measurement*, 18(2), 83–99.
- Williams, J. K., Kim, J.-I., Downing, N., Farias, S., Harrington, D. L., Long, J. D., Mills, J. A., Paulsen, J. S., & PREDICT-HD Investigators and Coordinators of the Huntington Study Group. (2015). Everyday cognition in prodromal Huntington disease. *Neuropsychology*, 29(2), 255–267. <https://doi.org/10.1037/neu0000102>
- Winkler, A. M., Ridgway, G. R., Webster, M. A., Smith, S. M., & Nichols, T. E. (2014). Permutation inference for the general linear model. *NeuroImage*, 92, 381–397. <https://doi.org/10.1016/j.neuroimage.2014.01.060>
- Winter, J. C. F. de, Dodou, D., & Wieringa, P. A. (2009). Exploratory Factor Analysis With Small Sample Sizes. *Multivariate Behavioral Research*, 44(2), 147–181. <https://doi.org/10.1080/00273170902794206>
- Wisnieff, C., Ramanan, S., Olesik, J., Gauthier, S., Wang, Y., & Pitt, D. (2015). Quantitative susceptibility mapping (QSM) of white matter multiple sclerosis lesions: Interpreting positive susceptibility and the presence of iron. *Magnetic Resonance in Medicine*, 74(2), 564–570.
- Wolff, S. D., & Balaban, R. S. (1994). Magnetization transfer imaging: Practical aspects and clinical applications. *Radiology*, 192(3), 593–599.

- Wood, N. I., Glynn, D., & Morton, A. J. (2011). “Brain training” improves cognitive performance and survival in a transgenic mouse model of Huntington’s disease. *Neurobiology of Disease*, 42(3), 427–437. <https://doi.org/10.1016/j.nbd.2011.02.005>
- Wood, T. C., Lythgoe, D. J., & Williams, S. C. (2013). *RBET: making BET work for rodent brains*. 21, 2706.
- Xiang, Z., Valenza, M., Cui, L., Leoni, V., Jeong, H.-K., Brilli, E., Zhang, J., Peng, Q., Duan, W., Reeves, S. A., Cattaneo, E., & Krainc, D. (2011). Peroxisome-proliferator-activated receptor gamma coactivator 1  $\alpha$  contributes to dysmyelination in experimental models of Huntington’s disease. *The Journal of Neuroscience: The Official Journal of the Society for Neuroscience*, 31(26), 9544–9553. <https://doi.org/10.1523/JNEUROSCI.1291-11.2011>
- Xiao, L., Ohayon, D., McKenzie, I. A., Sinclair-Wilson, A., Wright, J. L., Fudge, A. D., Emery, B., Li, H., & Richardson, W. D. (2016). Rapid production of new oligodendrocytes is required in the earliest stages of motor skill learning. *Nature Neuroscience*, 19(9), 1210–1217. <https://doi.org/10.1038/nn.4351>
- Xie, M., Tobin, J. E., Budde, M. D., Chen, C.-I., Trinkaus, K., Cross, A. H., McDaniel, D. P., Song, S.-K., & Armstrong, R. C. (2010). Rostrocaudal analysis of corpus callosum demyelination and axon damage across disease stages refines diffusion tensor imaging correlations with pathological features. *Journal of Neuropathology and Experimental Neurology*, 69(7), 704–716. <https://doi.org/10.1097/NEN.0b013e3181e3de90>
- Xu, X., Wang, Q., & Zhang, M. (2008). Age, gender, and hemispheric differences in iron deposition in the human brain: An in vivo MRI study. *Neuroimage*, 40(1), 35–42.
- Yakovlev, P. (1967). The myelogenetic cycles of regional maturation of the brain. *Regional Development of the Brain in Early Life*, 3–70.

- Yang, S.-H., Cheng, P.-H., Banta, H., Piotrowska-Nitsche, K., Yang, J.-J., Cheng, E. C. H., Snyder, B., Larkin, K., Liu, J., Orkin, J., Fang, Z.-H., Smith, Y., Bachevalier, J., Zola, S. M., Li, S.-H., Li, X.-J., & Chan, A. W. S. (2008). Towards a transgenic model of Huntington's disease in a non-human primate. *Nature*, *453*(7197), 921–924.  
<https://doi.org/10.1038/nature06975>
- Yhnell, E., Furby, H., Breen, R. S., Brookes-Howell, L. C., Drew, C. J. G., Playle, R., Watson, G., Metzler-Baddeley, C., Rosser, A. E., & Busse, M. E. (2018). Exploring computerised cognitive training as a therapeutic intervention for people with Huntington's disease (CogTrainHD): Protocol for a randomised feasibility study. *Pilot and Feasibility Studies*, *4*(1), 45. <https://doi.org/10.1186/s40814-018-0237-0>
- Yhnell, E., Lelos, M. J., Dunnett, S. B., & Brooks, S. P. (2016). Cognitive training modifies disease symptoms in a mouse model of Huntington's disease. *Experimental Neurology*, *282*, 19–26. <https://doi.org/10.1016/j.expneurol.2016.05.008>
- Yin, H. H., Mulcare, S. P., Hilário, M. R. F., Clouse, E., Holloway, T., Davis, M. I., Hansson, A. C., Lovinger, D. M., & Costa, R. M. (2009). Dynamic reorganization of striatal circuits during the acquisition and consolidation of a skill. *Nature Neuroscience*, *12*(3), 333–341. <https://doi.org/10.1038/nn.2261>
- Younes, L., Ratnanather, J. T., Brown, T., Aylward, E., Nopoulos, P., Johnson, H., Magnotta, V. A., Paulsen, J. S., Margolis, R. L., Albin, R. L., Miller, M. I., Ross, C. A., & PREDICT-HD Investigators and Coordinators of the Huntington Study Group. (2014). Regionally selective atrophy of subcortical structures in prodromal HD as revealed by statistical shape analysis. *Human Brain Mapping*, *35*(3), 792–809.  
<https://doi.org/10.1002/hbm.22214>

- Zalesky, A. (2011). Moderating registration misalignment in voxelwise comparisons of DTI data: A performance evaluation of skeleton projection. *Magnetic Resonance Imaging*, 29(1), 111–125.
- Zarotti, N., Simpson, J., Fletcher, I., Squitieri, F., & Migliore, S. (2018). Exploring emotion regulation and emotion recognition in people with presymptomatic Huntington's disease: The role of emotional awareness. *Neuropsychologia*, 112, 1–9.
- Zatorre, R. J., Fields, R. D., & Johansen-Berg, H. (2012). Plasticity in gray and white: Neuroimaging changes in brain structure during learning. *Nature Neuroscience*, 15(4), 528–536. <https://doi.org/10.1038/nn.3045>
- Zecca, L., Youdim, M. B., Riederer, P., Connor, J. R., & Crichton, R. R. (2004). Iron, brain ageing and neurodegenerative disorders. *Nature Reviews Neuroscience*, 5(11), 863–873.
- Zeitlin, S., Liu, J. P., Chapman, D. L., Papaioannou, V. E., & Efstratiadis, A. (1995). Increased apoptosis and early embryonic lethality in mice nullizygous for the Huntington's disease gene homologue. *Nature Genetics*, 11(2), 155–163. <https://doi.org/10.1038/ng1095-155>
- Zhang, H., Schneider, T., Wheeler-Kingshott, C. A., & Alexander, D. C. (2012). NODDI: Practical in vivo neurite orientation dispersion and density imaging of the human brain. *NeuroImage*, 61(4), 1000–1016. <https://doi.org/10.1016/j.neuroimage.2012.03.072>
- Zhang, J., Gregory, S., Scahill, R. I., Durr, A., Thomas, D. L., Lehericy, S., Rees, G., Tabrizi, S. J., & Zhang, H. (2018). In vivo characterization of white matter pathology in premanifest huntington's disease. *Annals of Neurology*, 84(4), 497–504. <https://doi.org/10.1002/ana.25309>

Zikopoulos, B., Liu, X., Tepe, J., Trutzer, I., John, Y. J., & Barbas, H. (2018). Opposite development of short- and long-range anterior cingulate pathways in autism. *Acta Neuropathologica*, 136(5), 759–778. <https://doi.org/10.1007/s00401-018-1904-1>